# Maximising the Science Returns of the LINC-NIRVANA Multi-Conjugated Adaptive Optics System

**Kalyan Kumar Radhakrishnan Santhakumari**

*Max-Planck-Institut für Astronomie / Universität Heidelberg*

**Heidelberg 2017**

**Dissertation**
**submitted to the**

**Combined Faculties of the Natural Sciences and Mathematics**

**of the Ruperto-Carola-University of Heidelberg, Germany,**

**for the degree of**

**Doctor of Natural Sciences**

**Put forward by**

***Kalyan Kumar Radhakrishnan Santhakumari***

**born in Thiruvananthapuram, Kerala, India**

**Oral examination: November 22nd, 2017**

# Maximising the Science Returns of the LINC-NIRVANA Multi-Conjugated Adaptive Optics System

**Referees:** **Prof. Coryn Bailer-Jones**
**Prof. Roberto Ragazzoni**

*To Radhakrishnan and Santhakumari*

# Abstract

Earth's fully turbulent atmosphere prevents ground-based optical and near-infrared telescopes (larger than 30 cm) to reach their full potential, i.e. their diffraction-limited capabilities. In order to overcome this limitation, real-time correction of the aberrations caused by the atmosphere is essential. This is done using a technique called Adaptive Optics (AO). Achieving wide-field correction requires an extension to this technique known as Multi-Conjugated Adaptive Optics (MCAO). My PhD concentrated on maximising the scientific return of one such MCAO system, the LINC-NIRVANA (LN) instrument currently undergoing commissioning at the Large Binocular Telescope. Starting from alignment and calibration in the lab to the on-going commissioning, I have contributed to the optical assembly, integration, verification, and software development of the LN MCAO system. I also solved a particular challenge faced by the MCAO systems, namely the "partial illumination issue". In addition, I also developed a concept that can improve the AO performance, which we call as the "wind predictive control". Finally, to understand the astrophysical capabilities of an AO system, I studied a pre-main sequence star system, the T Tauri, using observations from two instruments with advanced AO systems capable of providing high-contrast high-resolution near-infrared imagery.

# Zusammenfassung

Die turbulente Atmosphäre der Erde verhindert, dass das volle, beugungsbegrenzte Potential bodengebundener, im optischen oder nah-infraroten Wellenlängenbereich operierender, Teleskope ab einer gewissen Größe genutzt werden kann. Zur Überwindung dieser Einschränkung ist eine Echtzeitkorrektur der durch die Atmosphäre eingeführten Aberrationen unumgänglich. Dies wird mit Hilfe einer Technik erreicht, die sich "Adaptive Optik" nennt. Eine Erweiterung dieser Technik, die sogenannte "Multi Conjugate Adaptive Optics" (MCAO), erlaubt die Korrektur über ein großes Gesichtsfeld. Ein wesentliches Ziel meine Doktorarbeit bestand darin, den wissenschaftlichen Ertrag eines solchen MCAO Systems zu maximieren. Es handelt sich um das MCAO System des LINC-NIRVANA (LN) Instruments, das derzeit am Large Binocular Telescope in Betrieb genommen wird. Ich habe mitgewirkt bei Zusammenbau, Integration und Verifikation, sowie bei der Entwicklung der Software des LN MCAO Systems, beginnend mit der optischen Justage und Kalibration im Labor bis zur derzeit noch anhaltenden Phase der Inbetriebnahme am Teleskop. Für die MCAO Systemen inhärente Problematik der "partiellen Beleuchtung" habe ich eine Lösung erarbeitet. Des weiteren habe ich ein Konzept entwickelt, das wir "wind predictive control" nennen. Dabei wird die Leistungsfähigkeit des AO Systems gesteigert durch die Berücksichtigung von Eigenschaften des Windes in der AO Regelschleife. Zur Demonstration der astrophysikalischen Möglichkeiten, die ein AO System zur Verfügung stellt, habe ich abschließend beispielhaft das Vor-Hauptreihensternsystem T Tauri untersucht. Dabei verwendete ich Beobachtungsdaten von zwei Instrumenten, die mit Hilfe hochentwickelter AO Systeme Bilddaten liefern mit hohem Kontrast und hoher Winkelauflösung.

# Acronyms

| | |
|---|---|
| **ARF** | Absolute Reference Fiber |
| **dmCommands** | actuator commands |
| **AO** | Adaptive Optics |
| **ASM** | Adaptive Secondary Mirror |
| **AIV** | Alignment, Integration, and Verification |
| **CU** | Calibration Unit |
| **CU-mirror** | Calibration Unit folding mirror |
| **CCD** | Charge-Coupled Device |
| **DM** | Deformable Mirror |
| **XAO** | eXtreme Adaptive Optics |
| **FoV** | Field of View |
| **FFTS** | Fringe and Flexure Tracker System |
| **FWHM** | Full Width at Half Maximum |
| **GLAO** | Ground Layer Adaptive Optics |
| **GWS** | Ground-layer Wavefront Sensor |
| **HWS** | High-layer Wavefront Sensor |
| **KL** | Karhunen-Loève |
| **LBT** | Large Binocular Telescope |
| **LGS** | Laser Guide Star |
| **LINC-NIRVANA** | LBT INterferometric Camera and Near-InfraRed/Visible Adaptive iNterferometer for Astronomy |
| **LN** | LINC-NIRVANA |
| **ML** | Magic Lantern |

| | |
|---|---|
| **MPIA** | Max Plank Institute for Astronomy |
| **m2c** | modes-to-commands matrix |
| **MAD** | Multi-conjugated Adaptive optics Demonstrator |
| **MCAO** | Multi-Conjugated Adaptive Optics |
| **MFoV** | Multiple Field of View |
| **NGS** | Natural Guide Star |
| **NIR** | Near-InfraRed |
| **OPD** | Optical Path Difference |
| **PSF** | Point Spread Function |
| **PAE** | Preliminary Acceptance Europe |
| **PWFS** | Pyramid Wavefront Sensor |
| **RFP** | Reference Fiber Plate |
| **RMS** | Root Mean Square |
| **SCAO** | Single-Conjugated Adaptive Optics |
| **SNR** | Signal to Noise Ratio |
| **SE** | Star Enlargers |
| **SR** | Strehl Ratio |
| **TTS** | T Tauri Stars |
| **TFFH** | Taylor's Frozen Flow Hypothesis |
| **TAN** | Twice As Nice |
| **WFE** | WaveFront Error |
| **WFS** | Wavefront Sensor |
| **YSO** | Young Stellar Objects |

# Contents

# Chapter 1

# Introduction

Astronomy is one of the oldest sciences, and it has evolved into a systematic and elegant discipline with very many branches, many of them linked directly to new developments in technology. The popularity and success of astronomy is a proof for continuing human curiosity, thirst for knowledge, and the drive to explore Nature.

Telescopes and improving detector technologies are pushing back the heavenly boundaries. We are able to observe farther and fainter objects, and acquire better quality images and spectra than ever before at multiple wavelengths. We are building extremely large (30-40 m class) telescopes on Earth. Many very large (8-10 m class) telescopes are already running successfully. Although the increase in collecting area allows us to go deeper and fainter, the spatial resolution and quality of observations are limited by the continuously-varying Earth's atmosphere (due to spatial and temporal variations in refractive index). We have space telescopes which observe the deep sky and are not affected by the Earth's atmosphere. However, the cost of production and transporting them to space is very high, and maintenance or upgrades introduce complications and further cost. Even international collaborations have so far been unable to deliver a large aperture astronomical telescope to space. All these difficulties have lead astronomers and astrophysicists to build very large to extremely large telescopes on the ground.

## 1.1 Observing through the turbulent atmosphere

### 1.1.1 Diffraction-limited telescope

A telescope[1] receives a part of the incoming wavefront[2] from a celestial source. This light is focused onto the focal plane, where a detector captures the image. In the ideal case (geometrical

[1] Henceforth, when I mention telescope, I mean optical/infrared ground-based telescope.

[2] defined as the surface over which the optical wave has a constant phase.

optics), the image of a point source is itself a point. However, even with perfect optics, we cannot obtain a perfect image, due to *diffraction*. When a light wave encounters an obstacle, such as a telescope aperture, the direction of propagation changes as explained by the Huygens principle. In the absence of atmosphere, the wavefront reaching the telescope from a distant source is flat.

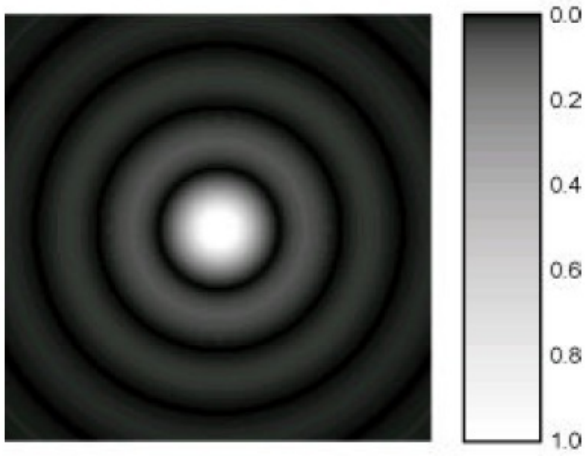


**Figure 1.1:** The Airy diffraction Pattern.

The telescope stop, or aperture, allows only a portion of the wavefront to pass through and reach the focal plane. The stop defines an area through which the photons can move. This introduces an uncertainty in the direction of motion of the photons, as explained by *Heisenberg's uncertainty principle*. The result is image enlargement of the point-like source. When we have a circular aperture, the diffraction pattern consists of a bright central region, surrounded by a series of dark and bright rings, which get fainter and fainter as the distance from the central maximum increases. This is called the *Airy* pattern, as depicted in Figure 1.1. The response of an imaging system to a point source is called the Point Spread Function (PSF).

Two point sources are said to be just *resolved* when the maximum of the diffraction pattern of one of them lies at the first minimum of the other. For an ideal telescope in the absence of the atmosphere, the minimum angular distance between two resolved sources corresponds to the radius (in radians) of the first dark ring of the Airy pattern, given by

$$d\theta_{airy} = 1.22\,\frac{\lambda}{D}, \tag{1.1}$$

where $\lambda$ is the wavelength and $D$ is the diameter of the telescope. However, in the real world, the image suffers from other distortions as well. The minimum angular separation that can be

resolved into two close-by sources ($d\theta_{total}$) in a real-world scenario can be summarised as follows:

$$d\theta^2_{total} = d\theta^2_{airy} + d\theta^2_{al} + d\theta^2_{opt} + d\theta^2_{opt}(t), \tag{1.2}$$

where $d\theta_{al}$ represents the errors in the instrument manufacture and alignment of the optical surfaces, the $d\theta_{opt}$ term is due to the net static optical aberrations introduced within instrument, $d\theta_{opt}(t)$ accounts for the effects of the atmosphere ($t < 1s$; minimised by adaptive optics, discussed later), and mechanical distortions, like flexures and long term temperature variation effects ($t > 1s$; active optics regime). When $d\theta_{total} = d\theta_{airy}$, the telescope is "diffraction limited".

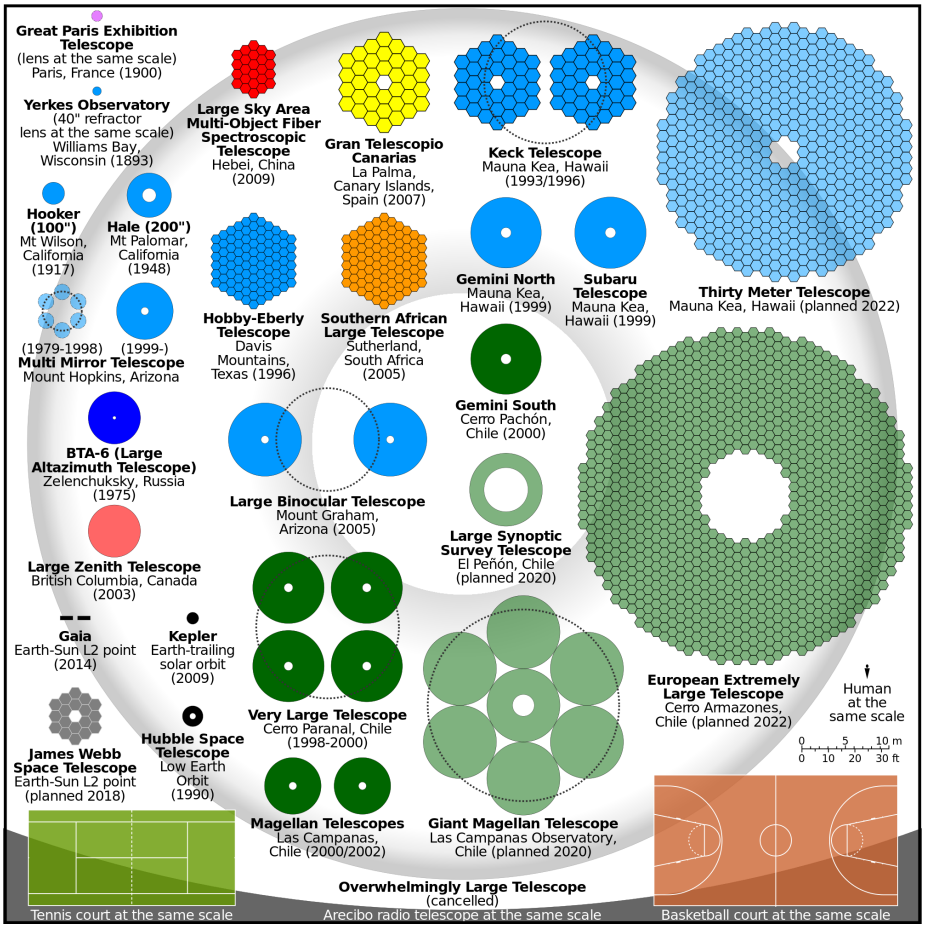


**Figure 1.2:** Comparison of nominal sizes of primary mirrors of notable optical telescopes. For multi-pupil telescopes such as the Large Binocular Telescope, dotted lines show mirrors with equivalent light-gathering ability. This image is taken from Wikipedia[3].

[3]https://commons.wikimedia.org/wiki/File%3AComparison_optical_telescope_primary_mirrors.svg (retrieved on 07 September 2017).

Since their first astronomical use, the diameter of telescopes has grown from a few centimeters to tens of meters. Figure 1.2 depicts this evolution. An increase in the collecting area of the light bucket allows us to observe fainter targets, and the spatial resolution increases when the telescope diameter increases from up to around 30 cm. However, optics larger than this do not improve the spatial resolution (for visible wavelengths). In fact, the best angular resolution at a reasonable telescope site is 1 arcsec (~5 $\mu$rad) at visible wavelengths, irrespective of the telescope size. For comparison, 0.013 arcsec is the theoretically possible resolution of an 8 m telescope at visible wavelengths. This is a direct consequence of the presence of the Earth's atmosphere, as explained in the following section.

### 1.1.2 Turbulent atmosphere

We receive almost all information about distant celestial objects via electromagnetic radiation (light). We should therefore be concerned about any variation or modification to the incoming light. The light reaching us is almost unperturbed till the top of Earth's atmosphere. In other words, until the last millisecond of its journey. It gets modified or altered when it enters the atmosphere.

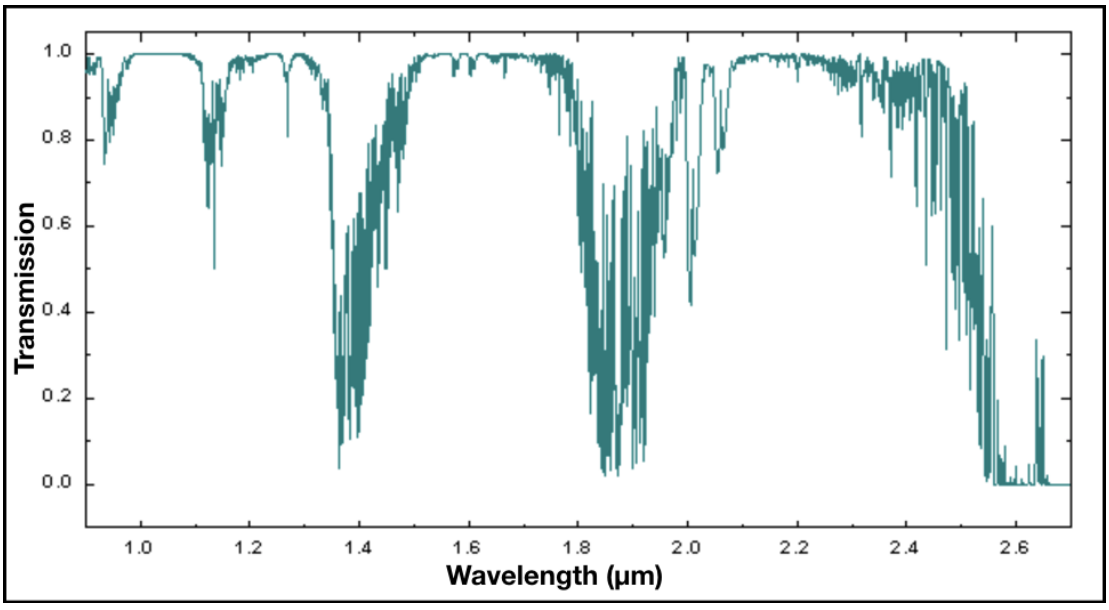


**Figure 1.3:** The atmospheric transmission window in the near-infrared regime at Mauna Kea. Image taken from the Gemini telescope website[4].

[4]https://www.gemini.edu/sciops/telescopes-and-sites/observing-condition-constraints/ir-transmission-spectra (retrieved on 07 September 2017). Full atmospheric transmission window can be seen in this link.

The atmosphere contains atoms, molecules and dust particles. The incoming radiation can interact with the atoms or molecules via scattering or absorption. Absorption usually happens at discrete wavelengths. However, molecules have high degrees of freedom, mainly rotational and vibrational, and the energy levels can be really close to one another. The absorption can hence occur over a wide band. There are some "windows" where the atmosphere is transparent (least absorption) to the incoming light - in the visible regime, radio domain, small regions in the near and mid infrared, and a small region in the near ultra-violet. Figure 1.3 shows the atmospheric transmission window at Mouna Kea in the near-infrared regime. Water molecules, carbon dioxide molecules, and ozone molecules cause the atmospheric transmittance to vary significantly in the wavelength range 1 to 10 micrometer. During moonless nights, most of the atmospheric radiation in the range 0.5 to 2.5 micrometer is due to airglow emission from hydroxyl molecules (OH). The brightness of the background sky sets a practical limit to observations of faint objects from Earth. The observations in this thesis use only the visible and infrared wavelength regimes. Unless otherwise mentioned, from now on, when I mention wavelengths ($\lambda$), I mean these wavelengths only.

Atmospheric turbulence is the cause of distortion of the incoming wavefront. Turbulence arises from the heating and cooling of the Earth's surface by the Sun. During the day, land masses warm up, in turn heating the air. The surface cools down during the night and this is also coupled with the air. This diurnal heating and cooling results in large-spatial-scale motions of the atmosphere. The motions eventually become turbulent. The large scale motions break down progressively into smaller scale motions, giving rise to randomly distributed and sized "pockets" of air. These pockets are called turbulent eddies and each has a characteristic temperature. We know that the refractive index ($n$) of air depends on temperature, and the variation of the temperature as a function of altitude can be seen in Figure 1.4. When a wavefront travels from one medium to another, with a different refractive index, the direction of propagation changes in accordance with *Snell's* law.

By definition, the refractive index in vacuum is $n = 1$. For the air near the Earth's surface, the refractive index varies at the $4^{\text{th}}$ decimal place with respect to vacuum. The variation of the refractive index is not monotonic as the light travels to the ground. If we assume that it does so for simplicity, considering Earth's atmosphere as series of concentric shells, the light will always bend towards the Earth's surface normal. The issue is that the refractive index has a gradient not only in the vertical direction but also horizontally. There are continuous spatial and temporal vertical and horizontal variations of refractive index on small scales. This continuously bends the wave trajectories, thereby changing the phase, or in other words the wavefront. The net result is wavefront perturbation. The resolution of the telescope is limited by the atmospheric turbulence

[5]https://commons.wikimedia.org/wiki/File:Comparison_US_standard_atmosphere_1962.svg (retrieved on 07 September 2017).

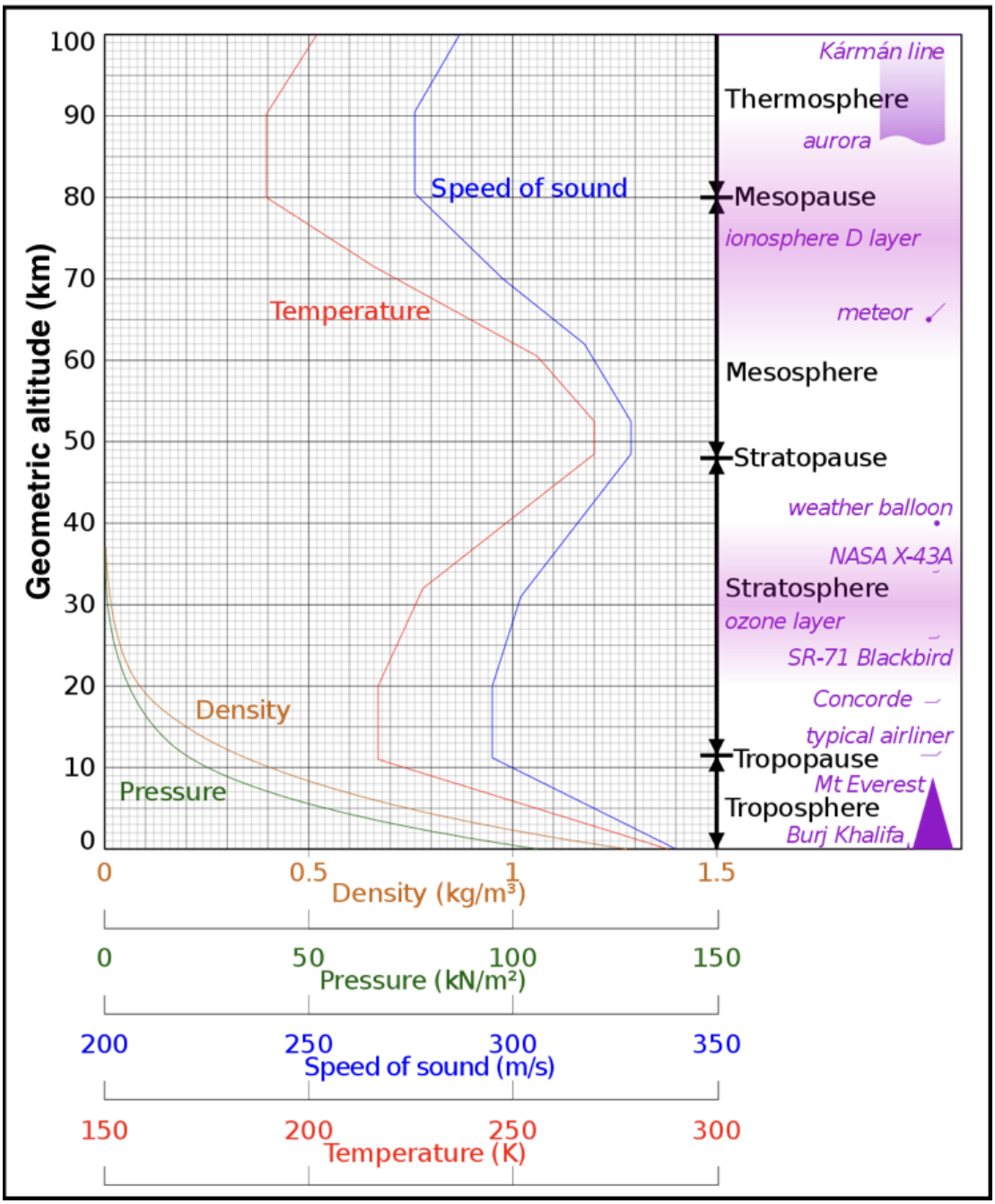


**Figure 1.4:** Comparison of the 1962 US Standard Atmosphere showing geometric altitude against air density, pressure, the speed of sound and temperature with approximate altitudes of various objects. Image taken from Wikipedia[5].

rather than by the optical design and the quality of the telescope. In fact, we need to consider the atmosphere when designing the optical system of any ground-based telescope.

### Kolmogorov theory of turbulence

The turbulent-induced aberrations cause the point spread function of the imaging system to split up and move around at the focal plane. Statistical models and methods are essential to fully understand as well as to mitigate these effects. Understanding the spatial structure of the turbulence comes from the study of fluid motions. Fluid motion can be laminar or turbulent, two regimes which can be distinguished using their Reynolds number, given by

$$R_e = \frac{V_0\, L_0}{\nu_0}, \tag{1.3}$$

where $V_0$ is the characteristic flow velocity, $L_0$ is the characteristic size of the flow and $\nu_0$ is the kinematic viscosity of the fluid. $R_e$ is dimensionless, and when it exceeds the critical value of 2000, the flow is fully turbulent [104]. If you plug in the average values for our atmosphere: $V_0$=10 ms$^{-1}$, $L_0$=25 m, and $\nu_0$ is of the order of 15x10$^{-6}$ m$^2$s$^{-1}$, we get $R_e$ of the order of $10^7$. This implies that Earth's atmosphere is in fully-developed turbulent motion.

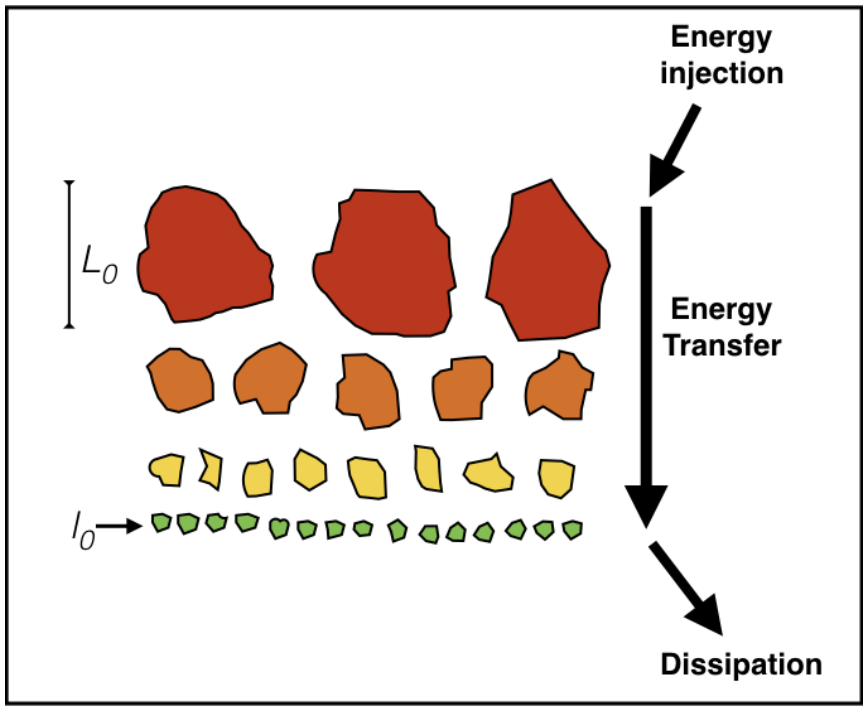


**Figure 1.5:** Kolmogorov theory of turbulence. Image based on the material at this link[6].

Kolmogorov theory [74] states that in fully-developed turbulence, the kinetic energy of the large scale motions is transferred to progressively smaller scales (see Figure 1.5). Kolmogorov assumed that these small scale turbulent motions are both homogeneous and isotropic. By homogeneous, he meant that the statistical characteristics of the turbulent flow are independent of the position within the flow field. By isotropic, he meant that the second and higher order statistical moments only have a dependence on the radial distance between any two points in the field. As the spatial scale reduces, the Reynolds number gets smaller. When it falls below a critical value, turbulent motion stops and the remaining kinetic energy is dissipated into heat by viscous friction.

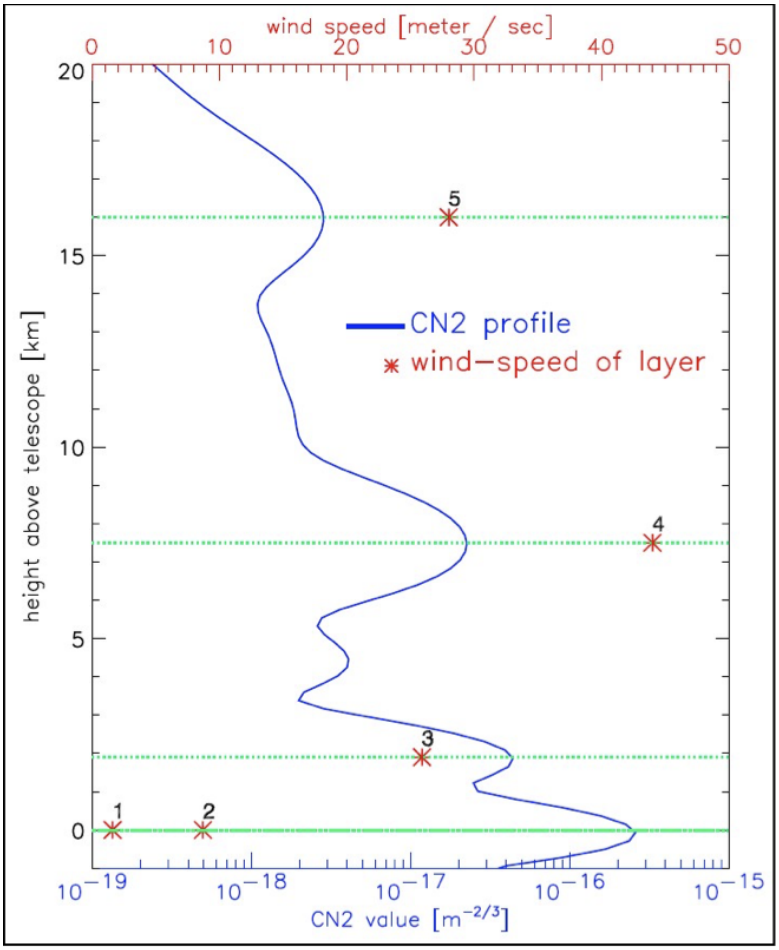


**Figure 1.6:** $C_n^2$ profile measured at Mt. Graham, Arizona. The numbers 1 to 5 represent the different turbulent layers with different wind speeds measured using the G-SCIDAR profiling technique. Image taken from Sebastian Egner's PhD thesis[7].

[6] http://career.ammarica.net/Turbulence/KolmogorovTurbulence.html
[7] http://archiv.ub.uni-heidelberg.de/volltextserver/6974/

The statistical distribution of the size and number of turbulent eddies is determined by the spatial power spectral density of the refractive index $n$, denoted by $\Phi_n(\mathbf{k})$. The variable $\mathbf{k}$ is the spatial wave number vector with orthogonal components ($k_x$,$k_y$,$k_z$). $\Phi_n(\mathbf{k})$ may be considered to be a measure of the relative abundance of the turbulent eddies with spatial scales $l_x=2\pi/k_x$, $l_y=2\pi/k_y$, $l_z=2\pi/k_z$. When turbulence is homogeneous and isotropic, $\Phi_n(\mathbf{k}) = \Phi_n(k)$, where k is related to the isotropic scale size $l=2\pi/k$.

Kolmogorov theory is valid only between a specific spatial scales $l_0$ and $L_0$. $l_0$, called the *inner scale* of the turbulence, represents the characteristic smallest dimension turbulent of eddies that can disappear by dissipating their energy as heat. The $l_0$ value ranges from a few millimeters near the ground to about 1 cm near the tropopause. $L_0$, called the *outer scale* of the turbulence, represents the largest turbulent eddies which break up following the Kolmogorov theory. Near the ground, $L_0$ is of the order of the height above the ground, and in the free atmosphere, it is believed to be several meters to tens of meters. Within the range $\frac{2\pi}{L_0} \leq k \leq \frac{2\pi}{l_0}$, $\Phi_n(\mathbf{k})$ is predicted by Kolmogorov theory to be:

$$\Phi_n(\mathbf{k}) = 0.033\, C_n^2\, k^{-1/3} \tag{1.4}$$

where $C_n^2$ is called the *refractive index structural constant* and has units of $m^{-2/3}$. This constant quantifies the strength of refractive index fluctuations or turbulence. The Kolmogorov theory was found to be consistent with observations [27]. We understand, and therefore can express atmospheric turbulence using the Kolmogorov spectrum. The next step is to remove the effects of the atmosphere as much as possible in real time (to make the wavefront as planar as possible), thus using the full capability of the very large telescopes. The goal is to eliminate the seeing (defined more precisely below) and make the telescope diffraction-limited.

### 1.1.3 Seeing parameters

In astronomy, the term *seeing* refers to the quality of the night sky. As mentioned is section 1.1.1, under ideal conditions, that is, in the absence of any kind of aberrations, the PSF is the Airy pattern and telescope is diffraction-limited. Aberrations, however, causes the PSF to be larger, making the telescope seeing-limited. Seeing is usually defined as the Full Width at Half Maximum (FWHM) of the PSF of a star seen through the uncorrected turbulent atmosphere. Higher seeing, therefore, indicates a worse night sky. The main parameters that characterise the seeing are:

- The **Fried Parameter** ($r_0$) represents the length scale, in the wavefront plane, after which the wavefront phase varies statistically by more than one radian [37, 38, 40]. It is given by

the relation:

$$r_0 \;=\; \left(0.434\,\frac{\pi^2}{\lambda^2}\,(\cos\phi)^{-1}\int_0^{\infty} C_n^2(z)\,dz\right)^{-\frac{3}{5}} \;\propto\; \lambda^{6/5} \tag{1.5}$$

where $\phi$ is the zenith distance, that is the angle defined by the normal to the Earth's surface and the direction of observation, $C_n^2$ is the refractive index structural parameter, and $\lambda$ is the wavelength. The Fried parameter can also be interpreted as the average size of the turbulent cell (see section 1.1.2). The parameter also corresponds to the aperture size of a diffraction limited telescope that has the same resolution. If the telescope has an aperture larger than the Fried parameter and it does not have an adaptive optics system, the angular resolution is limited to $\lambda/r_0$. It is evident from Equation 1.5 that infrared images are less affected by seeing. However, the resolution is not drastically better than in the visible, since the Airy disk size is proportional to the wavelength, with no adaptive optics system present. The typical value of $r_0$ in the K-band is 30 cm and in the V-band, 10 cm.

- The **isoplanatic angle** ($\theta_0$) is the angle on-sky within which the wavefront phase varies by less than one radian [39]. That is, it is the maximum angle of separation between two sources beyond which there is no longer a significant correlation between the distortions suffered by the wavefronts. The angle is:

$$\theta_0 = 0.314\,\frac{r_0}{\bar{h}} \;\propto\; \lambda^{6/5} \tag{1.6}$$

where $\bar{h}$ is the equivalent height of the turbulent layers. Within this angle, the perturbation introduced by the atmosphere affects the wavefront in a very similar way. The typical value of $\theta_0$ is a few arcsec. Two sources separated by more than $\theta_0$ will have different PSFs in images taken with short exposure times. For longer exposure times, the PSFs will be larger, smoother, and virtually identical, representing the average of many atmospheric fluctuations. This is the so-called "seeing disk". Although the wavefront has passed through different portions of the atmosphere, the average distortion suffered by the wavefront is the same for longer exposures.

- The **coherence time** ($\tau_0$) represents the time scale during which the wavefront phase varies by one radian. It is the measure of the time scale variability of atmospheric turbulence or distortion. Within this time, the PSF remains roughly the same, in the same isoplanatic patch. The definition is very simple :

$$\tau_0 = \frac{r_0}{v} \;\propto\; \lambda^{6/5} \tag{1.7}$$

where $v$ is the mean wind speed at the altitude of the turbulence. Of course, different altitudes usually have different wind speeds, therefore the coherence times as well. The coherence time is of the order of a few tens of milliseconds in the IR domain. The inverse

of $\tau_0$ is called the *Greenwood frequency*.

- The **Strehl Ratio (SR)** is defined as the ratio between the peak intensity of the observed PSF and that of the diffraction limited image.

$$SR = \frac{\mathrm{PSF}_{\mathrm{seeing}}(0,0)}{\mathrm{PSF}_{\mathrm{DL}}(0,0)} \tag{1.8}$$

where $\mathrm{PSF}_{\mathrm{seeing}}$ is the peak value of the observed PSF and $\mathrm{PSF}_{\mathrm{DL}}$ is that for the diffraction limited PSF. When the wavefront passes through a perfect optical system, SR=1. In all other cases, SR<1. Smaller values of SR correspond to poorer image quality.

## 1.2 Adaptive optics as a remedy

Atmospheric turbulence reduces the resolution that can be achieved by the telescope from $\sim \lambda/D$ (diffraction-limited) to $\sim \lambda/r_0$ (seeing-limited). In order to beat this limitation, we need to correct the aberrations caused by the atmosphere at ~kHz frequencies, that is, in real-time. Obviously, the frequency of correction also depends on the science goals and the respective requirements. Our understanding of turbulence, coupled with a relatively new technique to correct for the aberrations in real time, called *Adaptive Optics (AO)*, allows us to carry out short- as well as long-exposure science with diffraction-limited spatial resolution. Figure 1.7 shows an example of sharp imagery produced by AO.

An AO system removes the wavefront distortions introduced by the atmosphere. Using some optical components in the light path, we can compensate the wavefront distortion introduced by the atmosphere both spatially and temporally. The main optical component or the *corrector* is usually a mirror which can distort its surface, in other words, a *Deformable Mirror (DM)*. In order to control the DM, the wavefront distortions must be known. A *Wavefront Sensor (WFS)* measures the distortions with the help of a nearby star (*Natural Guide Star (NGS)*) or *Laser Guide Star (LGS)*. The light reflected off the DM, when the control works well, is corrected for the atmospheric perturbations and it will produce a diffraction-limited image. Figure 1.8 is a sketch of a classical AO system. Strictly speaking, this is true only for light that is on-axis. Making it true for elsewhere is one of the main objective of this thesis.

The concept of AO was introduced by Horace W. Babcock in 1953 [4]. However, it took almost two decades to implement his idea for astronomical purposes. The first attempt was made by Buffington and collaborators in the mid-1970s [21, 22] and later by Hardy in the 1980s [48].

[8] http://exoplanet.as.arizona.edu/ lclose/talks/ins/ESO_MMTAO_3
[9] https://cuna.nso.edu/clear/index.php/why-mcao/

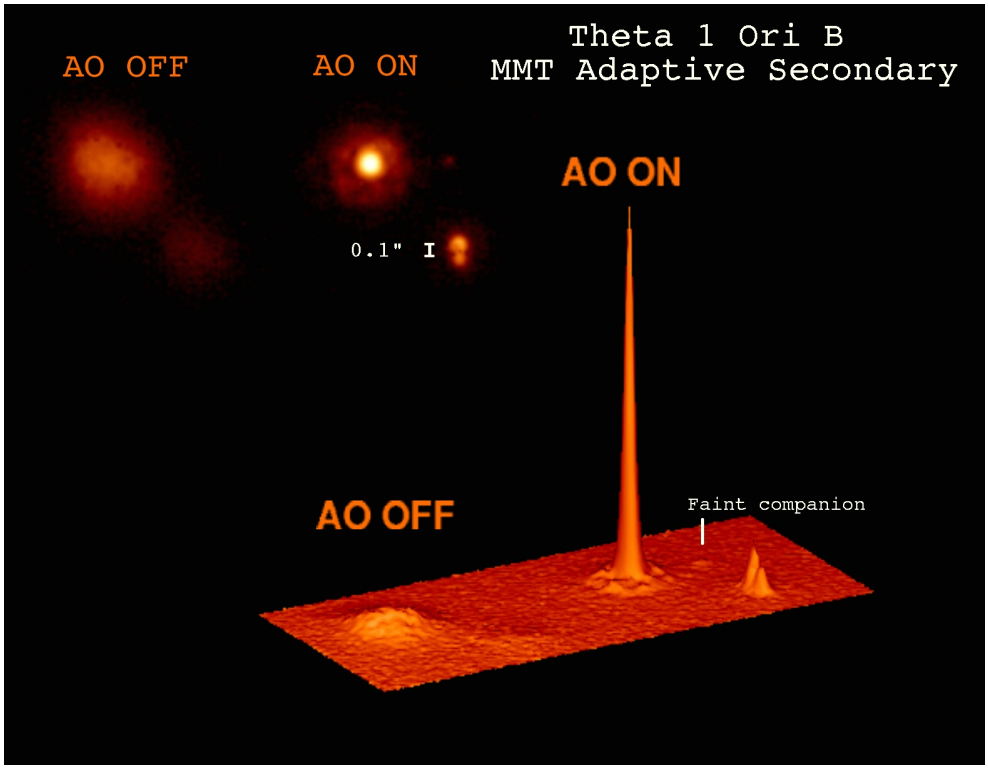


**Figure 1.7:** A typical example of how an AO system can make very sharp images. With AO "OFF", this object appears to be just 2 stars. With AO turned "ON", it is clearly a tight group of 4 visual stars (2 of these are in a tight 0.1" binary, one is the bright guide star, and the other is a rarely seen very faint companion slightly to the right (and 100 times fainter) than the bright star, see white arrow). This image is taken from this link[8]. Credit: Laird Close.

Although the results of these experiments were encouraging in demonstrating the concept, the complexity of the systems was high and they were very expensive. However, adaptive optics caught the attention of the astronomy community and is now becoming a part of every modern telescope. AO is now commonly a part of observatory infrastructure because of: (a) advancements in detector technology, (b) reduced complexity and limitations of AO at infrared wavelengths, (c) increases sky coverage and possible use of fainter NGSs for AO, with recent advancements in wavefront sensing, and (d) invention of practical laser guide stars.

### 1.2.1 Wavefront distortions

The spatially-varying wavefront distortions reaching the telescope are assessed and quantified using the measurements of the spatially resolved gradients or "tilts" of the wavefront. The AO

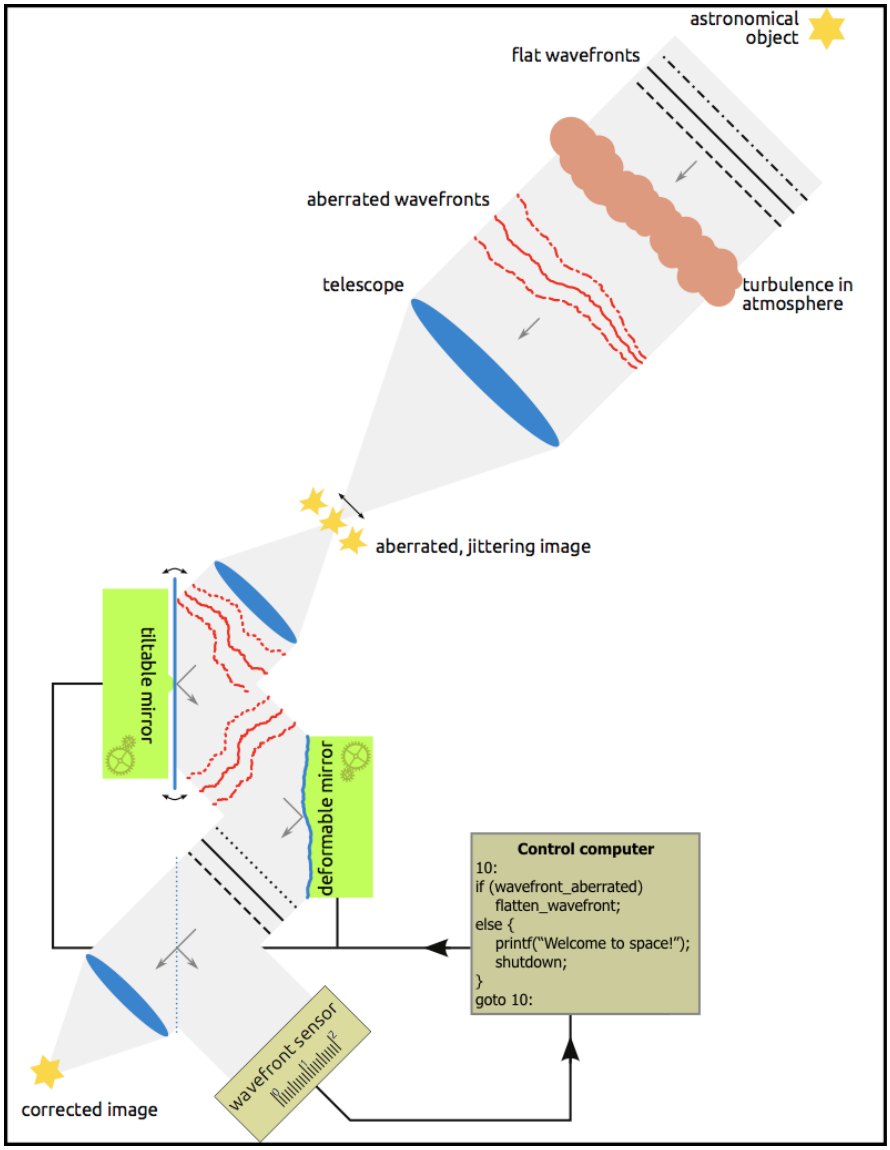


**Figure 1.8:** A sketch of the classical adaptive optics system. This image is taken from this link[9].

community typically separates the two main effects on the wavefront when it passes through the turbulence, due to tip-tilt and higher order distortions (see Figure 1.9).

Tip-tilt is the first derivative of the wavefront, the average inclination caused to the planar wavefront, as displayed in Figure 1.9. The center of light of the image shifts in the focal plane due to tip-tilt. These movements result in larger blurred images for long-exposures.

Higher-order distortions are the deformations of the wavefront at generally higher spatial frequencies. The portions of the wavefront separated by more than $r_0$ will undergo different phase

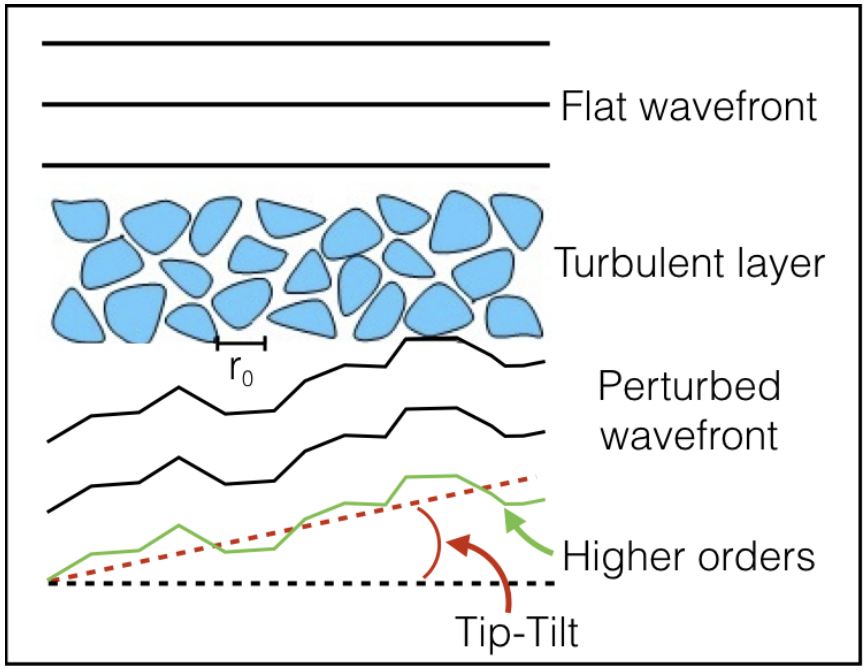


**Figure 1.9:** The tip-tilt and high-order aberrations, starting from the incoming flat wavefront.

delays. This results in the division or compartmentalisation of the wavefront into several parts in units of $D/r_0$. Each one will be locally planar and form separate diffraction-limited images of size $\lambda/r_0$. Long exposures will end up broadening the image, as explained in section 1.1.3. For telescopes with $D>>r_0$, the higher order perturbations dominate.

Telescopes with $D<r_0$ obviously do not suffer high order turbulent aberrations since the portion of the wavefront intercepted is smaller than the average size of the unperturbed wavefront. Such telescopes will be dominated by the tip-tilt.

### 1.2.2 Wavefront sensor

The wavefront sensor is the heart of any AO system. The shape of the incoming wavefront is typically determined by measuring changes in light intensities (described below). The intensity variations are directly related to the phase deviation and hence the slopes of the wavefront. Once we know the inclination at which the ray arrives, that is the first derivative of the local wavefront, the wavefront can be calculated. The slopes can be visualised on a detector using the basic optical principle that tilts in the pupil-plane correspond to displacements in the focal-plane (see Figure 1.10). Note also that displacements in the pupil-plane correspond to tilts in the focal-plane. This is not only true in the global scale, but also locally in the pupil. The basic duty of the

wavefront sensor is finding the tilts (slope of the wavefront) of the arriving wavefront.

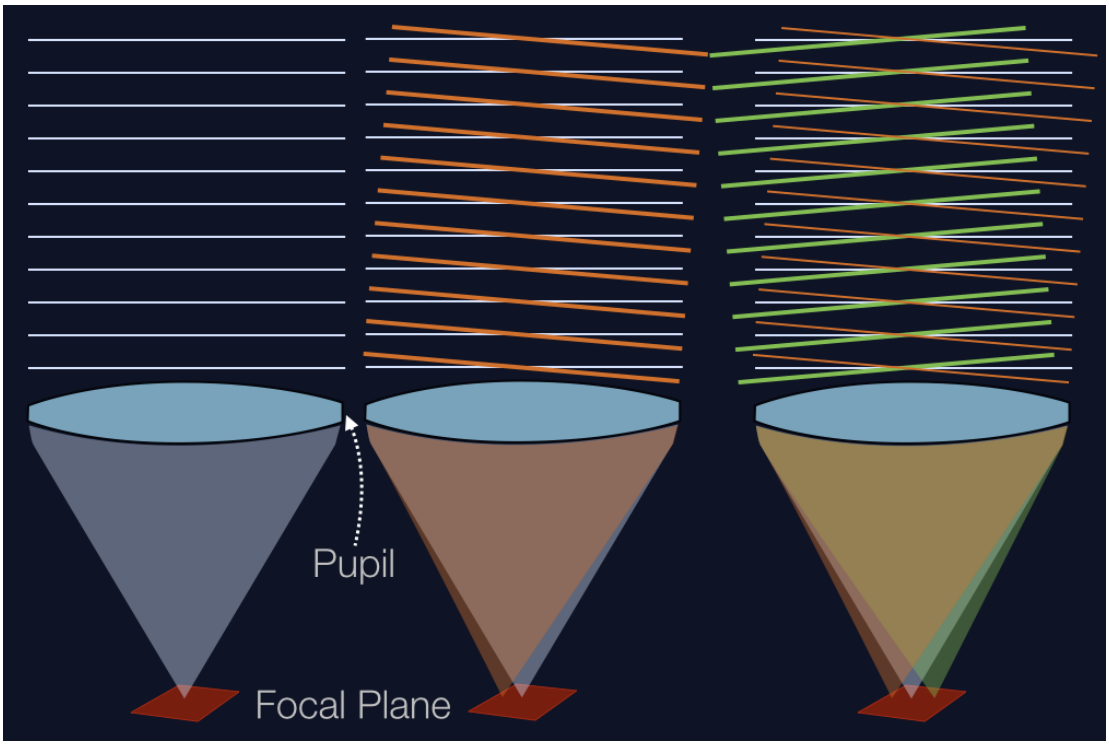


**Figure 1.10:** Concept for measuring the wavefront tilt. Tilts in the pupil-plane correspond to displacements in the focal-plane. Credit: Tom Herbst.

Naturally, in order to reconstruct the wavefront and to understand the aberrations affecting it, it is necessary to optically divide the wavefront into several smaller regions. These smaller regions are called *sub-apertures*. Inclination or tilt in each sub-aperture can be individually estimated. The greater the number of sub-apertures, the better the wavefront reconstruction will be. However, there are limitations imposed by various effects. The maximum number of sub-apertures is limited by:

1. The number of available actuators for correction. In order to take advantage of sampling at high spatial frequencies, we need to have enough actuators to make the correction (typically 1 actuator per sub-aperture).

2. The Signal to Noise Ratio (SNR) in each sub-aperture. The number of photons in each sub-aperture varies with the size and number of sub-apertures (and of course with the brightness of the guide star used) and how rapidly we sample.

3. The seeing. We do not need to sample the wavefront more finely than $r_0$ (see section 1.2.1). At finer scales, the wavefront can be considered unperturbed.

### Quad-Cell WFS

The basic principle of a WFS operation can be explained using the most simple one, the quad-cell WFS, which can be used to evaluate the tip-tilt of the wavefront. The incoming light from the reference source is split spatially into four parts on a 2x2 grid. The sensor is placed in the focal plane of the system so that its center will match where the diffraction limited PSF should focus in the absence of aberrations. The spot movements are measured by the WFS. This displacement is directly proportional to the first derivative of the incoming wavefront. In the absence of tip-tilt, the "center of light" of the image should be situated exactly at the center of the four quadrants. However, when the wavefront arrives tilted, the center of light moves, and the quadrant illumination will no longer be equal. Analytically determining the displacement of the image along the X and Y axes is very simple. Counting the number of photons that fall in the 4 quadrants, the displacement of the spot is:

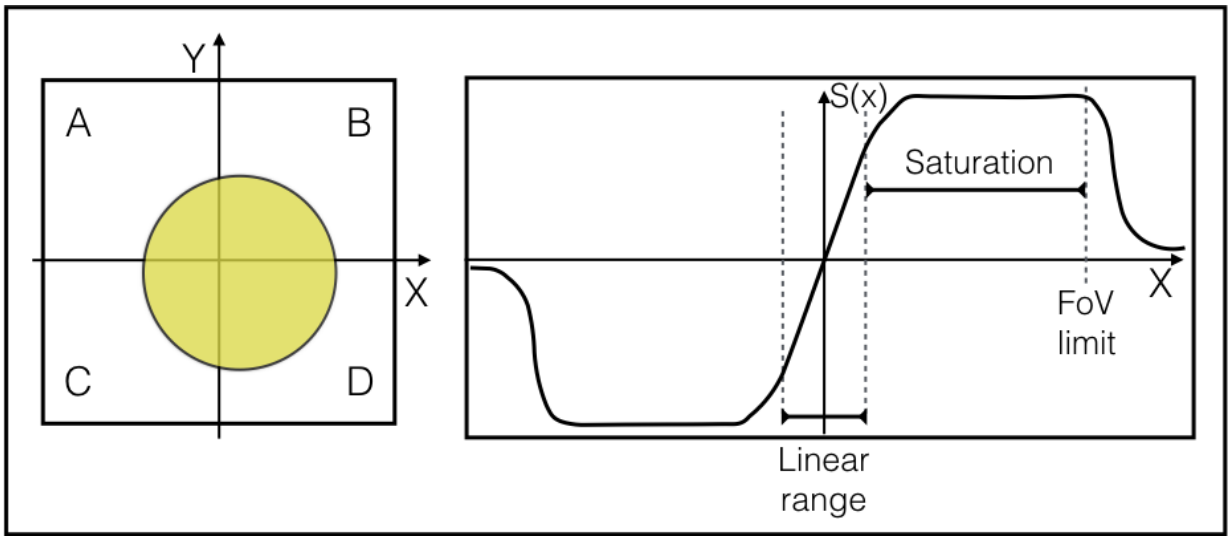


**Figure 1.11:** *left*: Quad-cell WFS concept. *right*: $S_x$ signal as a function of the spot displacement along the X-axis.

$$S_x = \frac{(B+D)-(A+C)}{A+B+C+D} \tag{1.9}$$

$$S_y = \frac{(A+B)-(C+D)}{A+B+C+D} \tag{1.10}$$

In these expressions, $A$, $B$, $C$, and $D$ are the integrated fluxes reaching the respective quadrants of the sensor, and $S_x$ and $S_y$ are proportional to the first derivative of the wavefront computed along the orthogonal directions for small shifts of the spot. The $S_x$ signal behaviour as a function of the shift of the spot along X-axis is plotted on the right side of the Figure 1.11. The Y-direction behaves similarly. The useful or linear range is the one in which $S_x$ and $S_y$ increases linearly. This occurs when at least some light is present in all the quadrants of the WFS. For example, if the spot illuminate only quadrants B and D, then $S_y$ will be linear, but $S_x$ will be "saturated"; $S_x$=1.

It is obvious that the linear range of the quad cell is related to the size of the spot. The smaller the spot, the more sensitive the sensor, but this comes at the cost of reduced dynamic range for measuring tip-tilt. When the sensitivity is high (and the spot is very small), tiny shifts will result in a high tilt signal, but the sensor can easily saturate.

The information obtained using the quad-cell WFS can be sent to the flat mirror positioned in the optical path to correct for the mean inclination of the incoming wavefront. The same basic idea of the quad-cell WFS is used in the Shack-Hartmann WFS and the Pyramid WFS.

### Higher-order WFS

To correct for higher order perturbations, we need to sample the wavefront spatially, that is, not just measure the average tip and tilt. The pupil[10] with diameter D is divided into NxN sub-apertures with d=D/N. Note that almost all telescopes are round, resulting in a total number of sub-apertures $\sim 0.7N^2$. A properly-sampled wavefront can be used to retrieve the mean tilt in each of the sub-apertures using the quad-cell concept. The optimal number of sub-apertures for spatial sampling system will be $N \approx D/r_0$. As discussed in section 1.2.2, it is useless to oversample the pupil more than this value, since this will not give any additional information.

Several WFSs were proposed and used over time, including Foucault knife edge WFS, shearing interferometer WFS, Shack-Hartmann WFS (SHWFS), Pyramid Wavefront Sensor (PWFS), yet another WFS (YAW) etc. The most commonly used are the Shack-Hartmann- and pyramid-WFS. Here I will describe PWFS in detail.

[10]Pupil is the limiting aperture of an optical system. In astronomical IR systems, pupil limits the acceptable range of angles, thereby reducing the background.

### Pyramid WFS

The concept of the PWFS was proposed by Roberto Ragazzoni in 1996 [95]. It is simple and based on the Foucault knife edge test, which has traditionally been used to measure the conic shapes and aberrations of mirrors during fabrication. The PWFS has been tested and established on several telescopes, such as TNG, VLT, Calar Alto, and LBT.

**Operating principle**: A square based refracting pyramid is placed in a focal plane of the system, where the image of the reference star gets focused. The pyramid splits the light into four beams, like the four areas of the quad-cell WFS, but due to refraction, these four beams spread apart. The beams are re-imaged onto four pupil images on the detector (usually a Charge-Coupled Device (CCD)), each with intensity proportional to the number of photons that hit the respective face of the pyramid (see Figure 1.12). The focal length of the objective is properly tuned with the pyramid vertex angle so that the four pupils are well separated and maximise the use of the CCD pixels.

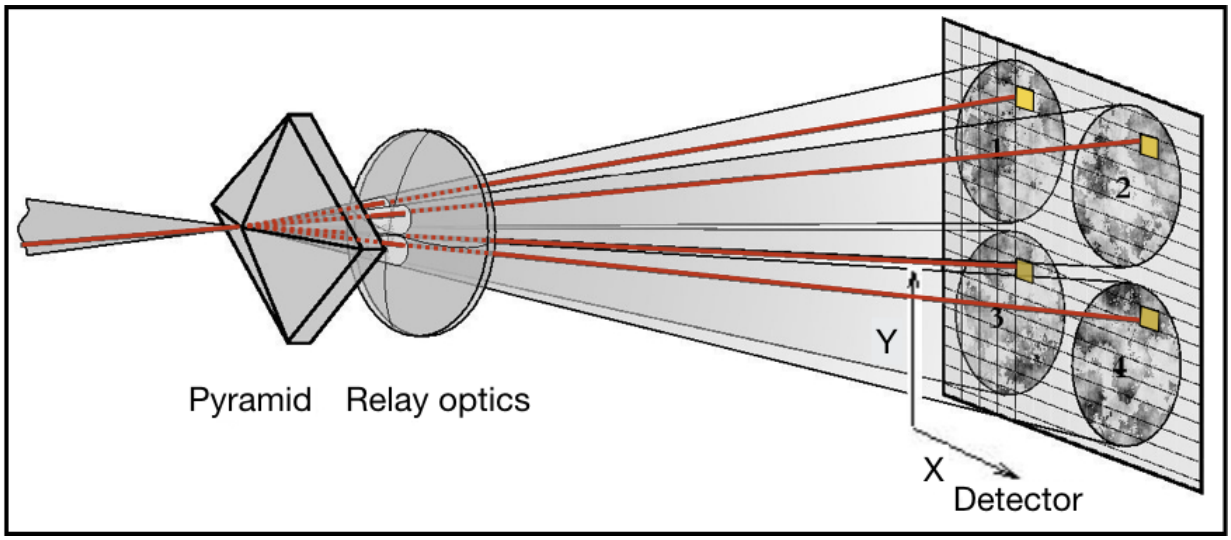


**Figure 1.12:** The operating principle of the pyramid wavefront sensor. An example of corresponding pixels are marked in yellow, traced by the rays in red. The gradient in this position of the pupils is calculated from the intensity differences between these pixels.

A comparison the intensities of the 4 pupil images gives the tip-tilt in exactly the same way as with the quad-cell WFS, as explained in section 1.2.2. Knowing the local tilts in individual sub-apertures, the wavefront can be stitched together. One of the main advantages of the PWFS is that the sub-apertures are defined at the level of the CCD. Therefore, by changing the binning of the CCD, the observer can change the spatial sampling, without changing any optics. This

is extremely useful, especially when the guide stars are faint. Higher binning can, therefore, increase the SNR in individual sub-apertures.

Another advantage of the PWFS is that the sensitivity can increase in closed loop. Indeed, during the first few cycles, the wavefront is strongly aberrated, and the size of the spot on the tip of the pyramid is dominated by seeing, i.e. of the order of $\lambda/r_0$. Over time, the correction improves, reducing the spot size, potentially down to the diffraction limit $\lambda/D$.

However, we must prevent that the spot on the top of the pyramid becomes too small, since sudden changes in atmospheric turbulence could move the spot to a location which leaves 2 or 3 sides of the pyramid un-illuminated. If this happens, some of the pupils would receive no photons, and the WFS would be in the saturation regime. This results in a degradation in correction, and an increase in the size of the spot on the top of the pyramid and a consequent loss of sensitivity. To prevent these conditions from occurring too frequently, it is possible apply a diffuser at the pin (tip of the pyramid), or modulate the spot (ie, an oscillatory movement of the spot around the top of the pyramid) with a frequency greater than the read-out rate of the CCD. In closed loop and if it is diffraction-limited, the size of the spot on the top of the pyramid is $\lambda/D$.

Increase in sensitivity of the PWFS in closed loop allows us to use fainter stars for wavefront correction, thereby increasing the sky coverage [99]. Therefore, the pyramid wavefront sensing can use 1 to 2 orders of magnitude fainter guide stars than, for example, the Shack-Hartmann WFS, for a 10 m class telescope.

### 1.2.3 Wavefront reconstructor

The WFS measures the local tilt of the wavefront. Since the wavefront is continuous, stitching together these measurements provides the full wavefront shape. This operation is called *reconstruction* of the wavefront. The reconstructor converts the signals to phase and sends the corresponding correction commands to the deformable mirror.

There are two main approaches to reconstruction: zonal and modal. The first describes the wavefront in terms of optical path difference in different regularly-spaced regions of the pupil of the telescope, usually rasterised and chosen to correspond to the sub-apertures. The modal approach describes the wavefront with coefficients of a polynomial expansion of a modal base. This may be mathematically represented in the following way :

$$W(x, y) = \sum_n C_n \, P_n(x, y) \tag{1.11}$$

where $(x, y)$ is the spatial coordinate, the $P_n$ are the polynomial terms (modes), and $C_n$ are the

linear combination coefficients. Since the $P_n$ terms are continuous, the gradient of the wavefront can be expressed as:

$$\begin{pmatrix} \dfrac{\partial W(x,y)}{\partial x} \\ \\ \dfrac{\partial W(x,y)}{\partial y} \end{pmatrix} = \begin{pmatrix} \sum_n C_n \dfrac{\partial P_n(x,y)}{\partial x} \\ \\ \sum_n C_n \dfrac{\partial P_n(x,y)}{\partial y} \end{pmatrix} \tag{1.12}$$

WFS measurement provides us the gradient of the wavefront in both the X- and Y-directions, that is, the left hand side of Equation 1.12. At every point $(x, y)$, we know the value of each of the polynomial term, and its derivatives. The only unknowns, coefficients $C_n$, can therefore be evaluated. Once the $C_n$ are known, the surface of the wavefront is obtained using Equation 1.11. Detailed information on the shape of the wavefront is contained in the $P_n$. It has been shown by Noll in 1976 that an effective basis set to describe the aberrations introduced by Kolmogorov turbulence is one in which the terms $P_n$ are the Zernike polynomials. They form an orthogonal basis for the functions, defined on a unit circle, and are defined in polar coordinates $(\rho, \theta)$ as:

$$Z_n^m(\rho, \theta) = \rho^n \cos(m\theta) \tag{1.13}$$

where $n$ is the radial order and $m$ is the azimuthal order. Each Zernike polynomial is the product of two terms: the first contains the radial part and the second the angle. The advantage of using these polynomials is that they are orthogonal and the low orders describe real-world Seidel aberrations, such as coma, defocus, astigmatism etc. In addition, all Zernike polynomials except the first have zero mean and can be calibrated in order to have the respective slope measurements at the WFS. This puts all polynomials on a common base, so that their relative magnitudes can be compared easily. The Karhunen-Loève (KL) basis set is another commonly used modal base.

### 1.2.4 Wavefront corrector

Adaptive optics corrects the perturbations in the wavefront in real time by introducing a controllable phase in the light path opposite to that introduced by the atmosphere. To correct the tip-tilt, a flat mirror mounted on a fast tip-tilt stage may be inserted in the light beam (see Figure 1.8). The deformable mirror then corrects the higher-order, small scale aberrations produced by the atmosphere. There are AO systems using a fast tip-tilt mirror and a DM, often called a "woofer-tweeter" configuration, as well as those using only a DM to compensate for both the tip-tilt and higher-order aberrations.

The surface of the DM can be modified by pushing and pulling *actuators* below the mirror (this depends on the kind of actuator). The time scale of the correction must be at least the same

as that of the evolution of the turbulence. In other words, the correction frequency should be at least the Greenwood frequency (see section 1.1.3).

The wavefront sensor gets the information to estimate the deformation to be applied to the DM. The WFS and a real time computer analyse the wavefront of a reference star present within the Field of View (FoV) and determine the distortions suffered by the wavefront, that is, how much it has deviated from the planar wavefront. Appropriate signals are then sent to the control electronics of the DM to flatten the wavefront.

### 1.2.5 Accuracy of wavefront correction

The accuracy of the wavefront correction by the AO system determines the quality of the image and hence the performance of the telescope. The Strehl ratio may be used as the merit function to quantify the accuracy or the quality of the image. The main errors that adversely affect the correction are the sampling error, the timing error, and the error due to anisoplanatism.

- The *sampling error* is due to the fact that, while the aberrated wavefront may have features on spatial scales of the order of millimeter, the sampling that is performed is usually limited by the number of actuators of the deformable mirror. The number of actuators is dictated by cost-performance optimisation done on a statistical basis. Under-sampling can therefore leave residuals. Some aberrations (those at higher order) cannot be corrected, thereby reducing performance.

- The *timing* or *latency error* is due to the time delay between the measurement of the turbulence and its effective correction. Predictive wavefront control techniques can be used to mitigate this error term, an approach which is explained in some detail in Chapter 4.

- The error due to *anisoplanatism* is associated with the angular distance on the sky between the scientific object of interest and the guide star used to make the correction [39]. The isoplanatic angle is typically very small, of the order of a few arcsec. In order not to excessively degrade the SR, it is necessary that the scientific object and the guide star be separated by less than the isoplanatic angle. A way to overcome anisoplanatism is described in section 1.3.1.

- Since the correction has to happen at ~kHz frequencies, the guide star must be bright enough (typically not fainter than 16 magnitudes in the V-band). This poses a huge problem for sky coverage, the portion of the sky where the adaptive optics system can be successfully exploited.

## 1.3 Multi-conjugated adaptive optics (MCAO)

### 1.3.1 Overcoming anisoplanatism using MCAO

As mentioned earlier, if the scientific target and the guide star are more than a few arcsec apart, that is, farther than the isoplanatic angle, the correction will degrade. The light cylinders corresponding to the science target and that of the guide star pass through different volumes of the atmosphere, and only the aberrations in the common region are corrected (see Figure 1.13). This partial correction leads to degradation of the science image, and the effect will be more

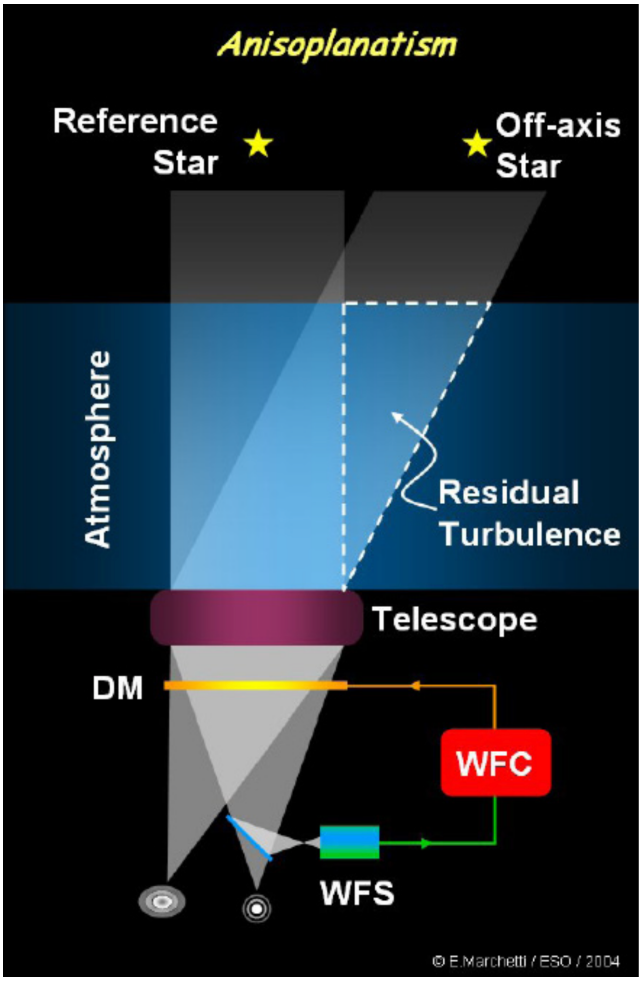


**Figure 1.13:** Anisoplanatism leading to degradation of the correction. The turbulence volume sensed by the WFS doesn't match the turbulence corrected by the DM. This image is taken from ESO website[11]. Credit: Enrico Marchetti.

pronounced when the distance from the guide star is greater. This is one of the shortcomings of classical adaptive optics [39], where only one guide star is used. Using multiple guide stars can beat this limitation, a technique called Multi-Conjugated Adaptive Optics (MCAO).

MCAO was first suggested by Beckers in 1988 [7]. The aberrations in the full volume of atmosphere within the entire FoV are measured using light coming from multiple guide stars and corrected using multiple DMs (see Figure 1.14). This process takes place in three stages.

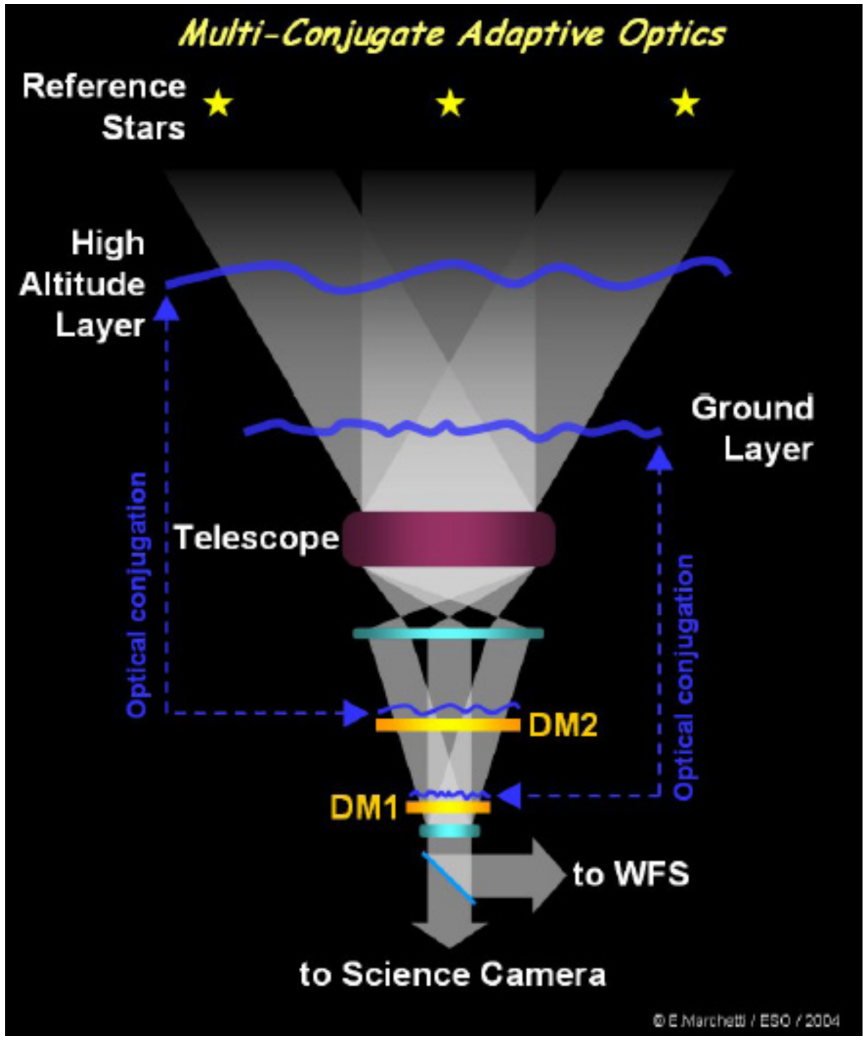


**Figure 1.14:** The principle of multi-conjugate adaptive optics. Several WFS' and DM's are combined in order to "optimize" the adaptive correction in a larger field of view. This image is taken from ESO website[12]. Credit: Enrico Marchetti.

[11] https://www.eso.org/sci/facilities/develop/ao/ao_modes/.html
[12] https://www.eso.org/sci/facilities/develop/ao/ao_modes/.html

First, the deformation of the wavefront due to atmospheric turbulence along different directions within the FoV is measured. This is possible using multiple wavefront sensors, measuring aberrations due to several guide stars in the FoV. The greater the number of guide stars used, the better is the knowledge of the wavefront distortion.

The second phase is atmospheric *tomography*, or reconstructing the full vertical distribution of the turbulence by observing it from different angles [100]. However, it is not possible to derive the turbulence at all heights, since the number of guide stars is limited and the computation is very complex. This can be resolved by assuming that the atmosphere is composed of multiple layers and considering only those layers where the turbulence is strong.

Finally, the third stage consists in applying the correction to the wavefront for the entire FoV, not only in one specific direction. More than one DM can be used to do this, each of which is optically *conjugated* to different atmospheric altitudes. Hence, the entire FoV can be corrected using MCAO.

### Pupils and Metapupils

The projection of the entrance pupil at any given altitude is called the *metapupil* (see Figure 1.15). Its size obviously varies with the height of conjugation (H) and with the radius of the FoV $\theta$ (expressed in radians) as:

$$D_{mp} = D + 2\,H\tan(\theta)\,, \tag{1.14}$$

where $D$ is the diameter of the telescope entrance pupil, and $D_{mp}$ is the diameter of the metapupil. To obtain a good correction of the turbulent layer at height $H$, it is necessary that the footprints (the projections of the entrance pupil in the direction of each guide star on the turbulent layer) completely cover the metapupil. From the expression above, the size of the metapupil is fixed and hence more guide stars are needed to cover the metapupil for greater heights.

Consider the following example at Large Binocular Telescope (LBT): in order to correct one turbulent layer at a height of 8 km and another at 15 km on a FoV of 2', and with an entrance pupil diameter of 8.25 m, the diameter of the metapupils are 12.9 m and 17 m respectively. Equation 1.14 then implies that, it is necessary to use at least 5 and 7 guide stars to cover them completely.

It is better to use more guide stars for the correction, but it is not always possible to find enough of them to sample the entire metapupil. This results in *partial illumination*, an effect explored in Chapter 3. This, along with the fact that the stars used will have different magnitudes, causes a reduction in the quality of the correction. Also, the SR may vary more within the FoV. In other

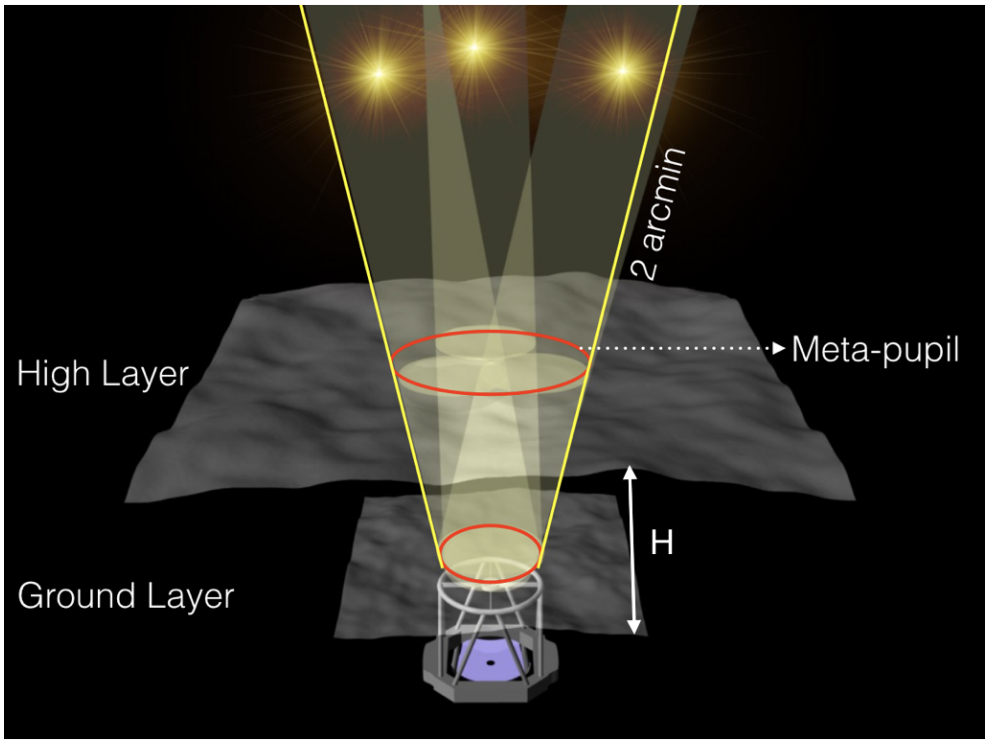


**Figure 1.15:** Representation of metapupil at any given altitude H for a 2 arcmin diameter FoV. While the footprints of the 3 guide stars overlap at the ground layer, they do not overlap at the high layer leaving a partially illuminated metapupil.

words, the result will be a somewhat field-dependent PSF.

### Star and layer-oriented MCAO

There are two approaches to implementing MCAO - *star-oriented* and *layer-oriented*. Figure 1.16 shows the two concepts.

In star-oriented MCAO [86], each reference star has an associated WFS, as shown in the left panel of Figure 1.16. Each of these measures the disturbance suffered by the respective wavefront along the column of atmosphere traversed. This is similar to the classical adaptive optics or Single-Conjugated Adaptive Optics (SCAO). The signals from each WFS are then combined to reconstruct the entire turbulence volume within the FoV. This method requires a lot of computing power and huge amounts of incoming data, thus resulting in a higher processing time and cost. Furthermore, only a part of the information obtained from the atmosphere is

[13] https://www.eso.org/sci/facilities/develop/ao/ao_modes/.html

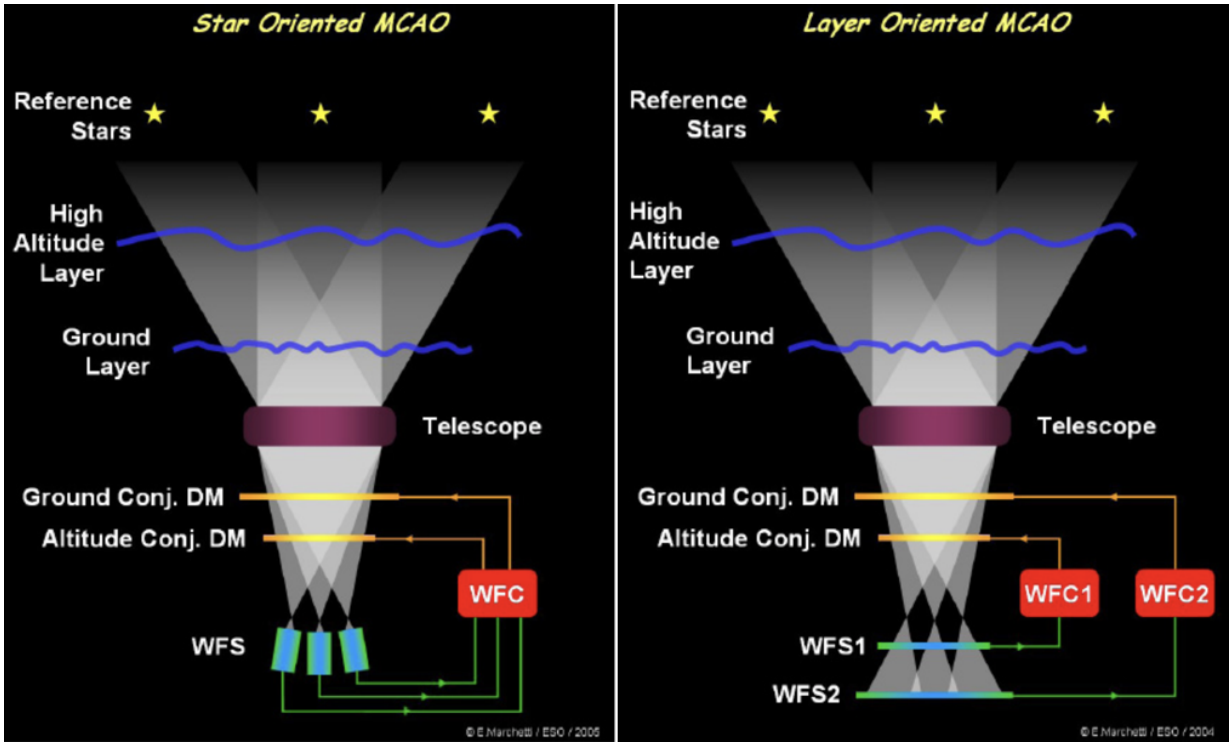


**Figure 1.16:** The concept of star-oriented MCAO (left) and layer-oriented MCAO (right). This image is taken from ESO website[13]. Credit: Enrico Marchetti.

actually used, since the correction applied to the DMs is calculated only for the conjugated altitudes. Also, the limiting magnitude for each of the guide stars is the same as that for SCAO. This approach does not significantly increase sky coverage. Also, the number of guide stars that one can use is obviously limited by the number of WFSs that are available. On the other hand, this technique allows the optimisation of the correction in particular directions within the FoV.

In the layer-oriented approach to MCAO [101], there are also multiple WFSs and respective DMs. Each WFS is optically conjugated to a layer at a given height and drives a DM conjugated to the same height (see right panel of Figure 1.16). Each WFS uses the light of all of the reference stars (optical combination) in the FoV simultaneously, thus leading to only a single CCD read-noise penalty. An example of this approach is the multi-pyramid WFSs used for correcting the ground and high layers for LINC-NIRVANA. In the focal plane, pyramids are placed at the location of each guide star. Re-imaging optics after the focal plane then superimpose the light from all stars optically on a CCD, forming four images of the conjugated pupil.

Layer-oriented MCAO independently measures and corrects aberrations introduced at each conjugated layer. It is therefore a local reconstruction, and the loops closing the different layers can be sequential (i.e. complete high layer correction followed by ground layer correction or

vice versa). This approach has the following advantages :

- The light coming from the guide stars is superimposed optically. This allows using fainter guide stars, provided that the sum of their magnitudes is greater than the classical threshold value (~16 mag in V-band). This results in greater sky coverage.
- The use of pyramid WFS allows a gain in sensitivity due to the correction and increases the sky coverage (explained in section 1.2.2).
- Layer-oriented MCAO uses a smaller number of WFS compared to star-oriented MCAO.
- The correction cycles for the WFS-DM system conjugated to a certain layer are independent from those for other layers. This results in faster calculation, reduces the computational complexity, and therefore improves the response of the control electronics.
- Since the correction for the different layers is sequential and independent, it is possible to optimize the parameters of the spatial and temporal sampling separately for each layer. The fact that the parameters $r_0$ and $\tau_0$ vary in the atmosphere (for example, in the higher layers, $r_0$ and the wind speed are greater than for the lower layers), allows individual sampling parameters, avoiding unnecessary oversampling of the wavefront.

One drawback of the layer-oriented implementation is the need for the CCD conjugated at high altitude to contain the full metapupil. The CCD used must therefore be larger than that for the star-oriented approach (which sees only single pupils) and would require a longer readout time. Another major issue is the need to separate the light to be sent to the WFS conjugated to various heights. This could be done with a beam splitter, but of course this allots a smaller number of photons to each WFS and consequently results in a lower SNR. To overcome this problem, we would have to use brighter and more guide stars or, more intelligently, use stars from different FoVs for each WFS, as explained below.

### 1.3.2 Multiple field of view (MFoV)

Using multiple fields of view to perform layer-oriented MCAO was introduced in 2002 [97]. The main idea is to associate each WFS with a different field of view. This partially avoids the problem of distributing the light among the various WFSs and the corresponding reduction in SNR.

The footprints of stars in the entire FoV pass through the same region at the ground layer (see Figure 1.17). We can therefore measure the ground-layer turbulence with stars anywhere in the

field delivered by the telescope. However, the same cannot be said for the higher altitude layers, since the overlap of the footprints diminishes with height, leaving some areas of the metapupil unsampled. For the correction of the layers at higher altitudes, it is therefore appropriate to choose guide stars in a narrower FoV. While selecting these guide stars, care must be taken to ensure good coverage of the central area of scientific interest.

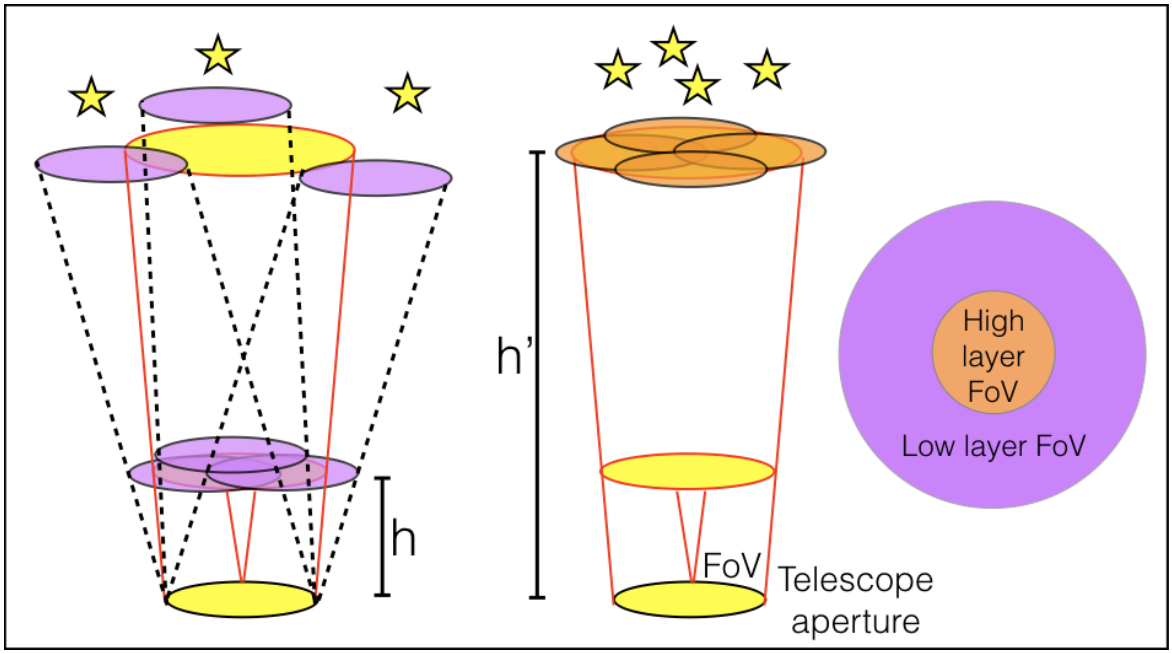


**Figure 1.17:** The Multiple-FoV concept. *left*: The footprints (purple coloured) of the 3 guide stars from a rather wide FoV fully fills the metapupil at height h. However, the same projections at height h' do not fill the respective metapupil. *middle*: the metapupil at a height h' is completely filled with footprints (orange coloured) of the 4 guide stars, selected from a narrower FoV. *right*: the FoV areas dedicated to the NGSs for different layers.

However, expanding the FoV unavoidably decreases the depth of focus [101]. This means that adjacent layers become blurred, and the effect will be greater for larger fields of view. This is the same effect as seen in the more rapid defocus (loss of depth of focus) for "faster" or lower $f/\#$ optical systems. Note that this multiple FoV approach offers better performance at sites where the turbulence is concentrated in a thin layer above the telescope. This is true in most cases.

The LINC-NIRVANA MCAO system makes use of the Multiple Field of View (MFoV) concept, using an annular mirror to divide the fields as shown in Figure 1.17. This approach increases the number of photons between the WFSs, leading to a gain in terms of photons by a factor of 2 for the WFS conjugated to higher altitude and a factor of 10 for the WFS conjugated to the ground, compared to the classical approach.

## 1.4 LINC-NIRVANA and its state-of-the-art AO system

### 1.4.1 LBT

The Large Binocular Telescope[14] [55] is the world's largest single-mount telescope. It is located on Mount Graham, Arizona, USA, at 3191 m above sea level. As the name suggests, LBT has two primary mirrors of 8.4 m diameter, and the telescope is mounted on a single alt-azimuth mechanical structure. The total collecting surface of the LBT is equivalent to that of a single telescope of 11.8 m in diameter. The distance between the two outer edges of the primary mirrors is 22.8 m. This corresponds to the diameter of a telescope with resolving power equivalent to the maximum resolution the LBT in its interferometric configuration. Under the best conditions, the site delivers seeing comparable to that of the best observing sites. The median seeing observed at LBT including the dome seeing is ~0.8" in the visible band [124].

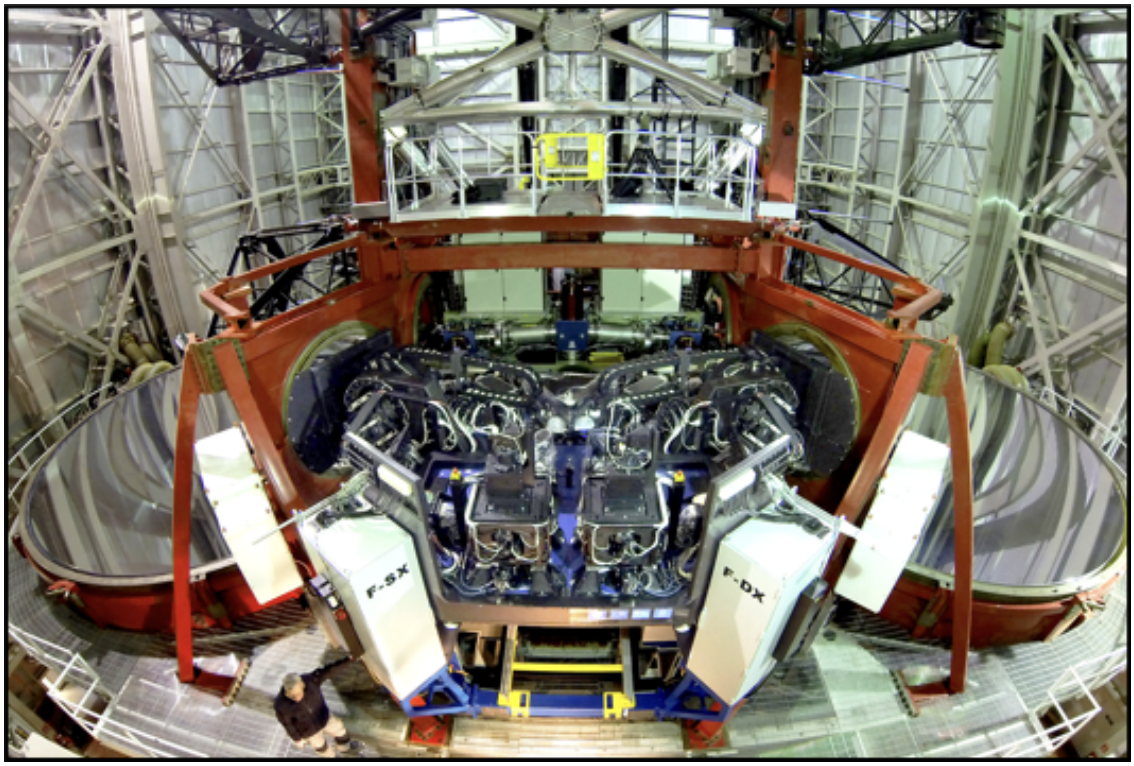


**Figure 1.18:** LINC-NIRVANA (dust cover removed) installed at the rear, shared, bent-Gregorian focus of the LBT.

[14] http://www.lbto.org

The secondary mirrors of LBT are adaptive (called the Adaptive Secondary Mirror (ASM)) and are 0.91 m in diameter. They are optically conjugated to an altitude of 100 m, that is the *ground layer*. Therefore, the light reflected off the secondary is corrected (for ground turbulence) when the loop is closed. Each of these mirrors has 672 electromagnetic voice-coil actuators [34, 105]. The two secondary mirrors are undersized, in order to avoid thermal infrared radiation emitted from the surrounding environment getting reflected towards the instrumentation. This places the telescope pupil at the secondary.

Two tertiary mirrors with elliptical shape, inclined by 45° with respect to the telescope optical axis, can be inserted in the light path before it passes through the hole of the primary. The two reflected beams allow interferometric operation. Favoured by its architecture, the LBT adopts *Fizeau* interferometry.

LINC-NIRVANA[15] (LN) is one of the instruments mounted on the LBT, situated at the rear, shared, bent-Gregorian focus of the telescope. Figure 1.18 shows LN installed on the LBT.

### 1.4.2 LINC-NIRVANA

When fully implemented, LINC-NIRVANA (LBT Interferometric Camera and Near-InfraRed / Visible Adaptive iNterferometer for Astronomy) will be a Fizeau interferometer working at Near-InfraRed (NIR) wavelengths (1.0-2.4 $\mu$m). LN has a unique and advanced MCAO system (described in detail in section 1.4.3) capable of providing a uniform diffraction-limited PSF across a 2' FoV. The instrument ultimately aims to provide a spatial resolution equivalent to that of a 22.8 m telescope in the NIR within a 10.5x10.5 square arcsec FoV via Fizeau interferometry. Fizeau interferometry is limited precisely by the isoplanatic angle. However, MCAO allows interferometry over extended fields, even of the order of a few arcmin, by providing more fringe tracking stars. In its first implementation phase, single eye observations using LN will provide users high-resolution NIR imagery.

Fully integrated, LN weighs around 11.5 tons and has dimensions of 5.7m x 4.5m x 4.1m, including the installed cover. LN consists of one large cryostat (including the cryogenic fringe tracker), two ground-layer wavefront sensors, two high-layer wavefront sensors, one piston mirror, two K-mirrors, and other optics. In total, LN contains more than 250 lenses and mirrors, 8 science-grade detectors (2 IR and 6 visible), 2 calibration systems, 133 motors, 40 control systems and around 1000 cables. Individual components are marked in Figure 1.19. Clearly, assembly, alignment, and integration of LN is a lengthy and complex procedure. Chapter 2 describes alignment to commissioning steps of LN, with a focus on my contributions.

[15] http://www2.mpia-hd.mpg.de/LINC/

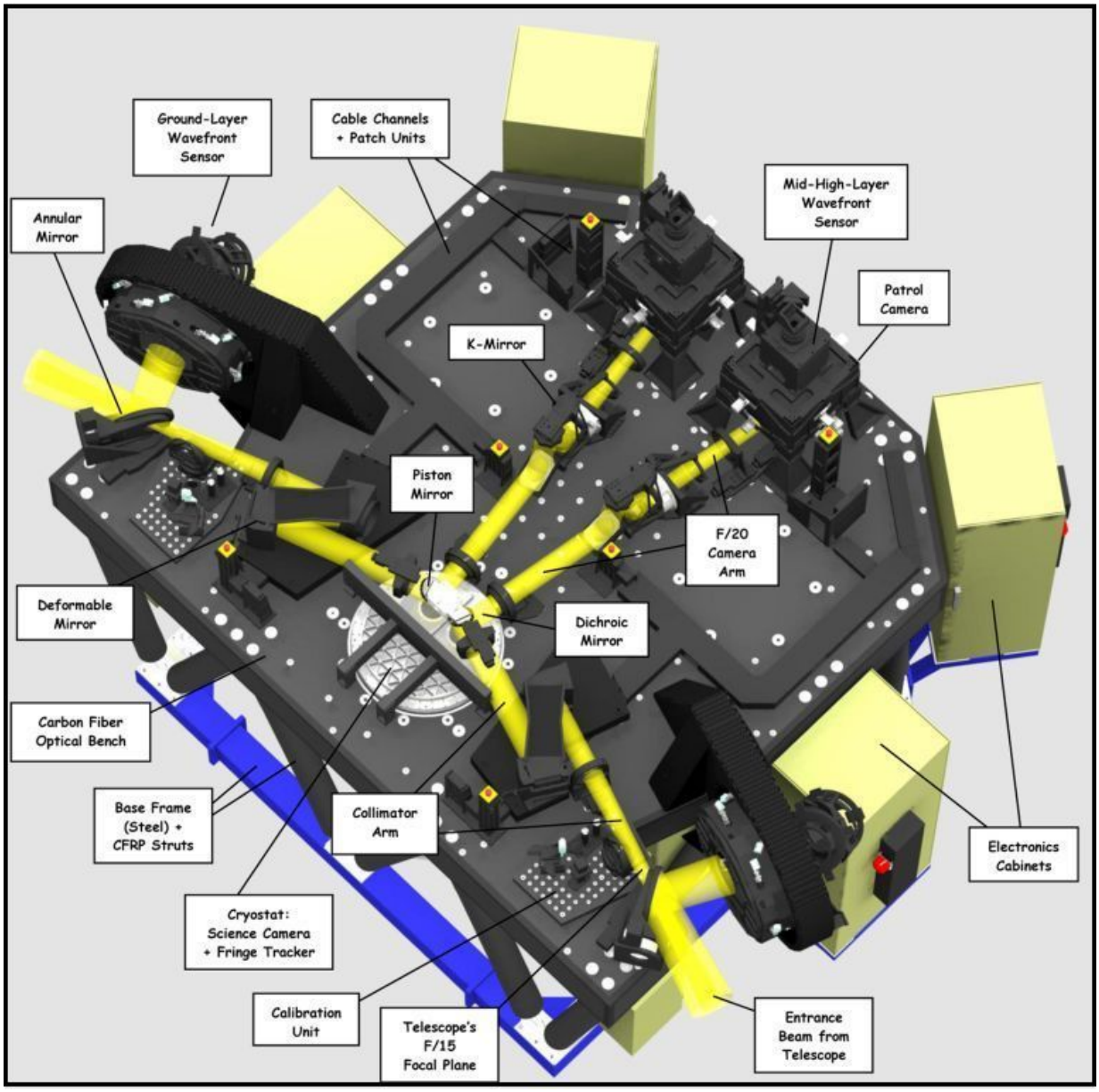


**Figure 1.19:** LN optical bench and its components. The optical path is indicated by the yellow beams.

### Light Path

Light from the primary mirrors of the LBT is directed to the LN, after reflection from the ASMs and the tertiary mirrors. Figure 1.19 displays the optical light path within the LN bench. The $f/15$ input beam from each telescope is divided into two parts by an annular mirror. Light from the annular 2'-6' diameter FoV is reflected to the Ground-layer Wavefront Sensor (GWS). The GWS measures the aberrations in the ground layer. The central portion of the beam, 2' in diameter, passes through a collimator, a folding mirror, the Xinetics DM, and a lens before reaching the piston mirror. The piston mirror takes care of the optical path difference between the beams from the two telescopes, acting as the delay line. Immediately followed the piston mirror is a dichroic, which separates infrared from visible light. The infrared part enters the cryostat, while the visible light, after passing through the lenses and the K-mirror, reaches the High-layer Wavefront Sensor (HWS). The HWS measures the aberrations caused by the atmosphere at an altitude of ~7.1 km above the telescope aperture.

The infrared light, forms an image of the focal plane at the infrared detector. A HAWAII-2 2048x2048 pixel NIR detector captures the image within the FoV of 10.5x10.5 square arcsec at a pixel scale of 0.0051 arcsec/pixel. Close to the detector lies the Fringe and Flexure Tracker System (FFTS). This consists of a roving NIR detector that captures images within an oval field of 1x1.5 square arcmin. This is to find a bright source to use as an Optical Path Difference (OPD) reference star for the piston mirror. The PSF is observed and compared with a theoretical PSF, allowing the determination of the phase difference between the beams from the two arms of LBT. The OPD signal then drives the piston mirror to cancel these differences.

To make the MCAO correction, LN uses a pair of WFSs, the GWS and the HWS, for each telescope. LN exploits the multiple fields of view approach (explained in section 1.3.2), in which the two sensors observe natural guide stars within different fields of view. The LN MCAO operation is explained in detail later, in section 1.4.3.

For resource reasons, LN will not initially function to its full capabilities. This means that the Fizeau interferometry will not be feasible in the first phase of its implementation. Rather, LN will provide 8 m diffraction-limited spatial resolution imagery at NIR wavelengths. We call this "lean-MCAO" mode. Since LN was designed for interferometry, the delivered imagery field will only be 10.5x10.5 square arcsec, given by the need to Nyquist sample the interferometric PSF. However, LN will be providing a 2' uniform FoV atmospheric correction. There are plans to upgrade the cryogenic optics to increase the MCAO FoV.

**Lean-MCAO science with LINC-NIRVANA**

The LN science team has selected the following 6 projects (listed below) to demonstrate the unique capabilities of LINC-NIRVANA in single eye lean-MCAO mode, i.e. near diffraction-limited imaging (~60 mas resolution in K-band) with near uniform Strehl ratio of up to 0.6 (in K-band) across the whole 10.5x10.5 square arcsec FoV.

The selection of projects was based on scientific impact, scientific interests of the LN team and exercising a wide range of initial AO parameters. The goal of the selected projects is to produce front-line research results on short time-scales and to demonstrate the capabilities of LN-Lean-MCAO to the wider astronomical community. The projects are:

1. The initial mass function of young massive clusters.
2. Intermediate mass black holes in Milky Way globular clusters.
3. Confirming the densest galaxies.
4. Observations of jets from young stellar objects.
5. The stellar mass profile and dark matter fraction of a high-mass compact elliptical galaxy at z ~ 1.3.
6. Galactic halo formation and evolution traced by globular clusters.

### 1.4.3 LINC-NIRVANA AO system

LN's AO module is the first of its kind. MCAO is realised using natural guide stars from multiple fields of view in the layer-oriented approach. Based on the atmospheric profiling and statistics, it is known that, at the LBT, there are two dominant turbulent layers. Strongest one being the ground layer, followed by higher turbulence at an altitude of ~7.1 km above the telescope pupil. Also, studies have shown that this particular layer is usually associated with high velocity winds (see the $C_n^2$ profile in Figure 1.6).

The GWS measures the aberrations caused by the ground layer, and drives the facility ASM of the LBT. The HWS measures the aberrations caused by the high layer at an altitude of ~7.1 km above the telescope pupil, and drives the commercial Xinetics DM on the LN bench. The wavefront sensing is performed in visible wavelengths. The HWS receives the ground-layer corrected wavefront. That is, the correction is sequential and the respective controls are independent of each other, making operation relatively easier.

LN implements AO using pyramid wavefront sensing, with the help of up to 40 pyramids, 4 CCDs in 4 WFSs, and 2042 actuators in total from 4 DMs. Alignment of each of the WFSs and their individual components was a cumbersome procedure, which took the team months of patience and tenacity. The aligned WFSs were then integrated and aligned to the rest of the LN bench. Details of the HWS alignment, and integration to the bench appear in Chapter 2.

There are probes in each of the WFSs, each capable of moving in the X-Y direction for the star acquisition. The probes are called Star Enlargers (SE). The star enlargers themselves have three optical components - two lenses and a pyramid, as displayed in Figure 1.20. The first lens

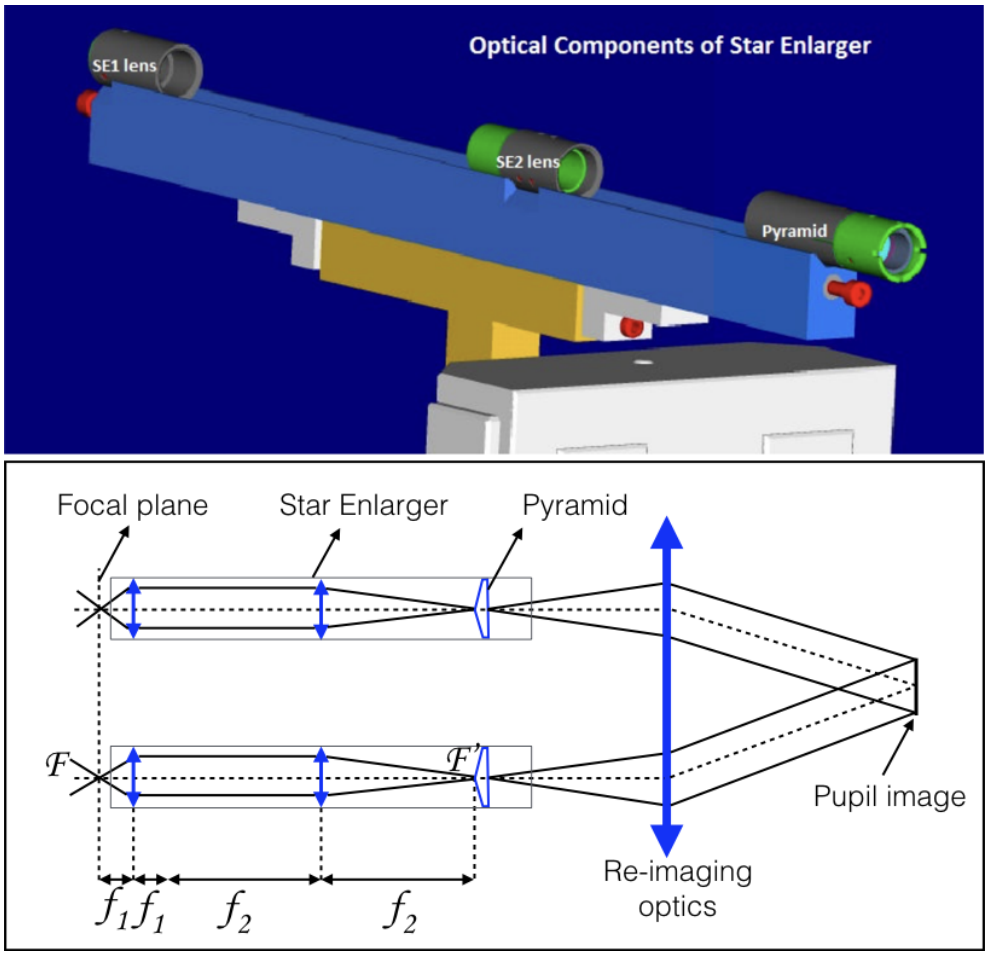


**Figure 1.20:** *above*: A star enlarger unit. *below*: The optical scheme of the star enlarger. The initial focal ratio $\mathcal{F}$ of the incoming beam is converted to $\mathcal{F}'$ using two lenses of focal length $f_1$ and $f_2$. The pupil re-imaging optics directs the beams onto the CCD at the conjugated pupil-plane.

is placed exactly a focal length away from the star image, thereby collimating the beam. The

pyramid is located at the focus of the second lens. Hence, the second lens focus the collimated beam at the pin of the pyramid. As the name suggests, the combination of lenses enlargers the star image at the pin of the pyramid, thereby avoiding the need for modulation. The pyramid splits the beam into four parts. The light then passes through a reimaging optics and falls onto a CCD.

The ASMs of the LBT, driven by the GWSs, are conjugated to ~100 m above the telescope pupil/aperture (i.e. to the ground layer). Each of the GWSs has 12 SEs in the focal plane, capable of acquiring up to 12 NGSs simultaneously, as shown in Figure 1.21. The LBT focal plane is curved. Therefore, the odd- and even-numbered SEs are offset from each other in focus by 2.6 mm so that the stars close to the inner field are acquired by the odd SEs and and those toward the outside by even SEs (see Figure 1.22). Under these conditions, the blur due to defocus is minimised and within specifications. The GWS CCD is also conjugated to ~100 m, like the adaptive secondary. In the ideal case, when everything is perfectly aligned and the incoming wavefront is planar, the four pupil images on the CCD are uniformly illuminated and of equal flux. Section 1.2.2 explains how a pyramid wavefront sensor works. The important point here is that the light coming from all of the acquired stars overlaps. In other words, they superimpose perfectly, since they are conjugated to the telescope pupil. This "optical co-addition" allows us to increase the SNR and also to use fainter stars, as long as the combined flux is equivalent to that of the limiting magnitude.

Apparently, at LBT, the ground layer contains of up to 60-80% of the total turbulence power, tip-tilt being the biggest contribution. This distribution varies from night to night and within nights as well. However, it has been shown that the ground layer correction alone (MCAO removing only the ground layer is called the Ground Layer Adaptive Optics (GLAO) correction) can improve the FWHM of the PSF by a factor up to 2.5 in K-band [124]. The light reaching the LN, when the GWS is in operation, is already partially corrected.

The partially-corrected central 2' diameter FoV wavefront finally reaches the HWS. The optics on the LN bench changes the incoming focal ratio to $f/20$, and flattens the focal plane. A K-mirror derotates the field before it reaches the HWS. Similar to the GWS, there are 8 star enlargers in each HWS unit, which can acquire up to 8 NGSs (see Figure 1.23). The light from the stars pass through these star enlargers, a pupil re-imager, and finally onto a CCD. When the higher layer wavefront sensor loop is closed, the reflected light from the Xinetics DM is corrected for the higher layer as well. The wavefront will be almost planar and therefore will allow diffraction-limited imaging at the science detector.

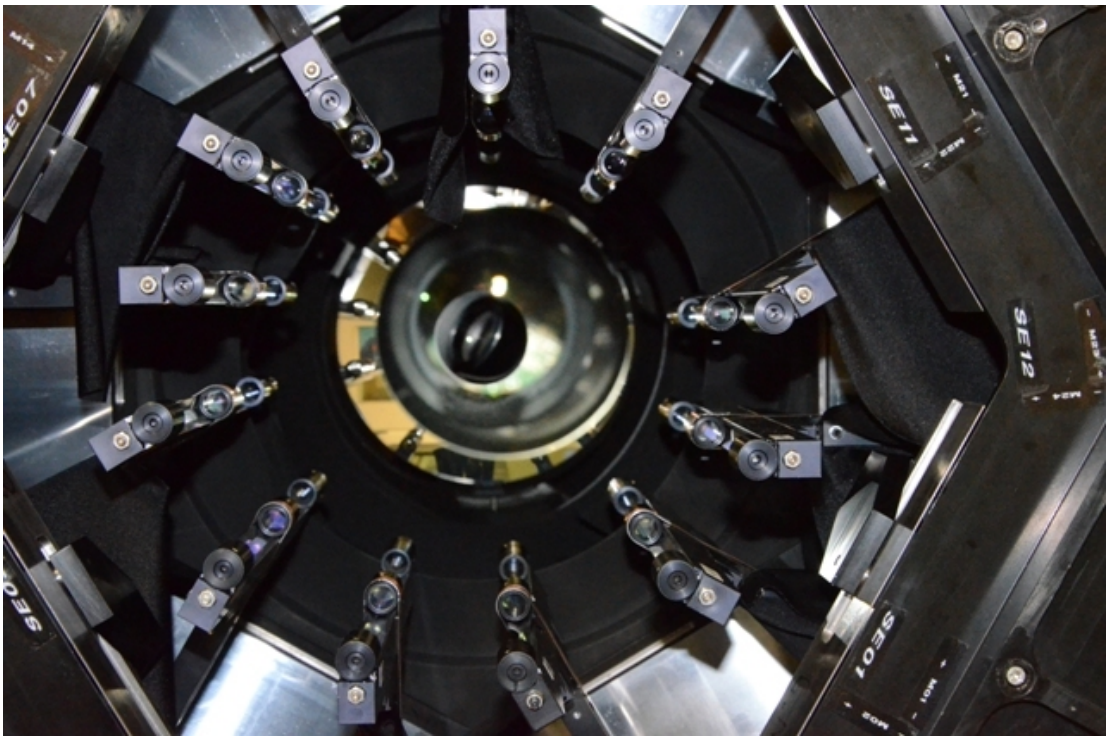


**Figure 1.21:** The 12 star enlargers inside the ground layer wavefront sensor.

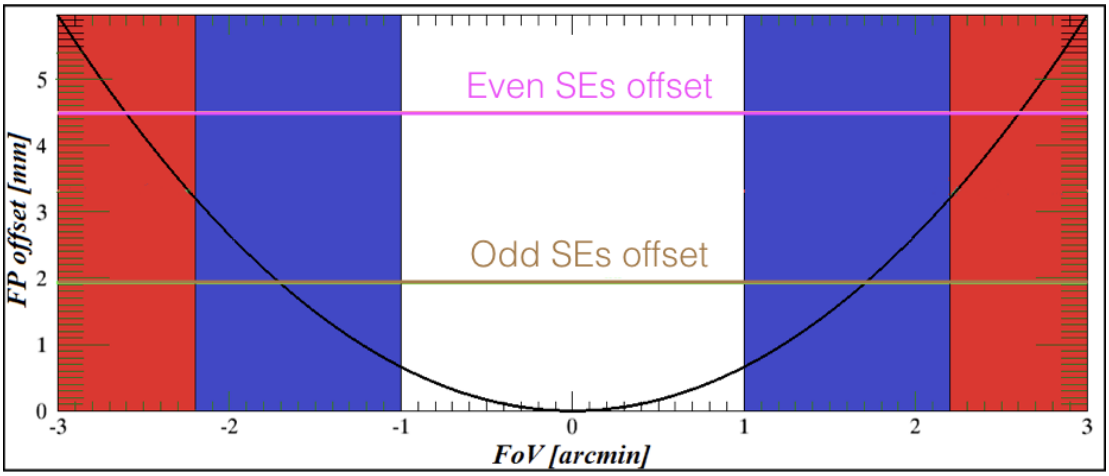


**Figure 1.22:** Curvature of the LBT focal plane for a 6 arcmin diameter FoV. The coloured areas highlight 2-6 arcmin annular diameter FoV re-imaged at the GWS entrance focal plane. The blue area is the FoV covered by the odd-SEs, focused on an offset represented by the brown line. The red area is the FoV covered by the even-SEs, focused on an offset represented by the magenta line. The two offsets are been chosen in order to minimize the residual defocus wavefront error on their respective regions.

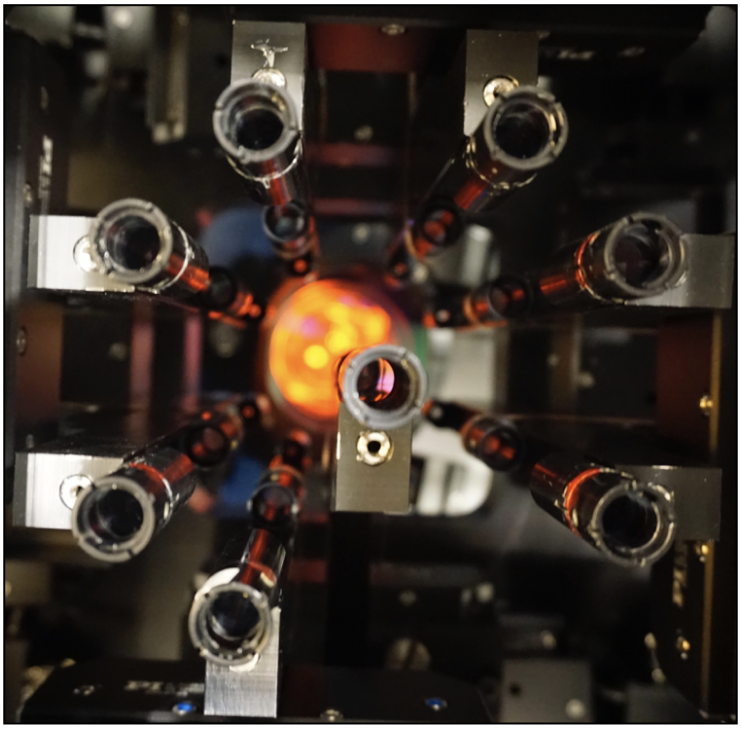

**Figure 1.23:** A view inside the high-layer wavefront sensor. 8 star enlargers can be seen.

The HWS CCD is conjugated to the Xinetics DM, which is in turn conjugated to an altitude of 7.1 km. Therefore, unlike the GWS, on the HWS CCD, the footprints of the stars do not fall one over the other (as explained in Figure 1.17). There will be an overlapping area, which depends on the asterism of the stars. In order to completely fill the metapupil, it is necessary to have about 8 stars. Without 8 stars in the FoV with reasonable separation, the metapupil will be partially illuminated. Therefore, the question is how to correct for this condition. This study of partial illumination form the subject of Chapter 3.

Since LN does layer-oriented wavefront sensing, we have telemetry about what is happening in each layer during the night. Using this information, we may be able to estimate the wind vector at each of these layers. Knowing the wind vector may be valuable in making the closed loop more stable. More importantly, we may even be able to predict how the turbulence is moving, or in other words, how the tilts are evolving as the wind blows the turbulent field across the sub-apertures. Especially, in the case of partial illumination for the HWS, knowledge of the wind vector can be used to effectively increase the illumination pattern. This could definitely improve the stability of the HWS in closed loop, and hence increase quality of correction. This study forms Chapter 4.

## 1.5 Observing the T Tauri

Thanks to the development of new techniques such as adaptive optics, we are now able to overcome the limitation imposed by the turbulent atmosphere. Some science programs require us to have a uniform PSF across a wider FoV, motivating the development of MCAO instruments. LINC-NIRVANA is one such instrument and it can produce diffraction-limited imaging at NIR wavelengths. In addition to the instrumentation aspects of an adaptive optics system, I also wanted to explore astrophysical applications, and my scientific interest lies mainly in understanding the star formation.

Stars are the fundamental building blocks of our visible universe. The formation of stars and its associated physical processes are essential to the understanding of the formation of the Universe as a whole. The present accepted theory of the stellar evolution, unfortunately, does not yet completely explain the formation of the star. This inability is due to the complicated physical processes involved. Recent advancements in observational technology at infrared and radio wavelengths allow us to investigate the physical processes using direct observations. We have now direct observations of the circumstellar disks, planets orbiting other stars, outflows from protostars etc. Diffraction-limited near-infrared observations, along with post-processing techniques, allow us to probe the immediate vicinity of the protostars. This provides us direct information on star formation.

T Tauri Stars (TTS) are the youngest known visible pre-main-sequence-stars. Usually, these stars are embedded in dense, dark clouds, which are identified as clear sites of star formation. Study of T Tauri stars at infrared wavelengths, exploiting advanced AO, high contrast imaging instruments, can provide new insights into the star formation process. T Tauri (commonly known as T Tau), is considered as the prototype of its eponymous class of pre-main-sequence-stars. T Tau is a complex and relatively rapidly evolving triple star system. I studied the T Tau system, using observations from two instruments on very large telescopes: SPHERE (VLT, Paranal, Chile) and LUCI (LBT, Mt.Graham, USA). Each of these instruments has its own advanced AO module capable of achieving high-contrast, high spatial resolution, NIR imagery.

### 1.5.1 Why NIR observations?

Stars form in relatively dense regions of cold giant molecular clouds, called *star-forming regions*. These clouds are extremely cold, around 10-20 K, so that gases are in molecular form, $H_2$ being the most abundant. The regions are so dense that they are opaque to visible light. IR or radio observations are therefore used to study these regions.

The first stage of the star formation is the collapse of the cloud cores, the densest region of $\sim 10^4$ solar masses, under their own gravity. As they collapse, they may also fragment into clumps of around 0.1 pc. These clumps become the protostars in millions of years. During protostar formation, gas falls into the clump core center, releasing kinetic energy in the form of heat. As the temperature rises, an IR source forms at the center, making observations possible.

The outflows and jets originating from the protostars may create shocks, cavities, fluorescence, and other phenomena. These features may be observed in continuum and/or line emission. From multi-epoch observations of these features, the relative motion and proper motion can be estimated, and the morphology can point to the origin of the outflows. From line emissions, we can constrain or estimate various parameters, such as the temperature, number density of molecules, possible radiation fields, etc. Also, from the line widths and shape, the turbulent and systematic motion of the gas in the probed region can be derived.

Quadrupole molecular hydrogen line emission is frequently observed in the vicinity of T Tauri stars. A number of physical processes may cause these emissions. The most common are shock excitation and ultraviolet fluorescence [120]. The ratio of the $\nu = 1 - 0S(1)$ line to the $\nu = 2 - 1S(1)$ line of molecular hydrogen can discriminate between these two mechanisms (these lines are both in the NIR K-band). Shock calculations predict a ratio of 5:1 or more, while ultraviolet fluorescence models give a ratio closer to 2:1. Another diagnostic is the forbidden line of Fe-II at 1.644 $\mu$m, which points to fast dissociative shocks.

From NIR and visible observations, it is also possible to find the spectral type of the protostar, measure the foreground extinction, detect any infrared excess due to the presence of disk, image the circumstellar or circumbinary disk, predict the geometry of the system, etc.

### 1.5.2 T Tauri

T Tau was first identified as a variable star in the mid 1940s [61] (see Figure 1.24). It is located in the Taurus-Auriga star-forming region at a distance of 146.7±0.6 pc [79] with an age of 1-2 Myr [70] and a total system mass of $4.6 \pm 0.1 M_{\odot}$ [73]. With every advancement in imaging and spectroscopic techniques at visible and near-infrared wavelengths, observations have provided new surprises and understanding about the T Tau system. Although considered as a prototype of YSOs, T Tau, unlike most other TTS, is a very complex system with at least three stellar components, and multiple outflows.

The primary component is the optically visible, early K star [24], commonly known as **T Tau N** (for T Tau North) after the discovery of the southern component. In 1982, speckle interferometry [33] revealed an infrared companion 0.7" to the South of T Tau N, called **T Tau S**.

**Figure 1.24:** T Tau photographed by W. Baade on 30 September 1940. [This image is taken from Joy, 1945 [61].]

T Tau S is very red (not yet observable at visible wavelengths), and its brightness fluctuates at all near-infrared and mid-infrared wavelengths [44]. In 2000, using speckle holography, Koresko et al. [76] found that T Tau S itself is a close (~0.1") binary, composed of the IR luminous **T Tau Sa** and the early M-star companion **T Tau Sb**. An adaptive optics, K-band image of the T Tau triple system observed on 9$^{th}$ December 2014 appears in Figure 1.25.

Recent studies [73, 115] were able to estimate the masses of T Tau Sa and T Tau Sb, the orbital period of the Sa-Sb binary, and to constrain the orbital period of N-S binary. Using continuum and line emission [32, 67], the infrared variability of the stars was associated to the accretion rates and foreground extinction [32, 66, 70, 126]. Details of this study appear in Chapter 5.

The near environment of T Tau is a source of strong and spatially extended molecular hydrogen ($H_2$) emission [8]. The spatial distribution of the $H_2$ displays a very complex pattern of multiple outflows on all observed angular scales [46, 51, 53, 114]. The $H_2$ emission is most likely generated by shock heating [53]. So far, no significant $H_2$ emission is associated with the stars themselves [32, 51, 66, 67].

There are many outflows observed from the T Tau system, and these are directly linked to the observed structures. This also means that by understanding the outflows, the geometry of the

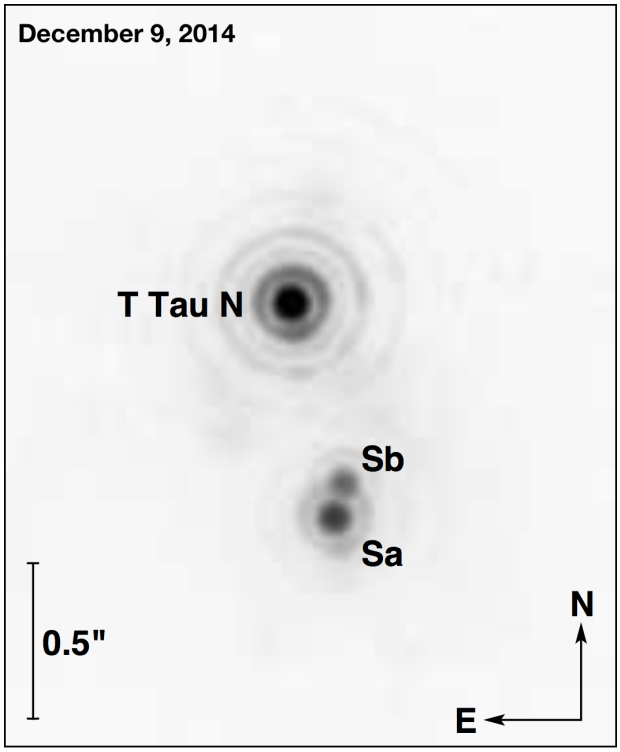


**Figure 1.25:** The T Tau triple system (K-band), imaged with the SPHERE instrument on December 9, 2014 and displayed with a logarithmic scale. [This image is taken from Köhler et al. [73].]

system may be deduced. My study described in Chapter 5, concentrates on understanding the dynamics, energetics and geometry of the T Tau system, associating each of the outflows and line emission features to their parent star, and imaging the circumstellar disks.

We have used diffraction-limited high-contrast observations using two state-of-the-art instruments, VLT-SPHERE and LBT-LUCI, each supported by their advanced adaptive optics systems to image the immediate circumstellar environment of T Tau [65, 66, 112] at near-infrared wavelengths. New outflows, fainter features and line emission were discovered. The two distinct outflow systems, the North-West outflow and the South-West coiling outflow, were associated with one of the southern stars (T Tau Sa or T Tau Sb) and T Tau N respectively [66]. For the first time ever, the enigmatic source, T Tau Sa, was detected in the J band [112]. Also, we have discovered new tadpole-shaped features, and new extended molecular hydrogen line emission [65, 112]. The study of the T Tau system using these observations forms the subject of Chapter 5.

# Chapter 2

# LINC-NIRVANA : Alignment to Commissioning

LINC-NIRVANA is one of the most capable and complex AO-fed near-infrared imagers that currently exists. LN was conceived as a Fizeau interferometer to make full use of the LBT by providing spatial resolution equivalent to that of a 22.8 m telescope. As described in Chapter 1, the LN adaptive optics module is unique and corrects for two different turbulent layers above the telescope pupil using a new concept of MCAO. All of these factors and the stringent requirements on interferometry resulted in an extended alignment, integration and implementation period.

The various sub-systems of LN were first internally aligned, tested, and verified at the partner institutes before being shipped to the Max Plank Institute for Astronomy (MPIA) in Heidelberg, Germany. MPIA is the coordinating partner and provided the facilities where all the sub-systems were integrated to the LN bench. Also, the science channel cryostat, the entire electronics, the software development, and the mechanical support were supplied by MPIA. The team at MPIA, supported by colleagues from INAF-Padova, carried out all the alignment on the LN bench, integrated the internally aligned sub-systems to the bench, and performed a series of tests and confirmed that the overall system requirements are met.

In this chapter, I describe the path LN has taken from alignment to commissioning, with a focus on my contributions. I was in charge of the alignment and integration of the adaptive optics sub-systems to the bench, especially the high-layer wavefront sensor part. We devised the alignment procedures and wrote python scripts supporting the alignment, testing and verification. Constant improvement of the software packages, providing inputs to debug services connecting the hardware to software, and development of the GUIs took place in parallel with the integration and testing. One of the main codes performs the calibration of the wavefront sensors. Another is the partial illumination code, which became part of the high-layer wavefront sensing loop service (see Chapter 3). All these activities formed a large part of my doctoral studies. Details of my contribution to LN alignment, integration and verification appear in the following sections.

## 2.1 The Pathfinder experiment

Before getting into the details of the LN alignment to commissioning timeline, it is worth noting here that LN had a precursor, called Pathfinder, that was used at the LBT for approximately 2 years. The Pathfinder experiment was designed to understand and assess the technical complexity of LN, especially the adaptive optics part of the instrument and its interaction with the telescope and its subsystems. We demonstrated operation of the ground layer wavefront sensor. That is the ability of the GWS to perform the correction driving the ASM of the LBT. This knowledge can be carried over directly to the full LN, since LN AO correction is sequential and decoupled (see section 1.4.3). We verified the interfaces and communication between the GWS and the ASM, identified possible software, mechanical or optical problems, and closed the loop on-sky. Details of the Pathfinder runs can be found in [9, 10, 25, 75].

## 2.2 Alignment to commissioning timeline

A sophisticated instrument, deploying several new techniques, requires implementation in a number of phases. We pursued the following Alignment, Integration, and Verification (AIV) strategy :

1. Sub-system alignment and verification.
2. Integration of sub-systems to the LN bench.
3. Instrument level verification.
4. Preliminary acceptance Europe.
5. Shipment.
6. Re-integration and verification in the LBT mountain lab.
7. Installation at the telescope.
8. Commissioning

Individual, detailed explanation of each of the steps above is far beyond the scope of this thesis. I therefore describe them briefly below.

### 2.2.1 Sub-system alignment, verification and integration to LN bench

The components on the LN bench are described in section 1.4.2 and are shown in Figure 1.19 along with the light path. Left arm of LN is called SX arm, and DX for the right arm. LN is divided into 4 sub-systems: warm optics unit, high-layer wavefront sensor unit, ground-layer wavefront sensor unit, and the cryogenics unit (as shown in Figure 2.1). Each of the components of the subsystems were individually verified to meet their requirements. In the chronological order of their integration to the LN, these sub-systems are described below. Note that the SX arm was aligned and integrated first, followed by the DX arm.

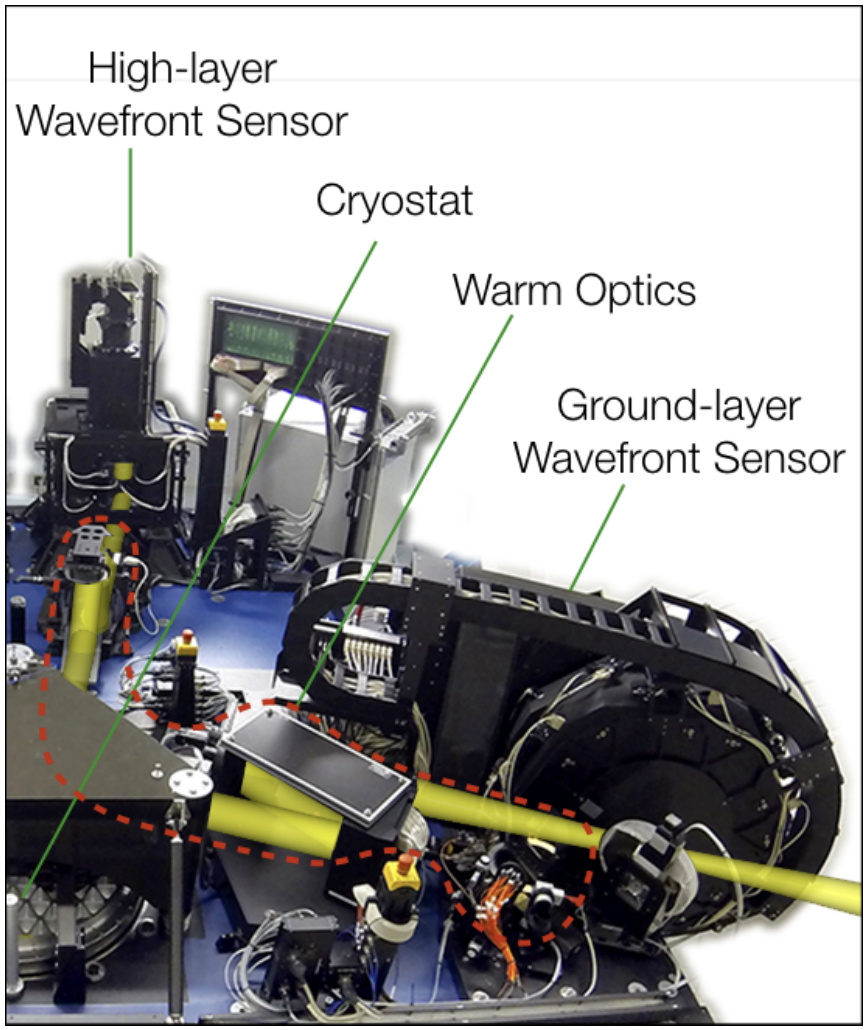


**Figure 2.1:** Aligned LN bench at MPIA. The sub-systems are indicated. The optical components within the dotted red curve compose the warm optics (here, just the SX channel). The light path is represented by the yellow beams.

### Warm Optics

The warm optics for each arm consists of collimating lenses, a folding mirror, a deformable mirror, a shared piston mirror, dichroics, lenses to change the focal ratio from $f/15$ to $f/20$, a K-mirror, a beam-splitter, filters, a patrol camera (contribution from INAF-Rome), and the calibration unit. All of these are marked on Figure 1.19. Basically, the warm optics represent all of the ambient temperature components on the bench from the telescope focus to the high-layer wavefront sensor unit. Colleagues from MPIA, including myself, performed this alignment. Many auxiliary optics and components were used to do this. The full description of the warm optics alignment can be found in [84, 85], and references therein.

### HWS

Section 1.4.3 describes the working principle of the ground-layer and high-layer wavefront sensors. The internal alignment of each of the star probes within the HWS units was performed by colleagues from INAF-Bologna. For the integration part, once the warm optics alignment was accomplished, the high-layer wavefront sensor unit alignment started. The internally aligned star probes were mounted to the HWS unit. These probes were then aligned in tip-tilt and focus to the $f/20$ focal plane, setting the pyramid rotation of each of the units within specifications, and finding the focus positions of the CCD corresponding to pupil conjugation and DM conjugation at the correct altitude (7.1 km above telescope pupil). This alignment was performed using the calibration unit on the bench. Details can be found in section 2.4 below and in [81].

### GWS

The ground-layer wavefront sensors measure and correct the atmospheric turbulence due to turbulence ~100 m above the telescope. The internal alignment of the GWS itself is complex and took around 6 months per sensor [10, 94]. Note that each of the GWSs has more than 100 degrees of freedom [80]. This was performed by our colleagues at INAF-Padova. The aligned GWS was mounted to the LN bench after HWS integration to the bench. We used a special optical alignment setup, called the Magic Lantern (ML), to align GWS to LN. The ML is mounted temporarily on the bench in front of the annular mirror, and is aligned to the aligned HWS, and therefore to the on-axis telescope focus position. The annular mirror is then adjusted so that the GWS is aligned to the bench. That is, the focal plane of the GWS is aligned to that of the telescope. Also, we ensured that the on-axis position coincides with the center of rotation of the GWS. Tests were performed to establish that all the requirements were met.

#### Cryostat and Fringe Tracker

The internal alignment of the optics within the cryostat was performed by colleagues at MPIA. This took place in parallel with the previously mentioned sub-systems. The details of the specifications, alignment, tests performed, and results can be found in [15–17]. The lower part of the cryostat houses the fringe tracker unit (FFTS) contributed by colleagues from Universität Köln, Germany. The very bottom part of the cryostat unit is actually warm. This is where the motorized stages for the fringe tracker detector are mounted. The Max Planck Institute for Radio Astronomy, Bonn, Germany provided the FFTS detector system. More details regarding the fringe tracker unit appear in [13, 57, 103, 107, 132].

The laboratory alignment of the sub-systems and their integration to the LN bench took slightly less than a year for the first arm. This was mainly due to the fact that we had to invent certain alignment procedures, work with unstable software packages under development, electronics issues, and the need to develop various codes to assist the alignment etc. The same procedure took only 8 months for the second arm.

### 2.2.2 After integration till commissioning

Once the integration was complete, we performed the calibration of the HWSs on both sides with the help of the calibration unit. The calibration procedure is discussed in detail in Chapter 3 (section 3.3.1). Also, we performed some closed loop tests and consistency checks. The flexure test was one of these tests. The fully aligned LN bench was tilted from 0° (looking at zenith) to close to 80° (close to horizon) to study the movement of individual components and the flexures caused (see Figure 2.2). These data will be used for look-up tables that will control the motorized stages of the optical components so that we maintain image quality and AO correction irrespective of the varying gravity vector.

After passing the Preliminary Acceptance Europe (PAE) in May 2015 and concluding the laboratory tests by end of June 2015, LN was shipped to the LBT. Due to its dimensions, weight, cost, and mechanical sensitivity, we disassembled the sub-systems and components and shipped them in separate boxes. The shipment consisted of 9 full-sized shipping containers (see Figure 2.4), as well as a large, custom box for the optical bench.

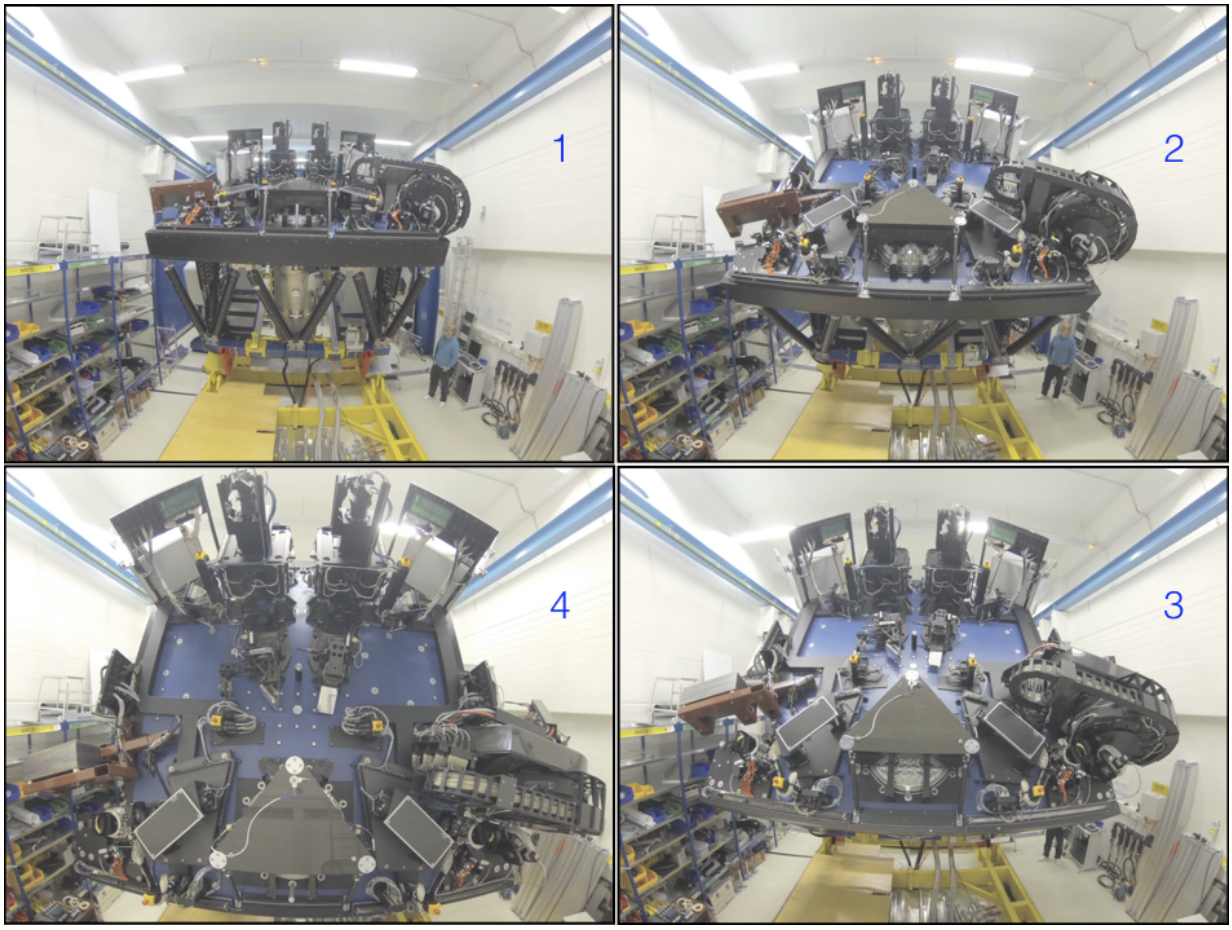


**Figure 2.2:** Flexure testing the populated LINC-NIRVANA optical bench. A large hydraulic ram tips the 10 ton instrument from zenith to horizon (1-4), allowing assessment and calibration of flexure effects. Note the LN team members for scale.

After delivery to LBT, the team made 9 separate trips to LBT, spanning slightly more than a year, to reintegrate the sub-systems, and realign the whole instrument (see Figure 2.5). This included testing the software, hardware and compatibility of LN with the LBT interfaces [52]. The timeline of the activities from shipping till the first semester of 2017 appears in Figure 2.3. LN is currently at the rear bent-Gregorian foci of the LBT, (see Figure 2.6 and Figure 2.7). As I write, LN commissioning is on-going, with science readiness planned for the second half of 2018.

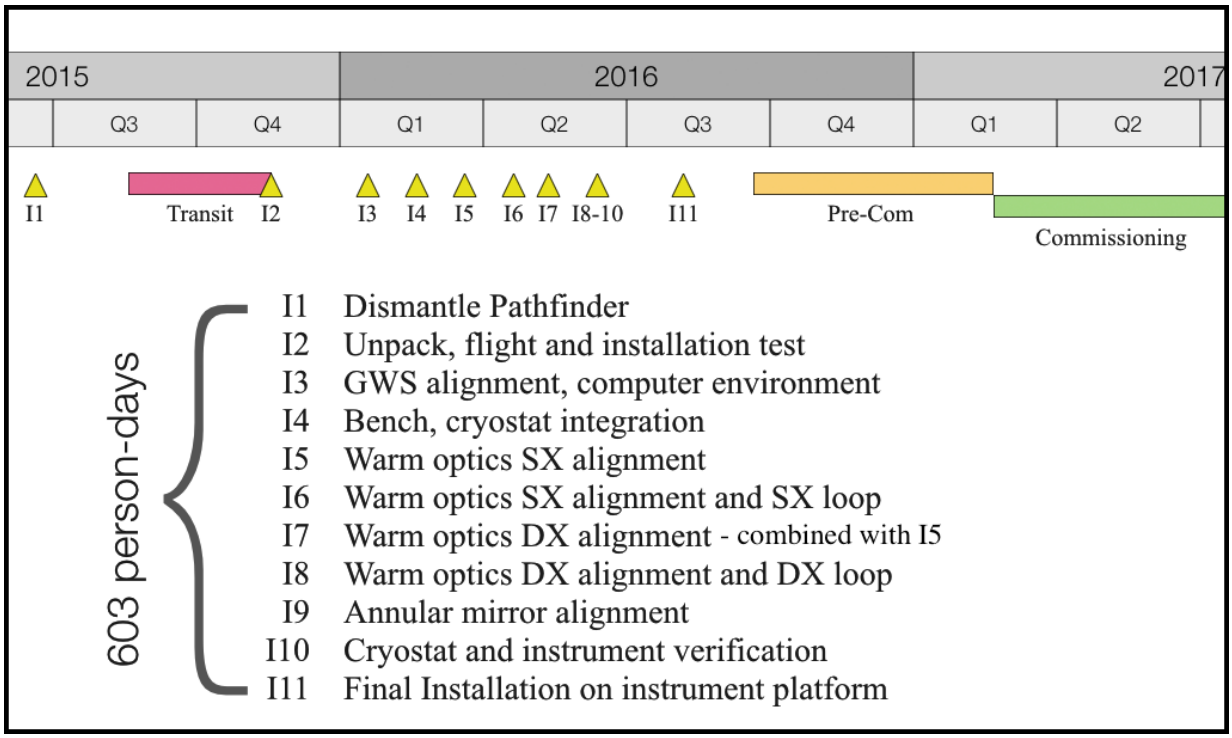


**Figure 2.3:** Timeline representing the dismantling of the Pathfinder unit, shipping duration from MPIA to LBT, the different assembly, alignment and re-integration runs, and the pre-commissioning and commissioning runs. In the pre-commissioning runs, we aligned the LN to the telescope and calibrated the GWSs.


**Figure 2.4:** Packing and shipping LN. (1) Packing of shipping boxes. Also the cryostat before packing can be seen, (2) The PI of the instrument, Tom Herbst in front of the LN bench shipping box, (3) Oversized LN box leaving MPIA, (4) Oversized LN box being moved to a boat at Neckar, Heidelberg, (5) Oversized LN box on the way to LBT, and (6) Oversized LN box reaching LBT.

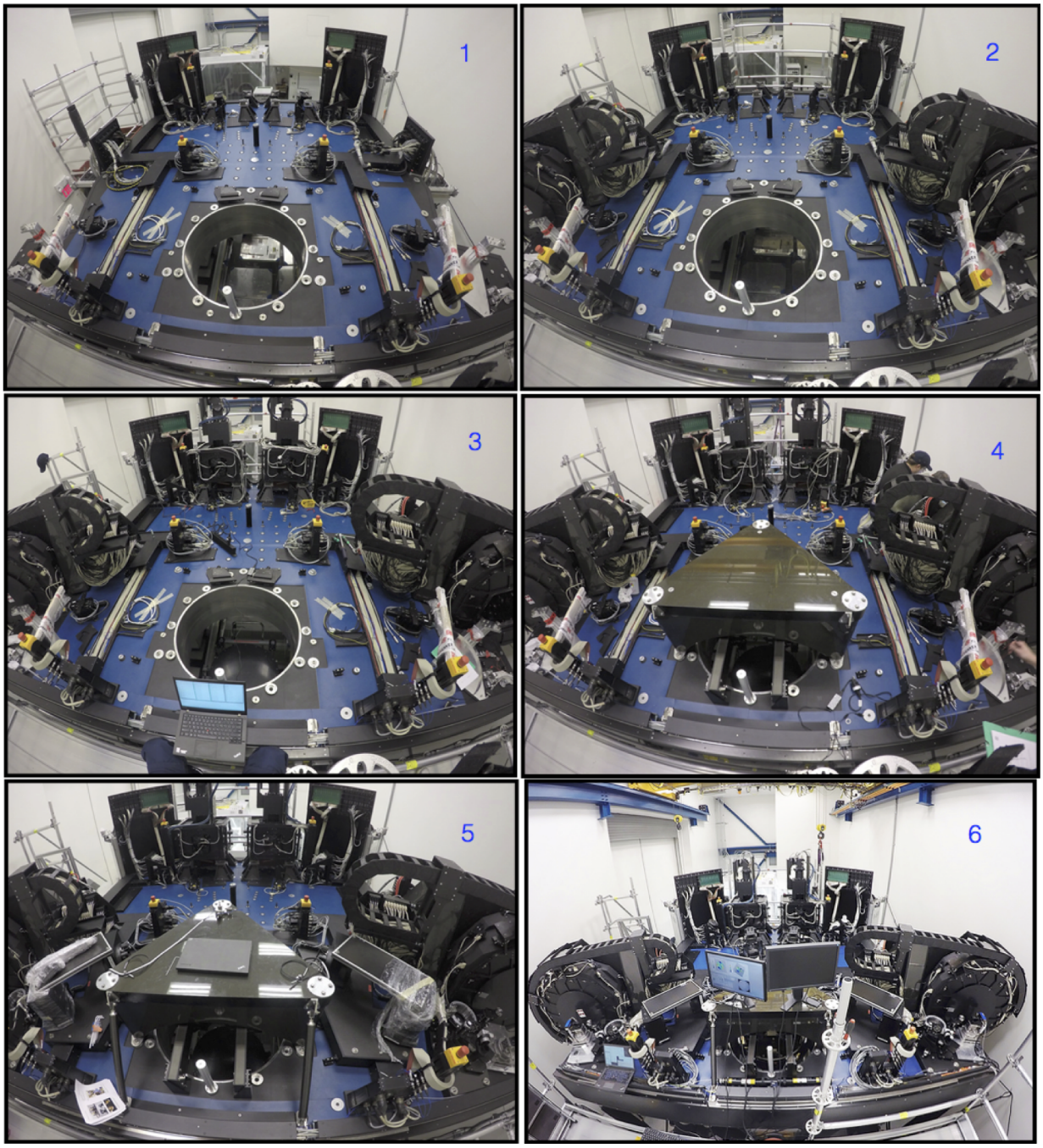


**Figure 2.5:** Re-assembly and re-alignment of the LN bench at the LBT lab. (1) LN bench before installing any components, (2) the ground layer wavefront sensors installed, (3) the high layer wavefront sensors installed, (4) coffee table (holding the piston mirror and dichroics) installed, (5) Xinetics DMs and folding mirrors installed, and (6) Fully re-assembled and re-aligned LN bench, ready to be lifted onto telescope platform.

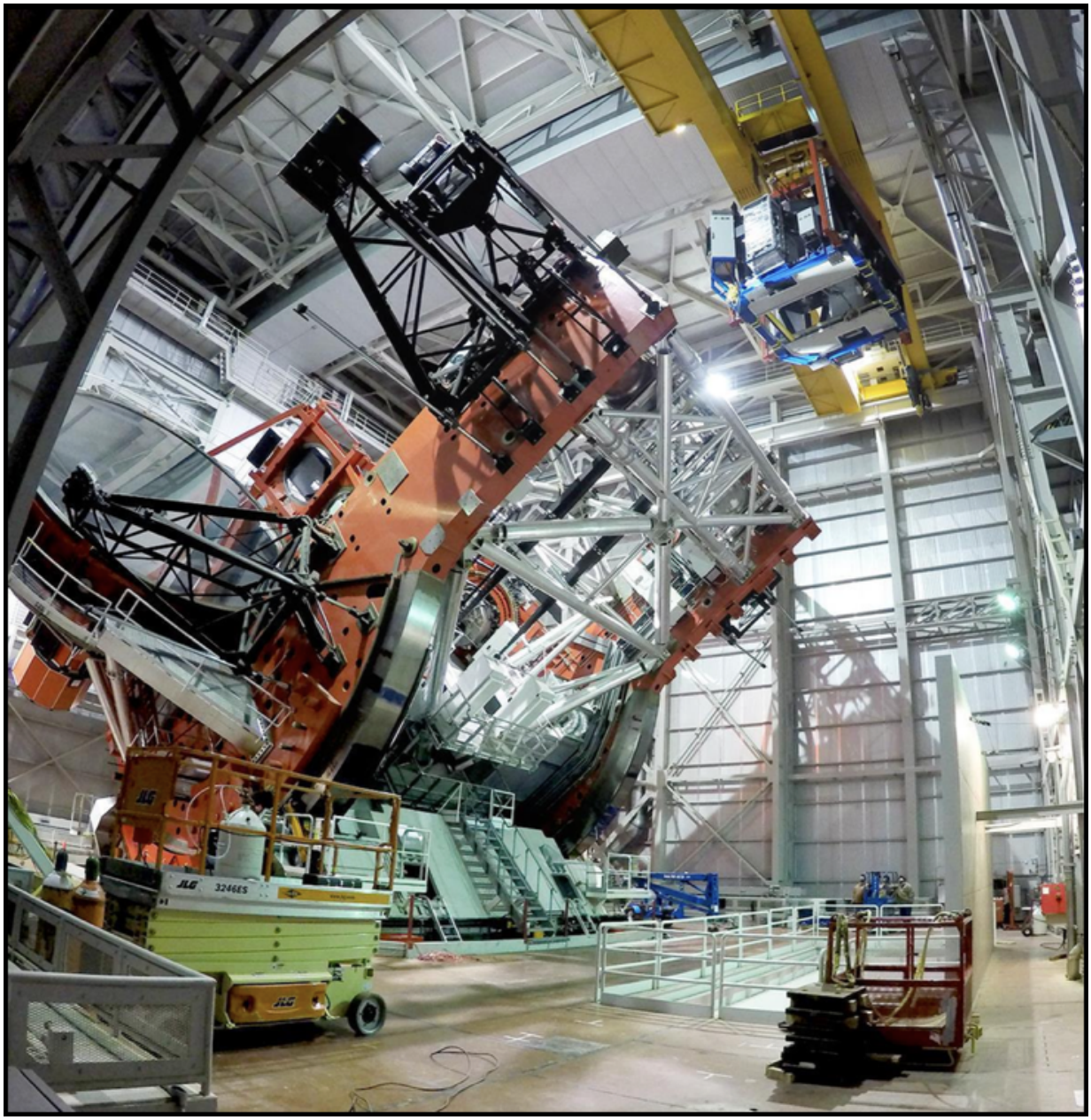


**Figure 2.6:** LINC-NIRVANA, suspended from the crane high above the dome floor to the upper right, has just emerged from the enclosure hatch at bottom center. The instrument-telescope dance is about to begin, allowing LN to fly over the midline of the LBT to its final mounting location on the bent-Gregorian instrument platform.

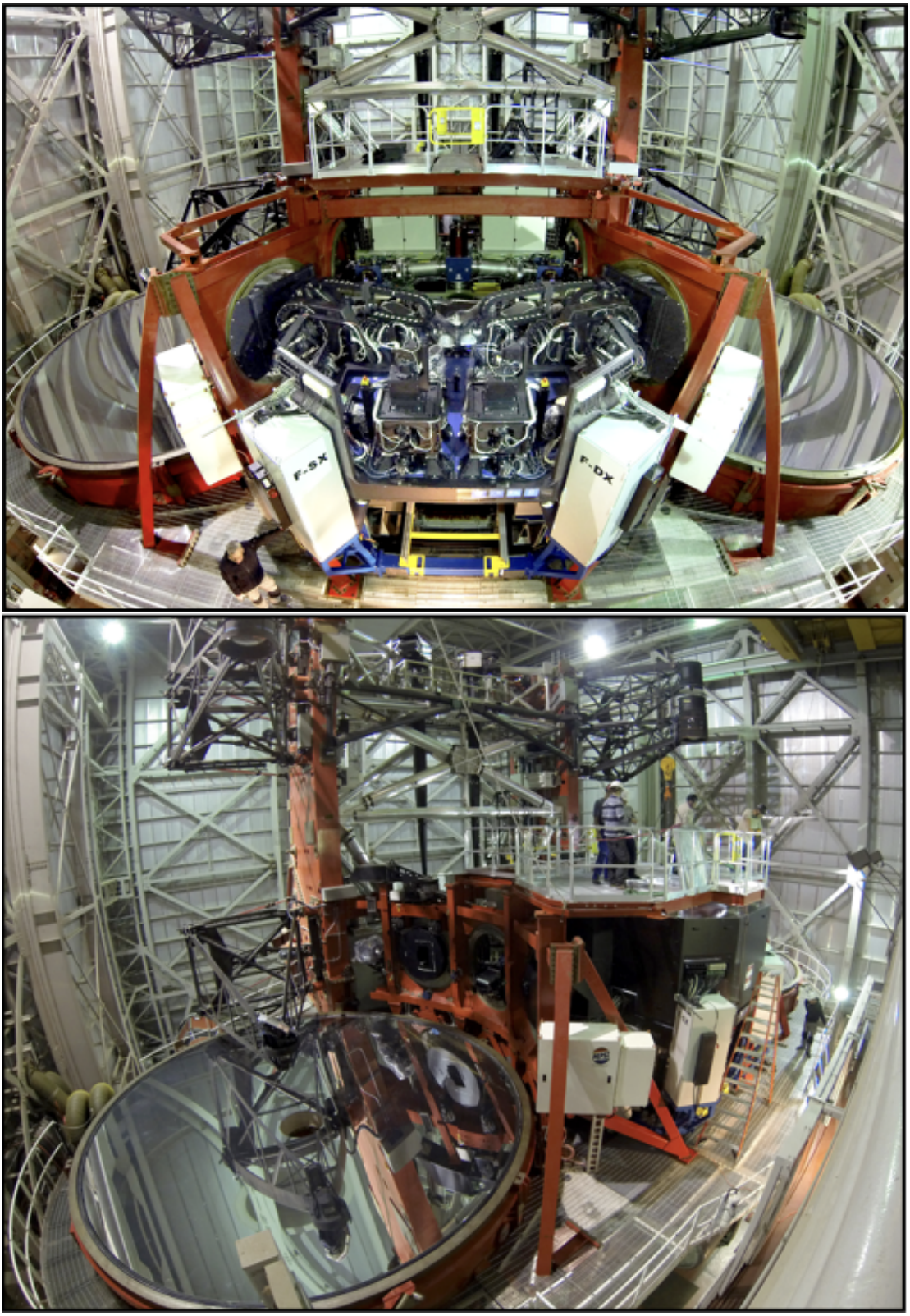


**Figure 2.7:** *top*: Fully aligned LINC-NIRVANA installed without the cover at the rear, shared, bent Gregorian focus of the LBT. *bottom*: LN in its final configuration with the (black) cover installed.

## 2.3 LN software development

The colleagues from MPIA are responsible for essentially all LN software. The overall architecture appears in Figure 2.8. The fundamental or low-level programming, what we call the Twice As Nice (TAN) framework, is written in C and C++. TAN is a new and flexible developer framework for high performance service-oriented architecture based systems. It uses the middleware ICE by ZeroC Inc. for interprocess communication and Digia Cross-Platform Rich Client Development Framework Qt. The LN software packages are built on top of the TAN, and are written mostly in Python. It is worth mentioning that TAN is the basis for other instruments such as ARGOS [93] and SHARK [36]. One step higher is the high-level code, also written in Python. One example of this code is the calibration script for the wavefront sensors. At the very top, we have the software packages mainly in the form of GUIs for general astronomy users. Over the years, the software packages and services have improved and are approaching their final form. More details can be found in [11, 19, 72, 125].

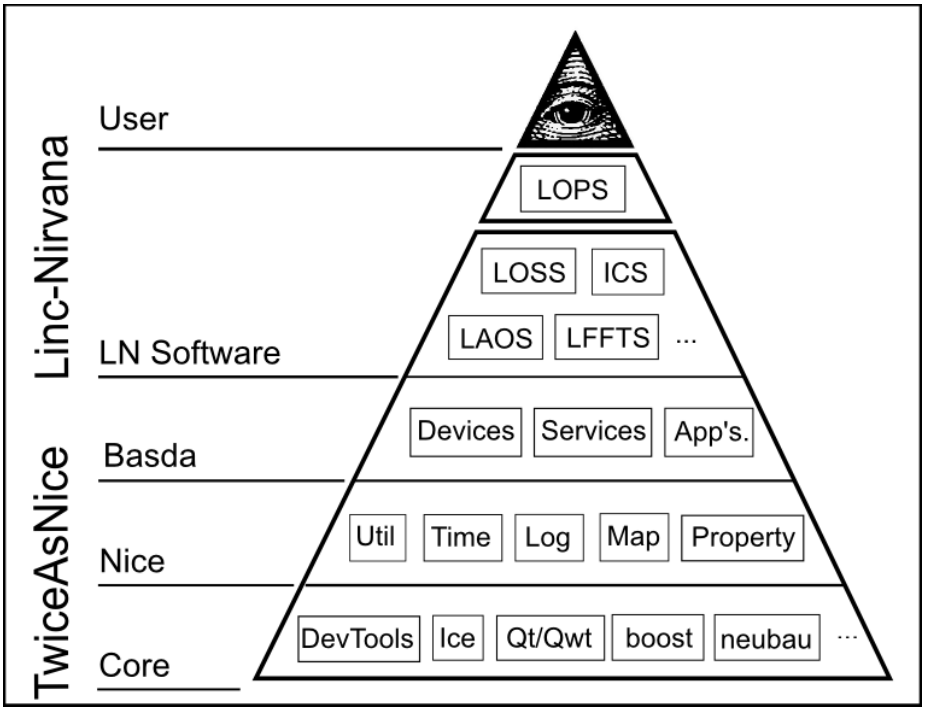


**Figure 2.8:** LN software structure. The foundation is Twice As Nice, developed by colleagues at MPIA, and written in C and C++. All the LN-specific software packages are built on the TAN framework. High level programming is written in Python connecting to various LN software packages or services. However, the astronomy user will only see the various GUIs at the top of the diagram.

The LN software can be broadly classified into three units, namely LSYS, LAOS, and LIRCS. The LSYS package and its services take care of instrument control, telemetry, and interfacing to the LBT. LAOS stands for LN Adaptive Optics Software. Its services control all the warm optics and AO-related activities. The LIRCS software package manages all the cryogenics camera functions.

All LN configuration files and software packages are under version control (SVN). We have the capability to remotely work on LN from MPIA, as well as the ability to monitor various conditions or aspects of the system, such as the temperature of the cabinets, the CCDs, etc. Each activity is logged and retrievable for analysis.

In the field of software development, I have mainly worked on the high level programming of the following services - AO loop services, guiding and acquisition services, and camera services. I have written fully automated HWS calibration procedures and implemented partial illumination in the HWS loop service. In addition, I have also provided feedback, suggestions, and bug-checking for the low level programming side.

## 2.4 My contributions

Over the past four years of my doctoral study, I have contributed to different aspects of the LINC-NIRVANA system, namely:

1. Optical assembly, alignment, integration of components of the sub-systems to sub-systems as well as sub-systems to the full system (see section 2.4.1 below).
2. As a liaison between the software developers and astronomers, as well as taking part in software development by writing high-level programs to accomplish various routines for alignment, calibration and working of the several services (see section 2.4.2).
3. Solving the partial illumination issue which is crucial in realising LN MCAO capabilities (see Chapter 3 for details).
4. Improving the stability of the adaptive loops using the knowledge of the wind vector from AO telemetry (see Chapter 4 for details).
5. Commissioning of the instrument at the LBT and making it more user-friendly (on-going work).

In this section, I will report the particulars of the optical part and the software development part of my contribution.

### 2.4.1 Aligning HWS to the bench

The warm optics alignment ensures that LN delivers a wavefront of the highest possible quality to the HWS, minimising static aberrations and keeping the wavefront sensor far from its saturation regime. The residual wavefront error delivered by the warm optics at the $f/20$ focal plane of the HWS was less than 50 nm at a wavelength of 633 nm for the SX arm, a majority of which is due to the DM. This number can be further minimised by shaping the DM to compensate for the rest of the static aberrations. A residual wavefront error of less than 50 nm is extremely good and meets the requirements. The DX arm performs similarly well.

Aligning the HWS to the bench follows the warm optics alignment. The HWS alignment we developed consists of 6 steps.

1. Alignment of the lateral position of the CCD
2. CCD conjugation to the pupil plane
3. Preliminary alignment of the star probes' tip-tilt
4. Fiber plate alignment
5. Star probes' fine alignment
6. CCD conjugation to the deformable mirror

In short, the alignment first addresses the CCD centering to the on-axis reference beam, then conjugates it to the proper height and co-aligns the 8 star probes in tip-tilt and focus. The unaberrated on-axis beam is materialised using a commercial ZYGO-FISBA interferometer (imitating the telescope on-axis beam), and is used for the warm optics alignment. However, the FISBA beam cannot be used for aligning the star probes distributed in the 2' FoV. Instead, we used the reference fiber plate in the calibration unit. The reference fiber plate contains 23 fibers: 1 on-axis mono-mode fiber fed by a near-infrared LED and 22 off-axis 200 micron multi-mode fibers fed by visible LEDs. The fibers are evenly distributed in the 2' FoV (see Figure 2.9). The alignment is described below.

#### 1. Alignment of the lateral position of the CCD

A mask with a small central hole is inserted in the light path, at the visible pupil plane, as shown in Figure 2.9. The star probes are not inserted into the path. The light enters the HWS, passing directly through the re-imaging optics and falling onto the CCD. The CCD is moved in its own

plane till the centroid of the spot produced by the on-axis beam falls at its center. However, because of the non-perfect perpendicular mounting of the stages where the CCD is mounted, a motion along the optical axis also shifts the spot in the X and Y directions. Therefore, this is only a preliminary adjustment. The lateral position is re-adjusted after the CCD is focused to the pupil plane.

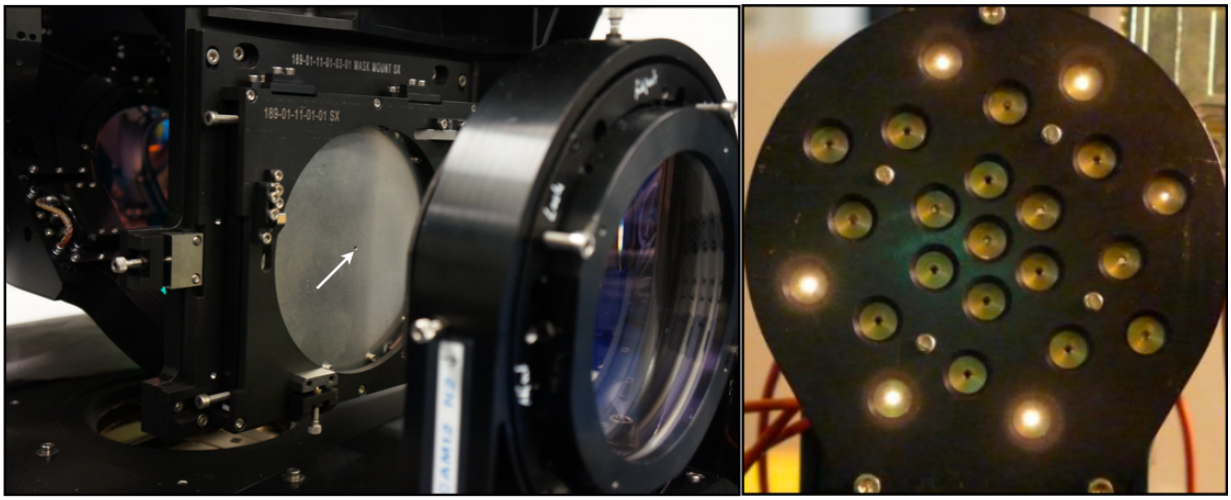

**Figure 2.9:** *left*: The mask with 2 mm central hole (indicated by the white arrow) positioned in the visible pupil plane, used for HWS CCD centering, conjugation to the pupil plane, and for the star probe's tip-tilt alignment. *right*: The reference fiber plate containing 23 fibers distributed in a 2' FoV. Six fiber "stars" are illuminated.

### 2. CCD conjugation to the pupil plane

Knowing the pupil conjugation position is important and makes the alignment of the star probes efficient. At the pupil conjugation position of the CCD, pupils created by each of the star probes due to their respective fibers will superimpose perfectly only if all the star probes are perfectly co-aligned in tip-tilt. Note that the pupil (~100 m) conjugation is different from the 7100 m conjugation. Misalignment between the probes leads to a relative displacement of the pupil images on the CCD. This can be easily evaluated in pupil conjugation, since all the pupils should have the same center of light position at pixel (20,20) in every quadrant, as seen in the bottom left panel of Figure 2.10. The CCD conjugation to the pupil plane is done using 4 fibers in the fiber plate. The position of the CCD when the spots perfectly overlap one another defines the pupil plane conjugation position. Once the CCD is properly focused to the pupil plane, its lateral position is fine tuned, as described in the previous paragraph.

### 3. Preliminary alignment of the star probes' tip-tilt

The only reference source at this point is the on-axis FISBA beam. Using the FISBA beam, the pyramid rotation angle of each star probe was verified to be within specifications. Each of the star probes was finely centered on this beam. The tip and tilt of the stages were adjusted by looking at the 4 spots produced by the 2 mm mask in the pupil plane. We then adjusted the tip-tilt of the individual star probes by centering the spots to at fixed pixel (20,20). The misaligned

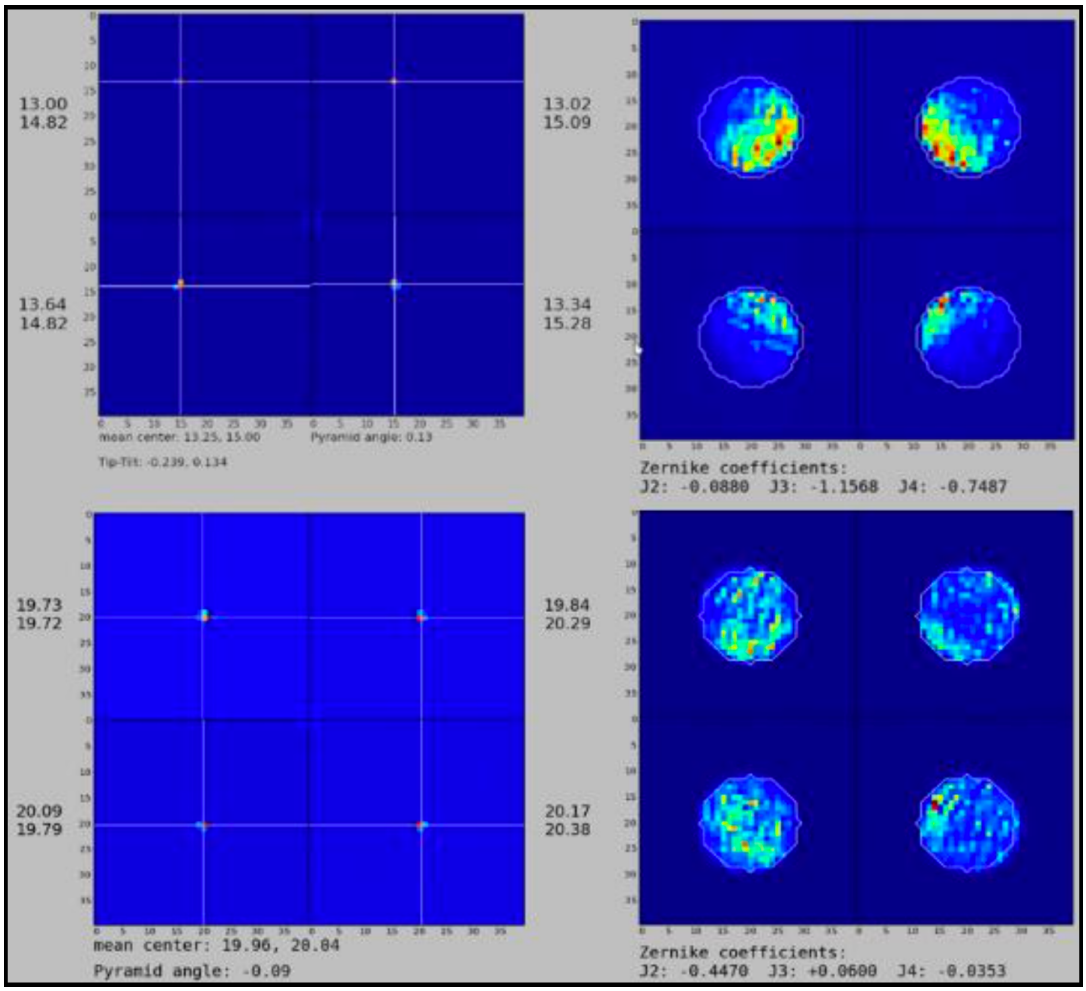


**Figure 2.10:** *left*: The four small spots produced by a star probe used for the tip-tilt alignment, as mentioned in step 3 of the HWS alignment to the bench. *right*: The four pupils produced by a star probe used for focus alignment (a clear intra-focus signal is visible in the top-right panel). The top panels represent the signatures of the misaligned star probes, and the bottom panels represent the signatures after alignment (centroids of the 4 spots on the correct pixel within the requirements and the pupils evenly illuminated). Note that the pupil image are centered at coordinate (20,20) in each quadrant.

and aligned star probe signatures can be seen in the upper and lower panels of Figure 2.10, respectively. The goal of the alignment is to place the centroid of the 4 spots on the same CCD pixels with a maximum discrepancy of 0.1 pixels. When this is achieved, all the star probes are well co-aligned in tip-tilt and can be used as a reference for the tip-tilt alignment of the fiber plate.

#### 4. Fiber plate alignment

The fiber plate simulates the curved $f/15$ focal plane delivered by the LBT. Its alignment to the reference beam is critical to refine the alignment of the HWS star probes. The initial step is to align the central fiber of the fiber plate to the telescope focal plane, as defined by the FISBA beam. A star probe positioned on-axis, intercepting the light of the FISBA beam produces 4 equally illuminated pupil images on the detector. The calibration unit folding mirror (mounted on a rotating stage) is positioned to reflect the light from the central fiber towards the HWS. The fiber plate is moved in X and Y until the PSF produced by the central fiber is perfectly centered on the on-axis star probe, and then along Z to minimize the de-focus term measured by the WFS. The central fiber of the fiber plate is now aligned to the FISBA beam. Four different star probes are then centered, one at the time, on the on-axis fiber and aligned in focus. The same 4 star

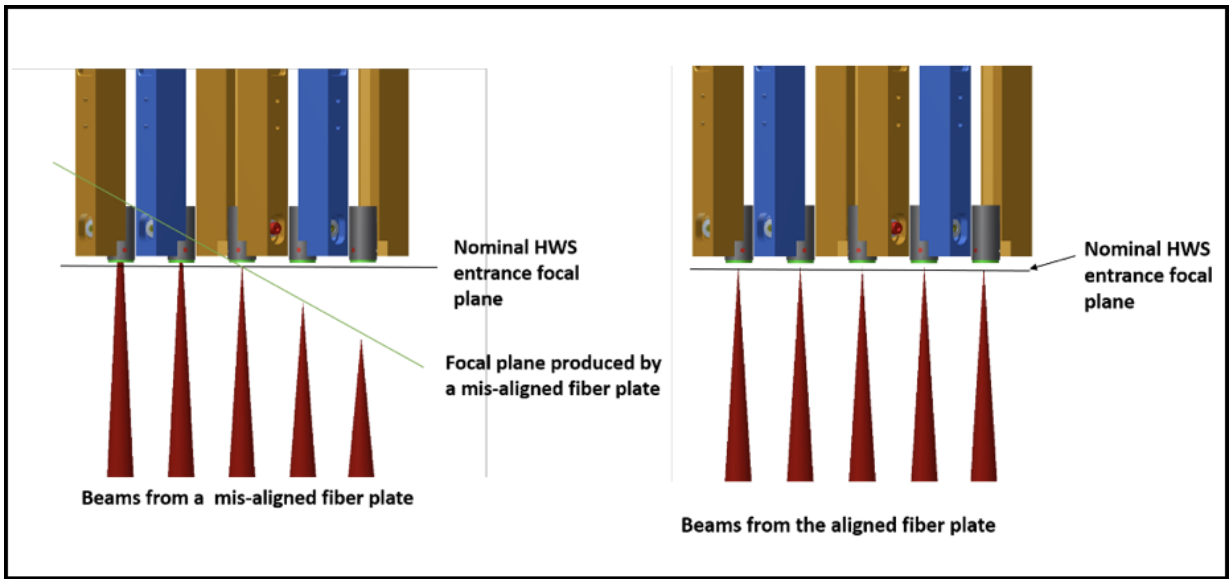


**Figure 2.11:** *left*: the focal plane delivered (green line) by a tilted fiber plate (the effect is here greatly magnified). *right*: the focal plane when the fiber plate is perfectly aligned.

probes are used for the tip-tilt alignment of the fiber plate. This is done iteratively, centering the aligned star probes on the on-axis and off-axis fibers. Since the curved focal plane delivered

by LBT is flattened at the HWS entrance by the warm optics, the fiber plate tip tilt alignment is performed by simply minimizing the focus gradient along each tilt axis by tilting the fiber plate (see Figure 2.11).

### 5. Star probes' fine alignment

The aligned fiber plate allows fine alignment of each star probe in tip, tilt and focus. Since the linear stages moving the star probes suffer from mechanical pitch, roll and yaw, each of the star probes is aligned close to the center of its travel range using the closest fiber. The tip-tilt alignment procedure is same as in step 3 above.

| **Star Probe** | **Defocus** (nm WFE) | **Tip-Tilt mean center (pixels)** |
|---|---|---|
| SE01 | 7 | 20.09,19.99 |
| SE02 | 20 | 20.03,19.98 |
| SE03 | 4 | 20.03,19.97 |
| SE04 | 4 | 19.97, 20.02 |
| SE05 | 10 | 20.00, 20.00 |
| SE06 | 2 | 20.05, 20.03 |
| SE07 | 20 | 20.01, 20.06 |
| SE08 | 3 | 20.00, 20.01 |
| **Goal** | **20** | **(20.00, 20.00) ±0.1** |

**Table 2.1:** Results of the HWS star probes' fine alignment.

The focus alignment is performed by shifting the whole star probe along the optical axis to minimize the defocus signal as measured by the HWS. The goal is to have, for all the probes, a residual defocus wavefront error less than 20 nm, corresponding to 0.15 arbitrary units in our measurement system. The results of the alignment for the SX arm appear in the Table 2.1, showing that the requirements have been successfully met for all the probes.

### 6. CCD conjugation to the deformable mirror

To conclude the alignment of the HWS, the CCD was conjugated to the correct altitude. A mask with a central hole is placed as close as possible to the optical surface of the deformable mirror, which is itself optically conjugated to the correct altitude of 7100 m by the design of the LN fore-optics. One star probe is centered on the on-axis fiber and another star probe is centered on

an off-axis fiber (more than one probe and respective fiber may also be used), the CCD is then moved along the optical axis until the spots produced by the 2 probes overlap on the detector. As in the case of the pupil conjugation (step 2), we image the hole onto the CCD, and when we are conjugated to 7100 m altitude the spots will overlap perfectly. The stages are moved in X and Y so that the spots' center of light is at pixel (20,20). The HWS CCD is then conjugated to 7100 m.

Completion of the above steps achieves the HWS alignment to the bench. At this point, the system is ready for calibration and further tests.

### 2.4.2 Calibration support software development

An appreciable amount of time was spent on developing various codes (written in Python), such as alignment scripts, automatisation of the bias calibration of the CCDs, acquisition and centering of the star probes, calibration of the HWS, partial illumination code etc. The two major scripts are "calibrateIM.py" and "partialIllumination.py". As the name suggests, the first script performs the calibration of the HWS, whereas the second takes care of the partial illumination issue. The latter script is now part of the high-layer wavefront sensing loop. Both codes are fully automatic scripts and are used extensively. Note that section 3.3.1 explains the principle of the HWS calibration procedure and the first script while section 3.3.2 describes the partial illumination code.

## 2.5 Conclusions

Performing the LN bench alignment, integration, shipping, re-integration, and installation was quite a journey during the last four years, not only for me, but also for the entire LN team. Pathfinder was a great success, and we confirmed the operation of the GWS and its interfaces. We were able to close the loop in very bad seeing and still achieve modest correction (see Figure 2.12). In parallel, at MPIA, we assembled, aligned and integrated the sub-systems to the bench. Also, various tests were performed, confirming that all the requirements were met. Packing and shipping such a huge instrument took months of planning.

Once we had LN at the LBT, we used more than 600 person-days spread across almost a year to re-assemble, re-align, and re-integrate the system. Also performance and consistency tests were executed before lifting the fully-aligned instrument to its final destination. It was also a challenge for the LBT mountain crew to execute the lift and balance the telescope without wasting a single minute of night time operations. During the pre-commissioning runs, we aligned LN to the telescope and calibrated the ground layer wavefront sensors. We also had the first ever

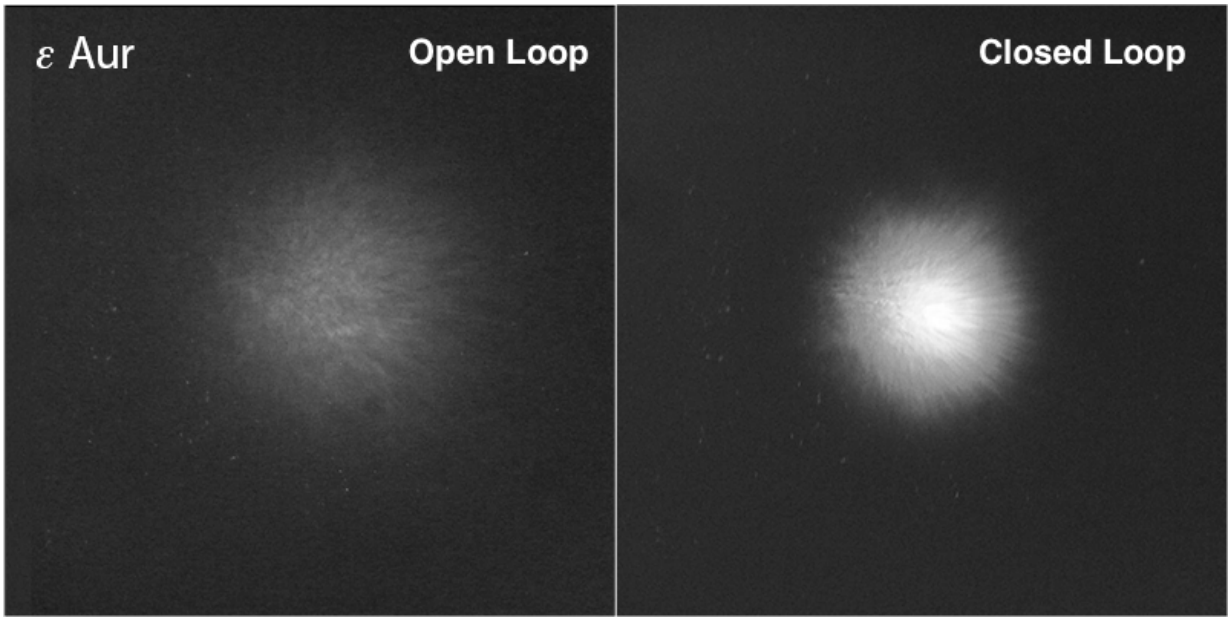


**Figure 2.12:** Pathfinder closed the loop on an on-axis star, $\varepsilon$-Aurigae, which is 3rd magnitude in the V-band. The images are taken with a visible digital SLR camera. The seeing was 2.3", exceeding the star probe FoV, but the improvement in the image quality is still clear. The left panel shows the star in open loop, on the right the star in closed loop with 50 modes.

"technical" photons reaching our science camera (see Figure 2.13).

As I write this thesis, we have had two short commissioning runs, the first focusing on the GWS and the second on the HWS on the left side. We accomplished the ground layer correction or GLAO in the first commissioning run. The results can be seen in Figure 2.14. For the first time ever, LN accomplished MCAO in the second commissioning run. However, we achieved only modest improvement in the quality or Strehl ratio, due to small number of modes corrected and the CCD displacement issue (mentioned in section 3.4). The results of the MCAO correction is discussed in Chapter 3, and in Figure 3.17. We hope to complete the commissioning runs in about a year and have LN ready for science verification by the second half of 2018.

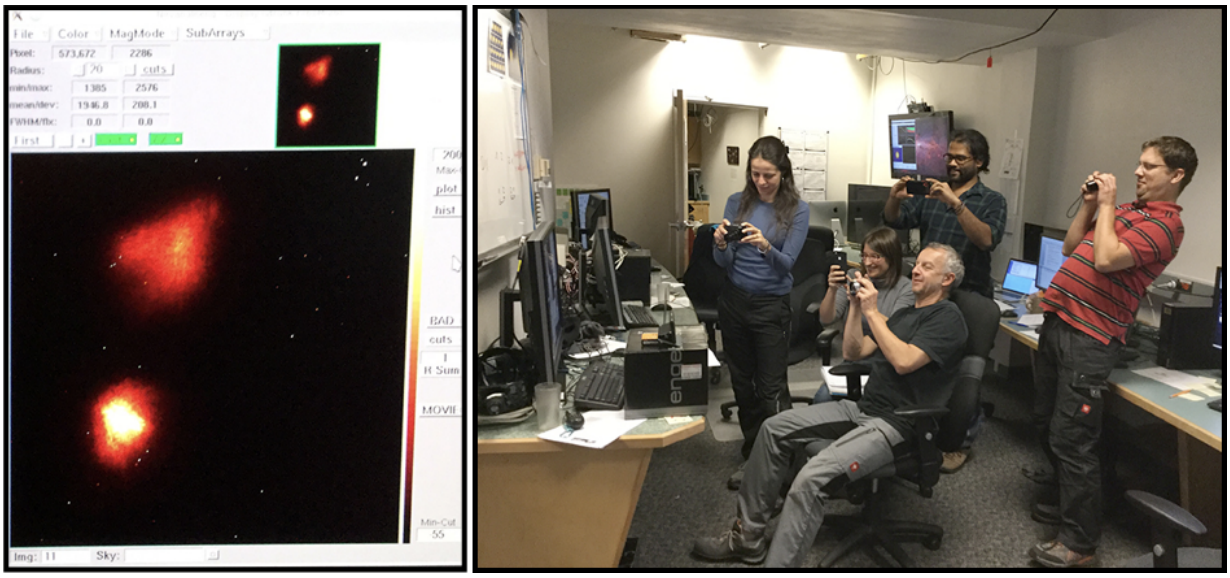

**Figure 2.13:** In the first pre-commissioning run, the LN science camera acquired the first ever "technical" photons. The right panel shows the happy LN team capturing the moment.

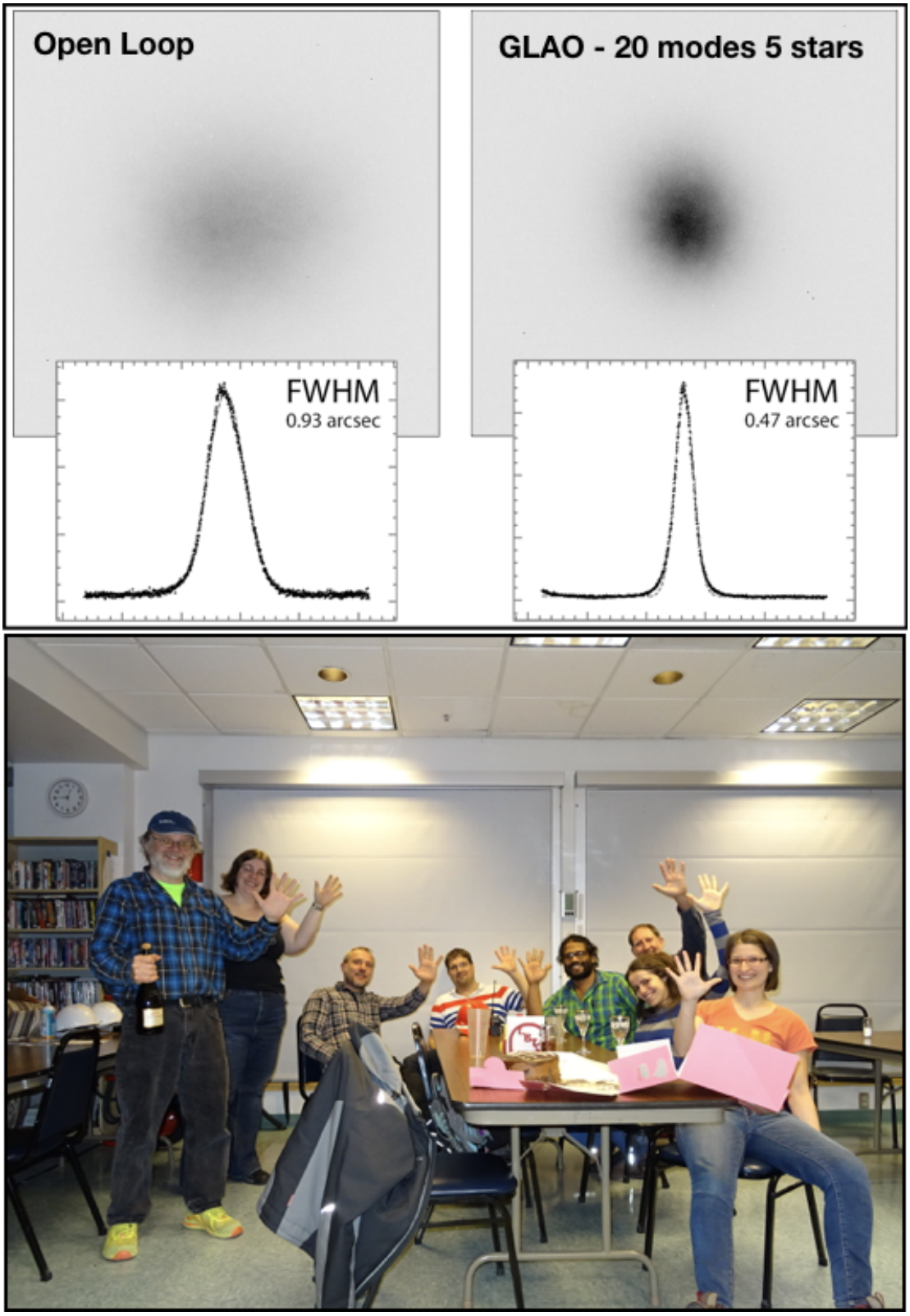


**Figure 2.14:** The LN commissioning-1 team accomplished ground layer adaptive optics correction using 5 natural guide stars (with magnitudes of 7.25, 10.48, 10.70,10.44, and 10.81 in R-band). The top image shows the expected improvement of the FWHM in K' band from 0.93" to 0.47". The lower frame shows the team celebrating success with five stars.

# Chapter 3

# A Solution to the MCAO Partial Illumination Issue

As explained in Chapter 1, telescopes or instruments equipped with MCAO provide uniform turbulence correction over a wide FoV, thereby overcoming the problem of anisoplanatism and enabling previously challenging science. However, in order to achieve the uniform correction over a wide FoV, it is essential to overcome the "partial illumination issue", common to both the star-oriented and the layer-oriented MCAO approaches (see sections 1.3.1 and 1.4.3). In this chapter, we address this issue in the context of the LINC-NIRVANA MCAO system.

As mentioned in section 1.4.3, LN adopts the optical co-addition of layer-oriented, multiple-FoV, natural guide star approach to MCAO with pyramid wavefront sensing. To re-iterate, GWSs drive the facility ASMs, correcting the ground-layer, while the HWSs drive the two commercial Xinetics deformable mirrors on the LN bench, correcting the high-altitude conjugated layer. Since LN adaptive correction is sequential, the HWS receives the ground-layer corrected wavefront. In addition, this makes the loop control simpler, since we may use two separate reconstruction matrices (explained later in section 3.3.1) for each of the loops. Note that, in order to correct the higher layer, we have to exploit the stars within the inner 2' FoV.

The some of the material in this chapter appears in an SPIE conference proceeding [110], and in an OSA conference proceeding [113]. Paper is in preparation presenting the partial illumination results from on-sky commissioning data [111].

## 3.1 Defining the partial illumination issue

At the ground layer, the star footprints overlap completely and every star footprint illuminates the entire pupil-plane, irrespective of the asterism (see Figure 3.1). However, the footprints spatially decorrelate for higher altitude conjugation. In other words, the footprints do not overlap, but rather illuminate different regions of the conjugated plane (see Figure 3.1, Figure 3.2, and Figure 3.4). A lack of stars, therefore, results in some regions of this metapupil-plane (defined in

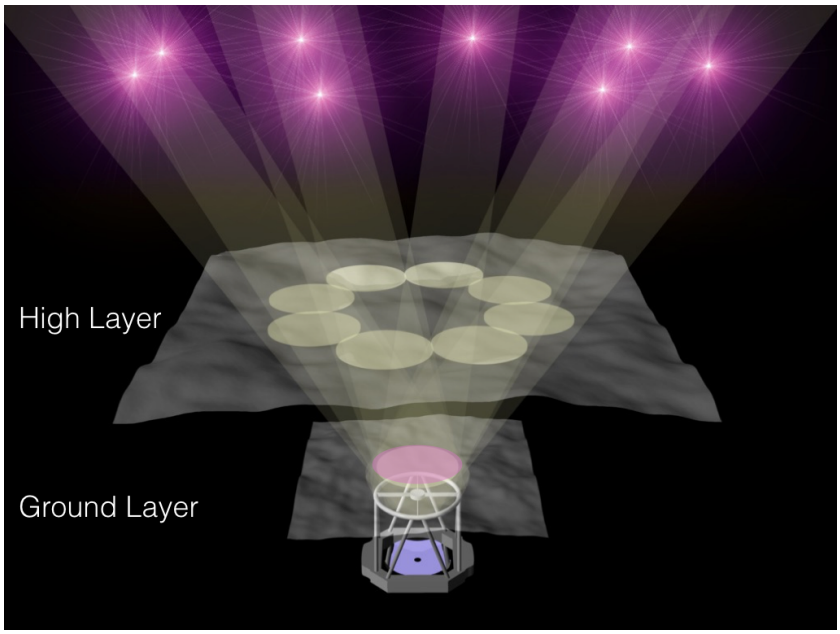


**Figure 3.1:** Footprints of the (purple) stars from the annular 2'-6' diameter FoV onto the ground layer and high layer. Evidently, at the ground layer, the footprints overlap. At the high layer, they hardly overlap and do not cover the inner 2' diameter FoV.

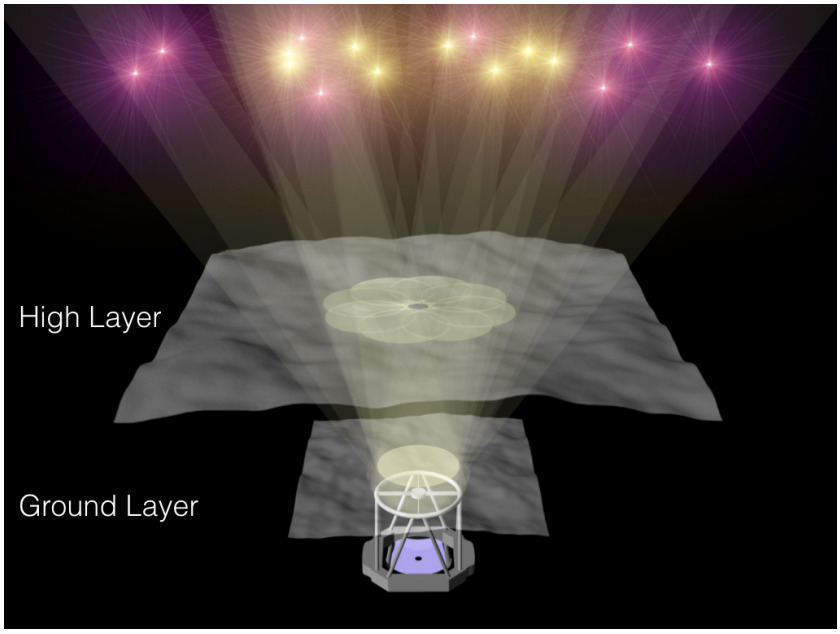


**Figure 3.2:** The inner 2' diameter FoV (yellow) stars cover the high layer. With LN, eight stars completely sample the high layer.

section 1.3.1) not being illuminated (see Figure 3.3 and Figure 3.4), and hence there is no information about the aberrations in these areas. The quality of correction and the uniformity of the PSF in the entire FoV may be affected by this partially-illuminated metapupil. The optimum way of correcting the high layer, and providing a stable closed loop, given this limited information, is the crux of the "partial illumination issue" [12, 110, 113]. Note that for the rest of this chapter, we talk about the HWS unless otherwise mentioned.

Any MCAO system that uses the layer-oriented (or star-oriented) approach will face this issue, especially if the high layer conjugated metapupil is larger than about 130-150% of the pupil, or in the case of very fine spatial sampling of the high plane. The partial illumination issue will be relevant in the context of the ELTs. For the MAORY module of the (European) Extremely Large Telescope [30], the plan is to use star-oriented MCAO correction instead of layer oriented. Star-oriented MCAO faces a similar issue, since the high-layer conjugated DMs will be partially-illuminated by the guide stars. However, there may be subtle differences from the layer-oriented scenario.

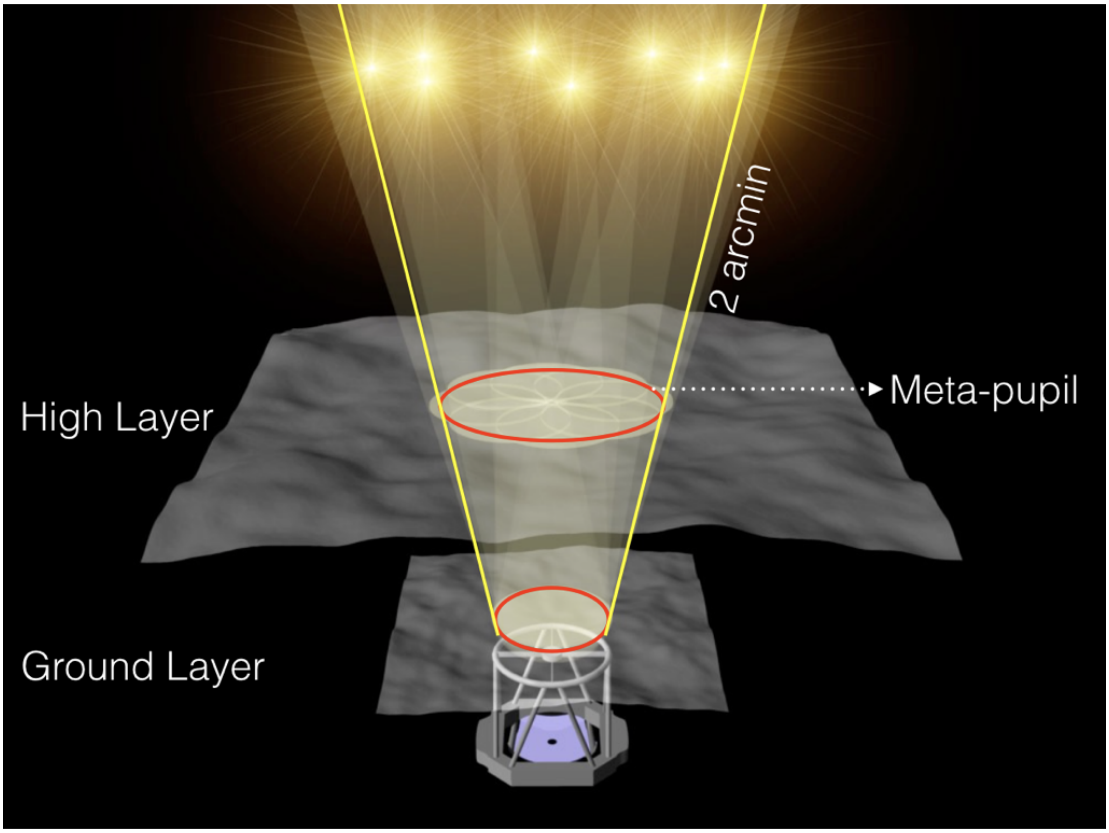


**Figure 3.3:** Fully-illuminated high layer metapupil using 8 stars. The red circle represents the metapupil.

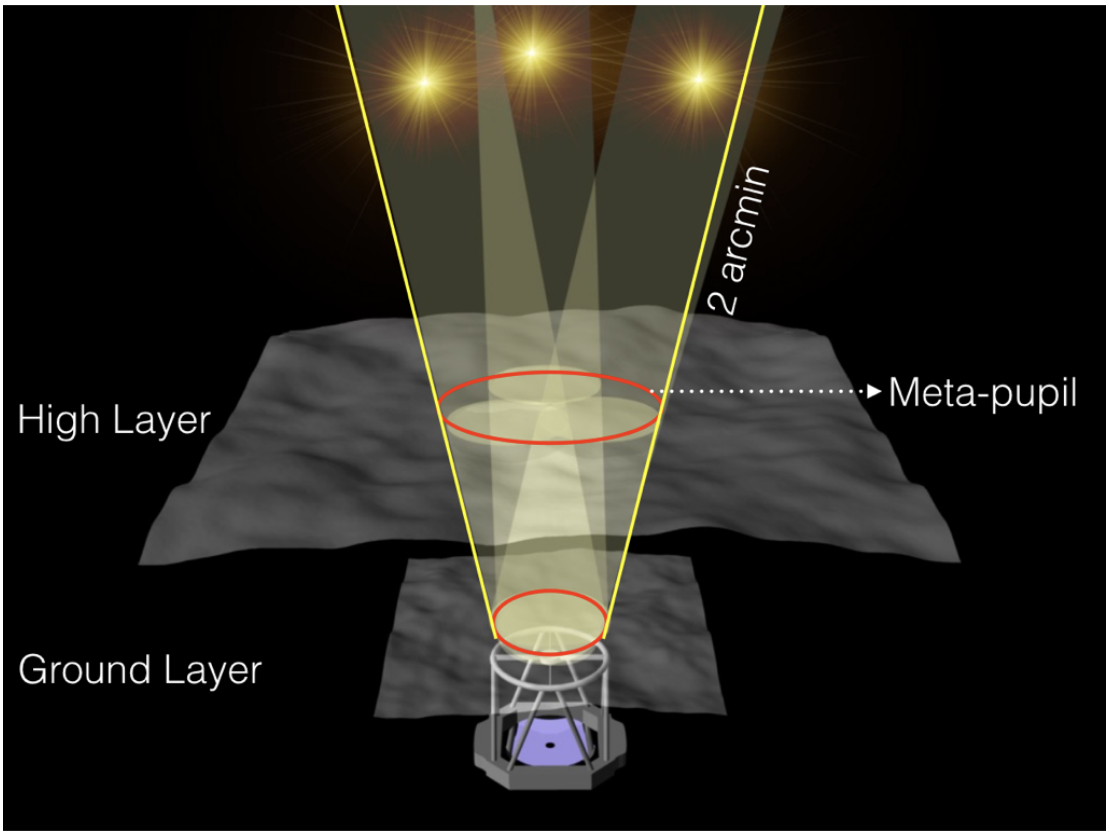


**Figure 3.4:** Partially-illuminated high layer metapupil. Only 3 stars are present in this case. Note that only part of the metapupil is illuminated, and each of the stars illuminate different parts of the metapupil.

As the shape of the DM obviously affects the science image, care has to be taken not to break the loop during an observation. At the same time, we wish to correct for the full 2' FoV region (metapupil) seen by the HWS. Recall that the scaled version of the metapupil is imaged (i.e. conjugated) onto the DM. In order to fill the entire metapupil, in our case, eight well-distributed stars are required. Unfortunately, it is very rare to find 8 bright stars (brighter than 15 mag in R-band) within the 2' diameter FoV centered around the science target. Statistically speaking, the probability of finding the stars with brightness greater than or equal to 12 mag and 15 mag within the 2' FoV in the galactic plane is 0.25 and 1.25, respectively [3]. This means that the chances of finding 4, 3, 2, and 1-star combinations within the 2' FoV brighter than 15 mag are 4%, 13%, 36%, and 71%, respectively. The corresponding chances of finding 3, 2, and 1 star combinations brighter than 12 mag are 0.2%, 3%, and 22%, respectively. Clearly, LN needs to address this situation. A tested solution (for the layer-oriented MCAO approach) to correct the entire metapupil region optimally without breaking the loop, causing degradation of the science image, or taking extra night sky time forms the subject of the rest of this chapter.

### 3.1.1 Using the full reconstructor

Unlike star-oriented MCAO (see section 1.3.1), in the layer-oriented case, there is one WFS for all the stars for the specific conjugation altitude. This WFS uses one interaction matrix (inverse of the reconstruction matrix) for any asterism of stars to deduce the commands to drive the DM for a given field rotation angle and fully-illuminated metapupil. However, due to partial illumination, the wavefront sensor sees and measures only the aberrations caused by the atmosphere in the illuminated region. The use of the reconstruction matrix corresponding to the fully-illuminated metapupil will result in incorrect coefficients for the different modes calibrated for the illuminated region. This is especially true for the high spatial frequency modes, since their modal information lies in rather closely-spaced sub-apertures, at the spatial scale of the typical gaps between star footprints. If the illuminated regions do not cover these sub-apertures, incorrect modal coefficients arise. Incorrect modal coefficients will generate commands to the DM which can break the loop, for example, by triggering the inter-actuator stroke limit (the maximum "push-pull" value admissible between two neighbouring actuators) or driving the actuators out of range. Of course, they will also likely produce improper correction.

The challenge is to have a reasonable reconstruction matrix for the actually illuminated metapupil that can close the loop stably and producing acceptable correction. Note that for each science target, the asterism and brightnesses of the guide stars will vary. We designed an algorithm to generate the reconstruction matrix corresponding to the current illumination pattern in real time from previously calibrated (day time) data for the fully-illuminated metapupil, according to the prevailing rotation angle. The concept behind this algorithm is explained in section 3.3, which was tested in the lab as well as on on-sky, and proved to be effective.

## 3.2 Partial illumination laboratory setup

The experimental setup to develop and test the partial illumination was the fully integrated and aligned LN bench, as shown in Figure 3.5. We used this setup both in Heidelberg and on Mt.Graham.

We use the Calibration Unit (CU), shown in Figure 3.6, for calibration purposes and testing the algorithms. The CU consists of the Calibration Unit folding mirror (CU-mirror), Absolute Reference Fiber (ARF) and Reference Fiber Plate (RFP). The CU-mirror is mounted on a precision rotating stage that allows us to direct the calibration unit light to the HWS. The ARF defines the location of the on-axis telescope beam. The RFP is mounted on a tip-tilt stage, which can also move along the XYZ axes. The RFP has 23 fibers mounted to it, defining "stars" in the 2' FoV (see right panel of Figure 3.6). The central star is a mono-mode near-infrared fiber, whereas all

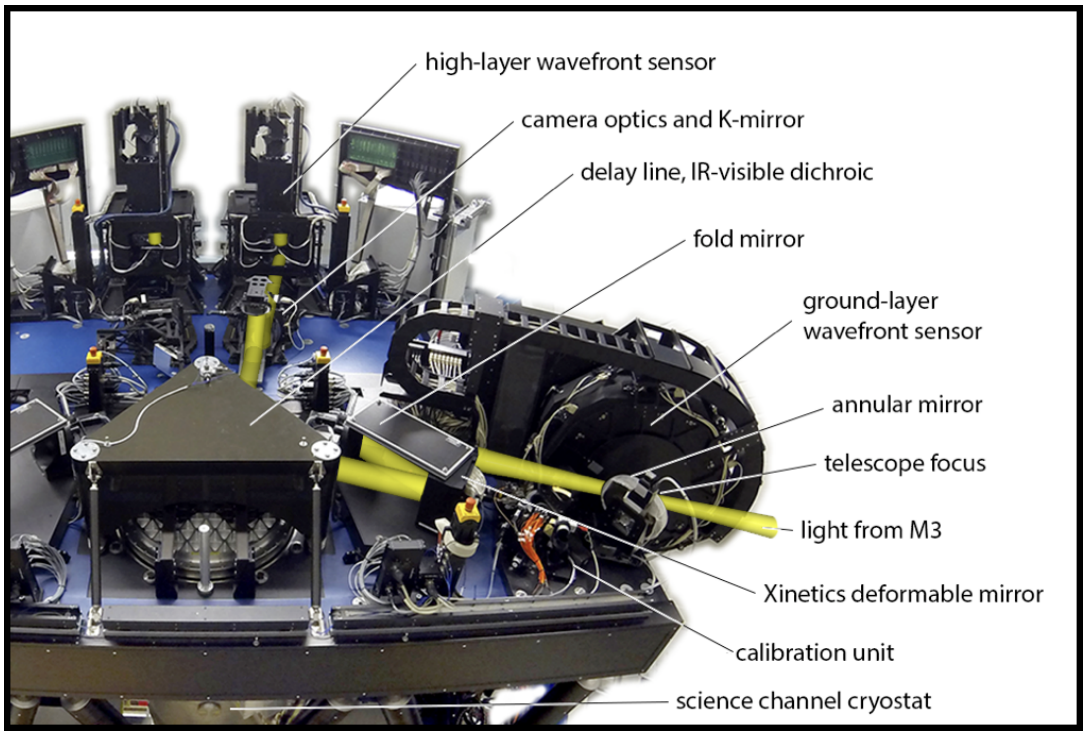


**Figure 3.5:** Fully aligned LN bench and various components. The yellow beams indicate the light path. Note that there is an identical setup for the other half of the telescope, partially visible at left.

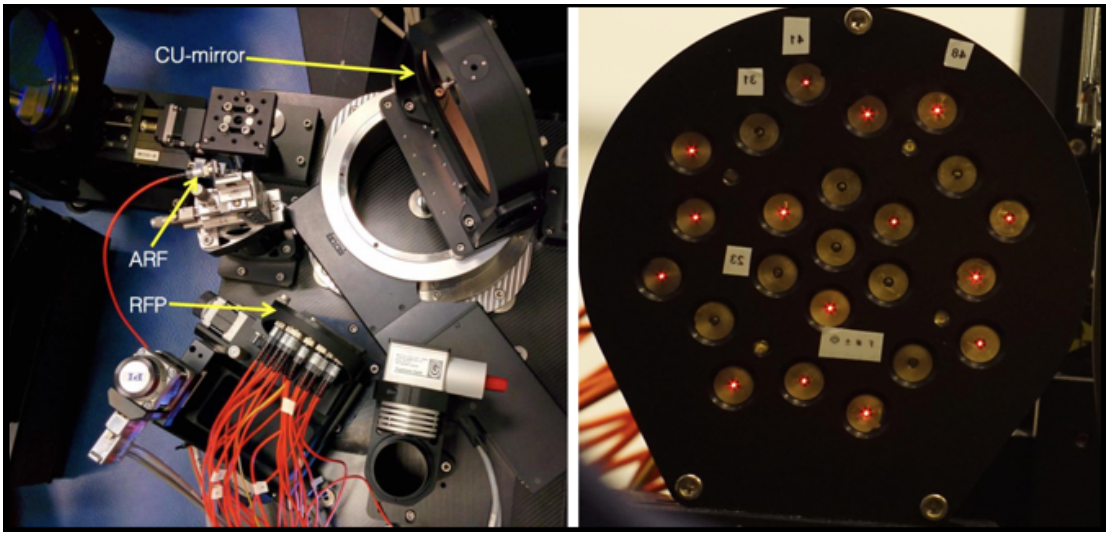


**Figure 3.6:** *left*: Calibration unit on the LN bench. The calibration unit consists of Calibration Unit folding mirror (CU-mirror), Absolute Reference Fiber (ARF) and Reference Fiber Plate (RFP). *right*: Front view of the RFP. Some of the fibers are (red) illuminated.

the others are multi-mode, 200-micron fibers fed by visible-wavelength LEDs. The intensities of the fibers can be individually and remotely controlled. We can therefore imitate defined star asterisms and vary the star brightnesses. Note also that the RFP is slightly concave, mimicking the curved focal plane of the LBT.

The fully-illuminated metapupil is generated by illuminating the 8 outermost fibers in the RFP. Each of the fibers in the RFP has been calibrated for brightness in real, on-sky magnitudes. We did this knowing the throughput of the system, quantum efficiency of the detector, the gain factor etc. We then estimated the fiber intensity corresponding to a range of R-band magnitudes. For calibration purposes, the fiber intensity of each of the 8 stars is set to 6 mag. This ensures good SNR at the HWS CCD, while avoiding saturation.

The HWS has 8 probes (see Figure 1.23) that can move in the 2' FoV to acquire and center the stars. We can therefore calibrate the HWS, create partial illumination test cases, inspect and check our algorithm, and close and optimize the high-layer loop for various cases in the lab.

## 3.3 Partial illumination algorithm

As mentioned in Chapter 1, LN uses pyramid wavefront sensing. Therefore, the sub-apertures are defined at the level of the CCD (see section 1.2.2), which is optically conjugated to the Xinetics DM and the 7100 m layer. Changing the on-chip binning allows us to change the size and number of sub-apertures covering the metapupil, thereby allowing us to use fainter guide stars readily. Such real-time binning can be considerably more difficult with other types of WFSs. Without on-chip binning (or binning=1), the number of sub-apertures for a fully-illuminated metapupil is ~600 (i.e. with 8 stars in a suitable asterism). However, if we have 3 stars, the number of illuminated sub-apertures drops typically to ~400. We then have a partially-illuminated metapupil. We made a study to see the best way to find if a sub-aperture (pixel) is illuminated or not. The calculated geometrical positions of the star footprints on the CCD, a SNR threshold, and a combination of both were considered. After careful scrutiny and awareness of the flexures and positioning of the HWS CCD (due to the changing gravity vector as the telescope moves) the SNR threshold criterion was found to be superior to the geometrical position method and was therefore chosen to identify the illuminated sub-apertures. The SNR criterion will produce a mask, according to the illumination actually reaching the detector. The CCD positioning algorithm (discussed in section 3.4) will then take care of placing the CCD in the correct position. According to the brightness of the available guide stars, the right SNR criterion has to be used. We have a look-up table for this. Note that any partially-illuminated mask created by the SNR threshold criterion will be a subset of the fully-illuminated mask. An example can be seen in Figure 3.8.

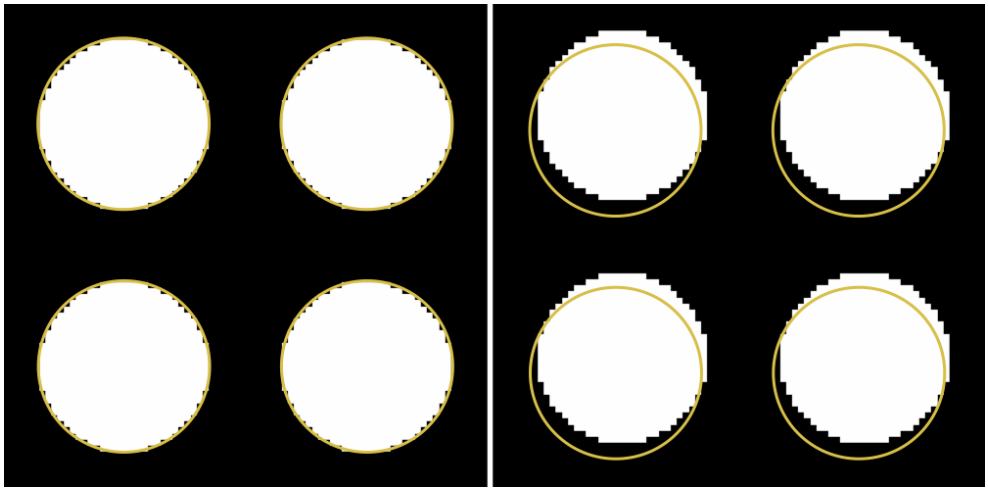

**Figure 3.7:** *left*: Mask corresponding to the fully-illuminated metapupil for the HWS. The yellow circle show the ideal position of the metapupil at the CCD. Here, the HWS CCD is in its nominal position. *right*: The HWS CCD is shifted from its nominal position due to gravitational flexure. Clearly, the illuminated region does not match the ideal location of the metapupil. Therefore, choosing the mask according to the calculated geometrical positions of the guide stars will certainly cause issues.

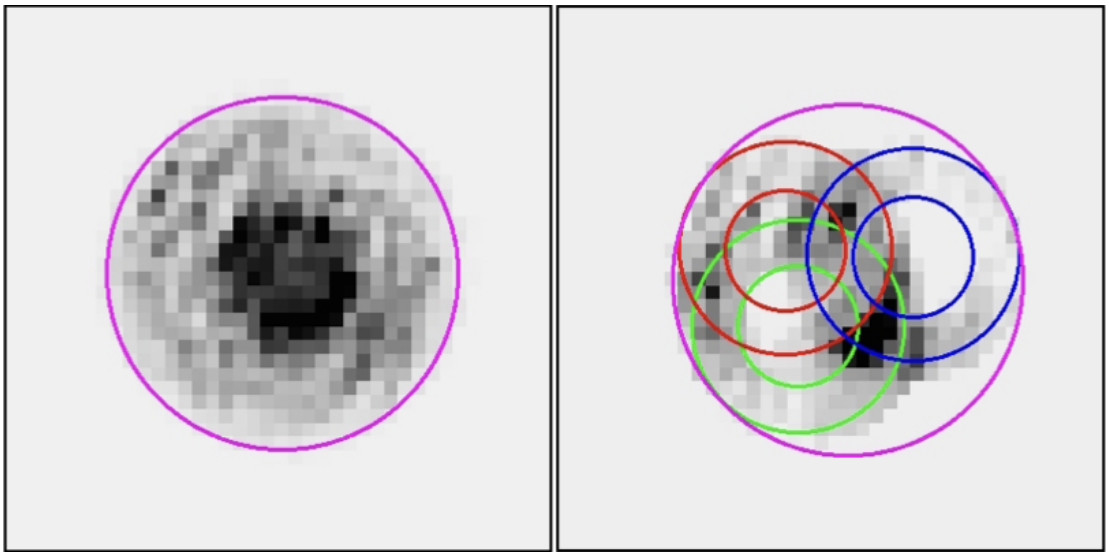

**Figure 3.8:** *left*: Fully-illuminated metapupil at the HWS CCD using the 8 outermost "stars" in the RFP. *right*: An example of the partially-illuminated metapupil at the HWS CCD using 3 outermost stars. Clearly, the partially-illuminated sub-apertures are a subset of the fully-illuminated sub-apertures.

A previous section (3.1.1) described why we cannot use the same reconstruction matrix as for full illumination. In our solution, depending on the illuminated region, a new interaction matrix is extracted from the fully-illuminated interaction matrix for the current rotation (K-mirror) angle. We name the fully-illuminated interaction matrix as the "mother interaction matrix" and the reduced, partially-illuminated one the "daughter interaction matrix".

We have tested our solution in the lab with simulated stars as well as on-sky. Before going to the analysis and results in section 3.5, we present below the details of the calibration and extraction of the daughter interaction matrix.

### 3.3.1 Calibrating the mother interaction matrix

Our partial illumination algorithm depends fundamentally on a well-calibrated, fully-illuminated, well-conditioned[16] mother interaction matrix for the given injection matrix (the response of the DM to the orthonormal modal base). The block diagram in Figure 3.9 shows how the injection and interaction matrices are calibrated or generated, as well as how we close the loop, starting from the slope measurements to commands to the DM.

For the calibration, we use a SNR threshold of 20 to identify the illuminated sub-apertures. This SNR threshold uses the $6^{th}$ magnitude stars illuminating the metapupil, and we cross-check the illuminated mask geometry with the known geometrical shape of the metapupil. After acquiring and centering the 8 HWS star probes using the 8 fibers in the outermost ring of the RFP, we measure the fully-illuminated metapupil. Setting the corresponding mask, we then run the interaction matrix calibration script. We apply the various modes defined by the injection matrix to the Xinetics DM and receive the slope measurements at the HWS. Analyzing the slopes, we extract the interaction matrix (top box of Figure 3.9).

Depending on the number of modes to be calibrated, the user can set the number of times the code runs, such that there is sufficient SNR to get a well-conditioned matrix. Rather than running the script for 200 modes directly, we go in steps. Figure 3.10 shows the flowchart of the calibration explained here. First, we calibrate for two modes (tip and tilt). Once we have the corresponding interaction matrix, we close the loop for the two modes and download the actuator commands (dmCommands). The average of the dmCommands, when added to the DM flat, will get us the shape of the DM corresponding to the "pyramid flat". The pyramid flat provides the HWS with the right shape, removing the static aberrations in the optical path, as well as other

[16]Condition number describes the sensitivity of the function to changes or errors in the measurement data. In other words, the condition number is a proportionality factor in the error. The higher the condition number of a matrix, the more singular or rank deficient is the matrix. For a well-conditioned matrix, small changes in the measurement produce small changes in the error.

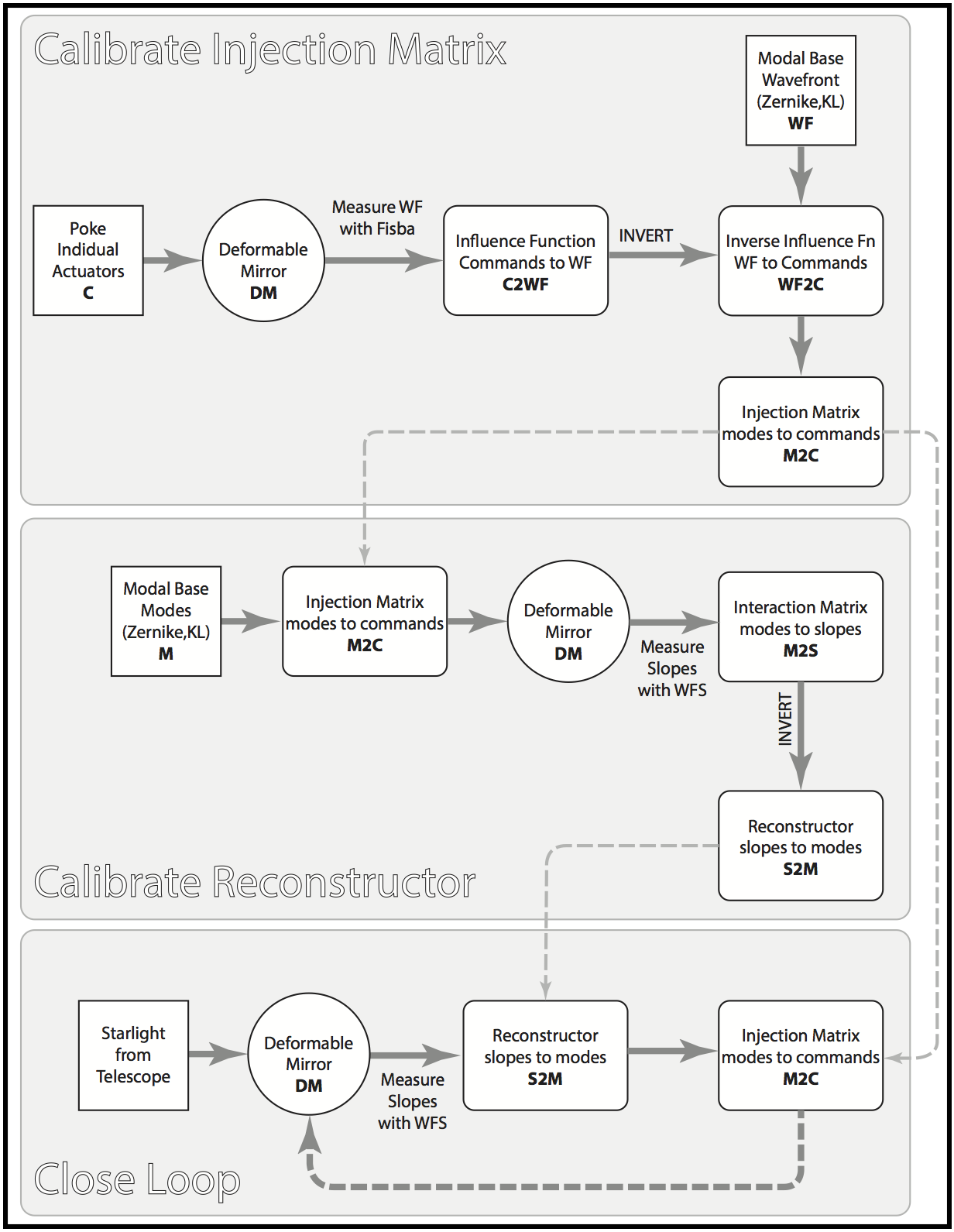


**Figure 3.9:** Step by step description of the calibration of the injection matrix and the reconstruction matrices. The figure shows how we close the loop starting from the slope measurements using various matrices.

irregularities and non-uniform illumination due to dust etc. Running the modes on the pyramid flat is superior to doing so on the "DM flat" (the shape of the DM closest to a perfect plane mirror), since this increases the pyramid sensitivity and avoids WFS saturation. We then proceed to 5-modes calibration with the pyramid flat and we follow the same procedure. Each time, the latest pyramid flat for the highest number of modes previously calibrated is used. Also, the number of iterations is increased as we calibrate a higher and higher number of modes. Finally, we get a well-conditioned mother interaction matrix. For example, we typically have a condition number of 9 for 100 modes for the mother interaction matrices.

All of these steps are performed using a script written in Python. The script communicates with the instrument and performs the calibration in a fully automatic way. Note that we do not have to do this calibration on-sky. Note also that, for the HWS, the K-mirror takes care of sky rotation. However, as the K-mirror rotates, the relationship between the sub-apertures and the actuators in the DM changes. We therefore need a corresponding mother interaction matrix for each K-mirror angle. Six different K-mirror angle calibrations are used to minimise the smoothing effect inaccuracy introduced by rotating the rasterised interaction matrix, and to produce similar quality mother interaction matrices [2], for every 1° of sky rotation ranging from 0° to 180°. Typically it takes 8 to 10 hours to calibrate these for six different K-mirror angles.

### 3.3.2 Extracting the daughter interaction matrix

As mentioned above, for both layer- and star-oriented MCAO systems, partial illumination is unavoidable. Each asterism and brightness combination will produce a different illumination pattern. It is essential to have the correct interaction matrix matching the sub-apertures to close the loop.

The interaction matrix is the response of the WFS to the DM, and this matrix has dimensions ((2 x number of sub-apertures) x number of modes). For our fully-illuminated case, this will typically be ((2 x 600 sub-apertures) x 200 modes) or (1200 x 200) elements. There is a one-to-one or many-to-one relationship between the sub-apertures of the WFS and the actuators of the DM, depending on the binning and sampling. Note that we carefully align the bench such that individual CCD pixels in the HWS map to individual DM actuators. For every illuminated sub-aperture, there are two corresponding rows in the interaction matrix - one corresponding to the X-slope and the other to the Y-slope. The sub-apertures illuminated in the partially-illuminated case are of course illuminated in the fully-illuminated case as well. Removing those rows in the mother interaction matrix corresponding to the non-illuminated pixels from the partial illumination case generates the daughter interaction matrix. Figure 3.11 illustrates this.

Obviously, the effect of lack of information cannot be ignored. Generating a reconstruction

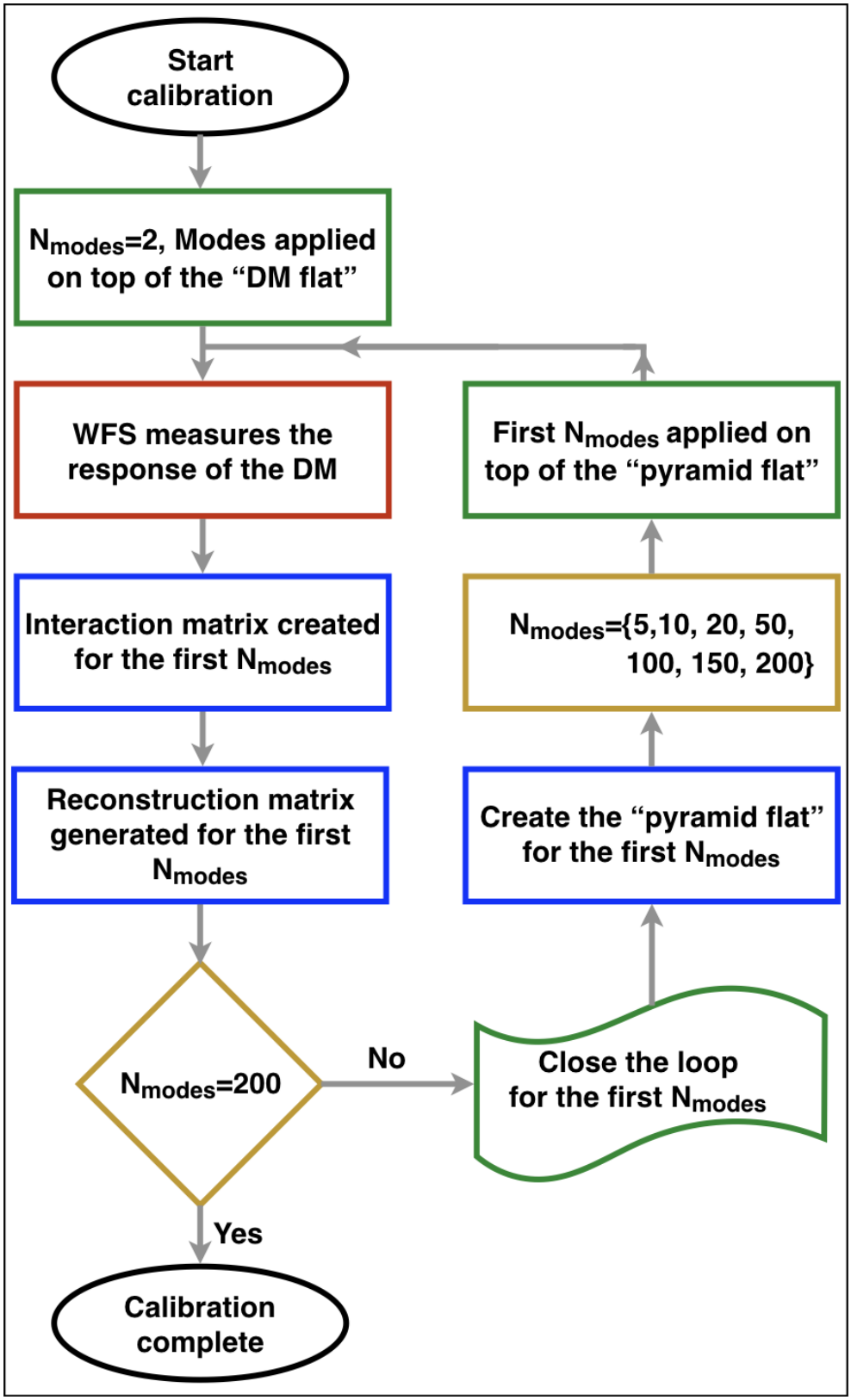


**Figure 3.10:** Flowchart explaining the calibration procedure for 200 modes.

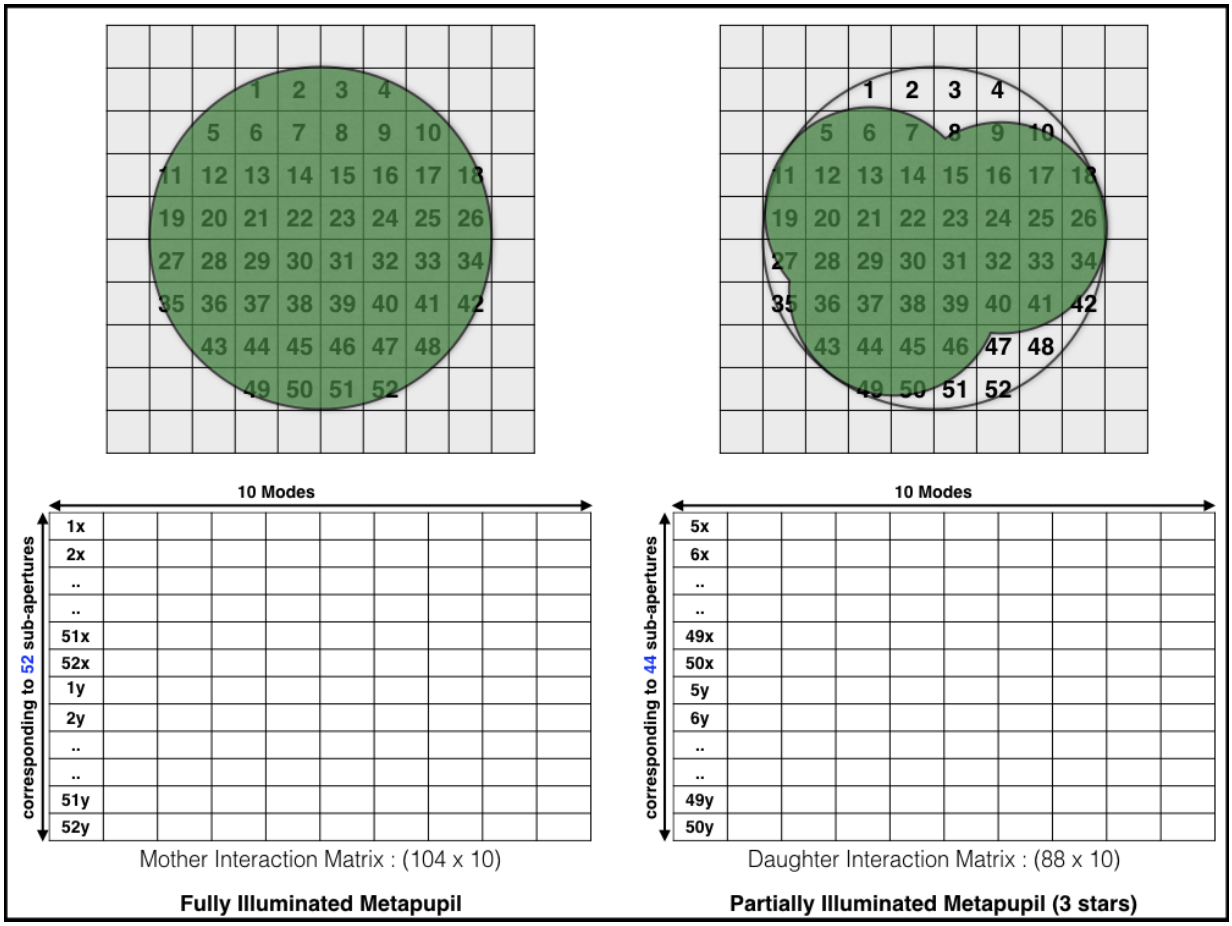


**Figure 3.11:** A schematic example explaining the extraction of the daughter interaction matrix from the mother interaction matrix for 10 modes. On the left, the fully-illuminated metapupil (52 sub-apertures) and the corresponding interaction matrix can be seen. On the right, the partial illuminated metapupil appears, along with the daughter interaction matrix extracted out of the mother and corresponding to only those rows which are illuminated (44 sub-apertures in this case).

matrix from the daughter interaction matrix will have a higher condition number. If the condition number is very large, then the matrix is said to be ill-conditioned. In other words, for a high condition number matrix, small measurement errors will translate to large actuator errors, which can cause divergence or instability. The higher the condition number, the lower the number of modes that can be corrected in a stable loop. For example, high spatial frequency modes may not be corrected, resulting in lower Strehl ratios. We make sure that all the low-order modes (especially tip and tilt) are present in the "truncated singular-value-decomposed reconstructor"[17].

[17]Singular Value Decomposition (SVD) is a factorisation of a real or complex matrix. SVD may be used to compute the pseudo-inverse of any rectangular matrix. In our case, we use SVD to get the reconstruction matrix

The modal base is defined over the entire metapupil. This means that we should get the modal coefficients from the slopes spread across the entire metapupil. However, we have only a subset of the slopes, depending on the partially-illuminated pattern. From these slopes, we retrieve the modal coefficients. This is what we do by extracting the daughter interaction matrix from the mother interaction matrix. In a way, it is like an interpolation or extrapolation or combination of both.

As the K-mirror rotates to compensate sky rotation, the one-to-one relation between the pixels and actuators also changes. However, the K-mirror rotation also ensures that the stars seen by the HWS do not change their position, so the illumination mask does not change. Therefore, for every 1° of sky rotation, we extract a new daughter interaction matrix from the mother interaction matrix corresponding to that K-mirror angle. The inverted reconstructor is then uploaded to the loop service. This is done in real time by the partial illumination script written in Python. This routine is now a part of the high layer wavefront sensing loop.

## 3.4 Additional considerations

Before getting into the analysis of the partial illumination data obtained in the lab and on-sky, it is worth pointing out two observations made during the study of partial illumination issue.

### 3.4.1 Choosing the modal base for the injection matrix

The **injection matrix** or **modes-to-commands matrix (m2c)** (see Figure 3.9) is the response of the DM to the orthonormal modal base. The derivation of the m2c takes into account the individual responses of the actuators (the influence function), and the projection of the metapupil onto the DM (for example, we have to consider if all the actuators are not within the projected metapupil). The Zernike [87] and Karhunen-Loève (KL)[18] [29, 68] bases were considered as

from the interaction matrix (final step of middle box of Figure 3.9). Any rectangular matrix $A$ can be factorised using SVD as: $A = USV^*$, where $U$ and $V$ are the orthonormal eigenvectors, and $S$ is a diagonal matrix of eigenvalues. Then, $A^{-1} = VTU^*$ is the matrix inverse of $A$, where $T_{ii} = 1/S_{ii}$ and all the other elements of $T$ are zero. For ill-conditioned matrices, many of the eigenvalues, while not zero, can become quite small, causing the data inversion to blow up, is due to the presence of noise. To prevent this, the SVD is truncated using a defined threshold value so that $T_{ii} = 0$ above the threshold value.

[18]The Karhunen-Loève (KL) theorem is a representation of a stochastic process as an infinite linear combination of orthogonal functions, analogous to a Fourier series representation of a function on a bounded interval. KL expansion yields the best base, minimising the total mean squared error. The coefficients in the KL expansion are random variables and the base depends on the process. The orthogonal basis functions used in this representation are determined by the covariance function of the process. In other words, the KL transform adapts to the process, in order to produce the best possible base for its expansion. See [29] for more details.

candidates for the modal base to create the m2c. However, the m2c generated using the Zernike modal base showed many complications, the main one being the stability of the closed loop in the partially-illuminated case. The Zernike modal base produced large dmCommands values close to the edges of the metapupil when using a large number of modes, even for the fully-illuminated case. Note that the projection of the Zernike modal base on the DM actuator influence function space is not strictly orthonormal and the high spatial frequency modes have very high values at the edge actuators. In addition, in our case, the projection of the entire metapupil on the DM does not cover all the actuators. We therefore slave the actuators falling outside the metapupil to their neighbours (master actuators) radially just inside the metapupil. By slaving, we move the outer actuators the same way as their respective master actuators. With the Zernike base, the outer actuators trigger either an "out of range" error or an "inter-actuator spacing" error. On the other hand, the KL base, generated considering the Kolmogorov turbulence power spectrum, produced a rather stable loop and reasonable edge actuator values. We have, therefore, adopted the KL base to produce the m2c. This m2c was used for the calibration of the interaction matrices as well as for testing the partial illumination cases in the lab and on-sky.

### 3.4.2 Importance of maintaining registration

**HWS CCD positioning** is very crucial for closed loop operation. As mentioned in section 1.2.2, for pyramid wavefront sensing the sub-apertures are defined at the level of the CCD. Put another way, each of the pixels within the metapupil is a sub-aperture. There is a one-to-one relation between these pixels and the actuators on the DM, a situation that we call the "registration" between the HWS WFS and the Xinetics DM. Therefore, if the CCD position changes in closed loop, due to gravitational flexure for example, the reconstructor will send incorrect values to the DM. This can eventually break the loop. Consequently, it is essential to eliminate any CCD displacement. This is true not only for the HWS CCD, but also for the GWS CCD. We have observed that there is a displacement of the CCD as the telescope moves from zenith to horizon, and also during the flexure test in Heidelberg (mentioned in section 2.2.2). Currently, we are devising an algorithm to handle this issue, so that, the CCD can be maintained stationary to sub-pixel precision.

In the final configuration of LN, using the calibration unit, we have tested and analysed the partial illumination algorithm. The details form the following section.

## 3.5 Partial illumination lab experiment: analysis and results

The intensities of the fibers (simulated stars) in the RFP were adjusted to have R-band magnitudes between 5 and 10 for our study. We made use of different asterisms to generate the partial illumination scenario, using from 1 to 8 stars. In order to check that the extraction of the daughter interaction matrix, and hence the resulting reconstruction matrix, can close the loop and provide reasonable correction, we used a 3-star asterism to create the partial illumination. Each fiber was set to $6^{th}$ mag equivalent brightness. To compare, we used the full illumination case using 8-stars (6 mag each).

The two parameters we optimized are the gain vector[19] and the SNR threshold value, which decides the partial illumination mask. Typically, we split the modes into three groups - tip and tilt (modes 1 and 2), modes from 3 to 50, and modes higher than 50. Each of these groups were given an individual constant gain value while closing the loop. We introduced a known disturbance (i.e. dynamic wavefront error) on the Xinetics DM, imitating the turbulence in the high layer. Since the HWS receives the ground layer corrected wavefront, the introduced disturbance was selected to produce an open loop wavefront error of ~300 nm. This is the expected total Root Mean Square (RMS) wavefront error after the ground layer correction.

We used the RMS value of the modal coefficients obtained from (1) the residual wavefront slopes (by multiplying with the reconstruction matrix) and from (2) the dmCommands computed over the full pupil aperture (by multiplying with the m2c) as the merit function to quantify the correction performance.

Typically, we are used to quantify the performance using the Strehl ratio. However, from our measurements, it is not possible to get the correct estimate of the final SR. This is because the ground layer corrected disturbance we introduced on the DM has a different turbulence power spectrum and different altitudes' conjugation. Actually we should apply phase screens with power spectrum different than Kolmogorov one, as the ground layer will correct some part of the tip-tilt and low order modes from the high layer. Unfortunately, it is not straightforward to compute the power distribution. For the aims of testing the capabilities of the HWS, we apply on the DM, a turbulent phase screen based on Kolmogorov statistics with average RMS wavefront error of 300 nm over the whole metapupil. Therefore, the SR evaluated, using the conventional Maréchal approximation [82] (see Equation 3.1 below) from the RMS value of the residual wavefront error, will not represent the real SR.

[19] For every calibrated mode, we provide a value that will get multiplied to the modal coefficient obtained from the WFS before applying to the DM. This constant is called the gain. The gain values for all the calibrated modes form the gain vector.

$$SR_{K'} \sim exp\left(\frac{-(2\,\pi\,\sigma)}{\lambda_{K'}}\right), \tag{3.1}$$

where $\sigma$ is the RMS value of the residual WaveFront Error (WFE) in microns, and $\lambda_{K'}$ is the effective wavelength of $K^{'}$ in microns.

In addition, unlike the lab tests, where we have the disturbance just at the conjugated altitude, in the real-world scenario, there will be contribution from the ground layer (what is not corrected by the GWS) and from the neighbouring altitudes as the DM is not strictly perpendicular to the incoming beam. The Strehl ratio mentioned below does not have the same meaning as the conventional one, but rather is used as a visualisation parameter. Note that LN expects to have a maximum SR of 40% in K-band.

The tests were performed on both the SX and DX arms. On the SX arm, we used reconstruction matrices which can correct up to 100 modes, whereas on the DX side we used to 200 modes. The SX calibrations were performed recently after the installation of LN at the LBT. Due to gravitational flexures, and until we have a working HWS CCD positioning service, we will not be able to correct for more that 100 modes. Otherwise, the SX performance is similar to DX.

### 3.5.1 Dependence on star probes' acquisition and centering

One of the first tests performed was to check if the position accuracy achieved by the star probes affect the correction performance. For this test, we used six, $6^{\text{th}}$-magnitude stars with the same SNR threshold of 20 defining the partial illumination mask and the same gain vector each time. In simple words, everything remains the same, except that, each time, the stars are acquired and centered separately.

The motivation for this test was the observation of drift of the star probes' during the testing and optimisation of the gain vectors for different partial illumination cases (which took a few hours). These drifts are mostly due to temperature changes. The drifts produced larger and larger mis-positioning of the pyramid probes with respect to the guide stars and needed to be adjusted by pyramid re-centering. Nevertheless, these drifts are actually small (of the order of 100 microns in the $f/15$ focal plane). This affects the pyramid only during laboratory tests, since we were working with diffraction limited spot sizes (see section 1.2.2). On-sky, the spots will be much larger and immune to such drifts.

Figure 3.12 shows the result. The dashed lines represent the open loop cases, while the solid lines represent the closed loop cases. The left panel shows the RMS value of the modal coefficients in microns, evaluated from the dmCommands multiplied by the m2c. We can use the

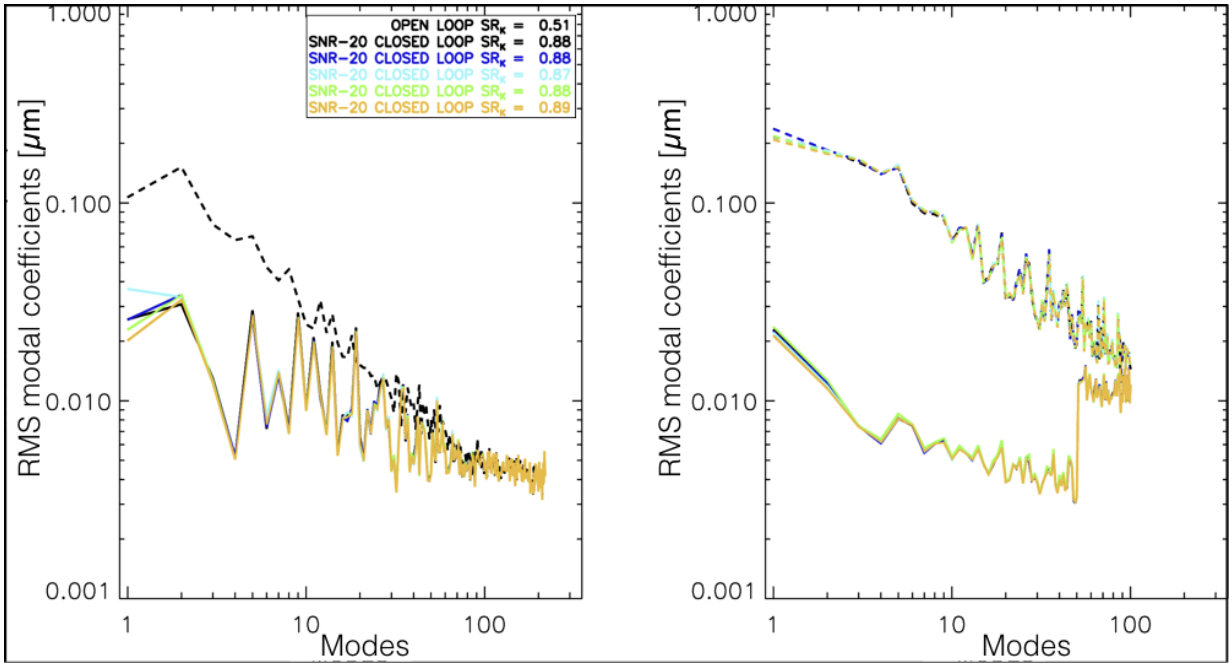


**Figure 3.12:** The correction performance for different trials of acquisition and centering of the star probes. For this test, every parameter remained the same, except that the star probes were re-acquired and re-centered for each trial. The RMS value of the modal coefficients is plotted against the modes. The dashed lines represent the open loop data whereas the solid lines show the closed loop performance. The left panel, the residual RMS modal coefficient is obtained directly from the dmCommands multiplied by the m2c, which consists of 235 modes, making the X-range extending up to 235. However, correction is done for the first 100 modes only, present in the reconstruction matrix. The right panel, residual RMS modal coefficients are evaluated using the slopes vector multiplied by the reconstructor matrix itself, therefore showing only 100 modes. Note that the Strehl ratio mentioned in the plot has no real meaning. See text in page 81 for details.

RMS modal coefficients as a proxy for performance for the following reason. The data are from the lab, where we apply known, pre-computed phase histories on the DM, in order to simulate turbulence evolution. This gives us the possibility to estimate the residual phase by analysing the deviation of the DM with respect to the average shape (the pyramid flat described above). However, this is not possible on-sky. There, we will have to use the RMS value of the modal coefficients in microns, evaluated from the slopes multiplied by the reconstruction matrix. This is shown on the right panel in the plot. The number of modes in the m2c is 235, whereas the reconstruction matrix has 100. This explains the differing X-axis ranges. The discrepancy in the Y-axis, which is visible even for the open loop scenario, is due to the fact that the sensitivity of the pyramid depends on the actual dimension of the PSF spot size and its position with respect to

the pyramid pin. Actually, the pyramid response is more and more linear for decreasing values of the residual phase [96]. This behaviour does not affect closed loop performance, since the closed loop residuals bring the pyramid into its linear regime, but, on the other hand, it makes the phase calibration challenging. For the plots in this section, we just made a rule-of-thumb calibration of the average tip and tilt open loop residuals.

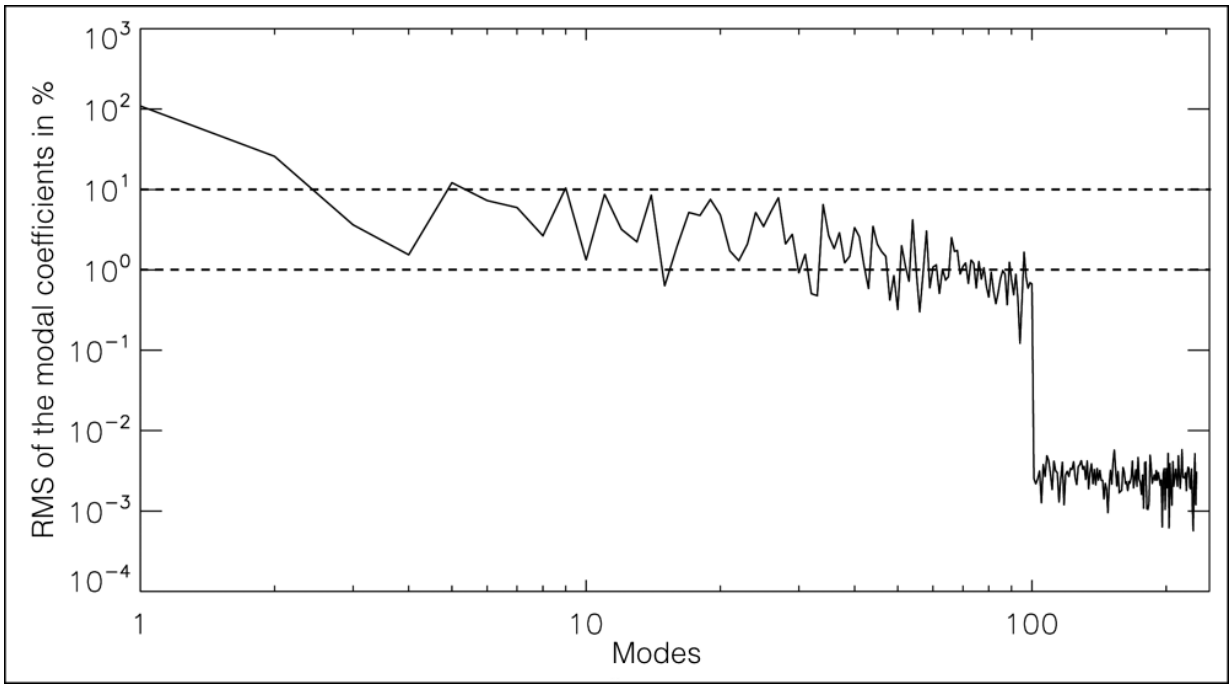


**Figure 3.13:** Plot showing the RMS value of the modal coefficients in percentage. The mode to mode scatter is less than 10%, except for the first two modes - tip and tilt. The residual RMS WFE was generated from the dmCommands multiplied by the m2c. Note that only 100 modes are corrected, explaining the drop in the plot at mode 100.

The analysis performed using the data shows that the scatter due to re-acquisition and re-centering of the star probes does not affect the correction performance. All the independent trials produced the same amount of correction. Figure 3.13 shows the dispersion in the modal coefficients. The data clearly show the effect of vibrations, which add a tip-tilt component that we cannot evaluate from the analysis of the dmCommands (but we can from slopes, given the limitation on the absolute calibration explained above). In general, the mode to mode scatter is less than 10%. This means that the performance of the correction is almost independent of the positioning of the star probes, as long as each of the star probes is centered on the individual star light while the GWS loop is closed.

### 3.5.2 Impact of the SNR threshold value

In order to study the impact of the SNR threshold value on the partial illumination algorithm, we varied the threshold to get slightly different masks, differing, of course, in the number of sub-apertures illuminated. Also, the gain vector was changed to study its impact. We concentrated mainly on an 8-star asterism and a 3-star asterism, representing the fully-illuminated and partial illumination cases, respectively.

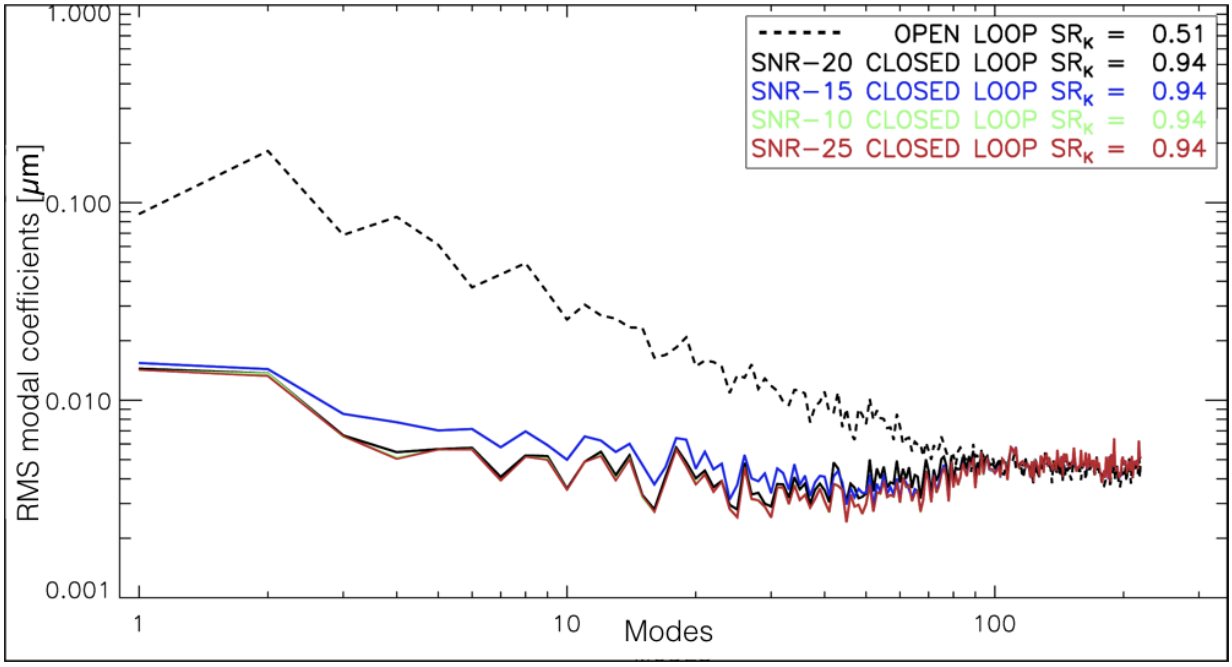


**Figure 3.14:** RMS value of the modal coefficients plotted against the modes for the case of full illumination using 8 stars. The dashed line represents the open loop data, while the solid lines are the closed loop performance. The different colours represent different SNR threshold values defining the illuminated sub-apertures. Clearly, the correction performance is almost independent of the SNR threshold. Closing the loop results in reducing the RMS wavefront error from 288 nm to 83 nm. The residual RMS modal coefficients were generated from the dmCommands multiplied by the m2c. Note that only 100 modes are corrected, so the closed loop residuals coincide with the open loop for modes higher than 100. The Strehl ratios mentioned in the plot are not real, but just a representation of the improvement from 51% (for the open loop) to 94% (for the closed loop). See text in page 81 for details.

The effect of the different SNR thresholds on the correction for the full illumination and a partial illumination case appears in Figure 3.14 and Figure 3.15, wherein the X and Y-axes represent the modes and the RMS value of the modal coefficients, respectively. The black dashed lines represent the open loop scenario, with a RMS WFE of 288 nm (or SR of 51%). For both

full and partial illumination cases, there is a clear improvement in the RMS value of the modes, or in other words, good correction. The RMS WFE reduces to 83 nm (or SR of 94%) and 101 nm (or SR of 91%) for the full and partial illuminations cases, respectively. The different coloured

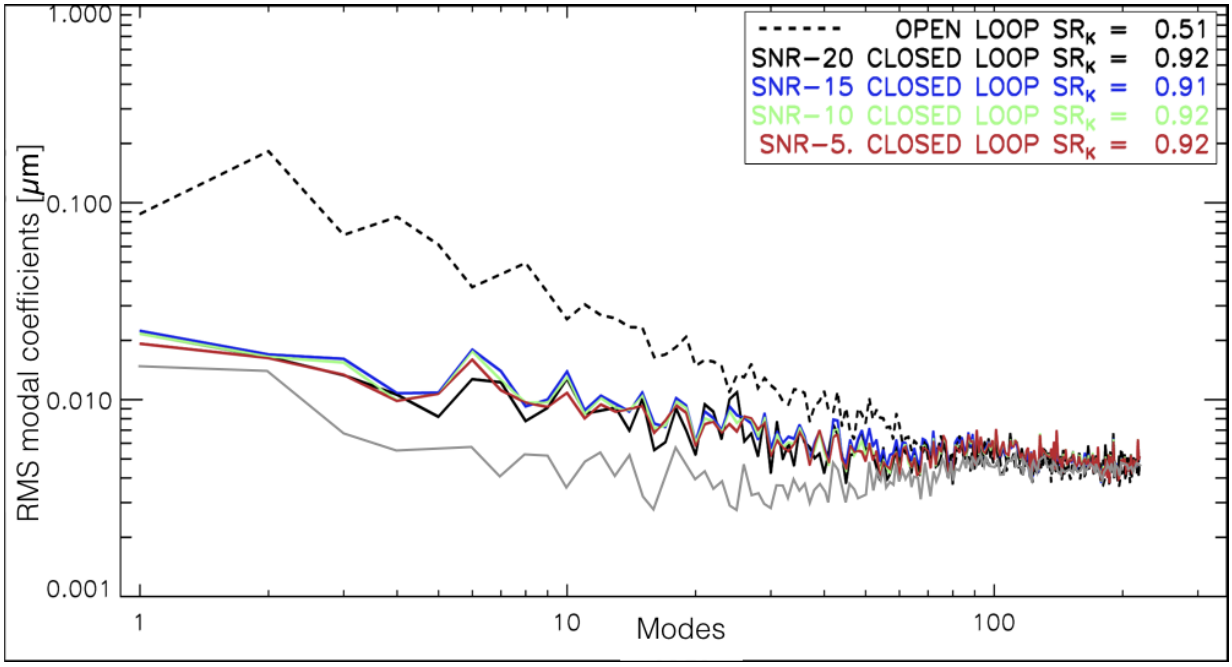


**Figure 3.15:** RMS value of the modal coefficients plotted against the modes for the case of partial illumination using 3 stars. The dashed line represents the open loop data, and the solid lines are the closed loop performance for different SNR threshold values defining the illuminated sub-apertures. The full illumination closed loop performance is over-plotted in grey. Clearly, the correction performance is almost independent of the SNR threshold, as in the case of full illumination. The RMS WFE reduces from 288 nm (SR of 51%) to 101 nm (SR of 91%), as the loop closes. The partial illumination performance is worse than the full illumination scenario, as expected. The residual RMS modal coefficients were generated from the dmCommands multiplied by the m2c. Note that only 100 modes are corrected, so the closed loop residuals coincide with the open loop for modes higher than 100. Note also that the Strehl ratio mentioned in the plot has no real meaning. See text in page 81 for details.

solid lines represent the different (reasonable) SNR thresholds used. The reduction in the RMS values for each of the modes is a clear indication of the effectiveness of the correction. Most importantly, we see that, irrespective of the different SNR threshold values, the correction is more-or-less the same. The effect of different gains for the same SNR threshold cannot be seen in these plots. We have chosen the gain vectors so that the loop provides stable correction. You may note that there is no correction for modes higher than 100. This is because the reconstructor we used were calibrated to correct for only the first 100 modes. However, the plot was created

using the dmCommands multiplying with the m2c. The m2c has 235 defined modes.

### 3.5.3 Closed loop performance on the DX arm

The aforementioned tests were performed on the SX arm. We also performed tests on the DX side. The plot in Figure 3.16 shows the residual RMS WFE estimated from the slope vectors for different scenarios on the DX side. In the plot, the X-axis shows the CCD frame counter, while the Y-axis represents the residual RMS WFE in nm. The frame counter range can be divide in to 4 sections. Frames 0-999 represent open loop with no disturbance applied, frames 1000-1999 show the closed loop with no disturbance applied (i.e. just removal of the static aberrations in the system), frames 2000-5999 are the open loop with the disturbance (equivalent to ~200 nm) introduced on the DM, and frames 6000-10000 are the closed-loop with the disturbance running as well. The different colours represent the different number of stars used for the study. For the 3-star case, notice that from frame count close to 8700, the residual RMS WFE is almost static. This is due to the fact that the loop opened, due to an "inter-actuator limit error".

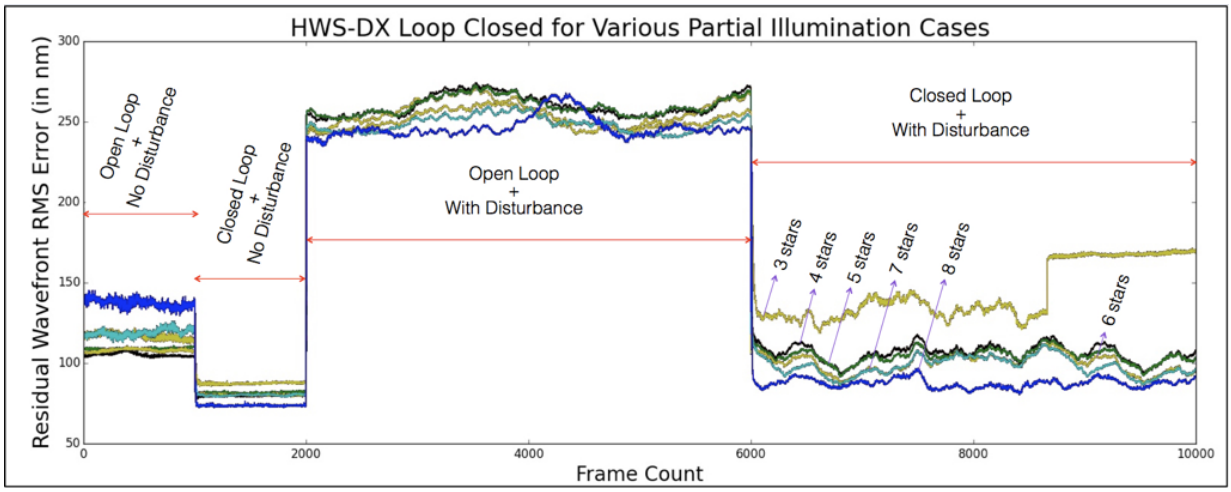


**Figure 3.16:** The residual RMS WFE (in nm) estimated from the slopes vectors plotted against frame count for the tests performed on the DX side. The frame counter range is divided into 4 sections. Frames 0-999 representing the open loop and no extra disturbance introduced, frames 1000-1999 representing closed loop and no extra disturbance (static aberrations in the system removed), frames 2000-5999 represent the extra disturbance introduced at the DM equivalent to ~250nm and the loop is open, and frames 6000-10000 representing the closed loop with the disturbance running as well. The different colours represent the different number of stars used for the study. For the 3 star case, note that from frame counter close to 8700, the residual RMS WFE is almost static. This is due to the fact that the loop broke, triggered by "inter-actuator limit error".

The closed loop with no disturbance case shows that there is 70-80 nm WFE, that is not correctable. In other words, 70-80 nm residual is the best correction possible. Closing the loop while the disturbance is also running on the DM produces a WFE of ~80 nm for the 8-star asterism, while with the 3-star asterism, the error is only corrected down to ~125 nm on average. Clearly, the residual wavefront error increases as the number of stars in the asterism decreases. In other words, the higher the number of illuminated sub-apertures, the better the correction.

Tests were performed to check the efficiency of correction and the stability of the loop for situations were the acquired stars have very different brightness levels. We noticed that for very different brightness levels (magnitude difference of more than 2), the loop gets unstable, or in other words, the gain vector has to be properly controlled. For example, for a 3 star asterism with 5 mag star, a 8 mag star, and a 9 mag star, the loop starts showing unstable behaviour for otherwise normal gain values. Generally, the stability of the loop and the uniform correction prefer to have more or less similar magnitude stars. Obviously, the brighter, the better.

### 3.5.4 On-sky testing and future improvements

On-sky testing of the partial illumination algorithm is continuing during our commissioning runs. As of now (September 2017), we have demonstrated the basic operation and functionality of the partial illumination code, as incorporated into the high-layer wavefront sensing service. During the second commissioning run, on 10$^{th}$ June 2017, and for the first time ever, we accomplished MCAO - the confirmation that the LN AO module works. The GWS loop was closed initially using two stars of magnitude 9.37 and 10.82 in R-band (up to 40 modes were corrected). Two stars of magnitudes 8.32 and 8.50 in R-band were then acquired and centered by the HWS, which was receiving the ground-layer corrected wavefront. Obviously we had partial illumination. We were able to close the loop with up to 10 modes for the high layer. While an improvement from 0.94” to 0.74” after the ground layer correction was noted, the high layer correction showed improvement from 0.74” to 0.67” in our science image (K’ filter). This was the first time the HWS had seen sky photons, so the improvement is modest (see 3.17). We also had only about 1 hour on sky with the HWS.

We are currently working on implementing the CCD positioning service, more efficiently centering the fainter stars, and removing the observed HWS CCD pattern noise. In the coming commissioning runs, we hope to achieve better correction when MCAO is running. Also, more thorough checking of the partial illumination code will be performed.

The laboratory and the on-sky tests confirm that the partial illumination algorithm and code work well. We expect improvement in the correction performance in the future, especially when the CCD positioning service is working. The concept of extracting the daughter interaction

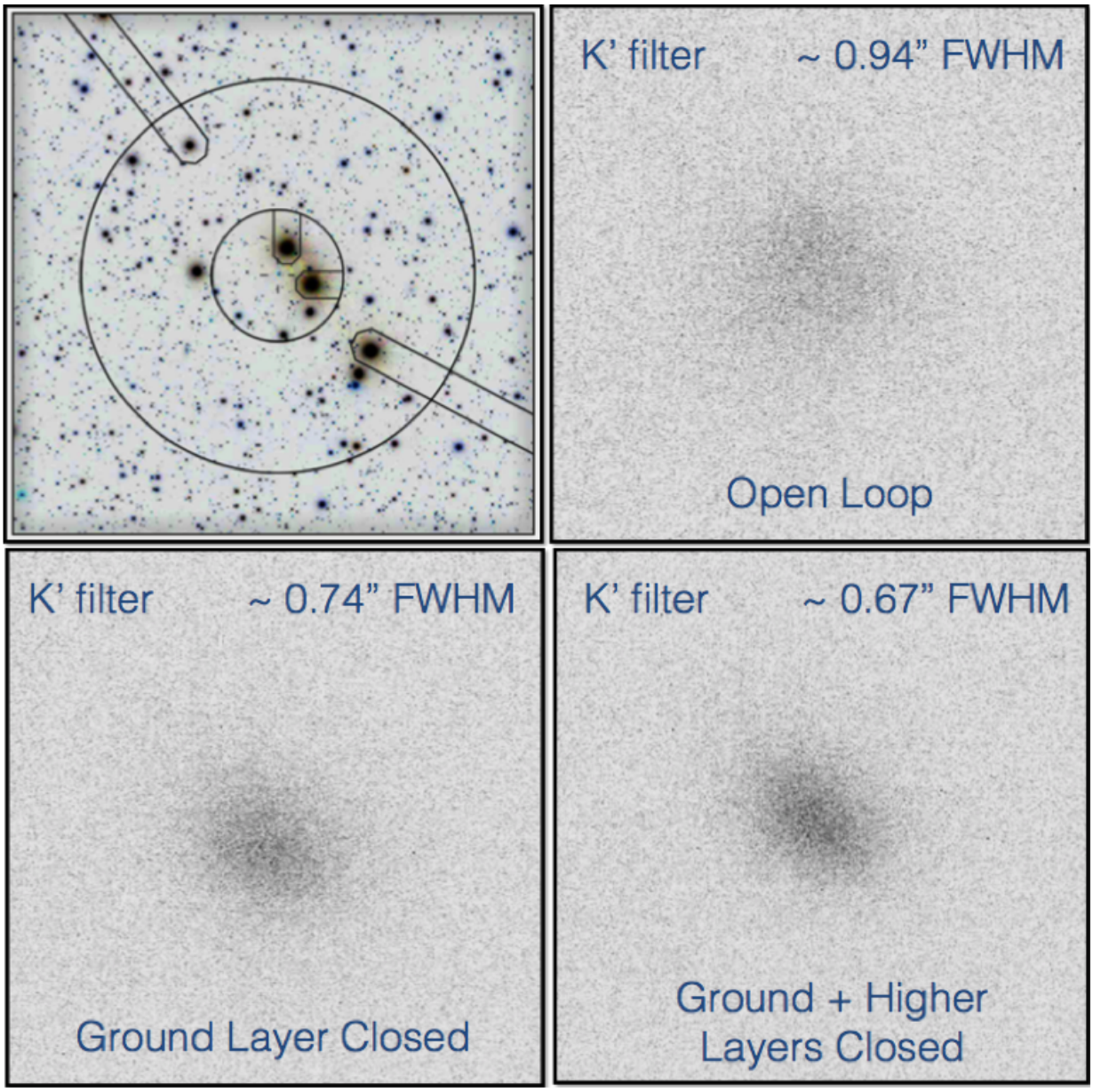


**Figure 3.17:** During LN Commissioning-2 run (June 10, 2017), for the first time, we performed MCAO, using two stars each for the ground layer and high layer correction, as shown in the top-left panel. The open loop image of the 16 mag star in K' filter (FWHM of 0.94"), ground layer corrected (GLAO) image (FWHM of 0.74"), and both ground layer and high layer corrected (MCAO) image (FWHM of 0.67") can also be seen. Of course, we had partial illumination at the high layer. We corrected the first 10 modes for the high layer, therefore the improvement is modest. However, this is our first confirmation of partial illumination on-sky.

matrix from the mother interaction matrix has been confirmed to be effective with as few as three stars in the partial illumination cases. Although simple, the code is robust and effective. We are in the process of studying the algorithm for 2-star and 1-star asterisms.

So far, we have used only a single SNR threshold to define the illuminated sub-apertures across the entire metapupil. This was chosen initially to make the code simple and robust. When using one SNR threshold, we may actually be losing some of the information available from the overlapped regions, in the case of asterisms with 2 or more stars. The overlapping region has information from both stars and has a higher SNR. This clearly appears in Figure 3.8. Therefore, we may use different levels of SNR thresholds to extract this information and weight its importance. One method would be the following. From different SNR threshold values, we would create the corresponding masks and their respective daughter interaction matrices. Higher SNR threshold values would have fewer illuminates sub-apertures, and therefore would only be used to estimate low spatial frequency modes while performing the truncated singular value decomposition to get the respective reconstruction matrix. For different masks, we would obtain different sets of truncated reconstructors. Using proper weighting factors, we would combine them to produce a better-conditioned reconstruction matrix than the one obtained using a single SNR threshold value. In this way, we would actually be using the information from the overlapping area most effectively. This is currently under study, and we hope to implement this at a later stage. For the time being, the analysis does not show a clear relation with respect to the dimension of the region. Other effects, such as the gain vector and, to a lesser extent, the conditioning number threshold for the matrix inversion, seems to have a larger impact.

## 3.6 Conclusions

Our solution to the partial illumination issue is simple, practical, and effective. Depending on the brightness and the spatial distribution of the stars, the correction efficiency varies. Nevertheless, we are able to close and produce a stable loop by controlling the gain vector.

We noted that more illuminated sub-apertures (more stars) leads to better correction and lower RMS wavefront error. Also, more modes can be corrected with more illuminated sub-apertures. It is also better to have more-or-less equal brightness stars (providing more-or-less uniform SNR). Obviously the brighter they are, the better. However, instabilities start appearing if there is one star that is really bright (say 5 mag) and others fainter (say, one 8 mag and one 7 mag). We are still studying the 2-star and 1-star asterisms.

In June 2017, LN accomplished MCAO with partial illumination. We will continue on-sky testing, operating with partial illumination in the upcoming commissioning runs.

We are also working on improving certain other aspects of the system to increase the efficiency of correction, such as the acquisition and centering of very faint stars, the CCD positioning service, and the reduction of the readout noise in the HWS CCDs. In the long run, we plan to implement a slightly improved partial illumination algorithm that will better use the information from the overlapping, higher SNR regions of the metapupil.

# Chapter 4

# Wind-Predictive Wavefront Control

Wavefront at a specific location changes on time scales of milliseconds, due to atmosphere turbulence. This necessitates its real-time spatial and temporal compensation. The structure of the turbulent atmosphere and its interaction with optical waves (aberrating the wavefront) are explained in Chapter 1. To recapitulate: the density of the atmosphere (which falls exponentially with altitude) and temperature variations (which give rise to the optical effects of turbulence and are significant in troposphere, i.e. below ~10 km) are the major contributors to atmospheric turbulence. For most telescope sites, the major part of the turbulence is concentrated in the ground layer, followed by the tropopause, due to wind shear.

Wind has two effects on atmospheric turbulence: it controls both the intensity and the temporal frequency of wavefront fluctuations [49]. The intensity of the turbulence depends on the energy of the process and therefore increases with the square of the wind velocity. The temporal bandwidth of the wavefront fluctuations increases linearly with the wind velocity. The strongest winds normally occur between 9 and 12 km above sea level [49]. Typically, the wind speed at the ground layer varies between 5 m/s and 10 m/s [49], whereas for the high layer, close to the tropopause, it varies between 15 m/s and 35 m/s [49, 92], albeit in a lower density atmosphere.

Proper use of AO telemetry in real-time can accomplish wavefront prediction, which, in turn, can improve the AO system and thus quality of correction. Wavefront prediction is an active research area in adaptive optics. In the past few years, there have been several new ideas for implementing them: the Strehl-optimal approach [42], the closed-loop Kalman filtering approach [108], the data-driven H2-optimal method [56], and predictive Fourier control [92]. These methods all have strong foundations in control systems and signal processing theory, and they provide a solid theoretical framework for prediction. These studies use the extracted information of the wind vector from the wavefront sensor data to create a first-order (linear) predictor. This linear predictor ideally increases the SNR at the wavefront sensor, thus providing more stable closed loop operation (explained in section 4.3).

Although wind-predictive wavefront control implementation has been found to be challeng-

ing and providing only marginal increase in performance for already existing AO systems, we propose to implement a wind-predictive control for the LN AO system. There are three main supporting arguments of this implementation: (1) the LN AO system can provide information leading directly to the wind vectors of the two layers (ground layer and high layer) of interest, unlike other AO systems which require complicate computations. (2) This implementation will directly impact the efficiency of the high-layer wavefront sensing by illuminating the non-illuminated sub-apertures virtually in the direction of wind (filling in the metapupil). (3) Increase in SNR at both ground- and high-layer wavefront sensors, thereby further stabilise the control loop. Also note that there is experimental confirmation of Taylor's frozen-flow hypothesis, that the wavefront is frozen in the atmosphere and translated by wind (see section 4.1). This chapter details our concept, basic assumptions and theories supporting it, and the proposed tests of the wind predictive wavefront control study in the context of the LN AO system. Let me also note that, presently, as I write the thesis, this study is in its early stage. Note also that we took data in June 2017 to verify some aspects of the wind-predictive algorithm. Unfortunately, these data were corrupt. We will be taking further data in October 2017, in the next commissioning run.

## 4.1 Taylor's frozen-flow hypothesis

To quote Taylor from [123] : "... a definite connexion exists between the spectrum of the time variation in wind at a fixed point in a wind stream and the curve of correlation between the wind variations at two fixed points. The spectrum curve and the correlation curve are, in fact, Fourier transforms of one another". The paragraph below explains this statement in perspective of atmospheric turbulence.

Astronomical AO systems correct phase aberrations caused by spatio-temporal refractive index variations in the atmosphere. The Taylor's Frozen Flow Hypothesis (TFFH) [123] states two points about the temporal evolution of the atmosphere. First, the refractive index variations are concentrated in distinct layers and stay spatially stable through time. Second, these layers are blown by the wind, leading to a translation of the phase aberration across the pupil. In other words, the atmosphere structure at a definite layer can be considered frozen in time as far as the radiation is concerned, and is just laterally translated by the wind. Of course, there is a time scale associated with this, over which the wavefront structure is constant, called the coherence time, the same mentioned earlier. The coherence time ($\tau_0$) is function of wavelength ($\lambda$) and varies as $\tau_0 \sim \lambda^{6/5}$.

**Experimental confirmation of frozen-flow**

Although the TFFH has been widely assumed in predictive control proposals and other studies [43,47,118], quantitative confirmation validating the hypothesis is rather recent [45,91]. In their paper, Poyneer et al. [91] confirms the existence of frozen flow, detecting it for more than 94% of the time during 117 nights on Mauna Kea using the Altair (Gemini) and Keck AO systems. Also, they mention that "for the spatial frequencies that Altair and Keck can measure and control, frozen flow normally causes between 20% and 40% of the total atmospheric power. For specific Fourier modes (spatial frequencies), this amount of power is higher and can be up to 70%. The velocity vectors of the layers of frozen flow are stable on time scales of seconds to minutes". They also present a case where the frozen flow was stable over 1 hour, for a specific altitude conjugated layer. Guesalaga et al. [45] also validated the frozen-flow hypothesis using GeMS turbulence profiler data obtained across 2 years. From their wind profile analysis, they showed "how the decay rate of the frozen-flow correlation of each layer can be estimated", and "found a linear relationship between the frozen-flow decay rate and the translational speed of the layers". Schöck et al. [118] also studied and tested the validity of the TFFH and measured the decorrelation times.

Often people get confused between the coherence time scale and the frozen-flow stability time. Recall that the coherence time is the ratio of the Fried's parameter to the wind velocity. Or, in other words, if you consider a specific location, how fast the wavefront is changed within that volume due to the motion of the turbulence by the wind. Frozen-flow, on the other hand, confirms that the wavefront is being translated by the wind, and the strength of the frozen-flow is a measure of how fast/slow the wavefront evolves as it is translated by the wind. If there is frozen-flow, the wind information from the AO telemetry may be used to improve the efficiency of the AO system.

## 4.2 Wavefront prediction

Time delays are inevitable in AO systems. Even with very fast read-out CCDs available these days, time delays, or latency, can arise due to processing of the wavefront data and setting the wavefront corrector. In other words, there is a delay between the measurement and the correction of the wavefront, called the *temporal error* or the *prediction error*. The magnitude of this error depends on the dynamics of the turbulence, which can be understood using the correlation of the wavefronts. The wavefront is translated by the wind. At the same time, the evolution of the turbulence causes the morphology of the wavefront to evolve in time. The correlation of atmospherically-distorted wavefronts decays with time with a the time constant (called the *coherence time*) typically between 1 ms and 10 ms [49], depending on the turbulence

strength, wind speed, and wavelength. The dynamics of the temporal decorrelation of phase at a fixed location in the atmosphere is called *boiling*.

The effects of time delays can be compensated using a prediction scheme to anticipate the corrections that will be required in the next computation cycle. Wavefront prediction may be based on data measured in previous sampling periods or on data from surrounding sub-apertures, as well as on data from the sub-aperture in question. There are three main prediction strategies:

1. **Zero-order prediction**, in which the current value of the wavefront is used as the best estimate for the next period. This is the optimum strategy for a stochastic or random process. Most closed-loop AO systems use this strategy. It is usually implemented in the form of an integrator that holds the current correction, with a decay factor until the next measurement. This method requires that the wavefront sampling interval be considerably shorter than the decay time of the turbulence, i.e. faster than the coherence time.

2. **First-order** or **linear prediction** is based on extrapolation from recent samples. This is the optimum strategy for a signal contaminated with white noise [49, 69]. Atmospheric turbulence is such a case. The predicted wavefront is a function of both time and position, and the prediction is done using measurements of the wind vector that transports turbulence across the telescope aperture. This prediction could be of considerable value at good astronomical sites, where the turbulence occurs mostly in well-defined layers. An example of a linear predictor and the improvement that can be achieved is described in section 4.3.

3. **Nonlinear prediction** is usually implemented by a neural network, and is appropriate for a chaotic process. There is evidence that atmospheric turbulence sometimes behaves like a chaotic process [59, 60, 78]. However, studies have shown that, with severe turbulence, the largest gain was obtained in going from a conventional zero$^{th}$-order predictor to a linear predictor, with only a small further gain for the neural network [59, 60].

For the rest of this chapter, we explore how the knowledge of the wind vector (from the AO telemetry) can be exploited for first-order or linear wavefront prediction.

## 4.3 Travelling wave predictor

The travelling wave predictor is an example of a linear predictor. Its principle is explained in Figure 4.1. Wavefront disturbances traversing the telescope aperture pass across the sub-apertures of the wavefront sensor with a velocity vector determined by the wind speed and direction. In normal operation, each wavefront measurement is independent, using whatever

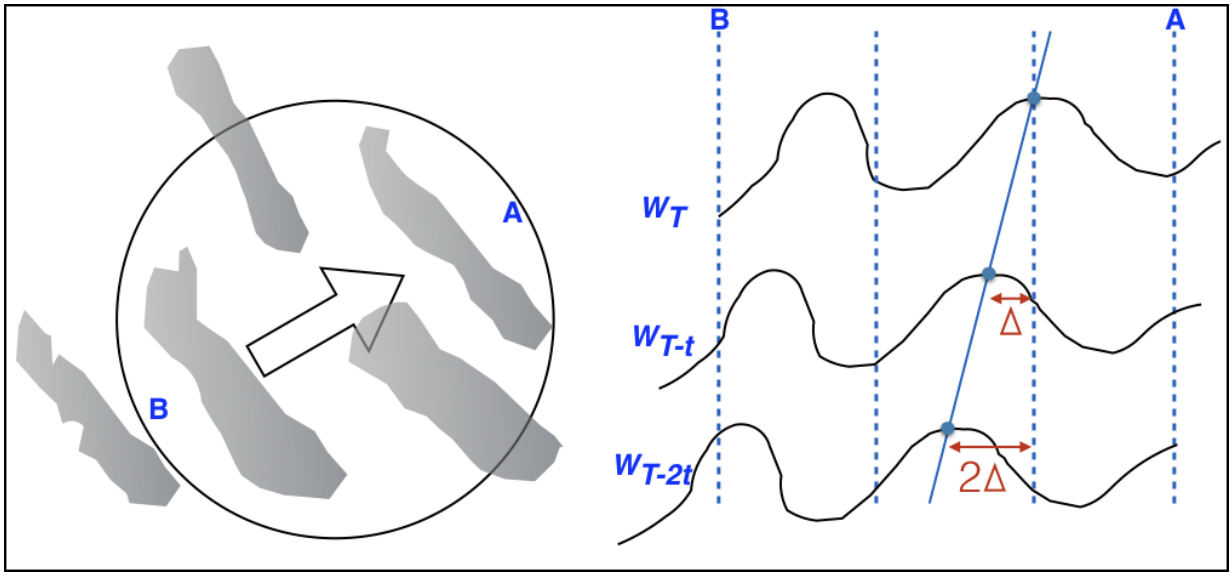


**Figure 4.1:** Schematic representation of the principle of the traveling wave predictor. *left*: Turbulence in motion across the telescope aperture. *right*: Wavefront profiles along the motion vector from B to A. Wavefront measurements $W_{T-t}$, $W_{T-2t}$, etc. are made along the motion vector at times *T-t*, *T-2t*, etc. and are shifted by Δ, 2Δ, etc. The earlier measurements are included in the current measurement.

photons are collected during the detector integration time. The motion of the turbulence can be detected using the wavefront sensor data. The wind speed, the coherence time, and wavefront sensor integration time are the important parameters. If the turbulence structure remains frozen (as mentioned in section 4.1) while it traverses the aperture, many additional samples may be obtained by combining previous measurements, with the appropriate spatial shift. This process increases the effective exposure time and, consequently, improves the SNR of the wavefront measurement. Also, if some or many of the sub-apertures are not illuminated, as in the case of partial illumination (see Chapter 3 for details), and the wind is in a favourable direction, those sub-apertures could be virtually illuminated using the previous cycle measurements from the illuminated regions (see section 4.5). Of course, in this instance, we are referring to turbulence blowing across the high-altitude layer, not the telescope aperture.

Sub-apertures on the lee (downwind) side of the telescope aperture (labelled A in the left panel of Figure 4.1) have the most favourable location. Here, the turbulence can be tracked across the full aperture, producing a large increase in the effective exposure time. On the other hand, B is the least favourable location, on the windward edge of the aperture. Here, the wave predictor produces no improvement. The average separation of all points within an aperture measured from one edge in one direction is $\pi D/8 = 0.39D$ for a circular aperture, where $D$ is the diameter

of the telescope (for a high conjugated altitude, $D$ will represent the metapupil diameter instead of the telescope diameter).

The improvement in effective exposure time can be estimated for the ideal case of frozen turbulence. We therefore assume that there is no change in the wavefront as it traverses the telescope aperture. If $d$ is the sub-aperture dimension at the telescope aperture, then the time required for the turbulence to traverse one sub-aperture is $d/v$ seconds, where $v$ is the wind velocity. If the aperture is divided into $N$ sub-apertures across the diameter (in other words, $N = D/d$), the wavefront can be measured over an average distance of $0.39N$ sub-apertures. The effective exposure time ($t_e$) is the product of the average number of sub-apertures used and the time taken to traverse one sub-aperture, given by :

$$t_e = 0.39\ N\ \frac{d}{v} \tag{4.1}$$

If $t$ is the measurement interval, the extra sampling factor $F_{TWP}$ is given by :

$$F_{TWP} = \frac{0.39\ N\ d}{v\ t} \tag{4.2}$$

For the typical case (of an 8 m class telescope) with $N = 20$, $d = 0.4m$, $v = 10m/s$, and $t = 0.002s$, $F_{TWP}$ has a value of 156. The SNR will be proportional to the square root of the effective exposure time. Therefore, the SNR improves by the square root of $F_{TWP}$, that is by $\sim$12.5. This is under ideal conditions only, with the assumption that the wavefront does not change as it passes across the aperture. In reality, therefore, the actual improvement would be less than this.

A significant improvement in the average SNR means lower wavefront error and higher stability of the loop. However, in order to implement such a system, it is necessary to extract the wind vector from the wavefront telemetry. In contrast to the calculation made above, in reality, the wavefront shape changes with time as it evolves and the frozen-flow is a valid assumption only within the coherence time. Therefore, the correlation has to be performed for frames within the coherence time. And the effective sub-apertures covered within this correlation time most likely do not fill the entire 8 m. A decay or weighting factor may be used to account for the decorrelation of the wavefront with time, reducing the contribution of earlier measurements.

All of the wind-predictive algorithms require a model for the temporal evolution of the atmosphere. If the statistical characterisation of the atmosphere embodied by this model accurately reflects present atmospheric conditions, the prediction will improve performance. If the model is wrong, on the other hand, the predictor will not improve performance and may even make things worse. Also, all of these models assume that the atmosphere follows the frozen flow hypothesis (explained in section 4.1).

## 4.4 Extracting the wind vector from AO telemetry

We have already seen a back-of-the-envelope calculation in section 4.3 showing the SNR improvement using the wind information in a rather ideal scenario. Depending on the type of AO system and methods used, the extraction of the wind vector from the AO telemetry varies slightly. However, the basic principle remains the same. One of the basic assumptions for the wind estimation is the frozen-flow hypothesis (explained in section 4.1). The mathematical foundation and concept behind the extraction of the wind vector is explained in section 4.4.2.

### 4.4.1 AO system type dependence

It is safe to assume the TFFH for our study of wind-predictive control and for extracting the wind vector from the AO telemetry. Of course, each of the layers may have a different wind speed and direction. This will also likely change over nights or across the same night. Boiling will contribute to the error term and also limits the accuracy of the wind vector estimation. One study incorporating the effect of boiling can be seen in [62].

The AO system type depends on the scientific goals associated with the instrument. For example, extreme AO (XAO) systems are used for a high-contrast imaging. There are also multi-object AO (MOAO) systems, laser-tomography AO (LTAO) systems, MCAO (layer-oriented and star-oriented) systems, etc. in use or in development today. For MOAO, LTAO and MCAO star-oriented systems, the wavefront sensor derives the full volume turbulence data. This means that each guide star provides the turbulence profile from the full cylinder or cone of the atmosphere through which it travels. From multiple such guide stars, the wind information must be extracted for the prominent turbulent layers. There are a few recent studies on how to perform this extraction [26, 45, 88, 89, 91].

For a layer-oriented MCAO system like the LN, we directly get the wavefront sensor data for the conjugated layer. Therefore, the wind vector can be retrieved directly from the wavefront data. This saves significant computations, which are necessary for the tomographic wavefront sensor, for example. However, we get information of the wind vector mostly from the conjugated altitude. If there is a strong wind-sheared layer relatively far above or below, we do not get that information and cannot perform the prediction accordingly.

Here, it is worth pointing out that for an MCAO system, each of the WFSs measures lower spatial frequencies from neighbouring layers as well. Under ideal and noise-free conditions, and with complete knowledge of the turbulence, the conjugated layers can be perfectly corrected [98]. However, the DM corrects only up to a spatial frequency of $f_c \propto 1/(\theta\,\Delta h)$ for the non-conjugated

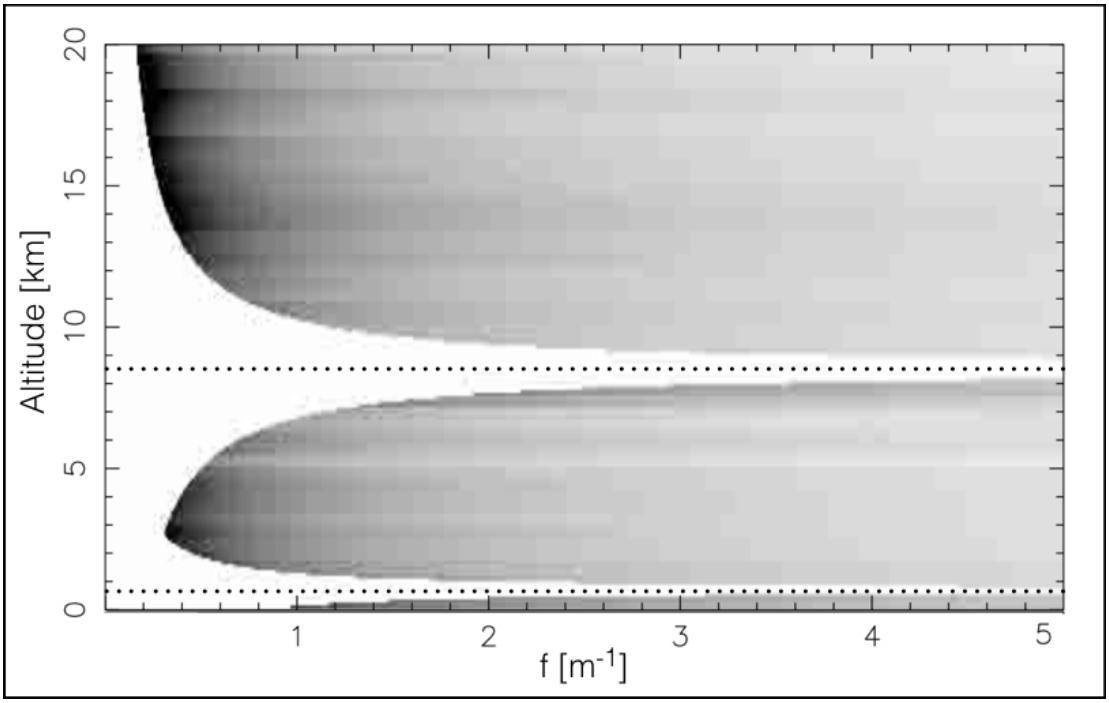


**Figure 4.2:** The average $C_n^2$ profile of Cerro Paranal compensated by a Multiple-FoV layer-oriented system with two DMs conjugated at 800 m and ~8.5 km (represented by dotted lines) and FoV of 6 arcmin and 2 arcmin respectively. This plot is adapted from Ragazzoni et al. [98].

layers, where $\theta$ is the FoV associated with the DM and $\Delta h$ is the distance of the layer from the conjugation plane. This relation, in the $(f, h)$ plane, describes a hyperbola [98].

Figure 4.2 plots the residual $C_n^2$ profile (see section 1.1.2 for details) with altitude (h) against the spatial frequency (f). The turbulence at the conjugated altitude is completely removed by the DM. However, for different altitudes, the compensation is partial, up to a spatial frequency inversely proportional to the distance from the conjugation altitude. This is the consequence of the smoothing effect introduced by the finite FoV of the DMs and related detectors. With LN, the DM conjugated to the ground corrects a larger FoV (6 arcmin), and hence the degradation of the correction is faster than for the other DM, characterised by a smaller FoV (2 arcmin). This is the same effect as seen in the more rapid defocus (loss of depth of field) for "faster" or lower $f/\#$ optical systems.

### 4.4.2 Basic signal processing theory to extract the wind vector

The TFFH tells us that the wavefront is translated by the wind. The wavefront sensor data provide us the first derivative of the wavefront, in other words the slopes in both the X and Y direction. Therefore, the cube of slopes data from the wavefront sensor (i.e., X-slope, Y-slope, time) has the information of the wind vector. We know from signal processing that the cross-correlation of signals from two different time steps will provide the displacement.

The cross-correlation between two signals is equal to the inverse Fourier transform of the product of the Fourier transform of one signal multiplied by complex conjugate of the Fourier transform of the other [77]. Mathematically, the cross-correlation between an image $f$ and a template $t$ is given by the equation:

$$T_{f,t}(\Delta x, \Delta y) = \frac{1}{N(\Delta x, \Delta y)\,\sigma_f\,\sigma_t} \,.\, \mathcal{F}^{-1}\left[\mathcal{F}\Big(f(x,y) - \bar{f}\Big) \,.\, \mathcal{F}^{*}\Big(t(x,y) - \bar{t}\Big)\right] \tag{4.3}$$

where $\mathcal{F}$ is the Fourier transform, $\bar{f}$ and $\bar{t}$ are the averages over the whole images, and $\sigma_f$ and $\sigma_t$ are their standard deviations. $N$ is the overlapping factor, which is equivalent to the number of overlapping pixels for each individual point of the cross-correlation [117]. This factor compensates the different number of overlapping pixels for each position $(\Delta x, \Delta y)$ in the cross correlation. N can be calculated by doing the auto-correlation of the pupil image, using the formula:

$$N(\Delta x, \Delta y) = \mathcal{F}^{-1}\left[\Big|\mathcal{F}\Big(pupil(x,y)\Big)\Big|^2\right] \quad , \tag{4.4}$$

where $pupil(x, y)$ equals 1 inside the pupil and 0 otherwise.

The spatio-temporal cross-correlation of the slopes data from the wavefront sensor data will provide the wind vector [45]. However, the extraction becomes complicated if the wavefront sensor data contains information from the full cylinder of turbulence through which the guide star light passes. From the cross-correlation, a number of peaks of different strengths will give the wind vector in different layers. However, in the case of LN AO WFS data, each of the WFSs provide information only about the conjugated layer - the ground layer and the high layer. We therefore expect one strong peak from the cross-correlation which gives the wind vector. However, for the ground-layer, if there is strong dome seeing, the cross-correlation may have a second, static peak at the center. Also, there may be fainter out-of-focus peaks from the very immediate neighbouring layers, if strong wind shears are present.

It is worth noting here that in a closed-loop AO system, due to the feedback control loop, the WFS measures the residual slopes after correction, not the slopes themselves. Therefore, the phase information obtained from the wavefront sensor corresponds to residual phase. For the wind estimation, full wavefront information is necessary. This can be obtained by the pseudo

open-loop (POL) procedure [45], using the shape of the deformable mirror and the WFS data. The POL data is calculated with the following formula:

$$S_i^{POL} = S_i^{res} + IM \,.\, V_{i-1} \tag{4.5}$$

where, $S_i^{POL}$ is the POL slope at time step $i$, $S_i^{res}$ is the wavefront sensor slope data for the time step $i$, $V_{i-1}$ is the shape of the DM at time step $i-1$, and $IM$ is the interaction matrix.

The accuracy in estimating the wind vector from the WFS measurements depends on several factors. Uncertainty in the slope measurements may depend on the type of wavefront sensing used. For example, pyramid wavefront sensors have different optical gain and sensitivity with the loop closed, which translates to better slope measurements. Also, the number of sub-apertures or the spatial sampling of the WFS, size of the sub-aperture, and centroid detection method directly set a lower limit to the accuracy in estimating the wind vector. This is in addition to the read-out noise and other effects due to the detector itself. Of course, as mentioned earlier, if there is a strong turbulence layer with strong wind in the neighbouring layer, the effects will also be seen in the WFS data. As mentioned earlier, the effect of boiling cannot be neglected, and to date, there is no good prediction method for the error due to boiling.

## 4.5 Wind-predictive control in the LN AO system

In addition to the fact that implementation of wind-predictive wavefront control in the LN AO system will be relatively easier due to separate AO telemetry directly available for the two layers, we expect performance gain in closed-loop operation. For the high layer wavefront sensor loop, implementing the wind-predictive control can improve the partial illumination scenario. This is described below in section 4.5.2. Another advantage will be the effective increase in the exposure time due to the predictive control, providing larger SNR. Larger SNR at the wavefront sensor makes the loops stabler.

### 4.5.1 Implementing in the ground-layer loop

In the case of the ground layer data, the “metapupil” is always fully illuminated and the scenario is very similar to that shown in Figure 4.1. The metapupil may be illuminated by multiple guide stars, making it possible to have fainter stars also for AO correction. Also, using multiple stars provides higher SNR. In this case, incorporating the wind prediction will provide an increase in the average SNR across the metapupil. This is the first test we plan to do, first in the lab, followed by on-sky testing.

### 4.5.2 Implementing in the high-layer loop

For the high layer, partial-illumination is inevitable (as explained in Chapter 3). Some or many of the sub-apertures will not be illuminated. Figure 4.3 schematically represents the scenario. The left panel of Figure 4.3 shows the partially-illuminated metapupil, where the yellow shaded regions represent the non-illuminated sub-apertures. If the wind direction is in a favourable direction for non-illuminated sub-apertures, as shown in the right panel of Figure 4.3 by the blue arrow, some or many of the non-illuminated sub-apertures will be virtually filled (green shaded region on the right panel of Figure 4.3) using wind prediction. The results of our study on partial illumination (see section 3.6) validates that the greater the number of illuminated sub-apertures, the better the correction and more stable the loop. Ultimately, implementing wind prediction should make the high layer loop more stable and provide a better correction.

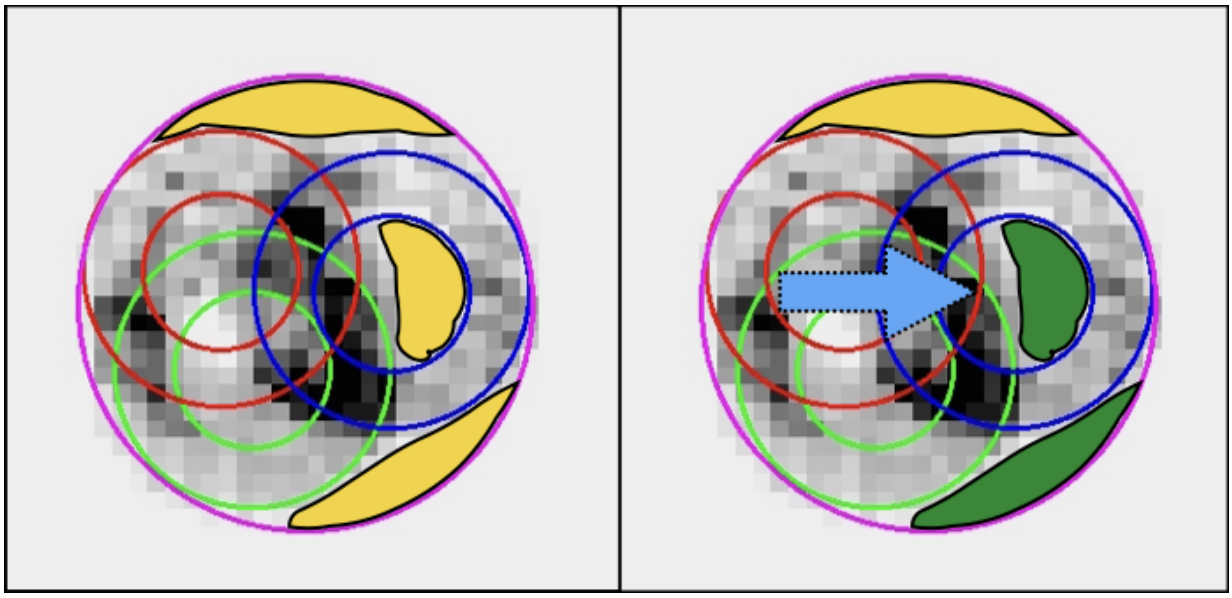

**Figure 4.3:** Virtually filling sub-apertures using wind-predictive wavefront control on the high layer loop. *left* : The partially-illuminated metapupil can be seen. The yellow shaded regions represent the non-illuminated sub-apertures. *right* : A favourable wind direction (blue arrow) allows us to virtually fill in some of the non-illuminated sub-apertures, represented by the green shaded regions.

### 4.5.3 Predicting differential piston

LN will eventually perform Fizeau interferometry. It is essential for interferometry to have zero optical path difference. In other words, the piston drift between the two eyes of the LBT should be reduced to zero. Widmann et al. [129, 130] studied the possibility of using wavefront sensor data to extract the wind vector and estimate the piston drift. The results of this work will be soon submitted. For this study, they used simulated data as well as data from the LBT FLAO system. They were able to retrieve the wind vector with reasonable precision and estimate the piston drift. Therefore, implementing the wind prediction control will be the first step for the estimation of the piston drift.

## 4.6 Proposed tests

The implementation of wind-predictive control for the LN AO system will involve a number of phases, starting with simulations to quantify the performance gain. We already have an aligned laboratory set-up, the aligned LINC-NIRVANA system at the LBT. Making use of the the calibration unit system, we will test our algorithm and software implementation. Once the laboratory tests provide proof of improvement and a consistent, working system, we will move to on-sky verification.

In this section, I chart out some of the tests to be implemented in the lab. We have the capability to generate known, artificial disturbances simulating atmospheric turbulence. We can change parameters like the turbulent power spectrum to follow (for example, Kolmogorov or von Karman), the wind speed and direction, add information of multiple layers, seeing, or strength of the turbulence etc.

Initial laboratory tests are planned to check the algorithm and working of the wind extraction code. We will first evaluate the accuracy with which the wind vector can be extracted using different disturbances created by varying the wind speed alone, direction alone, and both together with different strength combinations of frozen flow and boiling for the single conjugated layer. These same tests will be performed for a disturbance containing a reasonably strong wind in the conjugated layer and a stronger wind for a layer above or below the conjugated layer. Note that the information of the neighbouring layer may be embedded in the artificial turbulence created. Once the tests provide conclusive results on the wind extraction code, we move to the next step.

Software implementation is the next step, in which the wind prediction control will be tested for the ground-layer case. It will be relatively easier than for the high layer case, as the ground layer illumination always fills the “metapupil”. For the high layer case, the number of sub-

apertures that will be virtually filled in varies as a function of the wind vector. Accordingly, the illuminated mask, and therefore the daughter interaction matrix that has to be registered for the proper functioning of the loop, also changes. Software implementation of the high layer is therefore expected to be more time-consuming and complicated. However, once implemented, tested, and working, the performance of the high layer loop is expected to increase considerably, improving the science image quality as well. Note that I will be spending an additional year at MPIA after the thesis defence to continue working on this project.

## 4.7 Conclusion

A rigorous study of implementing wind-predictive wavefront control is planned in the context of the LN AO system. We will exploit the advantage of the layer-oriented LN AO system and expect to have improvement in the stability of the loop and AO performance in general. In the context of the high-layer wavefront sensor and partial illumination, wind-predictive wavefront control can bring considerable improvement of quality of the science image.

The first step is testing various scenarios in the lab, using the aligned LN bench at the LBT during daytime, with artificial disturbances simulating atmospheric turbulence layers. The software also has to be developed to support the predictive control. After successful testing, the wind-predictive control will be evaluated on-sky. If proved to be successful on-sky, this idea can be extended to other layer-oriented MCAO systems. We hope to have this implemented in the LN AO system by late fall 2018.

# Chapter 5

# An AO investigation of structure and dynamics in the T Tauri system

In the last three chapters, I have discussed my contribution to studies on the impact of observing through the atmosphere, and how we can overcome these challenges in the perspective of the LINC-NIRVANA instrument. The optical assembly, integration and verification of the LN AO system is the subject of Chapter 2, a specific challenge faced by any layer-oriented MCAO system (such as the LN AO system) is the subject of Chapter 3, and a possible performance gain that we are pursuing is explained in Chapter 4.

In this chapter, I look into an astrophysical application of an adaptive optics system. I have devoted almost a quarter of my doctoral study time to learning about star formation. Making use of state-of-the-art instruments on 8-m class telescopes equipped with adaptive optics systems, I investigated the T Tauri system. T Tauri (also commonly called T Tau) is a complex and relatively rapidly evolving triple star system. Over recent decades, there have been many observations and discoveries in this system as new technologies came along. However, there are continuing debates about the geometry of T Tauri and the association of various outflows to each of the three stars. My study concentrates on understanding the dynamics, energetics and geometry of the T Tauri system, associating each of the outflows and line emission features to their parent star, and imaging the circumstellar disks.

Note that, for the last three chapters, MCAO was the type of AO system under consideration. For this chapter, eXtreme Adaptive Optics (XAO) systems were used instead. XAO systems can deliver very high Strehl ratios within a rather small FoV of interest (a few arcsec across). XAO systems can therefore be used for many high-contrast imaging studies, such as planet detection or as in our case, to study the outflows, line emission, and circumstellar disks of pre-main sequence stars. Note also that this chapter focuses on science, not instrumentation. I will not be discussing the XAO system in any great detail. However, two unique parameters of an XAO system need to be introduced:

1. The **inner working angle** is defined as the 50% off-axis throughput point of a coronagraphic system [83].

2. The **correction radius** ($\theta_{AO}$) is the angular separation up to which the deformable mirror can suppress the aberrations [63]. It is given by $\theta_{AO} = \lambda/(2d)$, where $\lambda$ is the observation wavelength and $d$ is the inter-actuator spacing of the DM projected back to the telescope aperture.

As we will see below, these two parameters have a strong influence on the type and quality of information that can be extracted from XAO observations.

## 5.1 The T Tauri system overview

T Tauri stars (TTS) are a class of pre-main sequence stars or Young Stellar Objects (YSO) in the process of contracting to the main sequence along the Hayashi track [71]. Usually found in or near molecular clouds, TTS show optical variability and strong line emission. These stars are very active and have strong stellar winds, in addition to high-velocity bi-polar jets. TTS have been observed at wavelengths ranging from X-rays to radio waves. Advancements in imaging techniques have enabled observations of circumstellar disks around nearby TTS [116]. The T Tauri system is considered the prototype of the TTS.

T Tauri (hereafter T Tau) is located in the Taurus-Auriga star-forming region at a distance of 146.7±0.6 pc [79] with an age of 1-2 Myr [70] and a total system mass of 4.6±0.1$M_{\odot}$ [73]. T Tau was first identified as a variable star in the mid 1940s [61]. With every advancement in imaging and spectroscopic techniques at visible and near-infrared wavelengths, observations have provided new surprises and understanding about the T Tau System. Although considered as a prototype of YSOs, T Tau, unlike most of the TTS, is a complex system with at least three stellar components, multiple jets and outflows.

The primary component is the optically visible, early K star [24], commonly known as **T Tau N** (for T Tau North) after the discovery of the southern component. In 1982, speckle interferometry [33] revealed an infrared companion 0.7" to the South of T Tau N, called **T Tau S** (for T Tau South). T Tau S is very red (not yet observable at visible wavelengths), and its brightness fluctuates at all near-infrared and mid-infrared wavelengths [44]. In 2000, using speckle holography, Koresko et al. [76] found that T Tau S itself is a close (~0.1") binary, composed of the IR luminous **T Tau Sa** and the early M-star companion **T Tau Sb**.

Recent studies [73, 115] estimated the masses of T Tau Sa and T Tau Sb to be 2.12±0.1$M_{\odot}$ and 0.53±0.06$M_{\odot}$, respectively. This means that T Tau Sa is at least as massive as T Tau N,

despite the large contrast in visible light. The orbital period for the Sa-Sb binary is estimated to be 27±2 years with a semi-major axis of $12.5^{+0.6}_{-0.3}$ AU, and the inclination of the system is $20^{+10}_{-6}$ degrees [73]. The orbit of the T Tau N-S binary is not yet well constrained. The lower limit to the minimum semi-major axis and period are 300 AU and 800 years respectively. The true values may very well be considerably larger than this, based on the large range of orbital solutions still compatible with the data [73].

All three stars are actively accreting. Also, the stars are spatially unresolved, i.e., point-like, hydrogen recombination line emitters [32,67]. Due to changes in the accretion rate on timescales of days, the near-infrared brightness of T Tau Sa is highly variable. The long-term variability is caused by a combination of accretion and foreground extinction [126] with a "redder when faint" character [6]. The visible extinction toward T Tau N was estimated to be $A_V$=1.39 mag [70]. The extinction toward T Tau Sb is much higher, but only varies slightly around $A_V$=15 mag [32,66]. In order to estimate the extinction from NIR observations, we must consider the excess luminosity from accretion and warm circumstellar material. In the H-band, excess luminosity or spectral veiling of 0.8 has been measured for T Tau N [67]. For T Tau Sb, an H-band veiling of 0.7 and a K-band veiling of 2 were measured [32]. Photospheric features in the NIR spectra of T Tau Sa have not yet been detected, preventing an estimate of its excess emission. Only recently, we detected [112] T Tau Sa in the J-band for the first time ever (see section 5.3.2).

The near environment of T Tau is a source of strong and spatially extended molecular hydrogen ($H_2$) emission [8]. The spatial distribution of the $H_2$ emission displays a very complex pattern of multiple outflows on all observed angular scales [46, 51, 53, 114] (see Figure 5.1 and Figure 5.2). The $H_2$ emission is most likely generated by shock heating [53]. However, fluorescent $H_2$ pumped by Ly$\alpha$ was also found, suggesting the action of low density, wide opening-angle outflows driving cavities into the molecular medium [114]. Interaction of the wide angle wind produced by the outflow and the molecular material in the region can create shocks. Shocks in turn excite causing fluorescence. No significant $H_2$ emission is associated with the stars themselves [32, 51, 66, 67].

The outflows from the T Tau triple are directly linked to the observed structures. This also means that by understanding the outflows, the geometry of the system may be deduced. Initially, it was suggested that T Tau N fuels the jet pointing West and ending in the Herbig-Haro object HH 155 [20], while the Southeast-Northwest outflow originates in the then-unresolved T Tau S. Using ground-based adaptive optics and Fabry-Perot $H_2$ imaging, Herbst et al. [51] found evidence that the East-West outflow is instead triggered by either T Tau Sa or Sb. This means that the Southeast-Northwest outflow would have to be attributed either to T Tau N or to the southern component not driving the East-West outflow (see Figure 5.1). The presumably North-South orientation of T Tau Sa's edge-on disk [102] suggests that the East-West outflow indeed originates from T Tau Sa.

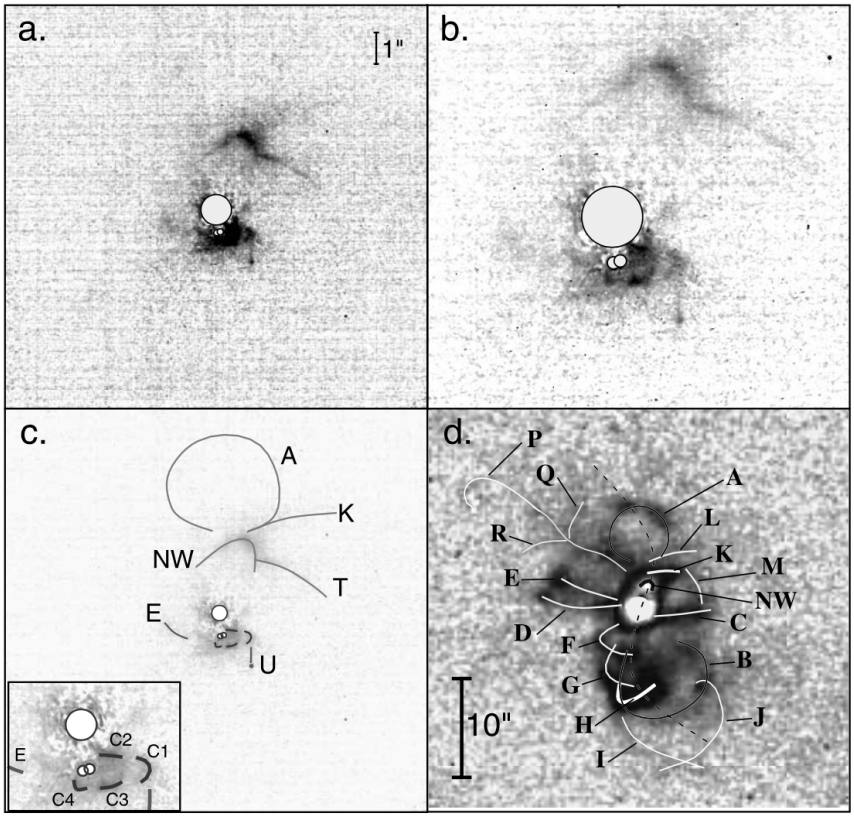


**Figure 5.1:** Continuum-subtracted Fabry-Perot images of T Tau in the 2.12 $\mu$m quadrupole line of $H_2$. The immediate area of the stars is blanked out to avoid distracting artefacts. Note the two prominent arcs, labeled NW and C1 in panel c, pointing back at the stars. Panel d reproduces Fig. 8 of Herbst et al. (1997), giving the naming conventions for the $H_2$ filaments in T Tau. [This image is taken from Herbst et al. [51].]

Although the orbit of T Tau S is now well understood, knowledge of the circumstellar and circumbinary disks remains limited. It is believed that the circumstellar disk of T Tau Sa (with radius 3-5 AU) is almost edge-on and oriented North-South, hiding the stellar photosphere [6,67, 76]. Also, the Sa-Sb circumbinary disk (if present) is believed to be edge-on. The circumstellar disk around T Tau Sb is believed to be nearly face-on, approximately coplanar with the T Tau N-S binary's orbit [102].

### 5.1.1 New XAO observations of T Tau

This chapter reports new diffraction-limited, high-contrast observations using two state-of-the-art instruments, VLT-SPHERE and LBT-LUCI, each supported by their advanced adaptive

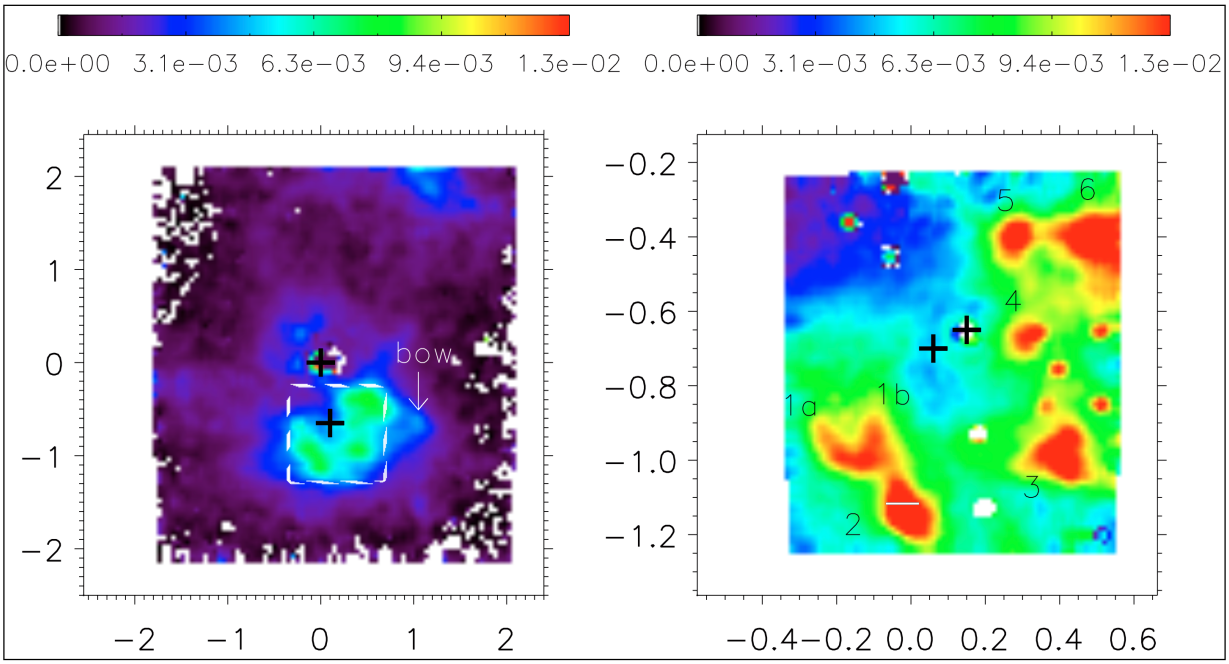


**Figure 5.2:** Near-infrared integral field unit images of $H_2$ $v$=1-0 S(1) emission. *left* : 100 mas pixel scale, *right* : 25 mas pixel scale. The colour-bars indicate the flux level in erg $s^{-1}$ $cm^{-2}$ $sr^{-1}$. The spatial coverage of the small field of view (right) is indicated by the white box in the left panel. The positions of the stars are marked with black crosses. [This image is adapted from Gustafsson et al. [46].]

optics systems to image the immediate circumstellar environment of T Tau [65, 66, 112] at near-infrared wavelengths. New outflows, fainter features and line emissions were discovered. The two distinct outflow systems, the North-West outflow and the newly discovered South-West coiling outflow, were associated with one of the southern stars (T Tau Sa or T Tau Sb) and T Tau N respectively [66]. For the first time ever, the enigmatic source, T Tau Sa, was detected in the J band [112]. Also, we have discovered new tadpole-shaped features, and new extended molecular hydrogen line emission [65, 112].

Details of these new observations form the subject of the rest of this Chapter. Section 5.2 presents the observations, and explains and interprets the results from the VLT-SPHERE instrument, while section 5.3 does the same for the LBT-LUCI observations. Finally the chapter concludes with a summary in section 5.4.

## 5.2 Observations with VLT-SPHERE

This section discusses observations of the T Tau System using the SPHERE instrument, our results, and their interpretation. This work has already been published in Astronomy and Astrophysics [66], a paper on which I am the second author. Most of the material presented in this section comes from the paper, but it has been modified to focus on my contribution to the work (in particular, understanding the newly discovered coiling outflow to the Southwest and the nature, proper motion, and origin of the T Tau NW shock).

### 5.2.1 Observational details

We observed T Tau with the SPHERE instrument [14, 64] as part of its Science Verification program. SPHERE provides high contrast imaging by combining extreme adaptive optics, coronagraphy, accurate calibration of non-common path instrumental aberrations, and post-observational data calibration through various differential methods. The instrument is integrated on a large optical table on Nasmyth platform A of the VLT Unit Telescope 3 at Paranal, Chile. Three scientific instruments are attached to this main bench: a differential near-infrared imaging camera and spectrograph (IRDIS, InfraRed Dual Imaging Spectrograph); a near-infrared low spectral resolution Integral Field Spectrograph (IFS); and a visible imaging differential polarimeter (ZIMPOL, Zurich Imaging Polarimeter). For the T Tau study, we used IRDIS and IFS.

On 9 December 2014, using IRDIS [31] in classical imaging mode, and on 23 January 2015 using IRDIFS extended (IRDIFS-EXT) mode, we observed T Tau. In IRDIFS mode, SPHERE observes simultaneously with the IFS [23] in J- and H-band (R~30), and with IRDIS in two K-band filters optimized for the spectral differential detection of extra-solar planets (IRDIS DBI, [128]). Both sets of observations were carried out in field-stabilized mode with (for IRDIFS-EXT) and without (for IRDIS classical imaging) the apodized Lyot coronagraph (ALC). The ALC is optimized for observations from Y- to H-band, providing an inner working angle (see page 106 for details) defined by the mask diameter of 185 mas. The extreme adaptive optics system SAXO [41] corrected the atmospheric turbulence.

The classical imaging data were acquired in different narrow-band filters: ContJ (1211 nm), Pa$\beta$ (1282 nm), $H_2$ (2122 nm), Br$\gamma$ (2167 nm), and ContK2 (2267 nm). For the astrometry and photometry, 160 two-second exposures were recorded in each filter using a neutral density filter with a factor of ten attenuation (ND1) to avoid point spread function saturation. For deep imaging in the $v$=1-0 S(1) line of $H_2$ and the adjacent continuum, 80 eight-second exposures were recorded in each filter without a neutral density filter. This led to saturation of the PSF core of T Tau N in all filters and of T Tau Sa in the K-band filters. Two hundred sixteen-second exposures

were recorded with the IFS. These data are not saturated, because T Tau N was masked by the coronagraph, and T Tau Sa is considerably fainter in the J- and H-bands than in the K-band.

Calibration data (sky, flat field, etc.) were recorded as part of the daily calibration. For the coronagraphic observations, we recorded images with T Tau N shifted away from behind the Lyot mask for flux calibration. In this case, the ND1 filter was inserted to avoid PSF saturation. For the IRDIS classical imaging, we also recorded the instrumental PSF in all narrow-band filters using a SPHERE-internal calibration point source. This is required to calibrate the ghosts and filter defects, which are unfortunately present in many of the SPHERE narrow-band filters. The IRDIS pixel scale and the IFS image plate scale are (12.251±0.005 mas) and (7.46±0.02 mas per pixel) respectively.

We used the SPHERE data reduction pipeline [90] to create sky-frames, bad pixel maps and flat fields. We reduced the raw data by subtracting the sky-frames, replacing bad pixels by the median of the nearest valid pixels, and finally dividing by the flat field. We also used the SPHERE pipeline to create the IFS x-y-$\lambda$ data cube. Parts of this cube were collapsed along the wavelength axis to create broad-band images in the J-band (1140-1350 nm) and the short end of H-band (1490-1640 nm).

### 5.2.2 Results of the SPHERE data

#### Continuum imaging

Figure 5.3 shows the J-band image, and Figure 5.4 zooms in on the area Southwest of T Tau N, which is centered on the upper left pixel. Figure 5.5 (IFS J-band image, 1140-1350 nm), Figure 5.6 (IFS H-band image, 1490-1640 nm), and Figure 5.7 (IRDIS K1-band image) have been generated from the IRDIFS-EXT observations. Here, a large fraction of the light from T Tau N is blocked by the ALC. The field of view of the reconstructed IFS cubes is 1.7" across. In IRDIFS-EXT mode, the reconstructed x-y-$\lambda$ data cube consists of 39 wavelength slices between 0.95 $\mu$m and 1.68 $\mu$m, spaced by $\Delta\lambda$=0.0191 $\mu$m, corresponding to R ~70. Slices of this data cube can be combined to create images at the desired wavelength and spectral bandwidth.

Some of the image structures in these figures are produced by the adaptive optics point-spread function. The large, diffuse ring-like structures centered on T Tau N with approximate radii between 0.6" (J-band) and 1" (K-band) corresponds to the so-called correction radius (see page 106 for details) of the deformable mirror. Beyond this radius, with its finite number of actuators, the deformable mirror can no longer reproduce and correct for optical aberrations. The correction radius scales with wavelength, so it is almost twice as large in the K-band as in the J-band. The cross-like structures centered on T Tau N are light diffracted by the telescope's secondary mirror

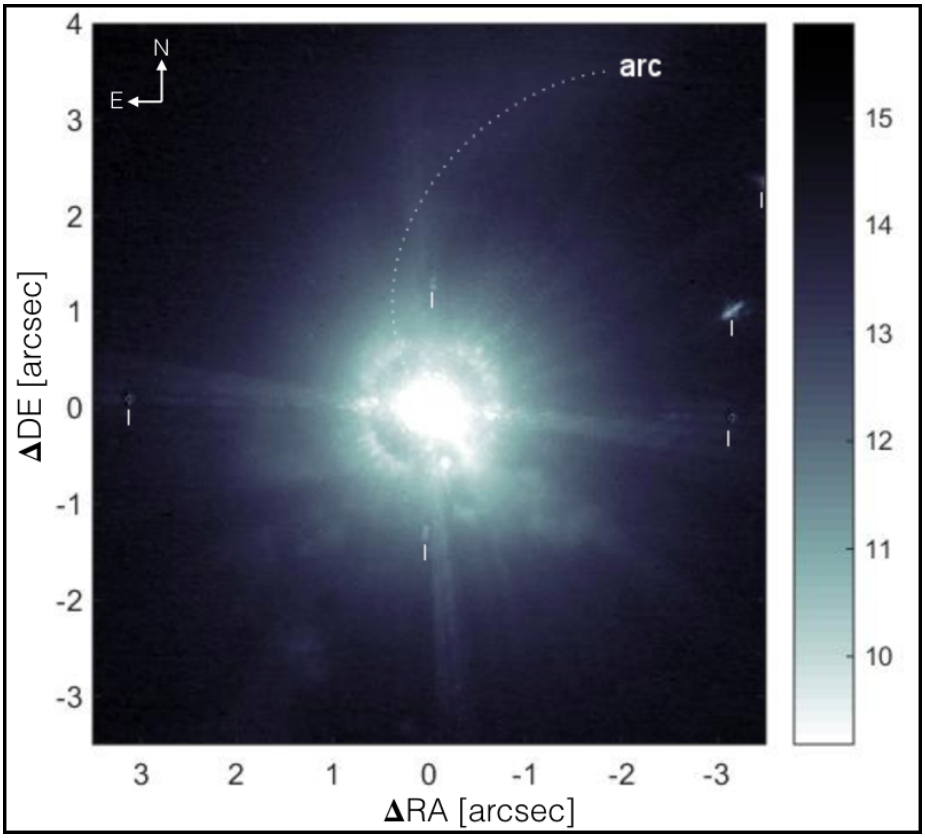


**Figure 5.3:** T Tau in J-band extended emission. The image is displayed with a logarithmic colour scale showing the flux level in magnitudes per square arcsecond. The dotted arc indicates the northern arm of the reflection nebulosity discussed by Stapelfeldt et al. [122]. The image also contains several artefacts created by the narrow-band filters (indicated by the vertical white lines) and by the AO correction (see text). [This image is adapted from our paper [66], with slight modifications.]

support spiders.

In the larger field of view in Figure 5.3, we detect an arc of reflection nebulosity with an approximate symmetry axis toward the West-Northwest. The northern arm of this arc is traced by the dotted line. This arc was first imaged with the HST in the F555W, F675W, and F814W filters by Stapelfeldt et al. [122], who interpreted it as scattered light within an illuminated, axisymmetric outflow cavity in a circumbinary envelope, viewed ~45° from the outflow axis. It is readily seen in the J-band image, but we can no longer detect it in K-band (Figure 5.7).

Also very prominent is a new structure stretching to the Southwest of T Tau N and resembling a coil. We trace it outwards to about 2.5" or 370 AU projected on the sky at the distance of T Tau. The coil is most easily seen in J-band, but is also detected in the K-band. The dashed line

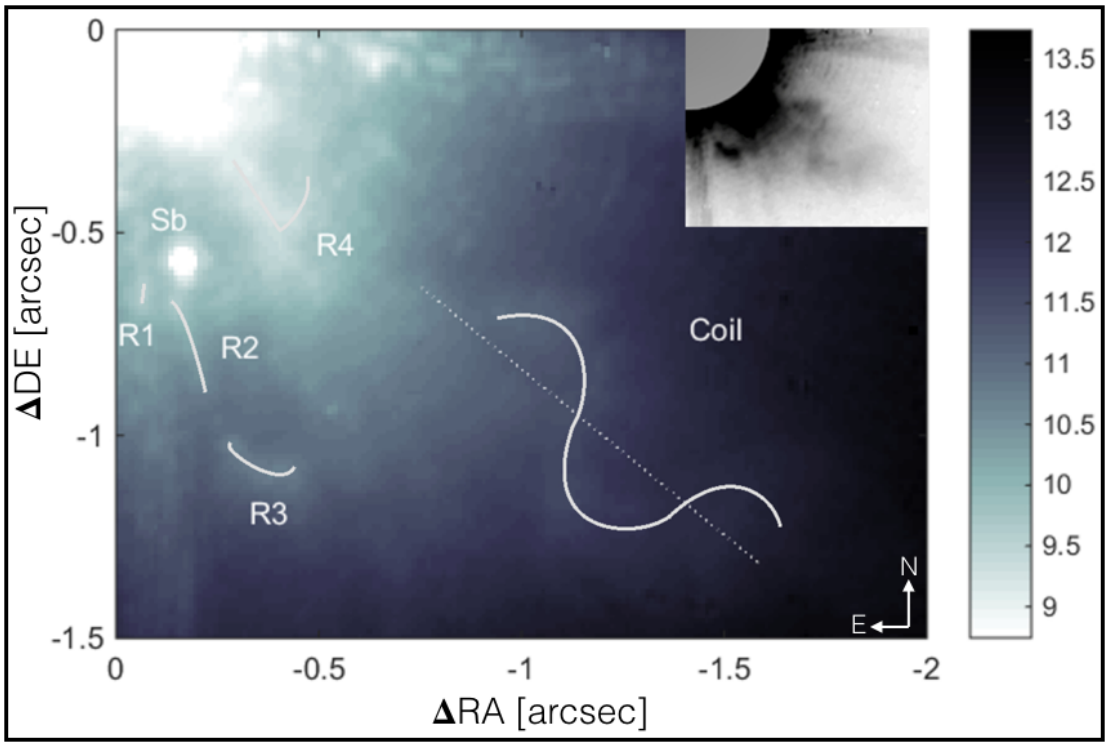


**Figure 5.4:** Zoom on the area Southwest of T Tau N of Figure 5.3, showing the coiling structure and the new reflection nebulosity features R1-R4 in the vicinity of T Tau S. The dashed line connects the inflection points of the coil and points back to the vicinity of T Tau N. The image tile in the upper right corner shows the same area after subtracting a radial fitted exponential in the outer part of the image to visually enhance the contrast of R3 and the coil. [This image is adapted from our paper [66], with slight modifications.]

in Figure 5.4 connects the inflection points of the coil, and points back to the vicinity of T Tau N at a position angle of ~230°.

The images also show several previously undetected features in NIR continuum emission, strongly suggesting that we are seeing reflection nebulosity. In Figure 5.4, we label these reflected light features R1-R4 to differentiate them from the $H_2$ emission features reported by Herbst et al. [51] (see Figure 5.1) and Gustafsson et al. [46] (see Figure 5.2). The inner ~0.65" shows a feature, labeled R4, that resembles a short, rather straight line ending in a bow. It is most easily seen at longer wavelengths in the H- and K-bands (see Figure 5.6 and Figure 5.7), and appears near the location of the $H_2$ features 4, 5, and 6 (see Figure 5.2) of Gustafsson et al. [46] and C2 (see Figure 5.1) of Herbst et al. [51].

In the J- and H-bands, the structure R2 resembles a line ~250 mas long pointing to the South from the current position of T Tau Sb. The morphology of R2 changes significantly in the K-

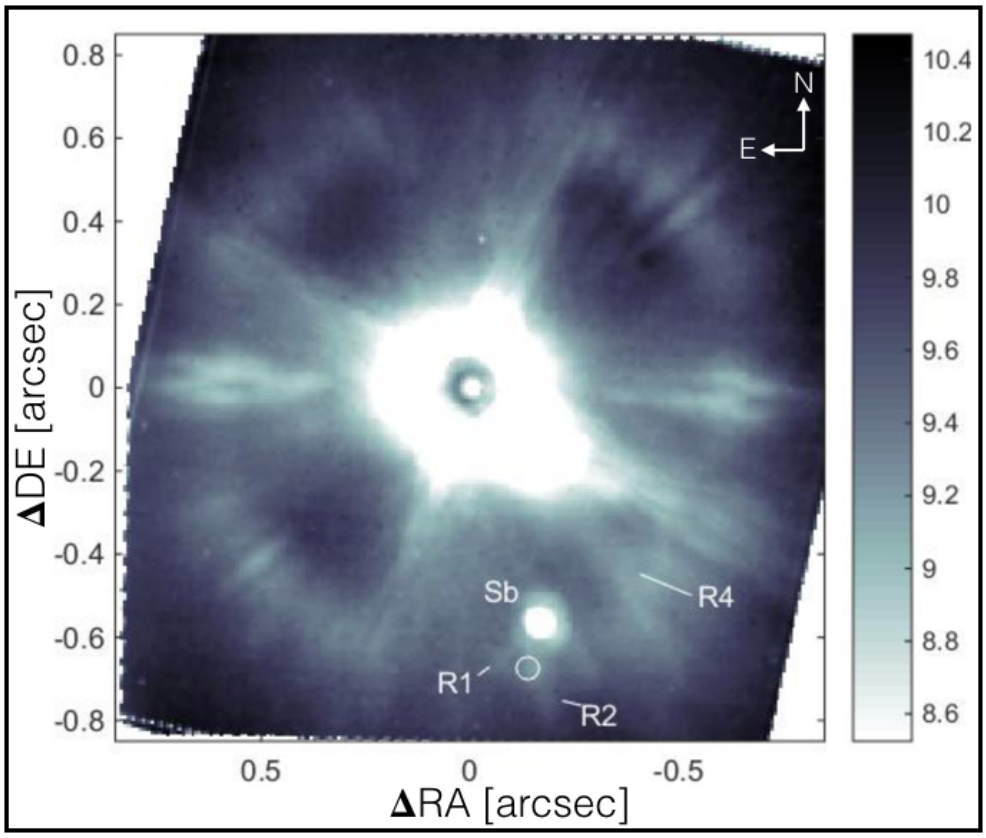


**Figure 5.5:** Coronagraphic J-band (1140-1350 nm) image obtained with the IFS displayed in a logarithmic colour scale showing the flux level in magnitudes per square arcsecond. The small circle indicates the position of T Tau Sa as seen at longer wavelengths. Note the faint extended ring at the AO correction radius. [This image is adapted from our paper [66], with slight modifications.]

band, where we can no longer detect the South-pointing line, but instead see a small structure of extended emission already reported by Csépány et al. [28]. Note that Csépány et al. also used the same Science Verification data. After a small gap of ~150 mas without a detection of significant emission, R2 appears to pass into the more prominent structure R3, roughly half an arcsecond South of T Tau S. R3 curves away toward the West (see Figure 5.4) and it appears near the location of $H_2$ feature 3 (see Figure 5.2) reported by Gustafsson et al. [46].

In the J-band, we also detect a small knot of spatially unresolved emission (R1) about 80 mas East of R2. This faint feature is seen with both instruments, IRDIS (Figure 5.4) and IFS (Figure 5.5). In the H-band (Figure 5.6), R1 appears as a flux enhancement within the first Airy ring of the PSF of T Tau Sa. We note that the similar region of the PSF of T Tau Sb does not show this enhancement.

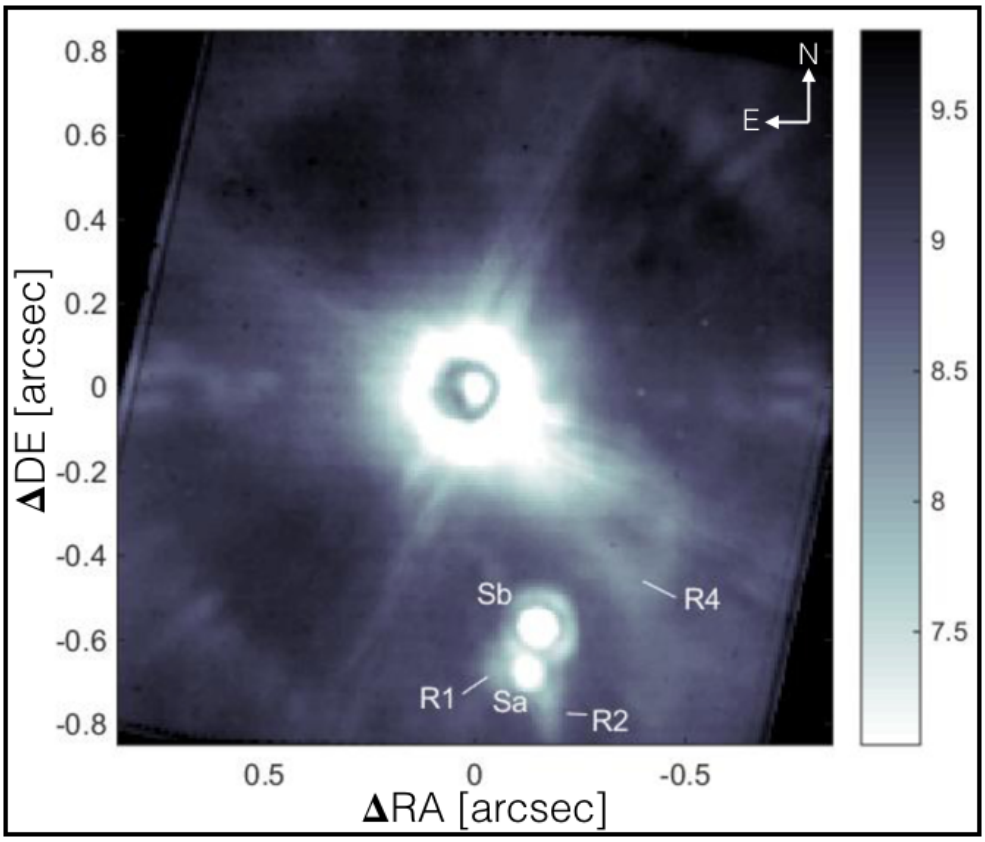


**Figure 5.6:** Coronagraphic H-band (1490-1640 nm) image obtained with the IFS displayed in a logarithmic colour scale showing the flux level in magnitudes per square arcsecond. The correction radius ring lies at the edge of the frame. [This image is adapted from our paper [66], with slight modifications.]

While point-like emission from T Tau Sa is readily detected in the H-band, the star is no longer seen in the J-band at the position where it appears at longer wavelengths (indicated by the white circle in Figure 5.5). The shortest wavelength at which we can still see emission from T Tau Sa is 1.425 $\mu$m.

### Molecular hydrogen line emission

Figure 5.8 shows $H_2$ line emission from the close vicinity around T Tau. The image was created by subtracting the Br$\gamma$ (2.167 $\mu$m) image from the $H_2$ (2.122 $\mu$m) image. The Br$\gamma$ emission originates from the immediate vicinity of the stars and is not spatially resolved in published imagery or in our data, so it is a good proxy for a continuum filter image next to $H_2$. As the Airy pattern scales with wavelength, even the small difference of 45 nm between the two narrow-band

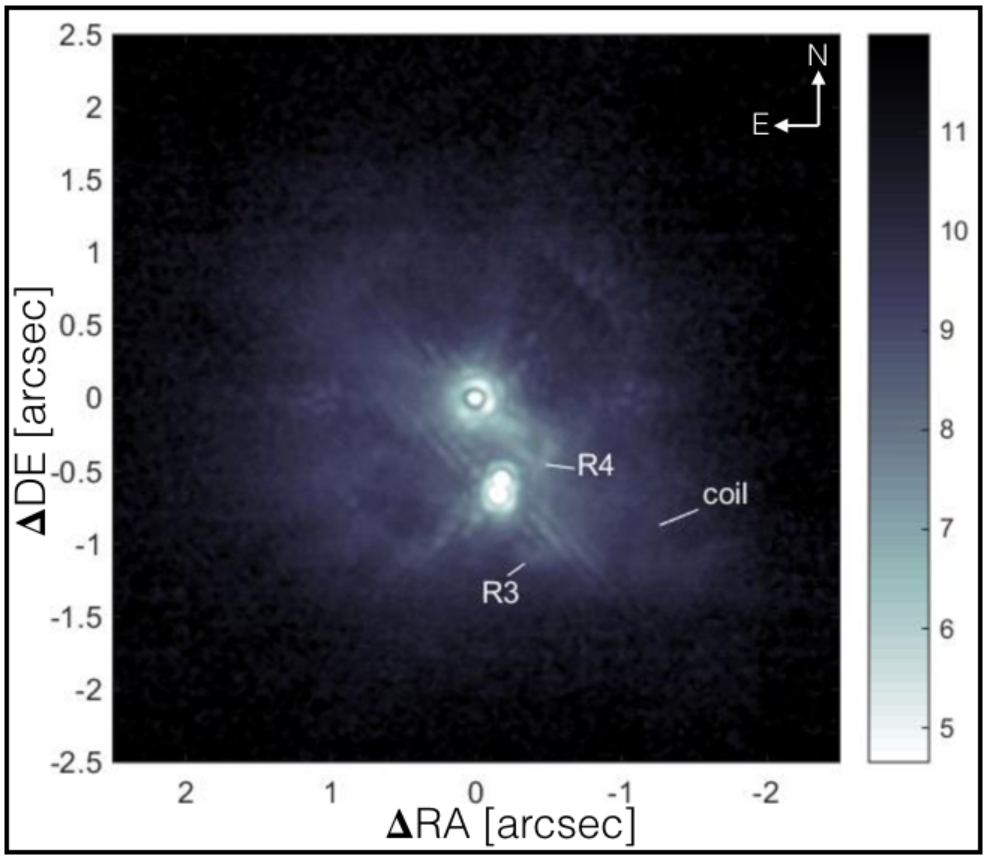


**Figure 5.7:** Coronagraphic K1-band image of T Tau displayed in a logarithmic colour scale showing the flux level in magnitudes per square arcsecond. T Tau N is masked by the ALC coronagraph. [This image is adapted from our paper [66], with slight modifications.]

filters leaves significant Airy ring residuals after subtraction. Also, the spectral width of the filters of 31 nm FWHM is much broader than the intrinsic line widths of less than 1 nm [32], thereby transmitting continuum flux and reducing the sensitivity to line emission. Finally, the observations in the two filters are separated in time by about ten minutes, during which time the telescope rotated with respect to the sky. Therefore, the cross-like structures with T Tau N in the center, produced by the M2 support structure diffraction residuals, is rotated as well and does not subtract out. These shortcomings lead to higher image residuals than achievable with a high spectral resolution IFS (line and continuum emissions are taken simultaneously), and do not allow us to obtain a high SNR $H_2$ image in the immediate vicinity of the stars. Nevertheless, the SPHERE narrow band imaging data clearly show spatially resolved $H_2$ near T Tau.

We readily identify the well-known $H_2$ region T Tau NW discussed by Herbst et al. [50, 51] in our data. It has moved further to the Northwest with respect to the stars when compared to its position in 2002 [51]. The apex of T Tau NW is now located at ~2.8" and position angle ~328°

from T Tau N.

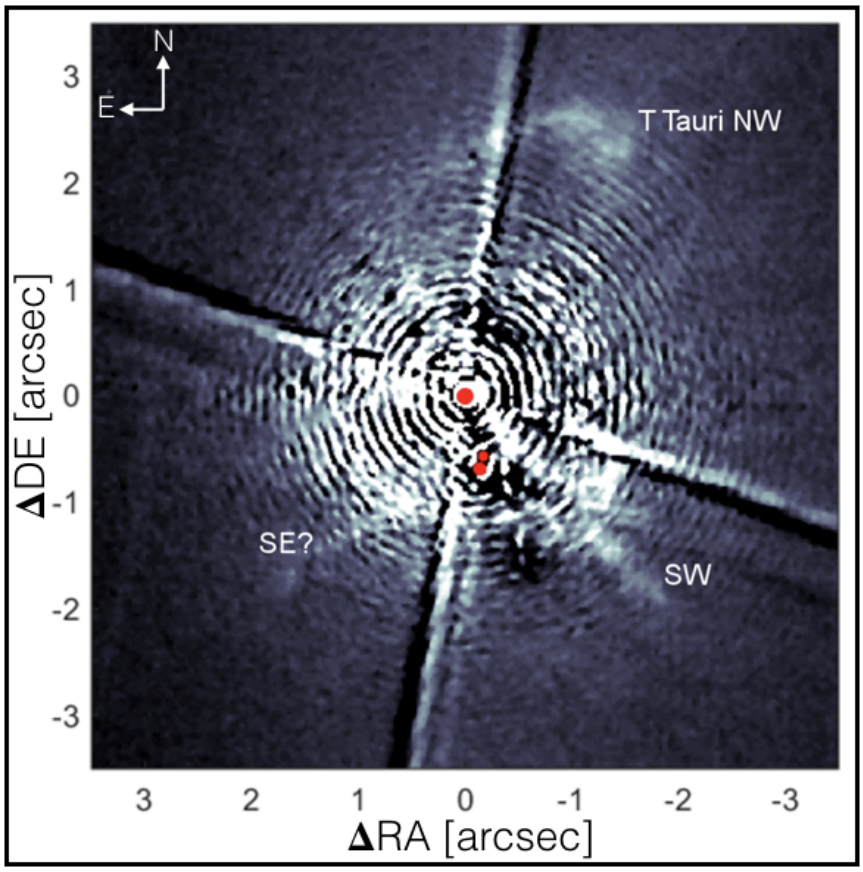


**Figure 5.8:** $H_2$ line emission near T Tau. The stars are indicated by the red circles. The arc/ring-like artefacts are due to the mismatch in wavelength between the two narrow band images and are made prominent by the grayscale stretch which has been adjusted to show the low surface brightness $H_2$ features. The well-known arc, T Tau NW, can be clearly seen. Also, a Southwest (SW) knot is seen near to the Southwest coiling structure (as seen in reflected light (see Figure 5.3)), but the features do not overlap. A similar extended feature with poor SNR pointing from T Tau S to the Southeast (SE) is noted as well. [This image is adapted from our paper [66], with slight modifications.]

Figure 5.8 also shows a knot of $H_2$ emission about 1.4" West and 1.5" s Southouth of T Tau N. Its position is similar to that of feature U reported by Herbst et al. [51]. At a position angle of 223±1°, this SW knot is also near to the coiling structure seen in reflected light (Figure 5.3), but the features do not overlap. The $H_2$ flux density of this SW knot is similar to that of T Tau NW, and it extends somewhat farther to the SW at lower intensity. There may be another similarly extended feature pointing from T Tau S to the Southeast at a PA of 119±1°, but the signal-to-noise ratio is too low to say this with certainty.

### 5.2.3 Analysis of the SPHERE data

#### Southwestern coiling structure and feature R4

Our data reveal a coiling structure to the Southwest of T Tau N, which can be traced from ~1" out to ~2.5", or from 150 to 370 AU projected on the sky at T Tau. It is apparently reflected light, since it is most prominent in the continuum J-band (shorter wavelength) and not visible in $H_2$ line emission. The coiling structure should correspond to areas of enhanced density of ambient matter illuminated by the stars. A line drawn through the inflection points of the coil points to the vicinity of T Tau N. The spatial length of one period of the coil is ~0.73" or ~108 AU projected at T Tau.

The coiling structure is reminiscent of that produced by the precessing jet of the pre-planetary nebula IRAS 16342-3814 [109]. In their paper, Sahai et al. argue that the IRAS 16342-3814 jet beam is not seen directly, but rather via its interaction with the ambient circumstellar medium, i.e., imprinting on the expanding shell, which produces a compressed structure of enhanced density in the shape of a corkscrew. Generally, a precessing outflow could be the consequence of a binary system, caused either by orbital motion of the outflow's source or by outflow precession due to tidal effects. In the first case, the precession period would be the binary's orbital period, while it would be much longer in the latter case.

Interferometric observations of T Tau N with a spatial resolution of a couple of milli-arcseconds [1] exclude the presence of a stellar companion to T Tau N with an orbital separation greater than a few tenths of an AU. The orbital period of a binary tighter than this would be measured in tens of days. Interestingly, Ismailov et al. [58] found periodic variation in spectral features of T Tau N on a timescale of 33 days that are not yet understood. In order to move by one cycle of the coil, or ~108 AU, in some tens of days, the interstellar medium would have to expand at a velocity of several thousand km/s, which is an order of magnitude higher than typical outflow velocities. We can therefore exclude that orbital motion of a tight binary in T Tau N is the origin of the coiling structure.

The actual oscillation period can be crudely constrained from the time interval required by the compressed material to traverse one period of the coiling structure, i.e., ~108 AU, projected on-sky. Assuming that we see the structure moving in the same direction as the spatially nearest $H_2$ features 5 and 6 of Gustafsson et al. [46] at an inclination ~20°, only about one-third of the motion is in the plane of the sky. Making the further assumption that the compressed material expands at a velocity ~50-100 km/s, a typical value for outflows from TTS, the coils would be seen moving by ~3.5-7 AU or ~25-50 mas/year. The resulting precession period would be of the order of 15-30 years. At larger inclination angles, if the outflow would be close to the plane of the sky, the projected motion could be up to three times larger and the precession period up to

three times shorter.

A period of 15-30 years could still be consistent with axial precession within a tight binary in T Tau N. Young stars are rapid rotators and are expected to show significant flattening. T Tau N itself has a rotation period of 2.8 days [54], which is one order of magnitude shorter than that of the Sun. As the precession period is inversely proportional to orbital distance cubed, and scales linearly with the flattening [131], axial precession rates of the order of a few tens of years can occur in a young and tight binary system.

Another explanation for the coiling structure could be a jet-like outflow launched from within the T Tau S system and imprinting on the cavity carved by another outflow, e.g., the cavity of the Northwest outflow from T Tau N, which has been proposed by Stapelfeldt et al. [122]. In this case, the orbital period for the T Tau Sa-Sb binary of 27±2 years [73] would be in good agreement with the predicted period of the coils.

Closer in toward T Tau N, the coiling structure appears to connect to the reflection nebulosity feature R4 (most prominent in the H- and K-band, see Figure 5.6 and Figure 5.7). Feature R4 is a rather straight line pointing from T Tau N to the South-West, where it merges at ~630 mas from T Tau N (or West-Northwest of the current position of T Tau Sb) into a bow. The straight part is too short to exclude that it actually has a curvature similar to that observed in the coiling structure. Feature R4 is seen near the location where Duchêne et al. [32] and Gustafsson et al. [46] (features 5 and 6) detected blue-shifted $H_2$ emission, and where Herbst et al. [51] placed the feature C2. Gustafsson et al. [46] found no proper motion of these features during a time-span of two years and suggested that the flow is hence moving mostly toward the observer and is seen at the low inclination (~20°) of T Tau N. The bow morphology of R4 pointing toward T Tau N provides further evidence that the features observed in the area are indeed produced by the T Tau N outflow.

**Molecular hydrogen emission : T Tau NorthWest and the SouthWest outflow**

$H_2$ line emission arises in a number of physical processes, the most common of which are shock excitation and UV fluorescence. T Tau is an interesting case in which both mechanisms occur [127]. The flux ratios between the 1-0 S(1) and 2-1 S(1) lines can help to discriminate between the two, with higher ratios favouring shock excitation [18]. Herbst et al. [50] determined a ratio of >15 for T Tau NW, which argues strongly for shock excitation as the dominant mechanism. In addition, its classical Herbig-Haro bow shock morphology unambiguously suggests a terminal shock arising from a stellar outflow [51].

Comparing our new 2014 data [66] to the 2002 NACO image of T Tau NW [51], we can

attempt to determine which star triggered the corresponding outflow. For this, we first matched the plate scales of the NACO and SPHERE images. Then, we created two sketches (one for 2002 and one for 2014) by drawing circles centered on T Tau N and Sa and by drawing the outline of T Tau NW by eye. From these, we finally created the two overlays shown in Figure 5.9. In the overlay shown on the left, the 2002 and 2014 sketches are depicted as moving away from T Tau Sa, while the overlay on the right shows the situation if T Tau N were the center.

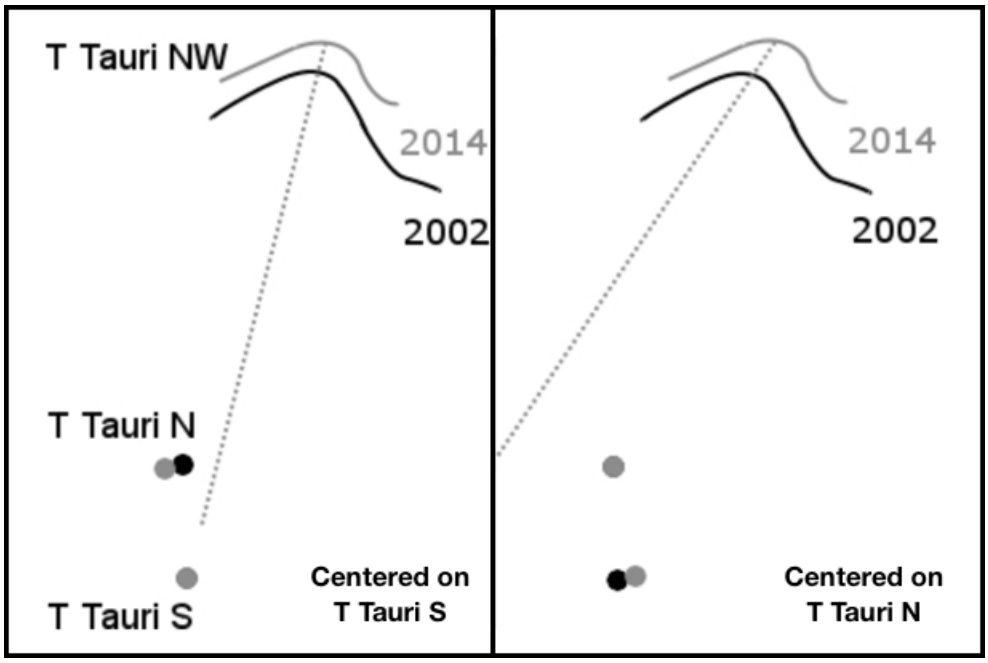


**Figure 5.9:** Overlay of the relative positions of T Tau NW, T Tau N, and T Tau Sa in 2002 (Herbst et al. [51]) and 2014 (our data [66]). These drawings were made by re-centering. The left panel shows the result when using T Tau Sa as the centering reference, while the right panel uses T Tau N. [This image is adapted from our paper [66].]

In the launching star's rest frame, the motion of T Tau NW should point directly away from the star, if accelerated orbital motion can be neglected. This is a reasonable approximation, as long as the time since the ejection of the T Tau NW outflow is small compared to the orbital period of the T Tau N/S binary of $4200^{+5000}_{-3400}$ years [73]. Figure 5.9 then strongly suggests that the T Tau NW outflow is launched from within the T Tau S system, because the motion of T Tau NW points to T Tau Sa in its rest frame (left panel). Instead, in the rest frame of T Tau N (right panel), the motion of T Tau NW points to a position well East of the stars. The accuracy of this qualitative analysis is, however, not sufficiently high to differentiate between T Tau Sa and Sb as a possible origin of the T Tau NW outflow.

T Tau NW has moved by about 200 mas at a position angle of ~345° from T Tau Sa between

2002 and 2014. This corresponds to an average velocity of ~17 mas/year or ~12 km/s perpendicular to the line of sight over the past 12 years. As the radial velocity of $H_2$ emission from T Tau NW is quite small with values between ~-3 km/s [53] and ~-7 km/s [46] with respect to the stars, T Tau NW moves at ~12-14 km/s with an inclination angle of ~60-75°. This is in good agreement with the SE-NW outflow inclination of ~70° derived by Gustafsson et al. [46] in the area Southeast of T Tau S. The inclination is, however, not consistent with the nearly face-on orientation of T Tau N [53, 54], providing further evidence that the T Tau S system is the source of the SE-NW outflow.

Figure 5.8 also shows an area (labelled SW) of enhanced $H_2$ emission resembling a knot merging into a straight line pointing to the Southwest of T Tau N at a position angle of 223±1°, similar to the direction of the coiling structure seen in reflected light (PA~230°). This $H_2$ emission could represent shocked material along a fast flow periphery where projected velocities are low enough to generate $H_2$ line emission efficiently as discussed by Herbst et al. [53]. Our SW $H_2$ emission is an extension to the line formed with the clumps of $H_2$ emission observed in the area Northwest and West of T Tau S by Duchêne et al. [32] and Herbst et al. [51]. These features were rather stationary over several years and blue-shifted, i.e., moving toward the observer [5, 46]. These features could therefore all belong to the same outflow launched by T Tau N. In addition, the close spatial match of our detected $H_2$ emission with the coiling structure to the South-West of T Tau N, suggests that it is associated with the same outflow as well.

### 5.2.4 Summary of the SPHERE data

With the SPHERE narrow-band imaging and integral field spectroscopy data, we have taken another step toward understanding the enigmatic T Tau System.

The newly detected coiling structure to the Southwest is a reflection nebulosity seen at NIR wavelengths, suggesting that it is ambient circumstellar medium compressed by a precessing jet in the shape of a corkscrew. The spatial period of the coils suggests a precession period on the order of 15 to 30 years, provided that the outflow is seen at a relatively high inclination. We identify two mechanisms which could produce such a precession period: (1) axial precession in a very tight (semi-major axis smaller than a few tenths of an AU) T Tau N binary system; or (2) orbital motion of the T Tau Sa/Sb binary, whose period of 27 years is in good agreement with the expected time span. The present data, however, do not allow us to unambiguously identify the star launching the coil-producing jet.

Toward T Tau N, the coiling structure appears to connect to the reflection nebulosity R4, which resembles a straight line merging into a bow. The orientation of the bow provides evidence that we see the effect of the T Tau N outflow. This conclusion is supported by the location of R4 near

previously detected $H_2$ emission features, which are seen at relatively low inclination to the line of sight, consistent with an outflow from T Tau N. Near the coiling structure to the Southwest, we detect a knot of $H_2$ emission merging into a straight line, which could represent shocked material along a fast flow periphery where projected velocities are low enough to generate $H_2$ line emission efficiently.

The well-known $H_2$ emitting region T Tau NW is readily detected in our narrow-band data. The comparison of the positions of T Tau NW with respect to T Tau N and T Tau S between 2002 (Herbst et al. [51]) and our 2014 data [66] provides further evidence that the Southeast-Northwest outflow triggering T Tau NW is likely to be associated with T Tau S. Over the past decade, it has moved with average velocity of ~12 km/s perpendicular to the line of sight at a position angle of 345° with respect to T Tau S.

## 5.3 Observations with LBT-LUCI

This section presents observations of the T Tau System using the LUCI instrument, our results, and their interpretation. Unlike the SPHERE project, which was collaborative work with a colleague at ESO, I have done almost all of the LUCI data reduction, analysis and interpretation. The paper is in preparation [112].

### 5.3.1 Observational details

LUCI [119] is the facility near-infrared (0.95 $\mu$m - 2.4 $\mu$m) imager and spectrograph at the LBT. LUCI can work in seeing-limited mode with a 4 arcmin FoV, as well as in adaptive optics imaging and long-slit spectroscopy mode with a 30 arcsec FoV. LUCI uses LBT's First Light Adaptive Optics (FLAO) system [35] to correct atmospheric turbulence. Although not formally an XAO system, FLAO, with its 672-actuator DM, is very capable of providing high-contrast, high-resolution imagery [35].

The T Tau System was observed using LUCI as part of its AO-commissioning on 22 October 2016 and 23 November 2016. As with the SPHERE observations of section 5.2, the visible star T Tau N acted as the AO reference. During the observations, the non-common path aberrations were not corrected. Non-common path aberrations are static optical aberrations present either in the science optical path not seen by the wavefront sensor, or present in the AO optical path not affecting the science channel. The latter will be corrected by the wavefront sensor, however, reducing imaging quality.

Unlike SPHERE, LUCI does not offer coronagraphy. Observations were carried out in field-stabilized mode. Diffraction-limited imaging was acquired for the broad J-band (1250 nm) filter and for the narrow-band filters - $H_2$ (2127 nm) and Br$\gamma$ (2171 nm). Details of the observations appear in Table 5.1. Calibration data (darks, flat field, etc.) were recorded as part of the standard daily calibration.

| **Parameter** | **J-band** | **$H_2$** | **Br$\gamma$** |
|---|---|---|---|
| Wavelength ($\lambda_c \pm \Delta\lambda$) | 1250±301 nm | 2127±23 nm | 2171±23 nm |
| Date of observation | 23 November 2016 | 22 October 2016 | 23 November 2016 |
| Exposure time | 2.6 s | 2.6 s | 2.6 s |
| Co-adds | 24 | 24 | 24 |
| Number of frames | 10 | 18 | 24 |
| Total exposure time | 10.40 minutes | 18.72 minutes | 24.96 minutes |
| Seeing conditions | 0.37” - 0.95” | 0.50” - 1.00” | 0.37” - 0.95” |
| Saturated | T Tau N | T Tau N, T Tau Sa | T Tau N, T Tau Sa |
| Ghosts | 2 or 3 | 1 | 2 or 3 |
| Cross-talk | due to T Tau N | due to T Tau N and T Tau Sa | due to T Tau N and T Tau Sa |

**Table 5.1:** LBT-LUCI observation details on the T Tau

The LUCI science camera uses a Teledyne HAWAII-2RG Mercury Cadmium Telluride detector with (2048 x 2048) pixels and pixel scale of 15 mas/pixel for the AO-imaging mode. This detector is known to have significant persistence and cross-talk. For the read-out, we used Line-Interlaced Read (LIR) mode.

### Persistence

Trapped charges in the detector that are not cleared out completely, even after the detector reset, cause persistence. Persistence manifests itself as an enhanced dark current. This occurs whenever a pixel is exposed to light that exceeds more than about half of its full well capacity. The persistence will start to decay (inversely proportional to time) as soon as the source flux is removed. Smith et al. [121] provide a very clear description of the physics of persistence and the effects in IR arrays.

To diminish the impact of persistence (see Figure 5.11), an A-B-B-A dither pattern (see Figure 5.10) was used, so that the same pixels in each of the quadrants were affected. In other words,

we identified "sacrificial" pixels in the two quadrants of the detector and always placed the bright stars there. Also, in order to avoid possible centro-symmetric ghosts (which are typical of optical systems), the dither locations A and B were chosen to be on the same side of the detector. Also, the dithered images taken close to one-another in time were used to subtract the sky, bias, and dark current simultaneously.

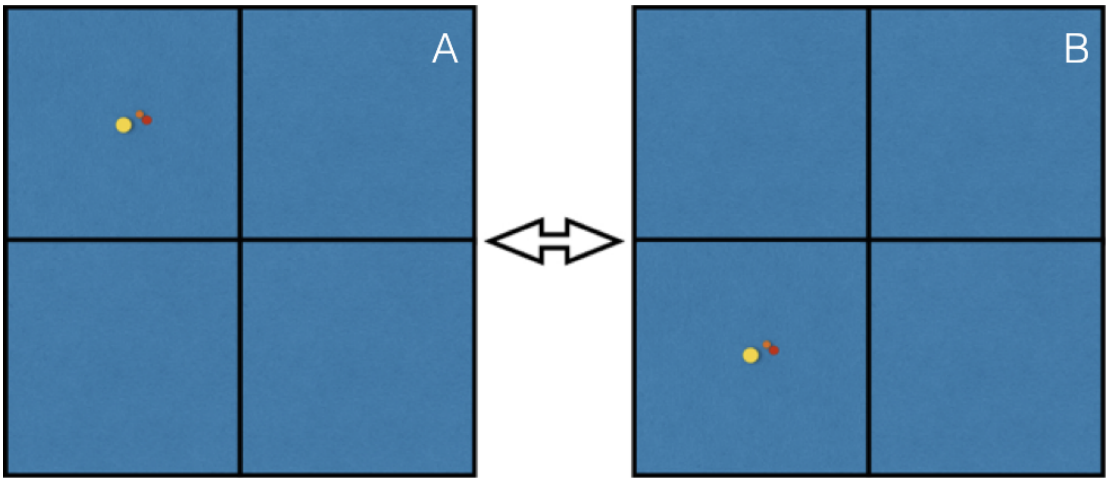


**Figure 5.10:** We followed the dither pattern sketched above. T Tau is placed either on quadrants on the left side (as shown above) or on the right side. Since T Tau is bright, this strategy avoids centro-symmetric optical ghosts.

### Crosstalk

The H2RG detector in LUCI also shows channel crosstalk. The detector is read out by 32 amplifiers in parallel, with each channel 2048 pixels wide and 64 pixels tall. When the detector is read out, a strong signal in one amplifier channel can induce a small signal in some or all of the other 31 channels. This is known as the *channel crosstalk*. The crosstalk appears perpendicular to the detector for position angle (PA) of zero (When the PA is zero, the LUCI detector is oriented in the standard astronomical fashion, with N up and E left).

It is very difficult to completely remove the effect of channel crosstalk. As you can see in Figure 5.11, the effect of cross-talk is dramatic, especially in the Br$\gamma$ (and $H_2$) frames where both T Tau N and T Tau Sa saturate. We call the regions affected by the crosstalk as the "bullet holes". Since we are interested in outflows and features mainly in the North-South direction, we oriented LUCI at PA=-90°. With this orientation, the T Tauri system will appear as shown in Figure 5.10, and the bullet holes will be in the East-West direction as shown in Figure 5.11. We

tried to remove the channel crosstalk in post-processing by masking like ghosts, but this was of limited success.

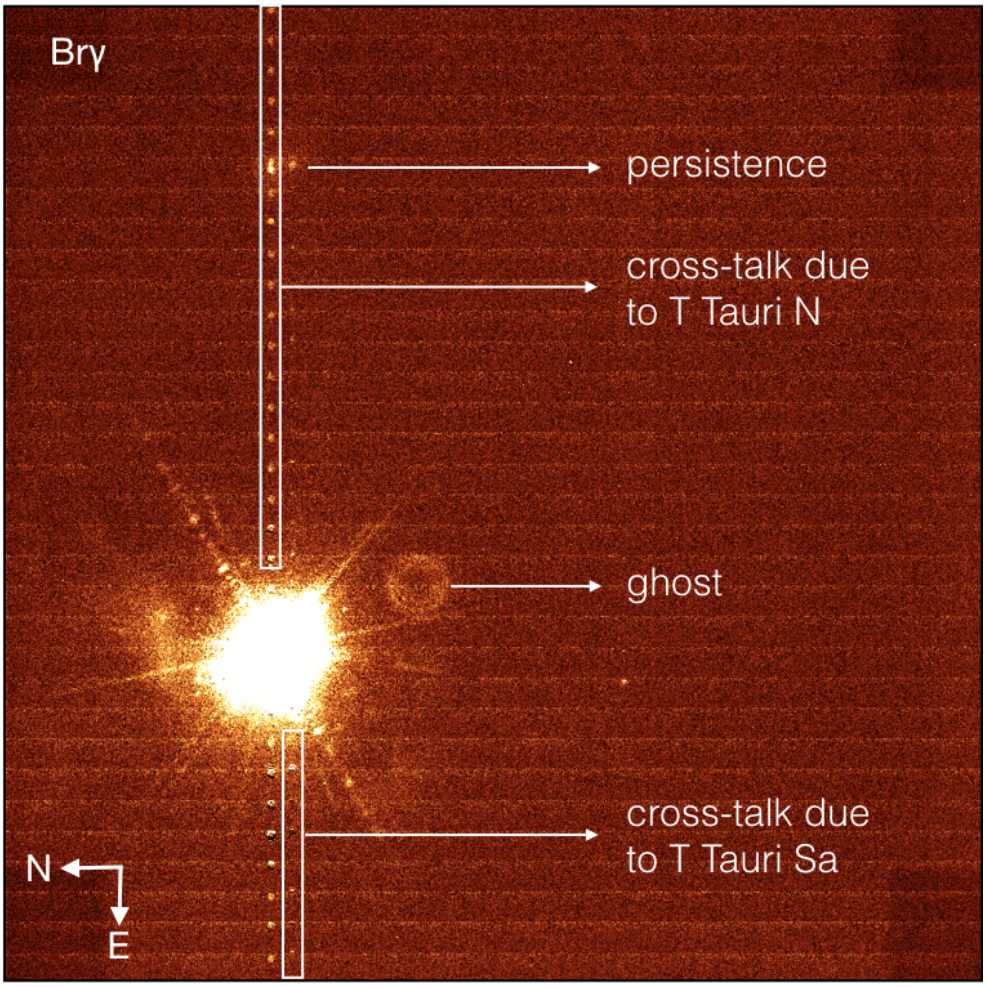


**Figure 5.11:** A raw Br$\gamma$ frame showing the cross-talk, persistence, and a filter ghost.

### Ghosts

Up to three ghosts are present due to T Tau N or due to T Tau N and T Tau Sa, depending on the filters used and in which quadrant the stars are imaged. In Figure 5.11, one ghost is present. The ghosts are removed by masking (see section 5.3.1 below).

**Data reduction**

We followed the normal near-infrared procedure for the data reduction using IRAF. As a first step, bad pixel maps and master flat fields were created using the calibration files and then applied independently to each of the science frames. For the $H_2$ filter, T Tau was placed on the upper-right (UR) or the lower-right (LR) quadrant of the detector. For the J- and Br$\gamma$ filters, T Tau

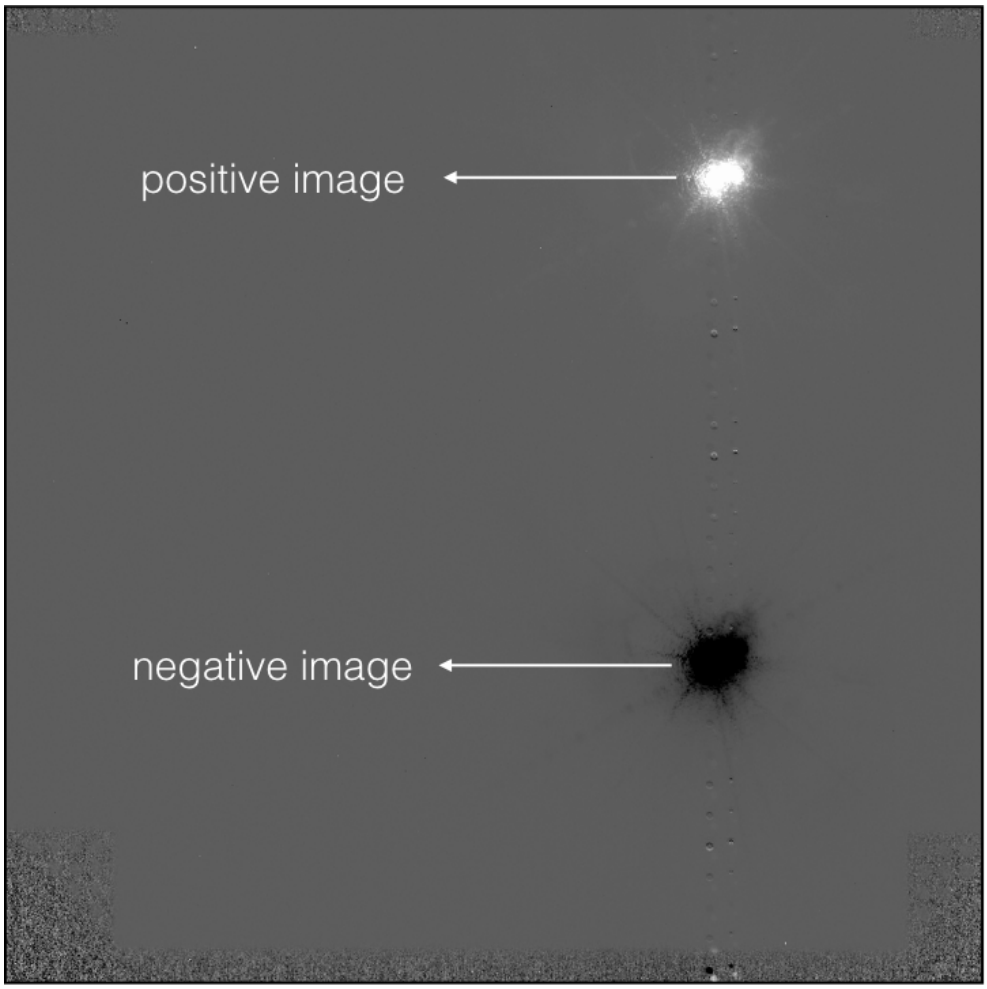


**Figure 5.12:** $H_2$ difference image. Both the positive and negative images of T Tau can be seen, along with the cross-talk.

was placed on the upper-left (UL) or lower-left (LL) quadrant of the detector. To subtract the sky, bias, and dark current, dithered pairs were subtracted. This creates a positive image on one quadrant and a negative image on the other (see Figure 5.12).

For these positive and negative images, mask images were created independently at the lo-

cations of the ghosts and "bullet holes". An example appears in Figure 5.13. The science images were then multiplied by the respective mask images. The resulting frames were then shifted (using bilinear interpolation) to allow averaging, using T Tau Sa/Sb as the reference (for J-band frames T Tau Sa was used, whereas for $H_2$ and Br$\gamma$ frames T Tau Sb was used). The shifted, masked science images and shifted mask images were summed separately (shown in Figure 5.14). The summed, masked science image (left panel of Figure 5.14) was then divided by the summed mask image (middle panel of Figure 5.14) to produce the final filter images (right panel of Figure 5.15). To produce the $H_2$ line emission frame, the normalized (to T Tau Sb flux) Br$\gamma$ final image was subtracted from the normalized (to T Tau Sb flux) $H_2$ final image (see Figure 5.15).

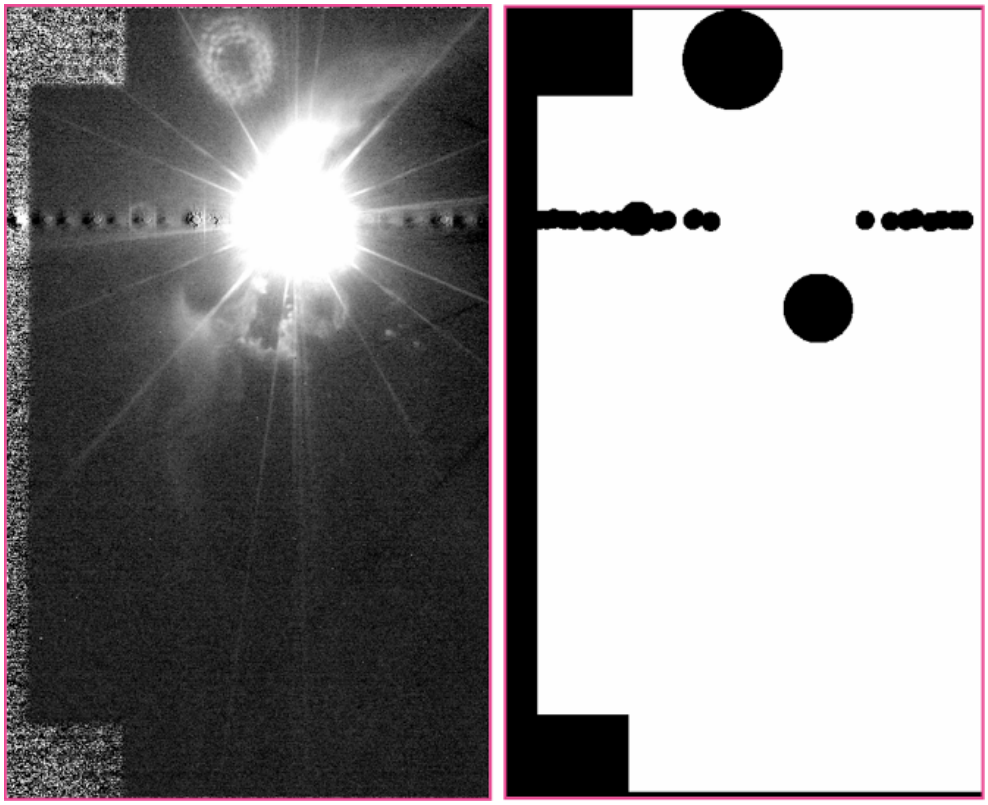

**Figure 5.13:** *left*: Sky, bias, and dark current subtracted J-band T Tau image. *right*: corresponding mask image of the left image. The ghosts, bullet holes and boundary pixels where flat-fielding did not occur are all masked out.

There are many radial lines (positive and negative) in these images. These are due to diffraction from the spiders holding the adaptive secondary and tertiary of the LBT. LBT is an altitude-azimuth telescope, and hence these spikes will rotate with respect to the sky and cannot be completely eliminated. Shifting and summing up produce positive and negative lines (due to

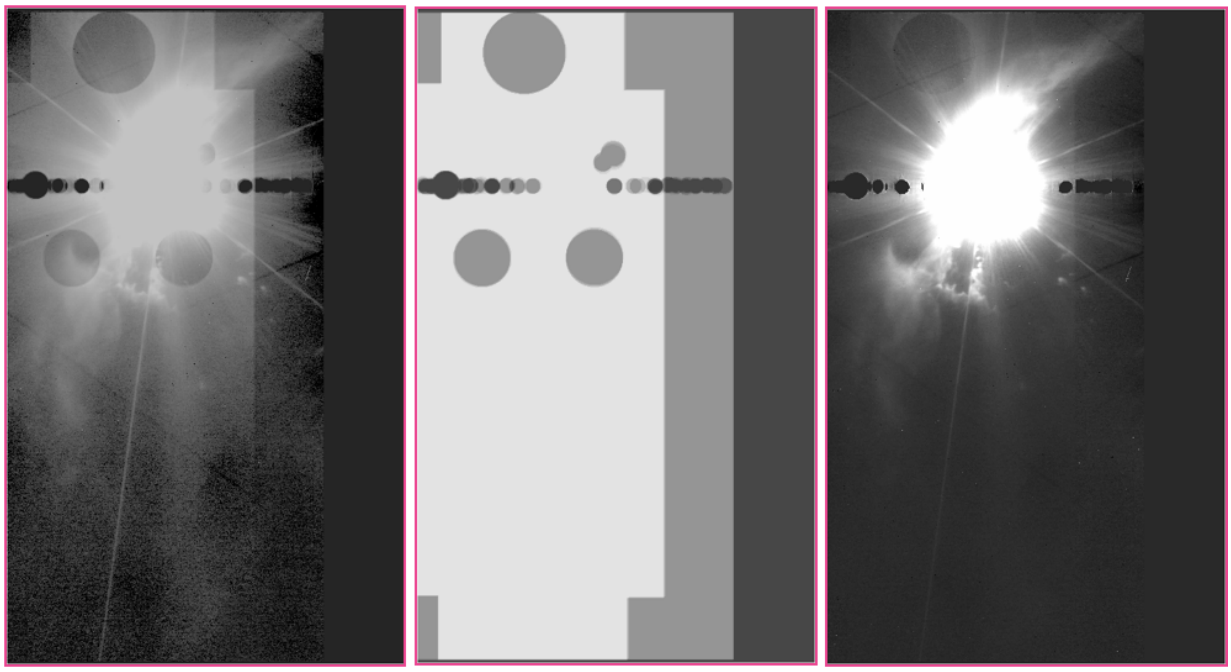

**Figure 5.14:** *left*: Summed masked J-band T Tau image. Images from dither locations A and B were considered (also the respective masks as well). *middle*: corresponding summed mask image of the left image. Note that the values of the masks are different in different regions (different grey scale). *right*: the final image obtained by dividing the left panel image by the middle panel image.

diffraction-spikes) in the final image. Also, in some final images, residuals from the ghost subtraction appear (for example, see the right panel of Figure 5.14), because of the time varying nature of diffraction spikes at the location of ghosts.

### 5.3.2 Results of the LUCI data

#### Continuum Imaging

We can study the continuum emission in T Tau using broad-band J imaging and narrow-band Br$\gamma$ imaging (as it is not spatially extended (see section 5.2.2)). Compared to the SPHERE data, the LUCI data covers a larger FoV. Almost all the features seen with SPHERE also appear in the LUCI observations. In addition, there are some previously unseen features.

The arc of reflection nebulosity, as discussed by Stapelfeldt et al. [122], appears in the J-band image (see Figure 5.16). However, in the Br$\gamma$ image, the arc has lower SNR and somewhat

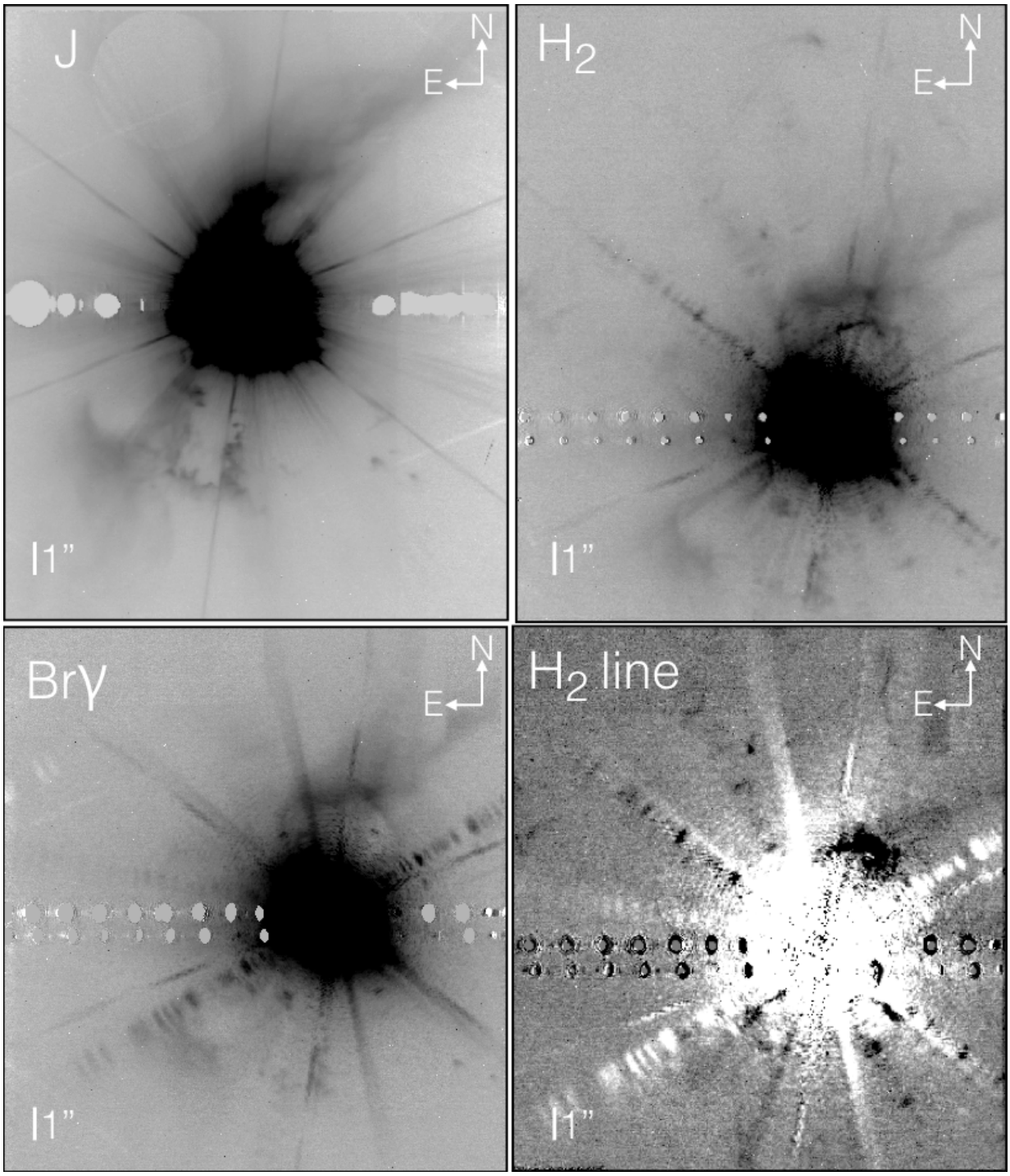


**Figure 5.15:** Reduced images in the J-band, $H_2$ line+continuum, Br$\gamma$, and $H_2$ line. The bullet holes (due to cross-talk) could not be completely removed. Also, in the J-band image, you may note some faint residuals from ghost removal. All the images are displayed in logarithmic grey scale.

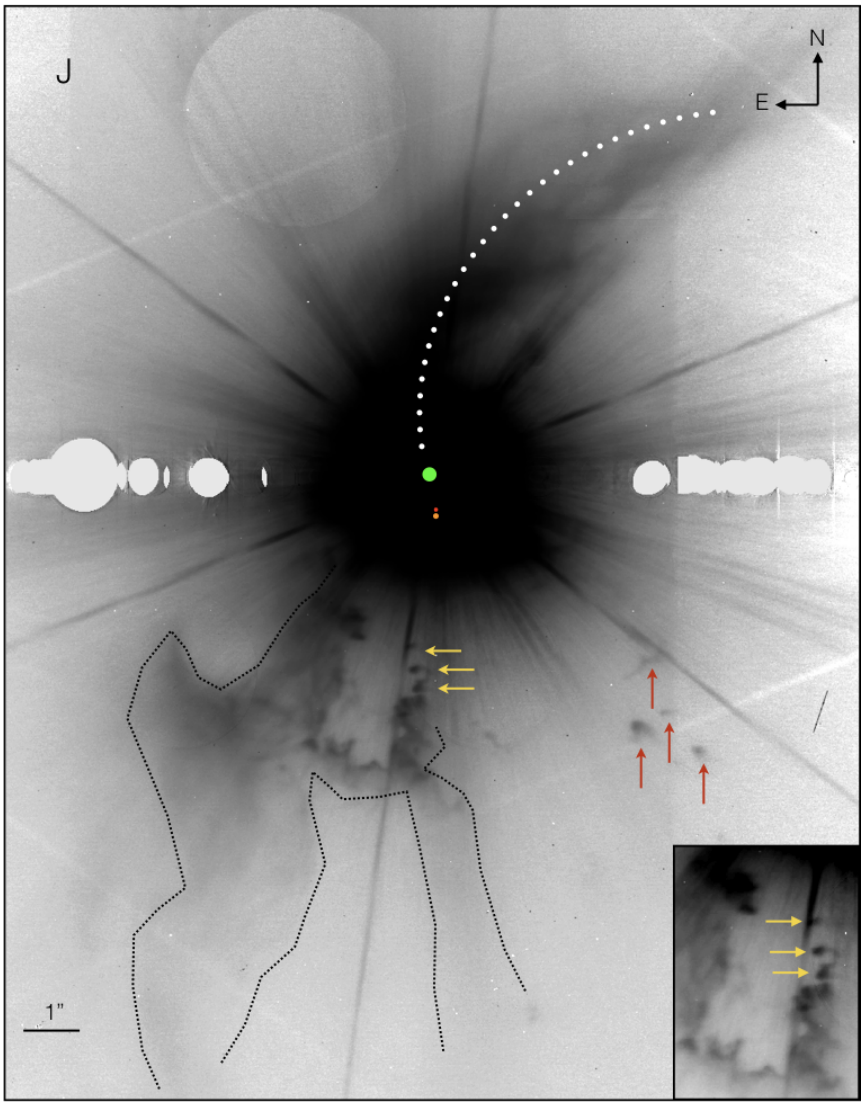


**Figure 5.16:** T Tau broad-band J image displayed in logarithmic scale. The dotted arc indicates the northern arm of the reflection nebulosity discussed by Stapelfeldt et al. [122]. The yellow arrows indicate the tadpole-like feature seen 3.4" almost South of T Tau N. The inset shows the tadpoles and the cavity with a different grey scale cut. This region has high signal-to-noise ratio extended features, enclosed within the black dotted lines. These extended features, along with the "tadpoles" give an impression similar to that of "pillars of creation" in M16, the Eagle Nebula. The green, red, and orange solid dots identify the locations of T Tau N, T Tau Sa, and T Tau Sb respectively.

different morphology. The beginning of the arc is hardly noticeable, but the feature extending to the NW is very distinct (see Figure 5.15).

Not all of the features R1-R4 from SPHERE (see Figure 5.4) appear in the LUCI J-band image. However, the higher SNR features, R2 and R3, are detected (see Figure 5.17). R4 is pretty close to T Tau N and West of T Tau S. The same region in the LUCI image has higher AO residuals (recall that the non-common path aberrations were not taken out during the LUCI observations) and the LUCI frame does not allow the same high contrast in this region as does SPHERE. This could be a reason for not detecting them. To be fair, LUCI is not optimized for high-contrast imaging.

Extended features toward the South-Southeast direction, enclosed within the black dotted lines in Figure 5.16, are detected. Clearly, a cavity pointing toward the stars also appears. Overlaying the J-band image and the $H_2$ image clearly shows that the geometry of the cavity points to T Tau S, although which of the southern stars (Sa/Sb) cannot be deduced. Also, the cavity orientation coincides with our previous conclusion from the SPHERE data that T Tau NW originates from one of the T Tau S stars. The other end of the bi-polar outflow that created T Tau NW may have created this cavity. The matching distances from T Tau S to T Tau NW and to the center of the cavity is another supporting argument.

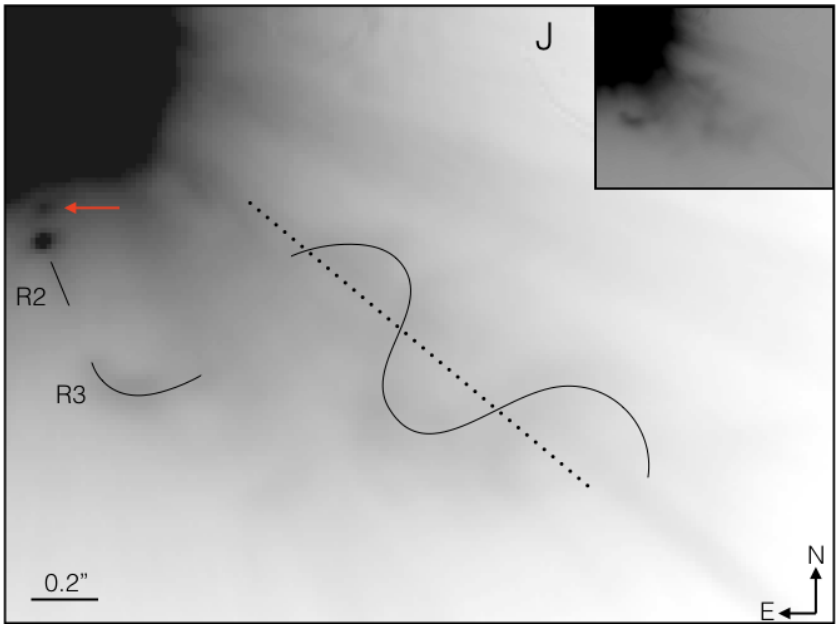


**Figure 5.17:** Zoom on the area Southwest of T Tau N of Figure 5.16 with different cuts showing the coiling structure and the reflection nebulosity features R2 and R3 (as shown in Figure 5.4) in the vicinity of T Tau S. As in Figure 5.4, the dotted line connects the inflection points of the coil and points back to the vicinity of T Tau N. The image tile in the upper right corner shows the same area with different cuts to visually enhance the contrast of R3 and the coil. The red arrow points toward T Tau Sa, imaged here for the first time ever in the J band.

We also detect "tadpole-like" features, indicated by the horizontal yellow arrows in Figure 5.16, toward the beginning of the cavity on the West side (they are clearer in the inset image of Figure 5.16). We are exploring the nature and origin of the tadpoles and extended features. Together, they give an impression similar to that of the "pillars of creation" in M16, the Eagle Nebula.

Other new features include the knots, linear feature, and bow-shaped feature in the J-band image toward the South-West of the stars, marked by the red arrows in Figure 5.16. All these features point toward T Tau N and lie in the same direction as, but further away than the South-West coiling structure discussed in section 5.2.3. The knots appear to have a morphology similar to that of proplyds discovered in the Orion nebula [106], but of course, the near environment of T Tau is not nearly as extreme.

The South-West coiling structure outflow detected in the SPHERE data also appears in the LUCI J-band data. Figure 5.17 shows the zoomed in image of Figure 5.16 with a different cut, showing the South-West coiling outflow (the black curve). The dotted line connects the inflection points of the coil, which again points back to T Tau N. The inset image shows a harder cut, making the SW outflow more easy to visualise.

The first ever detection of T Tau Sa in the J-band can also be seen in Figure 5.17; its location is marked by the red arrow. However, we do not see any evidence of unresolved emission pointing to its possible circumstellar disk. Note that Kasper et al. [66] predicted an edge-on disk for T Tau Sa.

In the narrow band Br$\gamma$ image, displayed in Figure 5.18, a crown-like feature North of T Tau N is clearly detected, marked by the white dotted lines. Looking at the $H_2$ image in Figure 5.15, clearly this crown feature is further North than T Tau NW. Although not directly visible in the J-band image, the crown lies within the Stapelfeldt arc of reflection nebulosity (see Figure 5.15). The Br$\gamma$ image also shows the tadpole-like features, the cavity, the SW knots, and arc with lower SNR.

### Molecular hydrogen emission

The T Tau $H_2$ line emission, shown in Figure 5.19, is obtained by subtracting the Br$\gamma$ image (as continuum) from the $H_2$ image. The fact that the Airy pattern scales with wavelength, and the two observations were a month apart and at different hour angle unfortunately results in quite a lot of diffraction residuals. Therefore, the previously unseen features seen radially away from the T Tau Stars are not considered for the study here. To aid visualisation, the $H_2$ line emission features are marked in different colours and pointed to by a black arrow in Figure 5.19.

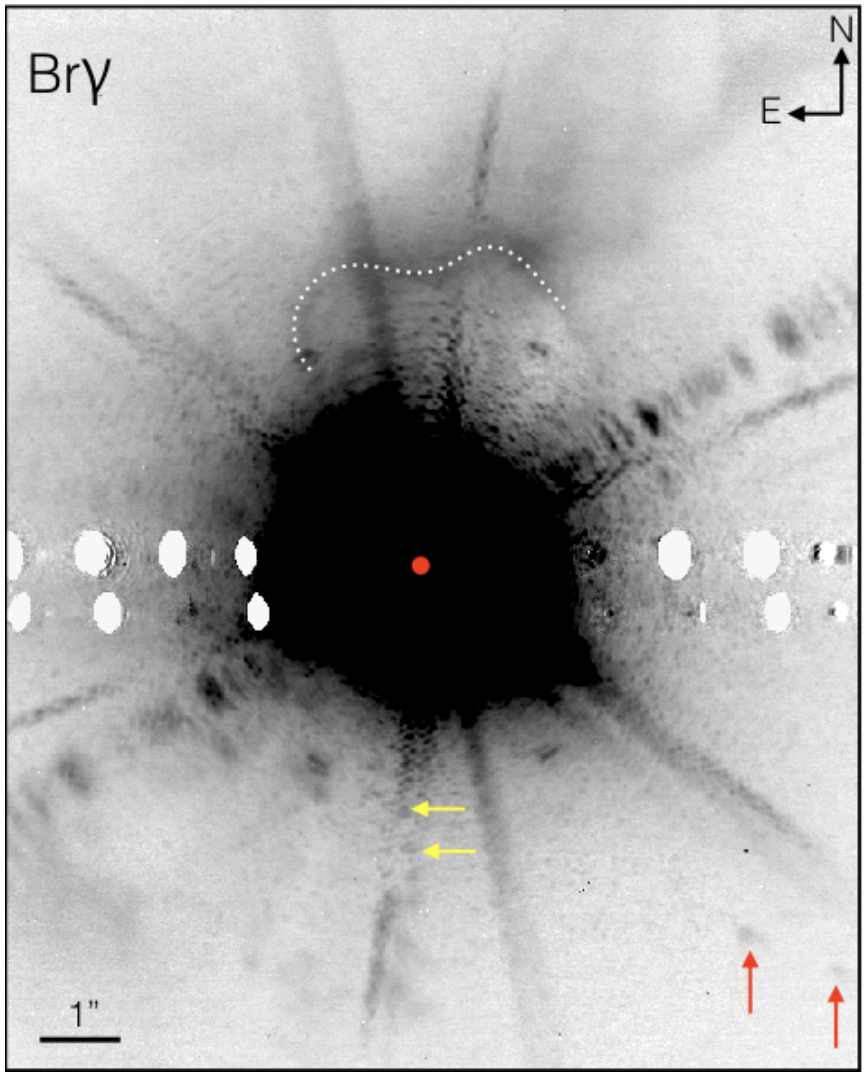


**Figure 5.18:** Narrow band Br$\gamma$ image of T Tau. The white dotted lines represent the crown feature observed. Note that this feature does not appear in the J-band image. The tadpole-like features and knots are detected with low SNR, and are marked by the yellow and red arrows respectively. Also, the extended features to the South-Southeast direction and the cavity are barely visible.

The feature within the blue solid lines and indicated by the blue arrow is not real, but rather an artefact from the continuum subtraction.

T Tau NW is clearly detected, and is marked within the cyan dotted lines (in Figure 5.19). Unlike in previous detections, T Tau NW has a clear hook-like feature curving toward the East, and this hook feature has rather low SNR. This could be due to different relative velocity within the material in the West part of the feature. This argument is supported by the fact that we found

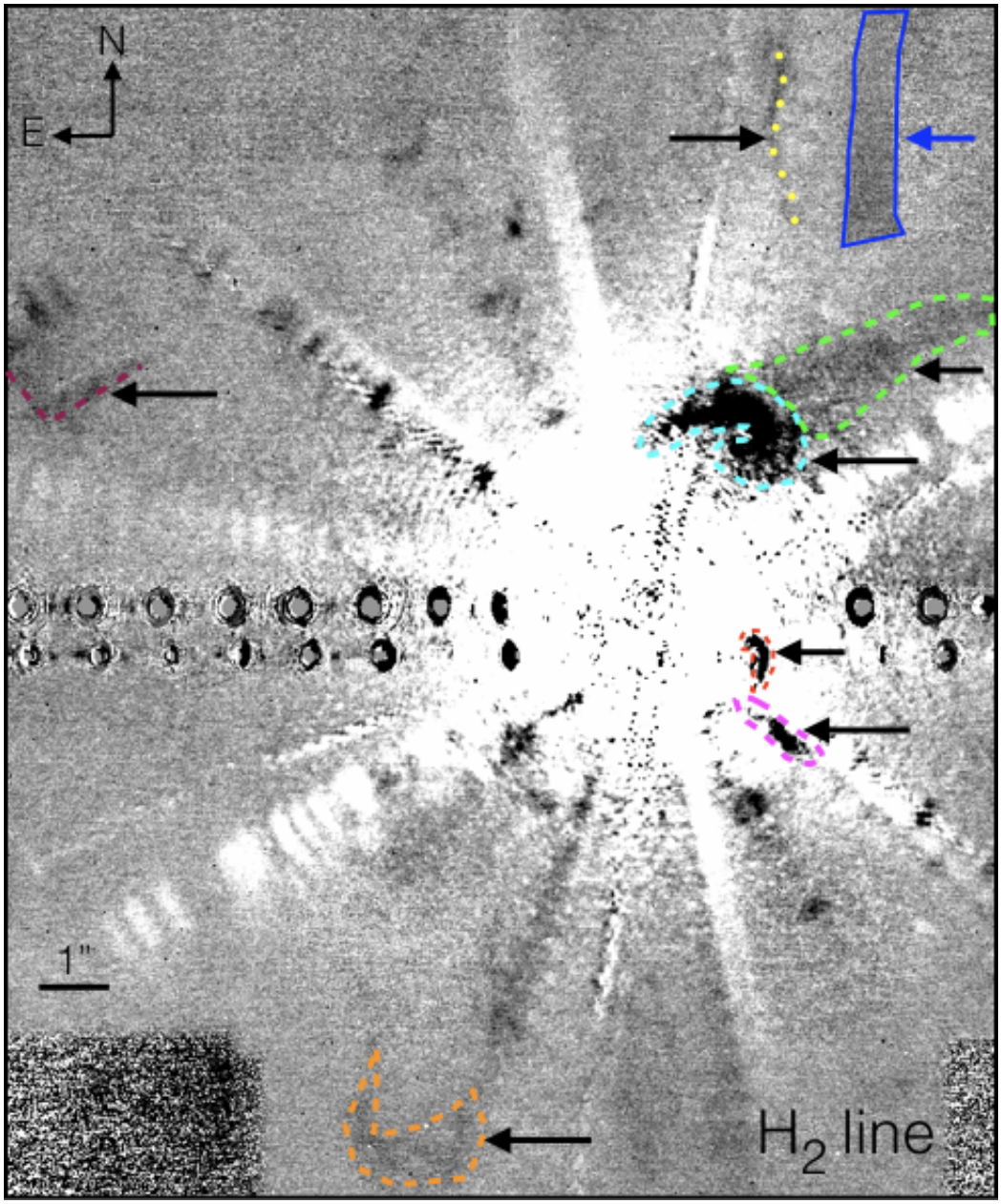


**Figure 5.19:** T Tau $H_2$ line emission. The features are marked in different colours and pointed to by a black arrow. T Tau NW is clearly detected, marked within the cyan dotted lines. Unlike the previous detections, T Tau NW has a clear hook-like feature toward the West side. The feature within the magenta dotted lines represents the same linear feature observed with SPHERE (see Figure 5.8). The coma-like feature West of T Tau S, marked with the red dotted lines, is the same C1 feature mentioned in Herbst et al. [51]. We detected several new features: (1) a relatively low SNR (compared to T Tau NW) extended feature (marked within the green dotted lines), which appears to be extending from T Tau NW in the North-West direction, (2) the slightly lengthy curvy feature toward the NW of the image (marked by the yellow dotted lines), (3) the L-shaped feature toward the East of the image (marked by maroon dotted lines), and (4) the rather low SNR patch of $H_2$ line emission (marked within the orange dotted lines) far away from the stars in the South-Southeast direction. The extended region toward the top-right corner of the image, marked within the blue lines and indicated by the blue arrow, is not a real feature. It is an artefact from the continuum subtraction.

larger movement toward the West than toward the North in Figure 5.9.

Along with the linear feature marked within the magenta dotted lines in Figure 5.19 (this is the same linear feature observed with SPHERE, shown in Figure 5.8), we also detected a coma-like feature West of T Tau S, marked with the red dotted lines. This is the same C1 feature mentioned in Herbst et al. [51]. In addition, we detected some completely new features: a long curvy feature North-Northwest of the stars (marked by the yellow dotted lines), an L-shaped feature toward the East of the image (marked by maroon dotted lines, almost in the same place as the E feature mentioned by Herbst et al in [53]), and a rather low SNR patch of $H_2$ line emission (marked within the orange dotted lines) far away from the stars in the South-Southeast direction.

### 5.3.3 Analysis of the LUCI data

#### Molecular hydrogen emission

From the SPHERE data, we concluded that T Tau NW must arise in one of the southern stars. The continuum J-band frames (see Figure 5.20) show a cavity toward the South-Southeast of the stars. From the geometric point of view, it is likely that the bipolar outflow that drives T Tau NW also created this cavity. Figure 5.20 examines whether such outflows arise in T Tau N or one of the T Tau S stars. The magenta line segments represent the high SNR part of T Tau NW. The cyan and brown solid line arrows connect T Tau S and T Tau N to the T Tau NW outflow vertex. The same-coloured dotted arrows show the vectors starting from the respective stars in the exact opposite direction. It is clear from Figure 5.20 that if the same outflow caused T Tau NW and the cavity, it very likely arises in one of the southern stars. In other words, this argument supports the claim by Kasper et al. [66] that T Tau NW is triggered by an outflow from T Tau S.

We observed a hook-like feature with relatively low SNR toward the West side of T Tau NW (marked within cyan dotted lines in Figure 5.19). On the average, the SNR of the hook-like part of T Tau NW is one-third of the highest SNR part of T Tau NW (represented by the green line segments in Figure 5.21). From back-of-the-envelope calculations, we see that the vertex of the T Tau NW has moved by about 137 mas in the Northwest-West direction relative to the 2014 data. Clearly, the previous trend of having more relative velocity toward the West direction continues (estimated using 2014 SPHERE Kasper et al. data and 2002 Herbst et al. data). However, Kasper et al. found a displacement of about 200 mas in 12 years (~17 mas/year or ~12 km/s perpendicular to the line of sight). Our estimation of 137 mas displacement in 2 years (~69 mas/year or ~49 km/s perpendicular to the line of sight) represent unusually high velocity for such a shock. We are looking into the calculations again to find errors. Also, cross-checking with the new set of data obtained using SPHERE GTO. Visibility of the hook-like

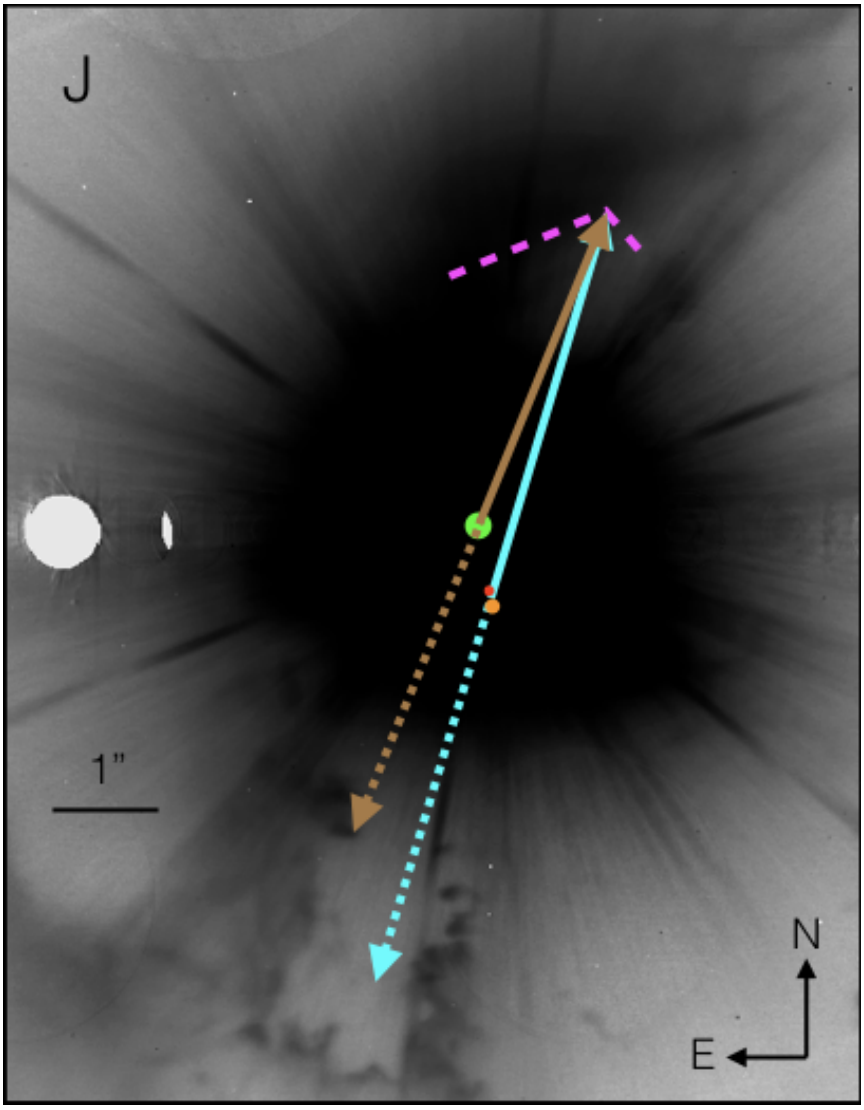


**Figure 5.20:** Cropped version of the Figure 5.16. The magenta dotted lines denote the position of the T Tau NW. The cyan and brown arrows represent the vectors from T Tau S and T Tau N to the T Tau NW outflow vertex. Same coloured dotted arrows are the vectors of same lengths, but in opposite direction, starting from the respective stars. It appears that, if the same bipolar outflow produces T Tau NW and the creation of the cavity, one of the southern stars is the origin.

feature, heading East, may be due to the fact that the materials in those region are being light up now. Our calculation, above also shows a significant high velocity toward the West direction. It may be possible that the materials are being pushed away more toward West giving the hook-like feature. Figure 5.21 supports this argument.

A rather low SNR feature, which appears to be extending from T Tau NW in the North-West

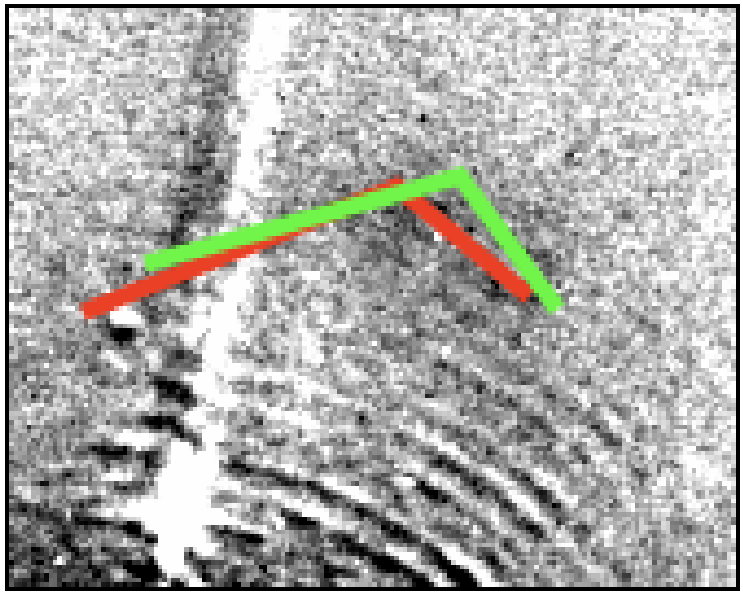

**Figure 5.21:** Present position of T Tau NW (in green line segments) overlaid on the 2014 SPHERE data [66]. The red line segment represent the T Tau NW position from the SPHERE data. Clearly, this image shows the different relative velocity of the material within T Tau NW.

direction (marked within the green dotted lines in Figure 5.19) does not directly point to any of the T Tau Stars, and it is clearly not an artefact from the continuum subtraction. There is no mention of such a feature before in the literature.This feature is not obviously pointing toward any of the T Tau Stars. Nor does it coincide with the Stapelfeldt arc. We are still investigating the physical process that can cause such emission. Also, study is on-going to provide explanations for the other molecular hydrogen emissions observed.

### Continuum imaging

We have detected T Tau Sa in the J band for the first time. The position was confirmed by comparing with the Br$\gamma$ image. Since we expect little veiling and the source is spatially unresolved in the J-band, future spectroscopic observations may be able to reveal photospheric features in T Tau Sa and allow us to determine its spectral type. From the LUCI data, we do not see any evidence of a hamburger-like morphology indicative of an edge-on disk, as predicted by Kasper et al. [66].

From the LUCI data, the South-West coiling structure can be traced from ~1" out to ~2.7" from T Tau N, which is 150 to 400 AU at the distance of T Tau. From the SPHERE data, we traced the coiling outflow from ~1" to ~2.5". Therefore, from LUCI data, we may say that the

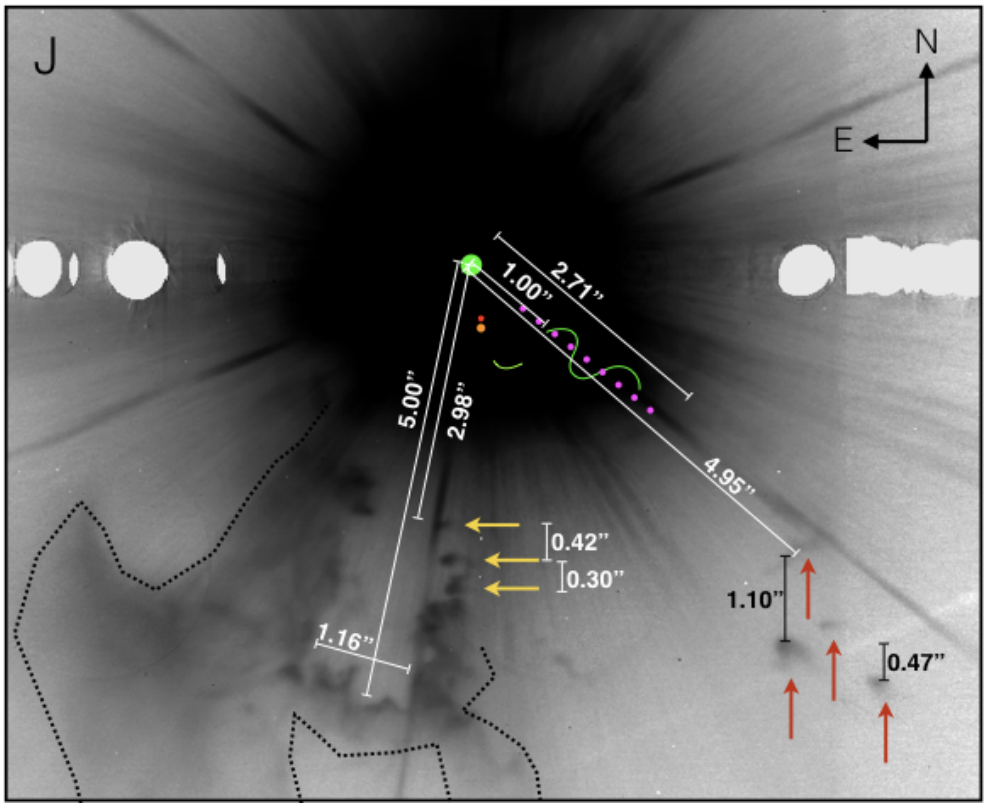


**Figure 5.22:** J-band image showing the distances between the different features observed.

coiling outflow has moved relatively or we see more of the coiling structure, which could not be traced out in the SPHERE data or both. Note that the LUCI J-filter has a band width of 301 nm, whereas the SPHERE J-band image we used for the coiling outflow had a band width of 240 nm.

Figure 5.22 shows the overall geometry of T Tau, including the distances. The start of the southern cavity is considered to be the position of the first tadpole-like feature, which is ~2.98” away from T Tau N. The cavity ends around ~5.00” away from T Tau N. The width of the cavity is ~1.16”.

The pillars in the pillars of creation, seen in the Eagle Nebula, are composed of cool $H_2$ and dust, and are being eroded by UV radiation from nearby hot and massive O stars. The environment in our scenario is completely different, although the tadpole features along with the extended emission (marked with the dotted lines in Figure 5.16) gives a similar impression. T Tau stars are much cooler and less luminous. Therefore, the production of sufficient UV radiation this far away from these stars, is very unlikely. However, Herbst et al. [51] and Gustafsson et al. [46] detected 2.05 $\mu$m He line emission from T Tau Sb, implying an energetic environment and possible presence of UV radiation. Is this UV radiation responsible for the features? Hopefully,

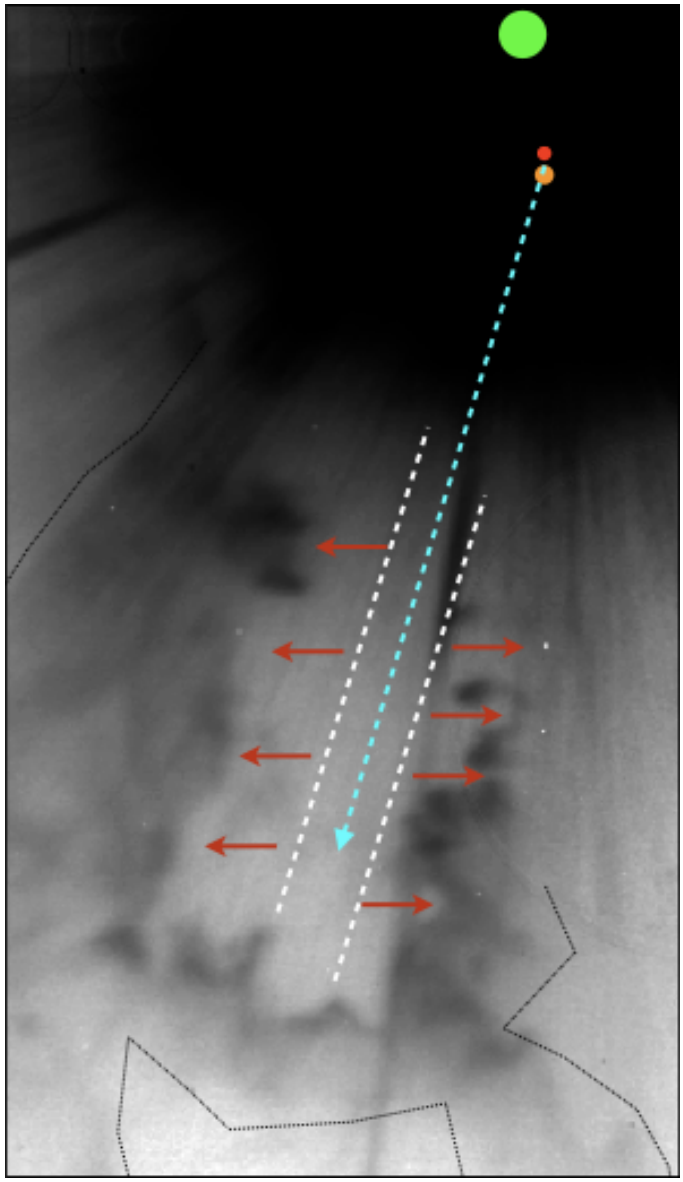

**Figure 5.23:** J-band image showing the tadpoles and the cavity. The cyan dotted vector originating from the T Tau S is the same as that in Figure 5.20. If the outflow from T Tau S was fast and streamlined with its strength decaying radially outwards toward the white dotted lines, the materials in the those regions might be pushed away in the direction indicated by the red arrows. This may be an explanation for the tails of the tadpoles heading West.

further spectroscopic studies will provide answers.

The tail of the tadpoles extend in the West direction. If the outflow from the T Tau S was fast and streamlined, as depicted in Figure 5.23, with its strength decaying radially outwards, the

materials may be pushed toward the West.

The knots (indicated by red arrows in Figure 5.22) appear morphologically similar to the proplyds in the Orion Nebula. They are around 5" away from the T Tau N in the Southwest direction, but do not line up with the coiling outflow feature. Again, there does not appear to be sufficient energy in the T Tau system to erode material and produce coma-shaped features representing proplyds. These enigmatic features, along with the tadpoles, will be the focus of upcoming observations for which we have been granted observing time on LBT in fall 2017.

### 5.3.4 Summary of the LUCI data

Thanks to the LUCI AO-imaging commissioning data, we have made further progress in understanding the secrets of the T Tau System. For the first time ever, T Tau Sa was detected in the J-band. Also, new features were seen in the continuum imaging as well as in $H_2$ line emission. From the continuum imaging, we have observed (1) the tadpole-like features and extended emission to the South-Southeast of the stars, (2) a cavity to the South-Southeast of the stars. If created by the same bipolar outflow that triggered T Tau NW, the origin should be one of the southern stars, and (3) proplyd-like knots toward the Southwest of the stars, farther than the coiling outflow, but also pointing in the direction of T Tau N. From the $H_2$ line emission, we detected (1) a hook-like feature in T Tau NW toward the West suggesting different relative velocity of materials in that region, (2) a low SNR extended emission region that appears to be an extension of T Tau NW, and (3) a longer curvy outflow to the North.

The study using the LUCI data on the T Tau System is not yet complete. We are confronting our analysis with earlier observations and conclusions in the literature. Once complete, we intend to publish these results. The paper is already in preparation.

Although these commissioning data suffered from many AO residuals, the data proved to be of sufficient quality to produce real science. We hope that LUCI will be able to produce even better quality images when the non-common path aberrations are removed. Also, these commissioning data prove the capability of LUCI to provide high-contrast images, allowing studies of faint outflows and structures near bright pre-main sequence stars.

## 5.4 Summary

Adaptive optics systems are becoming an integral part of all very large telescopes, allowing the astrophysics community to explore uncharted territories. The type of AO system used depends

substantially on the science goals of the investigator. My scientific interests lie in understanding star formation, in particular, the study of pre-main sequence T Tau Stars using near-infrared observations. With the help of the state-of-the-art instruments SPHERE (VLT, Paranal, Chile) and LUCI (LBT, Mt.Graham, USA), I studied the T Tau System. Both these instruments have advanced AO systems, capable of providing high-contrast, high-resolution imagery. Observations made using SPHERE and LUCI provided us new insights and better understanding of this source.

Although known to be the prototype of T Tau Stars, the T Tau is a multi-stellar (triple) system with complex outflows and line emission at all angular scales observed so far. Tracing back the faint outflows and features (in continuum and line emission) played a key role in our study. This was only possible due to the adaptive optics capabilities associated with each of these instruments. With a modest investment of observing time of ∼3 hours for SPHERE (science verification time) and ∼2 hours for LUCI (AO-imaging commissioning time), we have made progress in understanding T Tau. We look forward to further observations that could hopefully disentangle all the complex outflows, image circumstellar and circumbinary disks, and establish the geometry of the system. We also plan to follow up on the many new features we uncovered (coiling outflow, cavity, tadpoles etc.).

The SPHERE data are already published [66], and the paper presenting the results from LUCI is in preparation [112]. Recently, we obtained an additional ∼2 hours of data from SPHERE (GTO time). These data are being reduced and analysed as I write this thesis. We have also been granted additional observing time with LUCI (LBTB-GTO-B) for late fall 2017.

# Chapter 6

# Summary and Future Perspectives

## 6.1 Summary

Adaptive optics corrects for the aberrations caused by the Earth's fully turbulent atmosphere in real-time, allowing ground based optical and near-infrared telescopes to attain their diffraction-limited capabilities. Scientific programs that demand uniform, wide-field correction require an extension to the classical AO technique, multi-conjugated adaptive optics (MCAO). For my doctoral work, I concentrated on maximising the scientific return of one such MCAO system, the LINC-NIRVANA instrument.

Starting from alignment and calibration in the lab to the on-going commissioning, I have contributed to the optical assembly, integration, verification, and software development of the LN MCAO system. Much of this effort was published in SPIE and OSA conference proceedings. I also solved a particular challenge faced by all MCAO systems, namely the "partial illumination issue". This solution has been tested both in the lab and on-sky. However, we need to perform more tests to check the efficiency of the solution. This will be done in upcoming commissioning runs. We are currently writing a paper on this partial illumination work.

The LN MCAO system provides direct and real-time turbulence information about two conjugated layers in the atmosphere: the ground layer and a high layer about 7 km above the telescope. I developed a concept, which makes full use of AO telemetry available from each of the layers independently, to improve the performance of the system. We call this "wind-predictive wavefront control". Unlike with other systems, implementing wind-predictive control with LN MCAO is rather straightforward, and it should also improve the wavefront sensing efficiency. This is especially true for the high layer loop. Due to partial illumination, some or many of the sub-apertures in the metapupil will not be illuminated. If the wind vector is in the favourable direction, we may illuminate some of these non-illuminated sub-apertures virtually, thereby improving the WFS performance and the correction in general. This study is on-going, and will be presented at the

upcoming wavefront sensing workshop in Padova, Italy (October, 2017).

Finally, to understand the astrophysical capabilities of an AO system, and to further my interest in YSO's, I studied a pre-main sequence star system, T Tauri, using observations from VLT-SPHERE and LBT-LUCI. These two instruments are equipped with advanced AO systems capable of providing high-contrast, high-resolution, near-infrared imagery. Analysis of these observations provided new insights and better understanding of the T Tauri system. Tracing back the faint outflows and features (in continuum and line emission), we came a few steps closer to understanding the energetics, dynamics and geometry of the system. The SPHERE results are published, and the paper presenting the LUCI results is in preparation.

## 6.2 Future perspectives

I will be working in the LINC-NIRVANA project for another year as a post-doc at MPIA. I plan to continue and broaden my research in multiple directions:

1. Partial illumination issue: As mentioned in Chapter 3, further on-sky testing will be performed in the upcoming commissioning runs (the first is in October 2017). The efficiency of the correction will be checked, and the collected data will be analysed, and will be used for publishing this work.

2. CCD positioning issue: It is essential to have the WFS CCD fixed at its nominal position with sub-pixel precision for the best AO performance. Currently, mainly due to gravitational flexures, this is not true, and therefore, there is an upper limit in the number of modes that can be corrected. We are developing an algorithm that will take care of this issue, and its implementation is a higher priority now.

3. Working on the WFS CCD noise: The LN wavefront sensing CCDs show excess pattern noise and more read-out noise than specifications. As a result, we must use brighter stars for wavefront sensing, thereby decreasing sky coverage. The CCDs will investigated and replaced if necessary with new ones. With the recent LBT "SOUL" AO hardware and software update, we will also be able to make use of the better spatial sampling of the GWS. The GWS CCDs and the software should be ready for this.

4. Lean-MCAO Early Science plan: It is expected to have the first run of the Lean-MCAO Early Science plan by fall 2018. Various system level tests have to be performed in advance, and the AO performance has to be quantified. This will be taking place in the next commissioning runs.

5. Wind-predictive wavefront control: As mentioned in Chapter 4, we will be making lab tests and collecting on-sky data for the implementation of wind predictive control. The implementation will happen in two phases: first with the (simpler) GWS loop, followed by the HWS loop. The wind predictive control may be used to improve piston measurement. This will assist implementation of LN Fizeau interferometry.

6. Partial illumination algorithm 2.0: I will be working on the concept and implementation of a slightly more advanced algorithm for the partial illumination issue. This algorithm will make better use of the higher SNR information of available in the overlapping regions from multiple stars.

7. Software development: Currently, most of the GUIs are either engineering versions or under development to final stage. Improving the software packages and services is one of the important milestones for the coming year.

8. Wide field upgrade: An LN upgrade is also foreseen, increasing the scientific FoV from 10.5x10.5 square arcsec to 42x42 square arcsec or even 84x84 square arcsec, depending on the size of the detectors we may use. For this update, we only have to change the final camera optics inside the cryostat.

# Acknowledgments

The realisation of my Ph.D. is an outcome of support, friendship, and goodness of many kind-hearted people across the globe.

First and foremost, I extend my sincere gratitude to my supervisor, Tom Herbst. It has been great working with you. Thank you for guiding and supporting me throughout my four year journey. You have been so kind to go through this script multiple times and to help me with corrections and improvements.

Thanks are due to Carmelo Aricidiacono, Thomas Bertram, Robert Harris, Rosalie McGurk, and Felix Widmann for going through many sections of this script and suggesting improvements.

Being a part of the LINC-NIRVANA team was a great experience for me. Working with colleagues from MPIA and INAF-Padova, and learning from them about multiple disciplines in instrumentation, was invaluable. Thank you all for sharing your knowledge.

A great deal of appreciation goes to Jochen Heidt for observing my science target as a part of the LUCI-AO-commissioning, to the mountain crew at LBTO for helping me out with LN remote operations at LBT, to Markus Kasper for collaborating with me, and to all my friends and colleagues at MPIA for the great support, friendship, and lively scientific environment that brought out the researcher in me.

Special thanks goes to Coryn Bailer-Jones for officially supervising me, and for providing feedback through TCMs and canteen chats.

I thank my officemates Qian Qian, Alexander Hygate, and Tobias Schmidt for providing a fresh and cheerful environment. Also, I wish you the best for all the future endeavours.

My backbone has been my family - Achan, Amma, Meetu, Abhi, Joshya, and Kranthi. Thank you all for the unwavering support, encouragement, patience, and love you guys transferred to keep me awake and standing firm in all situations. Thank you for believing in me!

# Bibliography


[1] R. L. Akeson, D. R. Ciardi, G. T. van Belle, and M. J. Creech-Eakman. Constraints on Circumstellar Disk Parameters from Multiwavelength Observations: T Tauri and SU Aurigae. *Astrophysical Journal*, 566:1124–1131, February 2002.

[2] C. Arcidiacono, T. Bertram, R. Ragazzoni, J. Farinato, S. Esposito, A. Riccardi, E. Pinna, A. Puglisi, L. Fini, M. Xompero, L. Busoni, F. Quiros-Pacheco, and R. Briguglio. Numerical control matrix rotation for the LINC-NIRVANA multiconjugate adaptive optics system. In *Adaptive Optics Systems II*, volume 7736 of *Proc. SPIE*, page 77364J, July 2010.

[3] C. Arcidiacono, E. Diolaiti, R. Ragazzoni, J. Farinato, and E. Vernet-Viard. Sky coverage for layer-oriented MCAO: a detailed analytical and numerical study. In D. Bonaccini Calia, B. L. Ellerbroek, and R. Ragazzoni, editors, *Advancements in Adaptive Optics*, volume 5490 of *Proc. SPIE*, pages 563–573, October 2004.

[4] H. W. Babcock. The Possibility of Compensating Astronomical Seeing. *Publications of the Astronomical Society of the Pacific*, 65:229, October 1953.

[5] T. L. Beck, P. J. McGregor, M. Takami, and T.-S. Pyo. Spatially Resolved Molecular Hydrogen Emission in the Inner 200 AU Environments of Classical T Tauri Stars. *Astrophysical Journal*, 676:472–489, March 2008.

[6] T. L. Beck, G. H. Schaefer, M. Simon, L. Prato, J. A. Stoesz, and R. R. Howell. A High Spatial Resolution Infrared View of the T Tauri Multiple System. *Astrophysical Journal*, 614:235–251, October 2004.

[7] J. M. Beckers. Increasing the Size of the Isoplanatic Patch with Multiconjugate Adaptive Optics. In M.-H. Ulrich, editor, *European Southern Observatory Conference and Workshop Proceedings*, volume 30 of *European Southern Observatory Conference and Workshop Proceedings*, page 693, 1988.

[8] S. Beckwith, I. Gatley, K. Matthews, and G. Neugebauer. Molecular hydrogen emission from T Tauri stars. *Astrophysical Journal, Letters*, 223:L41–L43, July 1978.

[9] M. Bergomi, V. Viotto, C. Arcidiacono, L. Marafatto, J. Farinato, H. Baumeister, T. Bertram, J. Berwein, F. Briegel, A. Conrad, F. Kittman, D. Kopon, R. Hofferbert, D. Magrin, K. K. Radhakrishnan Santhakumari, A. Puglisi, M. Xompero, R. Briguglio, F. Quiros-Pacheco, T. M. Herbst, and R. Ragazzoni. First light of the LINC-NIRVANA Pathfinder experiment. In *Adaptive Optics Systems IV*, volume 9148 of *Proc. SPIE*, page 91482Y, July 2014.

[10] M. Bergomi, V. Viotto, J. Farinato, L. Marafatto, K. Radhakrishnan, R. Ragazzoni, M. Dima, D. Magrin, C. Arcidiacono, E. Diolaiti, I. Foppiani, M. Lombini, L. Schreiber, T. Bertram, P. Bizenberger, A. Conrad, T. Herbst, F. Kittmann, D. Kopon, D. Meschke, and X. Zhang. Multiple FoV MCAO on its way to the sky. In S. Esposito and L. Fini, editors, *Proceedings of the Third AO4ELT Conference*, page 40, December 2013.

[11] T. Bertram, F. Kittmann, and L. Mohr. Multiple guide star acquisition software for LINC-NIRVANA. In *Software and Cyberinfrastructure for Astronomy II*, volume 8451 of *Proc. SPIE*, page 845126, September 2012.

[12] T. Bertram, K. Kumar Radhakrishnan Santhakumari, L. Marafatto, C. Arcidiacono, J. Berwein, R. Ragazzoni, and T. M. Herbst. Wavefront sensing in a partially illuminated, rotating pupil. In *Adaptive Optics Systems IV*, volume 9148 of *Proc. SPIE*, page 91485M, August 2014.

[13] T. Bertram, J. Trowitzsch, T. M. Herbst, and R. Ragazzoni. Beam control for LINC-NIRVANA: from the binocular entrance pupil to the combined focal plane. In *Optical and Infrared Interferometry III*, volume 8445 of *Proc. SPIE*, page 844533, July 2012.

[14] J.-L. Beuzit, M. Feldt, K. Dohlen, D. Mouillet, P. Puget, F. Wildi, L. Abe, J. Antichi, A. Baruffolo, P. Baudoz, A. Boccaletti, M. Carbillet, J. Charton, R. Claudi, M. Downing, C. Fabron, P. Feautrier, E. Fedrigo, T. Fusco, J.-L. Gach, R. Gratton, T. Henning,

N. Hubin, F. Joos, M. Kasper, M. Langlois, R. Lenzen, C. Moutou, A. Pavlov, C. Petit, J. Pragt, P. Rabou, F. Rigal, R. Roelfsema, G. Rousset, M. Saisse, H.-M. Schmid, E. Stadler, C. Thalmann, M. Turatto, S. Udry, F. Vakili, and R. Waters. SPHERE: a 'Planet Finder' instrument for the VLT. In *Ground-based and Airborne Instrumentation for Astronomy II*, volume 7014 of *Proc. SPIE*, page 701418, July 2008.

[15] P. Bizenberger, H. Baumeister, A. Böhm, T. Herbst, A. Huber, W. Laun, U. Mall, L. Mohr, V. Naranjo, C. Storz, and J. Trowitzsch. LINC-NIRVANA, integration of an interferometric and cryogenic camera: first verification results. In *Ground-based and Airborne Instrumentation for Astronomy IV*, volume 8446 of *Proc. SPIE*, page 844647, September 2012.

[16] P. Bizenberger, H. Baumeister, P. Fopp, T. Herbst, W. Laun, L. Mohr, and J. Moreno-Ventas. LINC-NIRVANA: Diffraction limited optics in cryogenic environment. In *Ground-based and Airborne Instrumentation for Astronomy V*, volume 9147 of *Proc. SPIE*, page 91474B, July 2014.

[17] P. Bizenberger, H. Baumeister, T. Herbst, and X. Zhang. LINC-NIRVANA: cryogenic optics for diffraction limited beam combination. In *Imaging Spectrometry XVII*, volume 8515 of *Proc. SPIE*, page 84150Q, September 2012.

[18] J. H. Black and A. Dalgarno. Interstellar H2 - The population of excited rotational states and the infrared response to ultraviolet radiation. *Astrophysical Journal*, 203:132–142, January 1976.

[19] F. Briegel, J. Berwein, F. Kittmann, V. Volchkov, L. Mohr, W. Gaessler, T. Bertram, S. Rost, and Y. Wang. The LINC-NIRVANA Common Software. In *Society of Photo-Optical Instrumentation Engineers (SPIE) Conference Series*, volume 6274 of *Proc. SPIE*, page 62741M, June 2006.

[20] T. Buehrke, E. W. Brugel, and R. Mundt. An optical study of the shock-excited gas in the T Tau/NGC 1555 region. *Astronomy and Astrophysics*, 163:83–92, July 1986.

[21] A. Buffington, F. S. Crawford, R. A. Muller, and C. D. Orth. First observatory results with an image-sharpening telescope. *Journal of the Optical Society of America (1917-1983)*, 67:304, March 1977.

[22] A. Buffington, F. S. Crawford, R. A. Muller, A. J. Schwemin, and R. G. Smits. Correction of atmospheric distortion with an image-sharpening telescope. *Journal of the Optical Society of America (1917-1983)*, 67:298–303, March 1977.

[23] R. U. Claudi, M. Turatto, R. G. Gratton, J. Antichi, M. Bonavita, P. Bruno, E. Cascone, V. De Caprio, S. Desidera, E. Giro, D. Mesa, S. Scuderi, K. Dohlen, J. L. Beuzit, and

P. Puget. SPHERE IFS: the spectro differential imager of the VLT for exoplanets search. In *Ground-based and Airborne Instrumentation for Astronomy II*, volume 7014 of *Proc. SPIE*, page 70143E, July 2008.

[24] M. Cohen and L. V. Kuhi. Observational studies of pre-main-sequence evolution. *Astrophysical Journal, Supplement*, 41:743–843, December 1979.

[25] A. R. Conrad, C. Arcidiacono, H. Baumeister, M. Bergomi, T. Bertram, J. Berwein, F. Briegel, J. Farinato, T. Herbst, R. Hofferbert, F. Kittmann, M. Kürster, D. Kopon, L. Marafatto, M. Norris, R. Ragazzoni, and V. Viotto. Acquiring multiple stars with the LINC-NIRVANA Pathfinder. In *Observatory Operations: Strategies, Processes, and Systems V*, volume 9149 of *Proc. SPIE*, page 91491O, August 2014.

[26] C. Correia, K. Jackson, J.-P. Véran, D. Andersen, O. Lardière, and C. Bradley. Static and predictive tomographic reconstruction for wide-field multi-object adaptive optics systems. *J. Opt. Soc. Am. A*, 31(1):101–113, Jan 2014.

[27] C. E. Coulman, J. Vernin, Y. Coqueugniot, and J.-L. Caccia. Outer scale of turbulence appropriate to modeling refractive-index structure profiles. *Applied Optics*, 27, January 1988.

[28] G. Csépány, M. van den Ancker, P. Ábrahám, W. Brandner, and F. Hormuth. Examining the T Tauri system with SPHERE. *Astronomy and Astrophysics*, 578:L9, June 2015.

[29] G.-M. Dai. Modal wave-front reconstruction with Zernike polynomials and Karhunen-Loeve functions. *Journal of the Optical Society of America A*, 13:1218–1225, June 1996.

[30] E. Diolaiti, C. Arcidiacono, G. Bregoli, R. C. Butler, M. Lombini, L. Schreiber, A. Baruffolo, A. Basden, M. Bellazzini, E. Cascone, P. Ciliegi, F. Cortecchia, G. Cosentino, V. De Caprio, A. De Rosa, N. Dipper, S. Esposito, I. Foppiani, E. Giro, G. Morgante, R. Myers, F. Patru, R. Ragazzoni, A. Riccardi, M. Riva, F. M. Zerbi, M. Casali, B. Delabre, N. Hubin, F. Kerber, M. Le Louarn, E. Marchetti, S. Ramsay, S. Stroebele, and E. Vernet. Preparing for the phase B of the E-ELT MCAO module project. In *Adaptive Optics Systems IV*, volume 9148 of *Proc. SPIE*, page 91480Y, August 2014.

[31] K. Dohlen, M. Langlois, M. Saisse, L. Hill, A. Origne, M. Jacquet, C. Fabron, J.-C. Blanc, M. Llored, M. Carle, C. Moutou, A. Vigan, A. Boccaletti, M. Carbillet, D. Mouillet, and J.-L. Beuzit. The infra-red dual imaging and spectrograph for SPHERE: design and performance. In *Ground-based and Airborne Instrumentation for Astronomy II*, volume 7014 of *Proc. SPIE*, page 70143L, July 2008.

[32] G. Duchêne, A. M. Ghez, C. McCabe, and C. Ceccarelli. The Circumstellar Environment of T Tauri S at High Spatial and Spectral Resolution. *Astrophysical Journal*, 628:832–846, August 2005.

[33] H. M. Dyck, T. Simon, and B. Zuckerman. Discovery of an infrared companion to T Tauri. *Astrophysical Journal, Letters*, 255:L103–L106, April 1982.

[34] S. Esposito, A. Riccardi, E. Pinna, A. Puglisi, F. Quirós-Pacheco, C. Arcidiacono, M. Xompero, R. Briguglio, G. Agapito, L. Busoni, L. Fini, J. Argomedo, A. Gherardi, G. Brusa, D. Miller, J. C. Guerra, P. Stefanini, and P. Salinari. Large Binocular Telescope Adaptive Optics System: new achievements and perspectives in adaptive optics. In *Astronomical Adaptive Optics Systems and Applications IV*, volume 8149 of *Proc. SPIE*, page 814902, October 2011.

[35] S. Esposito, A. Riccardi, E. Pinna, A. T. Puglisi, F. Quirós-Pacheco, C. Arcidiacono, M. Xompero, R. Briguglio, L. Busoni, L. Fini, J. Argomedo, A. Gherardi, G. Agapito, G. Brusa, D. L. Miller, J. C. Guerra Ramon, K. Boutsia, and P. Stefanini. Natural guide star adaptive optics systems at LBT: FLAO commissioning and science operations status. In *Adaptive Optics Systems III*, volume 8447 of *Proc. SPIE*, page 84470U, July 2012.

[36] J. Farinato, F. Pedichini, E. Pinna, F. Baciotti, C. Baffa, A. Baruffolo, M. Bergomi, P. Bruno, E. Cappellaro, L. Carbonaro, A. Carlotti, M. Centrone, L. Close, J. Codona, S. Desidera, M. Dima, S. Esposito, D. Fantinel, G. Farisato, A. Fontana, W. Gaessler, E. Giallongo, R. Gratton, D. Greggio, J. C. Guerra, O. Guyon, P. Hinz, F. Leone, F. Lisi, D. Magrin, L. Marafatto, M. Munari, I. Pagano, A. Puglisi, R. Ragazzoni, B. Salasnich, E. Sani, S. Scuderi, M. Stangalini, V. Testa, C. Verinaud, and V. Viotto. SHARK (System for coronagraphy with High order Adaptive optics from R to K band): a proposal for the LBT 2nd generation instrumentation. In *Ground-based and Airborne Instrumentation for Astronomy V*, volume 9147 of *Proc. SPIE*, page 91477J, August 2014.

[37] D. L. Fried. Evaluation of $r_0$ for propagation down through the atmosphere: correction. *Applied Optics*, 14:2567, November 1975.

[38] D. L. Fried. Evaluation of $r_0$ for propagation down through the atmosphere: Correction 2. *Applied Optics*, 16:549, March 1977.

[39] D. L. Fried. Anisoplanatism in adaptive optics. *Journal of the Optical Society of America (1917-1983)*, 72:52, January 1982.

[40] D. L. Fried and G. E. Mevers. Evaluation of r sub zero for propagation down through the atmosphere. *Applied Optics*, 13:2620–2622, November 1974.

[41] T. Fusco, C. Petit, G. Rousset, J.-F. Sauvage, K. Dohlen, D. Mouillet, J. Charton, P. Baudoz, M. Kasper, E. Fedrigo, P. Rabou, P. Feautrier, M. Downing, P. Gigan, J.-M. Conan, J.-L. Beuzit, N. Hubin, F. Wildi, and P. Puget. Design of the extreme AO system for SPHERE, the planet finder instrument of the VLT. In *Society of Photo-Optical Instrumentation Engineers (SPIE) Conference Series*, volume 6272 of *Proc. SPIE*, page 62720K, June 2006.

[42] D. T. Gavel and D. Wiberg. Toward Strehl-optimizing adaptive optics controllers. In P. L. Wizinowich and D. Bonaccini, editors, *Adaptive Optical System Technologies II*, volume 4839 of *Proc. SPIE*, pages 890–901, February 2003.

[43] E. Gendron and P. Léna. Single layer atmospheric turbulence demonstrated by adaptive optics observations. *Astrophysics and Space Science*, 239(2):221–228, Sep 1996.

[44] A. M. Ghez, G. Neugebauer, P. W. Gorham, C. A. Haniff, S. R. Kulkarni, K. Matthews, C. Koresko, and S. Beckwith. Diffraction limited infrared images of the binary star T Tauri. *Astronomical Journal*, 102:2066–2072, December 1991.

[45] A. Guesalaga, B. Neichel, A. Cortés, C. Béchet, and D. Guzmán. Using the $C_n^2$ and wind profiler method with wide-field laser-guide-stars adaptive optics to quantify the frozen-flow decay. *Monthly Notices of the Royal Astronomical Society*, 440:1925–1933, May 2014.

[46] M. Gustafsson, L. E. Kristensen, M. Kasper, and T. M. Herbst. The origin, excitation, and evolution of subarcsecond outflows near T Tauri. *Astronomy and Astrophysics*, 517:A19, July 2010.

[47] O. Guyon. Limits of Adaptive Optics for High-Contrast Imaging. *The Astrophysical Journal*, 629:592–614, August 2005.

[48] J. W. Hardy. Instrumental limitations in adaptive optics for astronomy. In F. J. Roddier, editor, *Active telescope systems*, volume 1114 of *Proc. SPIE*, pages 2–13, September 1989.

[49] J. W. Hardy. *Adaptive Optics for Astronomical Telescopes*. Oxford University Press, July 1998.

[50] T. M. Herbst, S. V. W. Beckwith, A. Glindemann, L. E. Tacconi-Garman, H. Kroker, and A. Krabbe. A Near-Infrared Spectral Imaging Study of T Tau. *Astronomical Journal*, 111:2403, June 1996.

[51] T. M. Herbst, M. Hartung, M. E. Kasper, C. Leinert, and T. Ratzka. Molecular Hydrogen Outflows in the Central Arcseconds of the T Tauri System. *Astronomical Journal*, 134:359–366, July 2007.

[52] T. M. Herbst, R. Ragazzoni, T. Bertram, P. Bizenberger, F. Briegel, R. Hofferbert, and M. Kürster. LINC-NIRVANA at LBT: final preparations for first light. In *Ground-based and Airborne Instrumentation for Astronomy VI*, volume 9908 of *Proc. SPIE*, page 99080N, August 2016.

[53] T. M. Herbst, M. Robberto, and S. V. W. Beckwith. Wind-Disk-Ambient Cloud Interactions in the Near Environment of T Tauri. *Astronomical Journal*, 114:744, August 1997.

[54] W. Herbst, J. F. Booth, P. F. Chugainov, G. V. Zajtseva, W. Barksdale, E. Covino, L. Terranegra, A. Vittone, and F. Vrba. The rotation period and inclination angle of T Tauri. *Astrophysical Journal, Letters*, 310:L71–L75, November 1986.

[55] J. M. Hill and P. Salinari. The Large Binocular Telescope project. In J. M. Oschmann, Jr., editor, *Ground-based Telescopes*, volume 5489 of *Proc. SPIE*, pages 603–614, October 2004.

[56] Karel Hinnen, Michel Verhaegen, and Niek Doelman. Exploiting the spatiotemporal correlation in adaptive optics using data-driven h2-optimal control. *J. Opt. Soc. Am. A*, 24(6):1714–1725, Jun 2007.

[57] M. Horrobin, A. Eckart, U. Beckmann, C. Connot, J. Dierkes, B. Lindhorst, E. Nußbaum, S. Rost, S. Smajić, C. Straubmeier, I. Wank, T. Bertram, and J.-U. Pott. Performance of the LINC NIRVANA fringe and flexure tracker at delivery. In *Optical and Infrared Interferometry IV*, volume 9146 of *Proc. SPIE*, page 91462G, July 2014.

[58] N. Z. Ismailov, N. K. Quliev, O. V. Khalilov, and W. Herbst. Periodic variability in the emission spectrum of T Tauri. *Astronomy and Astrophysics*, 511:A13, February 2010.

[59] M. B. Jorgenson and G. J. M. Aitken. Prediction of Turbulence Induced Wavefront Degradation. In J. M. Beckers and F. Merkle, editors, *European Southern Observatory Conference and Workshop Proceedings*, volume 39 of *European Southern Observatory Conference and Workshop Proceedings*, page 309, March 1992.

[60] M. B. Jorgenson and G. J. M. Aitken. Wavefront Prediction for Adaptive Optics. In F. Merkle, editor, *European Southern Observatory Conference and Workshop Proceedings*, volume 48 of *European Southern Observatory Conference and Workshop Proceedings*, page 143, January 1994.

[61] A. H. Joy. T Tauri Variable Stars. *Astrophysical Journal*, 102:168, September 1945.

[62] R. Juvénal, C. Kulcsár, H.-F. Raynaud, and J.-M. Conan. LQG adaptive optics control with wind-dependent turbulent models. In *Adaptive Optics Systems V*, volume 9909 of *Proc. SPIE*, page 99090M, July 2016.

[63] M. Kasper. Adaptive optics for high contrast imaging. In *Adaptive Optics Systems III*, volume 8447 of *Proc. SPIE*, page 84470B, July 2012.

[64] M. Kasper, J.-L. Beuzit, M. Feldt, K. Dohlen, D. Mouillet, P. Puget, F. Wildi, L. Abe, A. Baruffolo, P. Baudoz, A. Bazzon, A. Boccaletti, R. Brast, T. Buey, O. Chesneau, R. Claudi, A. Costille, A. Delboulbé, S. Desidera, C. Dominik, R. Dorn, M. Downing, P. Feautrier, E. Fedrigo, T. Fusco, J. Girard, E. Giro, L. Gluck, F. Gonte, D. Gojak, R. Gratton, T. Henning, N. Hubin, A.-M. Lagrange, M. Langlois, D. L. Mignant, J.-L. Lizon, P. Lilley, F. Madec, Y. Magnard, P. Martinez, D. Mawet, D. Mesa, O. Müller-Nilsson, T. Moulin, C. Moutou, J. O'Neal, A. Pavlov, D. Perret, C. Petit, D. Popovic, J. Pragt, P. Rabou, S. Rochat, R. Roelfsema, B. Salasnich, J.-F. Sauvage, H. M. Schmid, N. Schuhler, A. Sevin, R. Siebenmorgen, C. Soenke, E. Stadler, M. Suarez, M. Turatto, S. Udry, A. Vigan, and G. Zins. Gearing up the SPHERE. *The Messenger*, 149:17–21, September 2012.

[65] M. Kasper, K. K. R. Santhakumari, and T. M. Herbst. Revisiting T Tauri system : A near-infrared high-contrast imaging study using the SPHERE. *To Be Submitted*, 2017.

[66] M. Kasper, K. K. R. Santhakumari, T. M. Herbst, and R. Köhler. New circumstellar structure in the T Tauri system. A near-infrared high-contrast imaging study. *Astronomy and Astrophysics*, 593:A50, September 2016.

[67] M. E. Kasper, M. Feldt, T. M. Herbst, S. Hippler, T. Ott, and L. E. Tacconi-Garman. Spatially Resolved Imaging Spectroscopy of T Tauri. *Astrophysical Journal*, 568:267–272, March 2002.

[68] M. E. Kasper, D. P. Looze, S. Hippler, M. Feldt, R. Weiss, A. Glindemann, and R. I. Davies. Practical approach to modal basis selection and wavefront estimation. In P. L. Wizinowich, editor, *Adaptive Optical Systems Technology*, volume 4007 of *Proc. SPIE*, pages 592–599, July 2000.

[69] A. Kawamura. A Noise Reduction Method Based on Linear Prediction with Variable Step-Size. *IEICE Transactions on Fundamentals of Electronics Communications and Computer Sciences*, 88:855–861, April 2005.

[70] S. J. Kenyon and L. Hartmann. Pre-Main-Sequence Evolution in the Taurus-Auriga Molecular Cloud. *Astrophysical Journal, Supplement*, 101:117, November 1995.

[71] S. J. Kenyon and L. W. Hartmann. On the apparent positions of T Tauri stars in the H-R diagram. *Astrophysical Journal*, 349:197–207, January 1990.

[72] F. Kittmann, W. Gässler, F. Briegel, and J. Berwein. LINC-NIRVANA Instrument Control Software. In R. A. Shaw, F. Hill, and D. J. Bell, editors, *Astronomical Data Analysis*

*Software and Systems XVI*, volume 376 of *Astronomical Society of the Pacific Conference Series*, page 661, October 2007.

[73] R. Köhler, M. Kasper, T. M. Herbst, T. Ratzka, and G. H.-M. Bertrang. Orbits in the T Tauri triple system observed with SPHERE. *Astronomy and Astrophysics*, 587:A35, March 2016.

[74] A. N. Kolmogorov. A refinement of previous hypotheses concerning the local structure of turbulence in a viscous incompressible fluid at high reynolds number. *Journal of Fluid Mechanics*, 13(1):82–85, 1962.

[75] D. Kopon, A. Conrad, C. Arcidiacono, T. Herbst, V. Viotto, J. Farinato, M. Bergomi, R. Ragazzoni, L. Marafatto, H. Baumeister, T. Bertram, J. Berwein, F. Briegel, R. Hofferbert, F. Kittmann, M. Kürster, L. Mohr, and K. Radhakrishnan. Pathfinder first light: alignment, calibration, and commissioning of the LINC-NIRVANA ground-layer adaptive optics subsystem. In *Adaptive Optics Systems IV*, volume 9148 of *Proc. SPIE*, page 914828, August 2014.

[76] C. D. Koresko. A Third Star in the T Tauri System. *Astrophysical Journal, Letters*, 531:L147–L149, March 2000.

[77] J. P. Lewis. Fast normalized cross-correlation, 1995.

[78] M. Lloyd-Hart and P. McGuire. Spatio-temporal prediction for adaptive optics wavefront reconstructors. In M. Cullum, editor, *European Southern Observatory Conference and Workshop Proceedings*, volume 54 of *European Southern Observatory Conference and Workshop Proceedings*, page 95, 1996.

[79] L. Loinard, R. M. Torres, A. J. Mioduszewski, L. F. Rodríguez, R. A. González-Lópezlira, R. Lachaume, V. Vázquez, and E. González. VLBA Determination of the Distance to Nearby Star-forming Regions. I. The Distance to T Tauri with 0.4% Accuracy. *Astrophysical Journal*, 671:546–554, December 2007.

[80] L. Marafatto, M. Bergomi, A. Brunelli, M. Dima, J. Farinato, G. Farisato, L. Lessio, D. Magrin, R. Ragazzoni, V. Viotto, T. Bertram, P. Bizenberger, M. Brangier, F. Briegel, A. Conrad, F. De Bonis, T. Herbst, R. Hofferbert, F. Kittmann, M. Kürster, D. Meschke, L. Mohr, and R.-R. Rohloff. Aligning a more than 100 degrees of freedom wavefront sensor. In *Adaptive Optics Systems III*, volume 8447 of *Proc. SPIE*, page 84476F, July 2012.

[81] Luca Marafatto, Kalyan Kumar Radhakrishnan Santhakumari, Thomas Bertram, Harald Baumeister, Maria Bergomi, Jurgen Berwein, Peter Bizenberger, Florian Briegel, Tom

Herbst, Javier Moreno-Ventas, Frank Kittmann, Jacopo Farinato, Roberto Ragazzoni, and Valentina Viotto. Aligning the linc-nirvana natural guide stars mcao system. *Adaptive Optics for Extremely Large Telescopes 4 –Conference Proceedings*, 1(1), 2015.

[82] A. Marèchal. Etude des effets combinés de la diffraction et des aberrations géométriques sur l'image d'un point lumineux. *Optical Review*, 2:257–277, 1947.

[83] D. Mawet, L. Pueyo, P. Lawson, L. Mugnier, W. Traub, A. Boccaletti, J. T. Trauger, S. Gladysz, E. Serabyn, J. Milli, R. Belikov, M. Kasper, P. Baudoz, B. Macintosh, C. Marois, B. Oppenheimer, H. Barrett, J.-L. Beuzit, N. Devaney, J. Girard, O. Guyon, J. Krist, B. Mennesson, D. Mouillet, N. Murakami, L. Poyneer, D. Savransky, C. Vérinaud, and J. K. Wallace. Review of small-angle coronagraphic techniques in the wake of ground-based second-generation adaptive optics systems. In *Space Telescopes and Instrumentation 2012: Optical, Infrared, and Millimeter Wave*, volume 8442 of *Proc. SPIE*, page 844204, September 2012.

[84] J. Moreno-Ventas, H. Baumeister, T. Bertram, P. Bizenberger, F. Briegel, D. Greggio, F. Kittmann, L. Marafatto, L. Mohr, K. Radhakrishnan, and H. Schray. Optical integration and verification of LINC-NIRVANA. In *Ground-based and Airborne Instrumentation for Astronomy V*, volume 9147 of *Proc. SPIE*, page 91473V, July 2014.

[85] J. Moreno-Ventas, P. Bizenberger, T. Bertram, K. K. Radhakrishnan, F. Kittmann, H. Baumeister, L. Marafatto, L. Mohr, and T. Herbst. Final integration and alignment of LINC-NIRVANA. In *Ground-based and Airborne Instrumentation for Astronomy VI*, volume 9908 of *Proc. SPIE*, page 99082Y, August 2016.

[86] Magalie Nicolle, Thierry Fusco, Vincent Michau, Gérard Rousset, and Jean-Luc Beuzit. Optimization of star-oriented and layer-oriented wavefront sensing concepts for ground layer adaptive optics. *J. Opt. Soc. Am. A*, 23(9):2233–2245, Sep 2006.

[87] R. J. Noll. Zernike polynomials and atmospheric turbulence. *Journal of the Optical Society of America (1917-1983)*, 66:207–211, March 1976.

[88] Y. H. Ono, C. M. Correia, D. R. Andersen, O. Lardière, S. Oya, M. Akiyama, K. Jackson, and C. Bradley. Statistics of turbulence parameters at Maunakea using the multiple wavefront sensor data of RAVEN. *Monthly Notices of the Royal Astronomical Society*, 465:4931–4941, March 2017.

[89] Yoshito H. Ono, Masayuki Akiyama, Shin Oya, Olivier Lardiére, David R. Andersen, Carlos Correia, Kate Jackson, and Colin Bradley. Multi time-step wavefront reconstruction for tomographic adaptive-optics systems. *J. Opt. Soc. Am. A*, 33(4):726–740, Apr 2016.

[90] A. Pavlov, M. Feldt, and T. Henning. Data Reduction and Handling for SPHERE. In R. W. Argyle, P. S. Bunclark, and J. R. Lewis, editors, *Astronomical Data Analysis Software and Systems XVII*, volume 394 of *Astronomical Society of the Pacific Conference Series*, page 581, August 2008.

[91] Lisa Poyneer, Marcos van Dam, and Jean-Pierre Véran. Experimental verification of the frozen flow atmospheric turbulence assumption with use of astronomical adaptive optics telemetry. *J. Opt. Soc. Am. A*, 26(4):833–846, Apr 2009.

[92] Lisa A. Poyneer, Bruce A. Macintosh, and Jean-Pierre Véran. Fourier transform wavefront control with adaptive prediction of the atmosphere. *J. Opt. Soc. Am. A*, 24(9):2645–2660, Sep 2007.

[93] S. Rabien, N. Ageorges, L. Barl, U. Beckmann, T. Blümchen, M. Bonaglia, J. L. Borelli, J. Brynnel, L. Busoni, L. Carbonaro, R. Davies, M. Deysenroth, O. Durney, M. Elberich, S. Esposito, V. Gasho, W. Gässler, H. Gemperlein, R. Genzel, R. Green, M. Haug, M. L. Hart, P. Hubbard, S. Kanneganti, E. Masciadri, J. Noenickx, G. Orban de Xivry, D. Peter, A. Quirrenbach, M. Rademacher, H. W. Rix, P. Salinari, C. Schwab, J. Storm, L. Strüder, M. Thiel, G. Weigelt, and J. Ziegleder. ARGOS: the laser guide star system for the LBT. In *Adaptive Optics Systems II*, volume 7736 of *Proc. SPIE*, pages 77360E–77360E–12, July 2010.

[94] K. K. Radhakrishnan Santhakumari, L. Marafatto, M. Bergomi, V. Viotto, J. Farinato, R. Ragazzoni, T. Herbst, T. Bertram, M. Dima, P. Bizenberger, F. Briegel, F. Kittmann, L. Mohr, and D. Magrin. Ground layer correction: the heart of LINC-NIRVANA. In *Adaptive Optics Systems IV*, volume 9148 of *Proc. SPIE*, page 91482R, July 2014.

[95] R. Ragazzoni. Pupil plane wavefront sensing with an oscillating prism. *Journal of Modern Optics*, 43:289–293, February 1996.

[96] R. Ragazzoni. Pupil plane wavefront sensing with an oscillating prism. *Journal of Modern Optics*, 43:289–293, February 1996.

[97] R. Ragazzoni, E. Diolaiti, J. Farinato, E. Fedrigo, E. Marchetti, M. Tordi, and D. Kirkman. Multiple field of view layer-oriented adaptive optics. Nearly whole sky coverage on 8 m class telescopes and beyond. *Astronomy and Astrophysics*, 396:731–744, December 2002.

[98] R. Ragazzoni, E. Diolaiti, J. Farinato, E. Fedrigo, E. Marchetti, M. Tordi, and D. Kirkman. Multiple field of view layer-oriented adaptive optics. Nearly whole sky coverage on 8 m class telescopes and beyond. *Astronomy and Astrophysics*, 396:731–744, December 2002.

[99] R. Ragazzoni and J. Farinato. Sensitivity of a pyramidic Wave Front sensor in closed loop Adaptive Optics. *Astronomy and Astrophysics*, 350:L23–L26, October 1999.

[100] R. Ragazzoni, E. Marchetti, and F. Rigaut. Modal tomography for adaptive optics. *Astronomy and Astrophysics*, 342:L53–L56, February 1999.

[101] R. Ragazzoni, E. Marchetti, and G. Valente. Adaptive-optics corrections available for the whole sky. *Nature*, 403:54–56, January 2000.

[102] T. Ratzka, A. A. Schegerer, C. Leinert, P. Ábrahám, T. Henning, T. M. Herbst, R. Köhler, S. Wolf, and H. Zinnecker. Spatially resolved mid-infrared observations of the triple system T Tauri. *Astronomy and Astrophysics*, 502:623–646, August 2009.

[103] C. Rauch, A. Eckart, M. Horrobin, B. Lindhorst, S. Rost, S. Smajić, C. Straubmeier, E. Tremou, I. Wank, and J. Zuther. Functional and performance tests of the fringe and flexure tracking system for LINC-NIRVANA. In *Optical and Infrared Interferometry III*, volume 8445 of *Proc. SPIE*, page 844538, July 2012.

[104] Martin Rhodes. *Fluid Flow through a Packed Bed of Particles*, pages 153–168. John Wiley & Sons, Ltd, 2008.

[105] A. Riccardi, M. Xompero, R. Briguglio, F. Quirós-Pacheco, L. Busoni, L. Fini, A. Puglisi, S. Esposito, C. Arcidiacono, E. Pinna, P. Ranfagni, P. Salinari, G. Brusa, R. Demers, R. Biasi, and D. Gallieni. The adaptive secondary mirror for the Large Binocular Telescope: optical acceptance test and preliminary on-sky commissioning results. In *Adaptive Optics Systems II*, volume 7736 of *Proc. SPIE*, page 77362C, July 2010.

[106] L. Ricci, M. Robberto, and D. R. Soderblom. The Hubble Space Telescope/Advanced Camera for Surveys Atlas of Protoplanetary Disks in the Great Orion Nebula. *Astronomical Journal*, 136:2136–2151, November 2008.

[107] S. Rost, A. Eckart, M. Horrobin, B. Lindhorst, C. Rauch, S. Smajic, C. Straubmeier, E. Tremou, I. Wank, J. Zuther, and J.-U. Pott. The LINC-NIRVANA fringe and flexure tracker control system. In *Optical and Infrared Interferometry III*, volume 8445 of *Proc. SPIE*, page 844539, July 2012.

[108] Brice Le Roux, Caroline Kulcsár, Laurent M. Mugnier, Thierry Fusco, Henri-François Raynaud, and Jean-Marc Conan. Optimal control law for classical and multiconjugate adaptive optics. *J. Opt. Soc. Am. A*, 21(7):1261–1276, Jul 2004.

[109] R. Sahai, D. Le Mignant, C. Sánchez Contreras, R. D. Campbell, and F. H. Chaffee. Sculpting a Pre-planetary Nebula with a Precessing Jet: IRAS 16342-3814. *Astrophysical Journal, Letters*, 622:L53–L56, March 2005.

[110] K. K. R. Santhakumari, C. Arcidiacono, T. Bertram, J. Berwein, T. M. Herbst, and R. Ragazzoni. Solving the MCAO partial illumination issue and laboratory results. In *Adaptive Optics Systems V*, volume 9909 of *Proc. SPIE*, page 99096M, July 2016.

[111] K. K. R. Santhakumari, C. Arcidiacono, T. Bertram, J. Berwein, T. M. Herbst, and R. Ragazzoni. A Solution to MCAO Partial Illumination Issue with On-Sky Results. *To Be Submitted*, 2017.

[112] K. K. R. Santhakumari, M. Kasper, and T. M. Herbst. Tadpole like features observed in the T Tauri system. A near-infrared high-contrast imaging study using the LBT-LUCI. *To Be Submitted*, 2017.

[113] Kalyan Kumar Radhakrishnan Santhakumari, Carmelo Arcidiacono, Thomas Bertram, Jürgen Berwein, Tom Herbst, and Roberto Ragazzoni. Solving the multi-conjugated adaptive optics partial illumination issue with laboratory results. In *Imaging and Applied Optics 2016*, page AOM4C.5. Optical Society of America, 2016.

[114] J. Saucedo, N. Calvet, L. Hartmann, and J. Raymond. The Spatial Distribution of Fluorescent $H_2$ Emission near T Tauri. *Astrophysical Journal*, 591:275–282, July 2003.

[115] G. H. Schaefer, L. Prato, M. Simon, and J. Patience. Orbital Motion in Pre-main Sequence Binaries. *Astronomical Journal*, 147:157, June 2014.

[116] G. Schneider, C. A. Grady, D. C. Hines, C. C. Stark, J. H. Debes, J. Carson, M. J. Kuchner, M. D. Perrin, A. J. Weinberger, J. P. Wisniewski, M. D. Silverstone, H. Jang-Condell, T. Henning, B. E. Woodgate, E. Serabyn, A. Moro-Martin, M. Tamura, P. M. Hinz, and T. J. Rodigas. Probing for Exoplanets Hiding in Dusty Debris Disks: Disk Imaging, Characterization, and Exploration with HST/STIS Multi-roll Coronagraphy. *The Astronomical Journal*, 148:59, October 2014.

[117] Matthias Schöck and Earl J. Spillar. Measuring wind speeds and turbulence with a wavefront sensor. *Opt. Lett.*, 23(3):150–152, Feb 1998.

[118] Matthias Schöck and Earl J. Spillar. Method for a quantitative investigation of the frozen flow hypothesis. *J. Opt. Soc. Am. A*, 17(9):1650–1658, Sep 2000.

[119] W. Seifert, I. Appenzeller, H. Baumeister, P. Bizenberger, D. Bomans, R.-J. Dettmar, B. Grimm, T. Herbst, R. Hofmann, M. Juette, W. Laun, M. Lehmitz, R. Lemke, R. Lenzen, H. Mandel, K. Polsterer, R.-R. Rohloff, A. Schuetze, A. Seltmann, N. A. Thatte, P. Weiser, and W. Xu. LUCIFER: a Multi-Mode NIR Instrument for the LBT. In M. Iye and A. F. M. Moorwood, editors, *Instrument Design and Performance for Optical/Infrared Ground-based Telescopes*, volume 4841 of *Proc. SPIE*, pages 962–973, March 2003.

[120] J. M. Shull and S. Beckwith. Interstellar molecular hydrogen. *Annual Review of Astron and Astrophys*, 20:163–190, 1982.

[121] R. M. Smith, M. Zavodny, G. Rahmer, and M. Bonati. A theory for image persistence in HgCdTe photodiodes. In *High Energy, Optical, and Infrared Detectors for Astronomy III*, volume 7021 of *Proc. SPIE*, page 70210J, July 2008.

[122] K. R. Stapelfeldt, C. J. Burrows, J. E. Krist, A. M. Watson, G. E. Ballester, J. T. Clarke, D. Crisp, R. W. Evans, J. S. Gallagher, III, R. E. Griffiths, J. J. Hester, J. G. Hoessel, J. A. Holtzman, J. R. Mould, P. A. Scowen, J. T. Trauger, and J. A. Westphal. Hubble Space Telescope Imaging of the Circumstellar Nebulosity of T Tauri. *Astrophysical Journal*, 508:736–743, December 1998.

[123] G. I. Taylor. The spectrum of turbulence. *Proceedings of the Royal Society of London A: Mathematical, Physical and Engineering Sciences*, 164(919):476–490, 1938.

[124] ARGOS Team. LUCI & ARGOS. http://www.mpe.mpg.de/4362784/LUCI_ARGOS_tech_notes.pdf, 2015.

[125] J. Trowitzsch and T. Bertram. Software-centric view on the LINC-NIRVANA beam control concept. In *Software and Cyberinfrastructure for Astronomy II*, volume 8451 of *Proc. SPIE*, page 84512H, September 2012.

[126] R. van Boekel, A. Juhász, T. Henning, R. Köhler, T. Ratzka, T. Herbst, J. Bouwman, and W. Kley. Variable accretion as a mechanism for brightness variations in T Tauri S. *Astronomy and Astrophysics*, 517:A16, July 2010.

[127] H. J. van Langevelde, E. F. van Dishoeck, P. P. van der Werf, and G. A. Blake. The spatial distribution of excited H2 in T Tau: A molecular outflow in a young binary system. *Astronomy and Astrophysics*, 287:L25–L28, July 1994.

[128] A. Vigan, C. Moutou, M. Langlois, F. Allard, A. Boccaletti, M. Carbillet, D. Mouillet, and I. Smith. Photometric characterization of exoplanets using angular and spectral differential imaging. *Monthly Notices of the Royal Astronomical Society*, 407:71–82, September 2010.

[129] F. Widmann and J-U. Pott. P-REx: The Piston Reconstruction Experiment. *To Be Submitted*, 2017.

[130] Felix Widmann. P-REX: a piston reconstruction experiment for large optical interferometers. *Master Thesis, Heidelberg University, Heidelberg, DE*, 2017.

[131] J. G. Williams. Contributions to the Earth's obliquity rate, precession, and nutation. *Astronomical Journal*, 108:711–724, August 1994.

[132] J. Zuther, A. Eckart, T. Bertram, M. Horrobin, B. Lindhorst, U. Lindhorst, J.-U. Pott, C. Rauch, S. Rost, S. Smajic, C. Straubmeier, I. Wank, U. Beckmann, R. Lenzen, and

E. Tremou. LINC-NIRVANA: optical elements of the fringe and flexure tracker. In *Optical and Infrared Interferometry III*, volume 8445 of *Proc. SPIE*, page 844536, July 2012.

# My Publications

1. A. R. Rao, S. Naik, M. Patil, J. P. Malkar, and **R. P. S. Kalyan Kumar**. *An alpha tagged X-ray source for the calibration of space borne X-ray detectors*. *Nuclear Instruments and Methods in Physics Research A*, 616:55-58, April 2010.

2. M. Bergomi, V. Viotto, J. Farinato, L. Marafatto, **K. Radhakrishnan**, R. Ragazzoni, M. Dima, D. Magrin, C. Arcidiacono, E. Diolaiti, I. Foppiani, M. Lombini, L. Schreiber, T. Bertram, P. Bizenberger, A. Conrad, T. Herbst, F. Kittmann, D. Kopon, D. Meschke, and X. Zhang. *Multiple FoV MCAO on its way to the sky*. In S. Esposito and L. Fini, editors, *Proceedings of the Third AO4ELT Conference*, page 40, December 2013.

3. J. Moreno-Ventas, H. Baumeister, T. Bertram, P. Bizenberger, F. Briegel, D. Greggio, F. Kittmann, L. Marafatto, L. Mohr, **K. Radhakrishnan**, and H. Schray. *Optical integration and verification of LINC-NIRVANA*. In Ground-based and Airborne Instrumentation for Astronomy V, volume 9147 of *Proc. SPIE*, page 91473V, July 2014.

4. **K. K. Radhakrishnan Santhakumari**, L. Marafatto, M. Bergomi, V. Viotto, J. Farinato, R. Ragazzoni, T. Herbst, T. Bertram, M. Dima, P. Bizenberger, F. Briegel, F. Kittmann, L. Mohr, and D. Magrin. Ground layer correction: the heart of LINC-NIRVANA. In Adaptive Optics Systems IV, volume 9148 of *Proc. SPIE*, page 91482R, July 2014.

5. M. Bergomi, V. Viotto, C. Arcidiacono, L. Marafatto, J. Farinato, H. Baumeister, T. Bertram, J. Berwein, F. Briegel, A. Conrad, F. Kittman, D. Kopon, R. Hofferbert, D. Magrin, **K. K. Radhakrishnan Santhakumari**, A. Puglisi, M. Xompero, R. Briguglio, F. Quiros-Pacheco, T. M. Herbst, and R. Ragazzoni. First light of the LINC-NIRVANA Pathfinder

experiment. In *Adaptive Optics Systems IV*, volume 9148 of *Proc. SPIE*, page 91482Y, July 2014.

6. T. Bertram, **K. K. Radhakrishnan Santhakumari**, L. Marafatto, C. Arcidiacono, J. Berwein, R. Ragazzoni, and T. M. Herbst. *Wavefront sensing in a partially illuminated, rotating pupil*. In Adaptive Optics Systems IV, volume 9148 of *Proc. SPIE*, page 91485M, August 2014.

7. D. Kopon, A. Conrad, C. Arcidiacono, T. Herbst, V. Viotto, J. Farinato, M. Bergomi, R. Ragazzoni, L. Marafatto, H. Baumeister, T. Bertram, J. Berwein, F. Briegel, R. Hofferbert, F. Kittmann, M. Kürster, L. Mohr, and **K. Radhakrishnan**. *Pathfinder first light: alignment, calibration, and commissioning of the LINC-NIRVANA ground-layer adaptive optics subsystem*. In Adaptive Optics Systems IV, volume 9148 of *Proc. SPIE*, page 914828, August 2014.

8. D. Magrin, J. Farinato, G. Umbriaco, **K. K. Radhakrishnan Santhakumari** ,M. Bergomi, M. Dima, D. Greggio, L. Marafatto, R. Ragazzoni, V. Viotto, M. Munari, I. Pagano, G. Scandariato, S. Scuderi, G. Piotto, T. Beck, W. Benz, C. Broeg, V. Cessa, A. Fortier, and D. Piazza. *Shaping the PSF to nearly top-hat profile: CHEOPS laboratory results*. In Space Telescopes and Instrumentation 2014: Optical, Infrared, and Millimeter Wave, volume 9143 of *Proc. SPIE*, page 91434L, August 2014.

9. J. E. Schlieder, T. M. Herbst, M. Bonnefoy, N. R. Deacon, **K. Radhakrishnan**, S. Lepine, E. L. Rice, C. Bergfors, T. Henning, E. Gaidos, and A. Kraus. The CASTOFFS Survey: High Resolution Optical Spectroscopy of Bright Targets. In G. T. van Belle and H. C. Harris, editors, 18th Cambridge Workshop on Cool Stars, Stellar Systems, and the Sun, volume 18 of Cambridge Workshop on Cool Stars, Stellar Systems, and the Sun, pages 919-928, January 2015.

10. Luca Marafatto, **Kalyan Kumar Radhakrishnan Santhakumari**, Thomas Bertram, Harald Baumeister, Maria Bergomi, Jurgen Berwein, Peter Bizenberger, Florian Briegel, Tom Herbst, Javier Moreno-Ventas, Frank Kittmann, Jacopo Farinato, Roberto Ragazzoni, and Valentina Viotto. *Aligning the linc-nirvana natural guide stars MCAO system. Adaptive Optics for Extremely Large Telescopes 4 - Conference Proceedings*, 1(1), 2015.

11. **K. K. R. Santhakumari**, C. Arcidiacono, T. Bertram, J. Berwein, T. M. Herbst, and R. Ragazzoni. *Solving the MCAO partial illumination issue and laboratory results*. In Adaptive Optics Systems V, volume 9909 of *Proc. SPIE*, page 99096M, July 2016.

12. **Kalyan Kumar Radhakrishnan Santhakumari**, Carmelo Arcidiacono, Thomas Bertram, Jürgen Berwein, Tom Herbst, and Roberto Ragazzoni. Solving the multi-conjugated adap-

tive optics partial illumination issue with laboratory results. In Imaging and Applied Optics 2016, page AOM4C.5. Optical Society of America, 2016.

13. J. Moreno-Ventas, P. Bizenberger, T. Bertram, **K. K. Radhakrishnan Santhakumari**, F. Kittmann, H. Baumeister, L. Marafatto, L. Mohr, and T. Herbst. Final integration and alignment of LINC-NIRVANA. In Ground-based and Airborne Instrumentation for Astronomy VI, volume 9908 of *Proc. SPIE*, page 99082Y, August 2016.

14. M. Kasper, **K. K. R. Santhakumari**, T. M. Herbst, and R. Köhler. *New circumstellar structure in the T Tauri system. A near-infrared high-contrast imaging study*. *Astronomy and Astrophysics*, 593:A50, September 2016.

15. **K. K. R. Santhakumari**, C. Arcidiacono, T. Bertram, J. Berwein, T. M. Herbst, and R. Ragazzoni. *A Solution to MCAO Partial Illumination Issue with On-Sky Results*. *To Be Submitted*, 2017.

16. **K. K. R. Santhakumari**, M. Kasper, and T. M. Herbst. *Tadpole-like features observed in the T Tauri system. A near-infrared high-contrast imaging study using the LBT-LUCI*. *To Be Submitted*, 2017.

17. M. Kasper, **K. K. R. Santhakumari**, and T. M. Herbst. *Revisiting T Tauri system : A near-infrared high-contrast imaging study using the SPHERE*. *To Be Submitted*, 2017.